



---

**Forschungszentrum Karlsruhe**  
in der Helmholtz-Gemeinschaft

**Wissenschaftliche Berichte**

FZKA 7087

SAM-LACOMERA-D09

# **Results of the QUENCH-10 Experiment on Air Ingress**

**G. Schanz, M. Heck, Z. Hozer, L. Matus,  
I. Nagy, L. Sepold, U. Stegmaier,  
M. Steinbrück, H. Steiner, J. Stuckert,  
P. Windberg**

**Institut für Materialforschung  
Programm Nukleare Sicherheitsforschung**

**Mai 2006**



**Forschungszentrum Karlsruhe**

in der Helmholtz-Gemeinschaft

Wissenschaftliche Berichte

FZKA 7087

SAM-LACOMERA-D09

# Results of the QUENCH-10 Experiment on Air Ingress

G. Schanz, M. Heck, Z. Hozer\*, L. Matus\*, I. Nagy\*, L. Sepold,  
U. Stegmaier, M. Steinbrück, H. Steiner, J. Stuckert, P. Windberg\*

Institut für Materialforschung  
Programm Nukleare Sicherheitsforschung

\* KFKI Atomic Energy Research Institute, Budapest, Hungary

Forschungszentrum Karlsruhe GmbH, Karlsruhe

2006

Für diesen Bericht behalten wir uns alle Rechte vor

Forschungszentrum Karlsruhe GmbH  
Postfach 3640, 76021 Karlsruhe

Mitglied der Hermann von Helmholtz-Gemeinschaft  
Deutscher Forschungszentren (HGF)

ISSN 0947-8620

urn:nbn:de:0005-070876

## Zusammenfassung

### Ergebnisse des Experiments QUENCH-10 zum Lufteinbruch

In den QUENCH-Versuchen wird der Wasserstoffquellterm bei der Einspeisung von Notkühlwasser in einen trockenen, überhitzten Reaktorkern eines Leichtwasserreaktors (LWR) untersucht. Die Testbündel bestehen aus 21 Brennstabsimulatoren mit einer Gesamtlänge von ca. 2,50 m.

Das Experiment QUENCH-10 (Versuch zum Lufteinbruch), das am 21. Juli 2004 im Forschungszentrum Karlsruhe durchgeführt wurde, war das erste von zwei Experimenten, die im Rahmen des LACOMERA-Programms finanziell durch die EU mitgetragen wurden. Der Versuch wurde von AEKI Budapest, Ungarn, vorgeschlagen und zusammen mit dem Forschungszentrum Karlsruhe und unter Mitwirkung des Paul Scherrer Instituts, Schweiz, definiert. Das Hauptziel des Experiments war die Untersuchung der Oxidation und Nitridbildung von Zircaloy während eines Lufteinbruchs, vor dem Fluten des Bündels mit Wasser.

Nach einer Voroxidationsphase von 113 min bei 1620-1690 K und einer Zwischenkühlphase von ~1690 bis 1190 K, die ~38 min dauerte, wurde die Lufteinbruchsphase ausgelöst. In dieser Phase wurde der Dampfstrom von 3 g/s durch einen Luftmengenstrom von 1 g/s ersetzt. Zum Ende der ~30-minütigen Phase wurde ein vollständiger Verbrauch des Sauerstoffs und ein teilweiser Verbrauch des Stickstoffs (etwa 0.1 g/s) beobachtet. Die insgesamt konsumierten O<sub>2</sub>- und N<sub>2</sub>-Mengen betragen 84 bzw. 8 g. Mittels Eckstäben, die zum Ende der Voroxidations- und der Lufteinbruchsphase aus dem Bündel entfernt wurden, wurde festgestellt, dass die angestrebte Oxidschichtdicke der heißen Zone von ~600 µm erreicht worden war.

Das Bündel wurde mit einer Wassereinspeiserate von 50 g/s vom Bündelfuß ausgehend geflutet. Die Bündeltemperaturen betragen zu dieser Zeit ~2200 K. Nahezu unverzüglich erfolgte die Abkühlung, während das vollständige Abschrecken des Bündels etwa 100-150 s dauerte. Zu Beginn der Flutphase kam es zu einer mäßigen Wasserstofferzeugung (~5 g). Zusätzlich wurden etwa 3,5 g Stickstoff freigesetzt (entsprechend 44 % der N<sub>2</sub>-Menge, die zuvor in der Teststrecke absorbiert worden war).

Die Auswertung der Wasserstofffreisetzungsrates ergibt eine Gesamtmenge von 53 g, wovon 47,3 g H<sub>2</sub> bis zum Beginn der Lufteinbruchsphase erzeugt wurden.

Nach dem Experiment zeigten sich Testbündel und Shroud in der Bündelhöhe zwischen 750 und 1000 mm als stark zerstört, d. h. vollständig oxidiert und daher extrem versprödet.

## Abstract

The QUENCH experiments are to investigate the hydrogen source term resulting from the water injection into an uncovered core of a Light-Water Reactor (LWR). The QUENCH test bundle consists of 21 fuel rod simulators with a total length of approximately 2.5 m.

Experiment QUENCH-10 on air ingress conducted at the Karlsruhe Research Center on 21 July 2004 was the first of two experiments to be performed in the frame of the EC supported LACOMERA program. It was proposed by AEKI Budapest, Hungary, and defined together with the Karlsruhe Research Center, supported by Paul Scherrer Institut (PSI), Switzerland. The main objective of this test was to examine the oxidation and nitride formation of Zircaloy during air ingress, before flooding the bundle with water.

After a 113-min pre-oxidation phase at 1620-1690 K and an intermediate cooling phase from ~1690 to 1190 K lasting ~38 min the air ingress phase was initiated. In this phase the steam flow of 3 g/s was replaced by 1 g/s of air. The duration of this phase was ~30 min. Complete consumption of oxygen and partial consumption of nitrogen (about 0.1 g/s) were observed toward the end of this phase. The total uptakes of oxygen and nitrogen were about 84 and 8 g, respectively. Corner rods withdrawn from the bundle toward the end of the pre-oxidation and air ingress phases confirmed that the target oxide layer thickness of ~600  $\mu\text{m}$  in the hot zone was achieved.

Reflood was conducted by injecting 50 g/s of water at the bottom of the test section. Bundle temperatures at the hot zone were then ~2200 K. Cooling was established almost immediately, and complete quenching of the bundle was achieved after about 100-150 s. A modest release of hydrogen, i.e. ~5 g, was observed during the early part of the reflood. Additionally, 3.5 g of the nitrogen were released, i.e. 44 % of  $\text{N}_2$  previously taken up in the test section.

The evaluation of the hydrogen release rates gives 53 g of  $\text{H}_2$  in total, 47.3 g of which was generated up to the beginning of the air ingress phase.

After the experiment the test bundle and its shroud appear severely damaged, i.e. completely oxidized, in the region between 750 and 1000 mm and is therefore extremely embrittled.

# Contents

List of Tables.....	1
List of Figures.....	2
Introduction .....	11
1 Description of the Test Facility .....	13
2 Test Bundle Assembly .....	15
3 Test Bundle Instrumentation .....	15
4 Hydrogen Measurement Devices.....	16
5 Data Acquisition and Process Control.....	18
6 Test Conduct and Pertinent Results.....	18
7 Results of the Aerosol Measurements .....	21
7.1 Objective of Aerosol Measurements.....	21
7.2 Main Characteristics of the Measuring System .....	21
7.3 Post-test Examination of Samples.....	22
7.3.1 Electron Beam Studies .....	22
7.3.2 Sample Preparation.....	23
7.3.3 Results.....	23
7.3.4 Analyses by Mass Spectrometric Methods.....	25
7.4 Summary of Aerosol Measurement .....	25
8 Posttest Examination .....	26
8.1 QUENCH-10 Posttest Appearance Prior to Bundle Sectioning .....	26
8.2 Sectioning of the Test Bundle.....	26
8.3 Metallographic Examination .....	27
8.3.1 Investigation Procedures .....	27
8.3.2 Axial Oxidation Profiles of Corner Rods B and D .....	27
8.3.3 Lateral and Axial Oxide Scale Thickness Distribution .....	28
8.3.4 Documentation and Interpretation of the Bundle Status .....	29
8.3.5 Supporting SEM Inspection and EDX Analysis .....	34
8.3.6 Summary and Conclusions.....	36
8.4 Hydrogen Absorption by Zircaloy .....	37
9 Computational Support .....	38
9.1 Analytical Work for Test Preparation by FZK/IRS and PSI with Help of the SCDAP/RELAP5 mod 3.1irs and MELCOR Codes.....	38
9.2 Modeling of the Central Rod Oxidation with the SVECHA Code.....	38
9.3 Investigation of Oxidation and Hydrogen Behavior with the CALUMO Code .....	39
10 References.....	44
Acknowledgments.....	46



## List of Tables

- Table 1: QUENCH Test Matrix
- Table 2: Design Characteristics of the QUENCH-10 Test Bundle
- Table 3: Diameters of the Material Used for the QUENCH High-Temperature Thermocouples
- Table 4: List of Instrumentation for the QUENCH-10 Test
- Table 5: QUENCH-10; Failure of Thermocouples
- Table 6: QUENCH-10; Change in Contact between Thermocouple and Cladding
- Table 7: QUENCH-10; Sequence of Events
- Table 8: QUENCH-10; Maximum Measured Test Bundle and Shroud Temperatures Evaluated for some Elevations
- Table 9: QUENCH-10; Reaction of Rod Cladding Thermocouples on the Boundary Between Superheated and Saturated Steam
- Table 10: QUENCH-10; Reaction of Fluid Thermocouples on the Boundary Between Superheated and Saturated steam
- Table 11: QUENCH-10; Estimation of Water/Steam Balance
- Table 12: QUENCH-10; Sequence of Aerosol Sampling
- Table 13: QUENCH-10; Results of EDX Investigations
- Table 14: QUENCH-10; Mass Data for the Collector Plates and the Pocket
- Table 15: QUENCH-10; Components Found in the Pocket
- Table 16: QUENCH-10; Components Found on the Ni Plate
- Table 17: QUENCH-10; Scale Readings on the Mass Gain of Epoxy Resin During the Filling Process
- Table 18: QUENCH-10; Cross Sections for the Metallographic Examination

## List of Figures

- Fig. 1: Flow diagram of the QUENCH test facility.
- Fig. 2: QUENCH Facility; Main components.
- Fig. 3: QUENCH Facility; Containment and test section.
- Fig. 4: QUENCH-10; Test section with flow lines.
- Fig. 5: QUENCH-10; Fuel rod simulator bundle (cross section, top view) including rod type indications.
- Fig. 6: Heated fuel rod simulator.
- Fig. 7: Unheated fuel rod simulator.
- Fig. 8: QUENCH-10; Test bundle, TC instrumentation and rod designation (top view).
- Fig. 9: Axial temperature measurement locations in the QUENCH test section.
- Fig. 10: QUENCH; High-temperature thermocouple.
- Fig. 11: QUENCH-10; Concept for TC fastening at the test rod.
- Fig. 12: QUENCH-10; Arrangement of the thermocouples inside the corner rods.
- Fig. 13: QUENCH; H<sub>2</sub> measurement with the GAM 300 mass spectrometer.
- Fig. 14: QUENCH; Mass spectrometer sampling position at the off-gas pipe.
- Fig. 15: QUENCH; Hydrogen measurement with the CALDOS analyzer.
- Fig. 16: QUENCH-10; Aerosol sampling system.
- Fig. 17: QUENCH-10; Main components of the aerosol sampling system.
- Fig. 18: QUENCH-10; Scheme of the impactor sampler.
- Fig. 19: QUENCH-10; Sampling location at the off-gas pipe for the aerosol sampler, top, Connection of the aerosol sampling device to the off-gas pipe, bottom.
- Fig. 20: QUENCH-10; Arrangement to hold the Ni-plate in the off-gas pipe of the QUENCH facility.
- Fig. 21: QUENCH-10; Off-gas pipe (top view).
- Fig. 22: QUENCH-10; Test conduct as planned, top, test as conducted, bottom.

- Fig. 23: QUENCH-10; Test phase definitions together with temperature at elevation 950 mm , electrical power input and heating rates during the air ingress phase.
- Fig. 24: QUENCH-10; Bundle temperatures during the test.
- Fig. 25: QUENCH-10; Shroud temperatures during the test.
- Fig. 26: QUENCH-10; Coolant temperatures at different elevations.
- Fig. 27: QUENCH-10; Overview of the TCI, top, and TCO temperatures, bottom.
- Fig. 28: QUENCH-10; Temperatures measured at different locations of outer pipe surfaces, downstream the test section inlet.
- Fig. 29: Temperatures at test section outlet (T 512), at the inner surface of the off-gas pipe (T307) together with gas temperature T 601, top, and central containment temperature at ~1450 mm together with inlet (T 002) and outlet (T 003) temperatures of the water coolant of the off-gas pipe, bottom.
- Fig. 30: QUENCH-10; Bundle and shroud temperatures during the air ingress phase together with the electric power history.
- Fig. 31: QUENCH-10; Temperatures during the quenching phase.
- Fig. 32: QUENCH-10; Quench water injection and steam generation.
- Fig. 33: QUENCH-10; Progression of the wetting front and of the boundary between superheated and saturated steam.
- Fig. 34: QUENCH-10; Argon pressure P 406 indicating shroud failure shortly after onset of reflood, i.e. at 13397 s, together with system pressure at the test section inlet (P 511), top, and helium release rate measured by MS, bottom.
- Fig. 35: QUENCH-10; Hydrogen release rates measured by mass spectrometer and Caldos analyzer (Caldos values were set zero during air ingress phase), top. Integral hydrogen release measured by MS and Caldos, bottom.
- Fig. 36: QUENCH-10; Nitrogen and oxygen rates measured by MS in the off-gas during the air ingress phase, top, and during the quench phase, bottom.
- Fig. 37: QUENCH-10; Timing of aerosol sampling.
- Fig. 38: QUENCH-10; Weight gain from aerosol sampling.
- Fig. 39: QUENCH-10; Digital BEI image and some EDX spectra for Sample 2/5 showing various Fe-containing particles.
- Fig. 40: QUENCH-10; Zr (Sn) containing particles and a typical EDX spectrum for Sample 2/9.

- Fig. 41: QUENCH-10; Typical SEI image taken from aerosols deposited on the Ni plate.
- Fig. 42: QUENCH-10; Typical BEI image (magnification 1000 x) and two EDX spectra of aerosols deposited on the Ni plate.
- Fig. 43: QUENCH-10; Microscopic image of sample Q5.
- Fig. 44: QUENCH-10; Results of SSMS measurements taken at the quartz fiber filters.
- Fig. 45: QUENCH-10; Posttest view of the QUENCH-10 bundle.
- Fig. 46: QUENCH-10; Posttest view of the QUENCH-10 bundle at the elevations of the hot zone (after removal of the shroud insulation).
- Fig. 47: QUENCH-10; Parts of shroud of the QUENCH-10 bundle which fell off during handling (at ~850 mm elevation).
- Fig. 48: QUENCH-10; Photographs taken by a videoscope inserted into the bundle from the bottom, at the (voided) position of extracted corner rod B.
- Fig. 49: QUENCH-10; Photographs taken by a videoscope inserted into the bundle from the bottom, at the empty position of extracted corner rod D.
- Fig. 50: Distribution of particles taken from the off-gas pipe after the QUENCH-10 experiment; Quantity distribution, top, mass distribution, bottom.
- Fig. 51: QUENCH-10; Oxide scale thickness of corner rod B at 750, 800 and 850 mm elevation.
- Fig. 52: QUENCH-10; Oxide scale thickness of corner rod B at 900, 950 and 1000 mm elevation.
- Fig. 53: QUENCH-10; Oxide scale thickness of corner rod B at 1050 and 1100 mm elevation.
- Fig. 54: QUENCH-10; Oxide scale thickness of corner rod D at 750, 800 and 850 mm elevation.
- Fig. 55: QUENCH-10; Corner rods as pulled out of the bundle: rod B (end of steam pre-oxidation) and rod D (at end of air oxidation phase).
- Fig. 56: QUENCH-10; Overview of the withdrawn corner rods B and D, and comparison of their oxidation at the previous bundle position 850 mm.
- Fig. 57: QUENCH-10; Cross sections at 635 mm, 650 mm, 735 mm, and 750 mm.
- Fig. 58: QUENCH-10; Cross sections at 800 mm, 833 mm, 835 mm, and 850 mm.
- Fig. 59: QUENCH-10; Cross sections at 937 mm, 950 mm, 1052 mm, and 1080 mm.
- Fig. 60: QUENCH-10; Oxide layer thickness at bundle elevation 500 mm (Cross section QUE-10-2)

- Fig. 61: QUENCH-10; Oxide layer thickness at bundle elevation 650 mm (Cross section QUE-10-3)
- Fig. 62: QUENCH-10; Oxide layer thickness at bundle elevation 750 mm (Cross section QUE-10-4)
- Fig. 63: QUENCH-10; Oxide layer thickness at bundle elevation 800 mm (Cross section QUE-10-8)
- Fig. 64: QUENCH-10; Oxide layer thickness at bundle elevation 850 mm (Cross section QUE-10-5)
- Fig. 65: QUENCH-10; Oxide layer thickness at bundle elevation 950 mm (Cross section QUE-10-6)
- Fig. 66: QUENCH-10; Oxide layer thickness at bundle elevation 1080 mm (Cross section QUE-10-7)
- Fig. 67: QUENCH-10; axial profiles of oxide layer thickness, given as mean values for all bundle components (top), average and standard deviation for simulator rods (bottom).
- Fig. 68: QUENCH-10; Cross section at 500 mm bundle elevation (QUE-10-2); overview from top.
- Fig. 69: QUENCH-10; Cross section at 500 mm (QUE-10-2); internal shroud scale at NW, showing post-transitional crack system formation and some embedded zirconium nitride phase (bottom, right).
- Fig. 70: QUENCH-10; Cross section at 500 mm (QUE-10-2), inner shroud scale at E and NE: Top-layer spalling (initiated by scratches), sub-layers cracking, and zirconia / zirconium nitride penetration.
- Fig. 71: QUENCH-10; Cross section at 650 mm bundle elevation (QUE-10-3); overview from top.
- Fig. 72: QUENCH-10; Cross section at 650 mm bundle elevation (QUE-10-3). Macrographs from bundle periphery, showing rod simulators 15 and 21, corner rods A, C, D, shroud, and rubble.
- Fig. 73: QUENCH-10; Cross section at 650 mm bundle elevation (QUE-10-3). Macrographs of some rod simulators of the first ring.
- Fig. 74: QUENCH-10; Cross section at 650 mm bundle elevation (QUE-10-3), central rod cladding: Scale with pre-transition morphology, and thick  $\alpha$ -Zr(O) sub-layer which shows some fracturing.
- Fig. 75: QUENCH-10; Cross section at 650 mm bundle elevation (QUE-10-3), cladding of rod 11: Scale with pretransition morphology and thick  $\alpha$ -Zr(O) sub-layer, both showing some fracturing.

- Fig. 76: QUENCH-10; Cross section at 650 mm bundle elevation (QUE-10-3), shroud, inner scale at NW: Cracked and partially spalled sub-layers, and innermost sub-layer of zirconia / zirconium nitride.
- Fig. 77: QUENCH-10; Cross section at 650 mm (QUE-10-3), shroud, internal post-transition scale at N. Inner sub-layer with ZrN (top, right), scattering of polarized light indicates scale degradation (bottom, left).
- Fig. 78: QUENCH-10; Cross section at 750 mm bundle elevation (QUE-10-4); overview from top.
- Fig. 79: QUENCH-10; Cross section at 750 mm bundle elevation (QUE-10-4). Macrographs of selected rods, showing typical partial cladding oxidation and different extent of pellet contact.
- Fig. 80: QUENCH-10; Cross section at 750 mm bundle elevation (QUE-10-4). Macrographs of corner rods A and C, showing filling of instrumented tubular section by internally relocated melt.
- Fig. 81: QUENCH-10; Cross section at 750 mm bundle elevation (QUE-10-4). Details of cladding oxidation of rod 9 at two positions, where some nitrogen penetration took place.
- Fig. 82: QUENCH-10; Cross section at 750 mm bundle elevation (QUE-10-4). Details of cladding oxidation of rod 3, illustrating local cladding scale defects and related growth morphology.
- Fig. 83: QUENCH-10; Cross section at 750 mm (QUE-10-4). Cladding of rod 16, showing presence of an inner scale, possibly formed during steam/air ingress through an axially elongated scale crack.
- Fig. 84: QUENCH-10; Cross section at 750 mm (QUE-10-4). Shroud at two positions, illustrating sound (left) vs. locally degraded scale, from which no  $\alpha$ -Zr(O) phase precipitates during cooling (right).
- Fig. 85: QUENCH-10; Cross section at 800 mm bundle elevation (QUE-10-8); overview from top.
- Fig. 86: QUENCH-10; Cross section at 800 mm bundle elevation (QUE-10-8). Macrographs of selected rods, showing the typical almost complete cladding oxidation, and some extent of pellet interaction.
- Fig. 87: QUENCH-10; Cross section at 800 mm bundle elevation (QUE-10-8). Corner rod A and shroud at SE (left side), corner rod C and shroud at NW (right side).
- Fig. 88: QUENCH-10; Cross section at 800 mm bundle elevation (QUE-10-8). Mostly oxidized cladding of central rod, showing, in comparison to polarization contrast, localized air-related morphology.
- Fig. 89: QUENCH-10; Cross section at 800 mm bundle elevation (QUE-10-8). Mostly oxidized cladding of rod 2, shown in comparison to polarization contrast; air ingress into cladding and pellet gap.

- Fig. 90: QUENCH-10; Cross section at 800 mm bundle elevation (QUE-10-8). Finally oxidized cladding of rod 6 after air attack, and indications of air ingress into gap and simulator pellet.
- Fig. 91: QUENCH-10; Cross section at 800 mm bundle elevation (QUE-10-8). Attack of the fully oxidized cladding of rod 7 during the air exposure phase of the experiment, resulting in residual ZrN phase.
- Fig. 92: QUENCH-10; Cross section at 800 mm bundle elevation (QUE-10-8). Attack of the cladding of rod 13 during the air exposure period, resulting in residual ZrN phase, embedded within the scale.
- Fig. 93: QUENCH-10; Cross section at 800 mm bundle elevation (QUE-10-8). External attack of the cladding of rod 20 during the air exposure period, and residual, internally confined  $\alpha$ -Zr(O) cladding matrix.
- Fig. 94: QUENCH-10; Cross section at 850 mm bundle elevation (QUE-10-5); overview from top.
- Fig. 95: QUENCH-10; Cross section at 850 mm bundle elevation (QUE-10-5). Region of rod 4, showing ZrN phase formation, related to air ingress into the cladding scale and the pellet gap.
- Fig. 96: QUENCH-10; Cross section at 850 mm bundle elevation (QUE-10-5). Cladding scale of rod 12, showing locally concentrated ZrN phase penetration by conversion of scale.
- Fig. 97: QUENCH-10; Cross section at 850 mm bundle elevation (QUE-10-5). Cladding / pellet gap region of rod 12 after air-starved exposure and partial re-oxidation.
- Fig. 98: QUENCH-10; Cross section at 850 mm bundle elevation (QUE-10-5). Inner side of shroud towards E, after air-starved (nitrogen-rich) exposure and movement of the re-oxidation front.
- Fig. 99: QUENCH-10; Cross section at 950 mm bundle elevation (QUE-10-6); overview from top.
- Fig. 100: QUENCH-10; Cross section at 950 mm bundle elevation (QUE-10-6). Shroud towards N, after the air-starved (nitrogen-rich) exposure of the inner scale, and the movement of a re-oxidation front.
- Fig. 101: QUENCH-10; Cross section at 950 mm bundle elevation (QUE-10-6). Shroud towards NW, after air-starved (nitrogen-rich) exposure, re-oxidation front movement, and top layer spalling.
- Fig. 102: QUENCH-10; Cross section at 1080 mm bundle elevation (QUE-10-7); overview from top.
- Fig. 103: QUENCH-10; Cross section at 1080 mm bundle elevation (QUE-10-7). Macrographs of selected rods, showing no localized effects of air exposure.
- Fig. 104: QUENCH-10; Cross section at 1080 mm bundle elevation (QUE-10-7). Macrographs of selected rods, showing cladding fragmentation as effect of local attack of air.

- Fig. 105: QUENCH-10; Cross section at 1080 mm bundle elevation (QUE-10-7). Oxidation status of the central rod, showing minor scale irregularities.
- Fig. 106: QUENCH-10; Cross section at 1080 mm bundle elevation (QUE-10-7). Oxidation status of rod 20 (left), compared to a regular position of rod 5 (right, see next figure).
- Fig. 107: QUENCH-10; Cross section at 1080 mm bundle elevation (QUE-10-7). Oxidation state of rod 5 at two positions, showing formation of scale fractures caused by air penetration.
- Fig. 108: QUENCH-10; Cross section at 1080 mm bundle elevation (QUE-10-7). Shroud oxidation, showing the typical pre-transition scale (left), compared to local presence of post-transition scale (right).
- Fig. 109: QUENCH-10; SEM analysis of rod 4 at 850 mm elevation (QUE-10-5). Comparison of LM and BSE contrast indicates presence of ZrN phase, EDX spectrum confirms this (see Fig. 95).
- Fig. 110: QUENCH-10; SEM analysis of rod 12 at 850 mm elevation (QUE-10-5). Comparison of LM and SE contrast indicates presence of ZrN phase, EDX spectra confirm ZrN or ZrO<sub>2</sub>, respectively (see Fig. 96).
- Fig. 111: QUENCH-10; SEM analysis of the shroud at 850 mm elevation (QUE-10-5). Comparison of LM, BSE and SE contrasts, and EDX spectra confirm presence of ZrN phase (see Fig. 98).
- Fig. 112: QUENCH-10; SEM analysis of the shroud at 950 mm elevation (QUE-10-6). Comparison of LM, BSE and SE contrasts, and EDX spectra confirm presence of ZrN phase (see Fig. 100).
- Fig. 113: QUENCH-10; SEM analysis of the shroud at 950 mm elevation (QUE-10-6). Comparison of LM and BSE contrast is sufficient to confirm presence of ZrN phase (see Fig. 101).
- Fig. 114: QUENCH-10; Temperature profiles for three of eighteen meshes (elevation 675, 925, and 1250 mm) calculated with SCDAP/RELAP 5 and used as an input for the SVECHA computations of test QUENCH-10.
- Fig. 115: SVECHA calculation of hydrogen production in QUENCH-10, extrapolated from the central rod to the whole bundle.
- Fig. 116: QUENCH-10; Evolution of the cladding layer thickness at different bundle elevations computed by SVECHA for experiment QUENCH-10.
- Fig. 117: QUENCH-10; Failure parameter  $f$  for the inner row of heated fuel rod simulators versus time.
- Fig. 118: Evolution of rod and shroud temperatures of QUENCH-10 at different axial locations, CALUMOqxf-calculated data in comparison with experimental values.
- Fig. 119: Evolution of rod and shroud temperatures of QUENCH-10 at different axial locations, CALUMOqxf-calculated data in comparison with experimental values.

- Fig. 120: QUENCH-10; Axial profile of the central rod temperature over the period of air ingress.
- Fig. 121: Evolution of the hydrogen production rate and the overall produced hydrogen for QUENCH-10 calculated with CALUMOqxf. (Overview on top, detailed graph bottom)
- Fig. 122: QUENCH-10; Axial distributions of the oxide scale thickness for the removed corner rods B and D (top, left), at the end of QUENCH-10 for the shroud (top; right) and all rods (bottom).



## Introduction

The most important accident management measure to terminate a severe accident transient in a Light Water Reactor (LWR) is the injection of water to cool the uncovered degraded core. Analysis of the TMI-2 [1] accident and the results of integral out-of-pile (CORA [2, 3]) and in-pile experiments (LOFT [4], PHEBUS [5]) have shown that before the water succeeds in cooling the fuel pins there will be an enhanced oxidation of the Zircaloy cladding that in turn causes a sharp increase in temperature, hydrogen production and fission product release.

Besides, quenching is considered a worst-case accident scenario regarding hydrogen release to the containment. For in- and ex-vessel safety analyses one has to prove that the hydrogen release rate and total amount do not exceed limits for the considered power plant. The hydrogen generation rate must be known to design appropriately accident mitigation measures for the following reasons.

- Passive autocatalytic recombiners require a minimum hydrogen concentration to start. Moreover, they work slowly, and their surface area and their position in the containment have to be quantified carefully.
- The air-steam-hydrogen mixture in the containment may be combustible for only a short time before detonation limits are reached. This limits the time period during which ignitors can be used.

The physical and chemical phenomena of the hydrogen release are, however, not sufficiently well understood. The increased hydrogen production during quenching cannot be determined on the basis of the available Zircaloy/steam oxidation correlations. Presently it is assumed that the following phenomena lead to an enhanced oxidation and hydrogen generation [6]:

- Melt oxidation,
- Steam starvation conditions.

In most of the code systems describing severe fuel damage, these phenomena are either not considered or only modeled in a simplified empirical manner.

In addition, no models are yet available to predict correctly the thermal-hydraulic or the clad behavior of the quenching processes in the CORA and LOFT LP-FP-2 tests. An extensive experimental database is therefore needed as a basis for model development and code improvement.

The Forschungszentrum Karlsruhe is therefore performing the QUENCH program on the investigation of coolability and determination of the hydrogen source term. The main objectives of this program are:

- The provision of an extensive experimental database for the development of detailed mechanistic fragmentation models,
- The examination of the physico-chemical behavior of overheated fuel elements under different flooding conditions,

- The provision of an improved understanding of the effects of water injection at different stages of core degradation,
- The determination of cladding failure criteria, cracking of oxide layers, exposure of new metallic surfaces to steam,
- The investigation of the oxide layer degradation under steam starvation conditions and influence of this phenomenon on subsequent flooding,
- The investigation of the melt oxidation process,
- The determination of the hydrogen source term.

The experimental part of the QUENCH program began with small-scale experiments using short Zircaloy fuel rod segments [7-9]. On the basis of these results well-instrumented large-scale bundle experiments with fuel rod simulators under nearly adiabatic conditions are performed in the QUENCH facility of the Forschungszentrum Karlsruhe. The large-scale bundle experiments are more representative of prototypic reactor accident conditions than are the single-rod experiments. Important parameters of the bundle test program (see [Table 1](#)) are: quench medium, i.e. water or steam, fluid injection rate, cladding oxide layer thickness, and the temperature at onset of flooding.

Test QUENCH-10, performed at the Karlsruhe Research Center on 21 July 2004, as the first of two experiments in the frame of the EC-supported LACOMERA program [10], was proposed by AEKI Budapest, and supported by PSI (Paul-Scherrer-Institut, Switzerland). The main objective of this test was to examine the oxidation and nitride formation of Zircaloy during air ingress, before flooding the bundle with water. The test should also support understanding of the consequences of a possible failure of heat removal in a spent fuel pool. Evaporation of the pool water may lead to fuel element degradation, and consequently fission product release from the damaged fuel elements [11]. Complimentary to air ingress test QUENCH-10 supported tests a series of single-effect experiments [12, 13] were performed, which showed very complex phenomena in the cladding material during the air ingress phase.

This report describes the test facility and the test bundle, and the main results of the QUENCH-10 experiment including the posttest examination and computational results using the SVECHA and CALUMO computer codes. Further analytical support by using the SCDAP/RELAP5 mod 3.1irs and MELCOR codes for the preparation of the entire test is published elsewhere [14].

# 1 Description of the Test Facility

The QUENCH test facility consists of the following component systems:

- the test section with 21 fuel rod simulators,
- the electric power supply for the test bundle heating,
- the water and steam supply system,
- the argon gas supply system,
- the hydrogen measurement devices,
- temperature, pressure, mass flow measurement devices,
- the process control system,
- the data acquisition system.

A simplified flow diagram of the QUENCH test facility is given in [Fig. 1](#), a three-dimensional schematic of the components in [Fig. 2](#). The main component of the facility is the test section with the test bundle ([Figs. 3 and 4](#)). [Fig. 4](#) also indicates the position for air ingress (80 % N<sub>2</sub> and 20 % O<sub>2</sub>). The superheated steam from the steam generator and superheater together with argon as the carrier gas for the hydrogen detection systems enter the test bundle at the bottom end. The steam that is not consumed, the argon, and the hydrogen produced in the zirconium-steam reaction flow from the bundle outlet through a water-cooled off-gas pipe to the condenser ([Figs. 1 and 2](#)). Here the steam is separated from the non-condensable gases argon and hydrogen. The quenching (water) or cooling (saturated steam) phase is initiated by turning off the superheated steam of 3 g/s whereas the argon flow rate remains unchanged. At the same time quench water is injected at the bottom of the test section.

The design characteristics of the test bundle are given in [Table 2](#). The test bundle is made up of 21 fuel rod simulators, each with a length of approximately 2.5 m, and of four corner rods (see cross section in [Fig. 5](#)). The fuel rod simulators ([Fig. 6](#)) are held in their positions by five grid spacers, four of Zircaloy, and one of Inconel in the lower bundle zone. The cladding of the fuel rod simulators is identical to that used in PWRs with respect to material and dimensions, i.e. Zircaloy-4, 10.75 mm outside diameter, 0.725 mm wall thickness.

Two minor changes concerning the test facility were realized prior to the QUENCH-10 test:

- The annulus between shroud and cooling jacket was connected to a flow-controlled argon feeding system in order to prevent steam access to the annulus after shroud failure. (In previous QUENCH experiments there was a static filling with argon at a slight overpressure related to the system pressure).
- The fuel rod simulators were filled with helium instead of an argon/krypton mixture. The gas filling of all rods was, as usual, realized by a channel-like connection system inside the lower sealing plate which was additionally connected to a controlled feeding system that compensated minor gas losses and allowed observation of a first cladding failure as well as a failure progression.

The rod internal pressure was (as usual) held at 0.22 MPa, i.e. a pressure slightly above the system pressure (0.2 MPa).

Twenty fuel rod simulators are heated electrically over a length of 1024 mm, the unheated fuel rod simulator is located in the center of the test bundle. The unheated fuel rod simulator (Fig. 7) is filled with ZrO<sub>2</sub> pellets (bore size 2.5 mm ID). For the heated rods (Fig. 6) 6 mm diameter tungsten heating elements are installed in the center of the rods and are surrounded by annular ZrO<sub>2</sub> pellets. The tungsten heaters are connected to electrodes made of molybdenum and copper at each end of the heater. The molybdenum and copper electrodes are joined by high-frequency/high-temperature brazing under vacuum using an AuNi 18 powder (particle size < 105 μm). For electrical insulation the surfaces of both types of electrodes are plasma-coated with 0.2 mm ZrO<sub>2</sub>. To protect the copper electrodes and the O-ring-sealed wall penetrations against excessive heat they are water-cooled (lower and upper cooling chambers filled with demineralized water). The copper electrodes are connected to the DC electric power supply by means of special sliding contacts at the top and bottom. The total heating power available is 70 kW, distributed among two groups of heated rods with 35 kW each. The first group consists of the inner eight rods (rod numbers 2–9), the second group consists of the outer twelve rods (rod numbers 10–21). The rod designation can be taken from Fig. 8.

The lower boundary for the lower cooling chamber is a sealing plate made of stainless steel with plastic inlays for electrical insulation, sealed to the system by O-shaped rings. The upper boundary of the lower cooling chamber is a sealing plate of stainless steel. An insulation plate made of plastic (PEEK) forms the top of the upper cooling chamber, and a sealing plate of Al<sub>2</sub>O<sub>3</sub>, functioning as a heat-protection shield, is the lower boundary of the upper cooling chamber (see Fig. 6).

In the region below the upper Al<sub>2</sub>O<sub>3</sub> plate the copper electrode is connected firmly to the cladding. This is done by hammering the cladding onto the electrode with a sleeve of boron nitride put between electrode and cladding for electrical insulation. The axial position of the fuel rod simulator in the test bundle is fixed by a groove and a locking ring in the top Cu electrodes. Referred to the test bundle the fixing of the fuel rod simulators is located directly above the upper edge of the upper insulation plate. So, during operation the fuel rod simulators are allowed to expand downwards. Clearance for expansion of the test rods is provided in the region of the lower sealing plate. Also in this region relative movement between cladding and internal heater/electrode can take place.

The test bundle is surrounded by a 2.38 mm thick shroud (80 mm ID) made of Zircaloy with a 37 mm thick ZrO<sub>2</sub> fiber insulation and an annular cooling jacket made of inconel (inner tube) and stainless steel (outer tube; see Fig. 5). The annulus between shroud and cooling jacket was filled (after several cycles of degassing) with stagnant argon of 0.22 MPa whereas the 6.7 mm annulus of the cooling jacket is cooled by an argon flow. Above the heated zone, i.e. above the 1024 mm elevation there is no ZrO<sub>2</sub> fiber insulation to allow for higher radial heat losses. This region of the cooling jacket is cooled by a water flow (Figs. 3 and 4). Both the lack of ZrO<sub>2</sub> insulation above the heated region and the water cooling force the axial temperature maximum downward.

The four corner positions of the bundle are occupied either by solid Zircaloy (Zry) rods with a diameter of 6 mm or by solid rods (upper part) / Zry tubes (lower part) of  $\varnothing 6 \times 0.9$  mm for thermocouple instrumentation at the inside (Figs. 5 and 8). The positioning of the four corner rods avoids an atypically large flow cross section at the outer positions and hence helps to obtain a rather uniform radial temperature profile. In the QUENCH-10 test bundle two of them, i.e. rods "A" and "C" were used for thermocouple instrumentation whereas the other two rods, i.e. rods "B" and "D" (solid Zry rods) were withdrawn from the bundle at the end of pre-oxidation and prior to quenching, respectively, to check the amount of  $ZrO_2$  oxidation at those times.

## 2 Test Bundle Assembly

The test section consists of three subassemblies pre-assembled separately. One subassembly comprises the cooling jacket with the bundle head casing; the second subassembly includes the instrumented shroud with the bundle foot; and the third subassembly is composed of the instrumented test bundle with the bundle head. The test bundle and the shroud, including the respective thermocouples, must be replaced for each experiment. The instrumentation of the bundle head and the foot as well as that of the cooling jacket, however, remains unchanged.

## 3 Test Bundle Instrumentation

The test bundle was instrumented with sheathed thermocouples (TC) attached to the rod claddings at 17 different elevations between -250 mm and 1350 mm and at different orientations according to [Figs. 8 and 9](#). The elevations of the surface-mounted shroud thermocouples are from -250 mm to 1250 mm. In the lower bundle region, i.e. up to the 550 mm elevation, NiCr/Ni thermocouples (1 mm diameter, stainless steel sheath 1.4541, MgO insulation) are used for temperature measurement of rod cladding and shroud as is illustrated in [Fig. 9](#). The thermocouples of the hot zone are high-temperature thermocouples with W-5Re/W-26Re wires,  $HfO_2$  insulation, and a duplex sheath of tantalum (internal)/Zirconium with an outside diameter of 2.1 mm ([Fig. 10](#) and [Table 3](#)).

The thermocouple attachment technique for the surface-mounted high-temperature TCs is illustrated in [Fig. 11](#). The TC tip is held in place by two clamps of zirconium (0.2 mm thick). As these clamps are prone to oxidation and embrittlement in a steam environment an Ir-Rh wire of 0.25 mm diameter is additionally used in the experiments with pre-oxidation as was the case in test bundle QUENCH-10. The leads of the thermocouples from the -250 mm to the 850 mm level leave the test section at the bottom whereas the TCs above 850 mm are routed to the top. Based on the results of experiment QUENCH-09 it was avoided to route the TC cables through the hot zone. Depending on their axial position, they exit the test section either to the top or the bottom. Additionally, the cables of shroud thermocouples TSH xx/x "I" were routed toward outside the shroud insulation to avoid heat transfer into the TC cable apart from the TC junction.

The [designations](#) of the surface-mounted cladding and shroud thermocouples are "TFS" and "TSH", respectively. The unheated fuel rod simulator of the QUENCH-10 bundle ([Fig. 7](#)) is

instrumented with two centerline thermocouples, i.e. TCRC 12 (at 850 mm, W/Re,  $\varnothing$  2.1 mm, routed to bottom) and TCRC 13 (at 950 mm, W/Re,  $\varnothing$  2.1 mm, routed to top) and two thermocouples at the rod cladding outer surface, i.e. TCR 7 (at 350 mm, NiCr/Ni,  $\varnothing$  1 mm, routed to bottom), TCR 9 (at 550 mm, NiCr/Ni,  $\varnothing$  1 mm, routed to bottom).

The wall of the inner tube of the cooling jacket is instrumented between -250 mm and 1150 mm with NiCr/Ni thermocouples (designation "TCI"). The thermocouples that are fixed at the outer surface of the outer tube of the cooling jacket (designation "TCO") are also of the NiCr/Ni type. The designation of the thermocouples inside the Zircaloy corner rods is "TIT". According to [Fig. 12](#) two of the four corner rods of the QUENCH-10 test bundle are instrumented as follows:

- Rod A: W/Re, 2.1 mm diameter, Zr/Ta duplex sheath, 950 mm elevation (TIT A/13)
- Rod C: W/Re, 2.1 mm diameter, Zr/Ta duplex sheath, 850 mm elevation (TIT C/12).

A list of the instruments for experiment QUENCH-10 installed in the test section and at the test loop are given in [Table 4](#). The thermocouples that failed prior or during the test are listed in [Table 5](#) and changes in contact between thermocouple and cladding in [Table 6](#).

## 4 Hydrogen Measurement Devices

The hydrogen is analyzed by two different measurement systems: (1) a Balzers mass spectrometer (MS) "GAM 300" ([Fig. 13](#)) and (2) a hydrogen detection system "Caldos 7 G" ([Fig. 15](#)) located in a bypass to the off-gas line downstream the condenser. Due to their different locations in the facility the mass spectrometer "GAM 300" responds almost immediately (less than 5 s) to a change in the gas composition whereas the Caldos device has a delay time of about 20-30 s. The time delay of the off-gas analyzing systems has been determined with several bundle flows and gas injections at the 700 mm level of a dummy test section particularly installed for calibration purposes. A first series was performed at room pressure and temperature with 3 and 6 g/s argon flow in the bundle and hydrogen as injection gas. A second series was performed at 1000 K maximum rod surface temperature with a mixture of 3 g/s argon and 3 and 50 g/s steam flow in the bundle at a system pressure of 0.2 MPa and with helium as injection gas. Besides the time delay, the signal shapes are different for the Caldos H<sub>2</sub> analyzer resulting in a broader peak due to the diffusion of the hydrogen in the offgas.

The mass spectrometer "BALZERS GAM 300" used is a completely computer-controlled quadrupole MS with an 8 mm rod system which allows quantitative measurement of gas concentrations down to about 10 ppm. For the MS measurement a sampling tube is inserted in the off-gas pipe ([Fig. 14](#)) located approx. 2.7 m downstream from the test section outlet (see also [Fig. 21](#)). It has several holes at different elevations to guarantee that the sampling of the gas to be analyzed is representative. To avoid steam condensation in the gas pipes between the sampling position and the MS the temperature of the gas at the MS inlet is controlled by heating tapes to be between 110 °C and 150 °C (the upper operating temperature of the MS inlet valves). This allows the MS to analyze the steam production rate.

Besides, the concentrations of the following species were continuously measured by the mass spectrometer during all test phases: argon, hydrogen, steam, nitrogen, oxygen, and helium. The fuel rod simulators are filled with helium as a tracer gas which can be used as an indicator for a cladding failure. Additionally, the MS is used to control the atmosphere in the facility, e.g., to monitor the gas composition at the beginning of the test.

The temperature and pressure of the analyzed gas are measured near the inlet valve of the MS. The MS is calibrated for hydrogen, oxygen and nitrogen with well-defined argon/gas mixtures and for steam with mixtures of argon and steam supplied by a Bronkhorst controlled evaporator mixing (CEM) device. The MS off-gas is released into the atmosphere because the amount of hydrogen taken out of the system is negligible. A heated measuring gas pump was used to ensure a continuous flow of the steam-gas mixture from the off-gas pipe to the mass spectrometer.

The principle of measurement of the Caldos system is based on the different heat conductivities of different gases. The Caldos device is calibrated for the hydrogen-argon gas mixture. To avoid any moisture in the analyzed gas a gas cooler, which is controlled at 296 K, is connected to the gas analyzer (see also [Fig. 15](#)). The response time of the gas analyzer is documented by the manufacturer to be 2 s, i.e. a time in which 90 % of the final value should be reached. In contrast to the mass spectrometer the Caldos device only measures the hydrogen content. Gases other than H<sub>2</sub> cannot be analyzed by this system.

For the Caldos device as well as for the MS the hydrogen mass flow rate is calculated by referring the measured H<sub>2</sub> concentration to the known argon mass flow rate according to equation (1):

$$\dot{m}_{H_2} = \frac{M_{H_2}}{M_{Ar}} \cdot \frac{C_{H_2}}{C_{Ar}} \cdot \dot{m}_{Ar} \quad (1)$$

with M representing the molecular masses, C the concentrations in vol-% and  $\dot{m}$  the mass flow rates of the corresponding gases.

With an argon-hydrogen (two-component) mixture that in fact exists at the location of the Caldos analyzer equation (1) can be written as follows

$$\dot{m}_{H_2} = \frac{M_{H_2}}{M_{Ar}} \cdot \frac{C_{H_2}}{100 - C_{H_2}} \cdot \dot{m}_{Ar} \quad (2)$$

An **aerosol** collection system previously used in CODEX tests was deployed by AEKI Budapest, comprising two independent devices: a nickel plate on which a pocket is mounted to collect the larger aerosols ([Fig. 16](#)), and a ten-stage impactor assembly (see [Figs. 17 and 18](#)) which was actuated for one minute at various times during each of the main test phases. The connection of the sampling and the feed-back lines to the off-gas pipe is located ~106 and ~202 cm, respectively, from the entrance of the off-gas pipe (flange at the

test section outlet). The locations of the sampling and the feed-back lines are illustrated in Figs. 19-21. The sequence of aerosol sampling is listed in Table 12.

## 5 Data Acquisition and Process Control

A computer-based control and data acquisition system is used in the QUENCH facility. Data acquisition, data storage, online visualization as well as process control, control engineering and system protection are accomplished by three computer systems that are linked in a network.

The data acquisition system allows recording of about 200 measurement channels at a maximum frequency of 25 Hz per channel. The experimental data and the date and time of the data acquisition are stored as raw data in binary format. After the experiment the raw data are converted into SI units and stored as ASCII data.

For process control, a system flow chart with the most important actual measurement values is displayed on the computer screen. Furthermore, the operating mode of the active components (pumps, steam generator, superheater, DC power system, valves) is indicated. Blocking systems and limit switches ensure safe plant operation. Operating test phases, e.g. heating or quenching phases, are pre-programmed and can be started on demand during the experiment. The parameter settings of the control circuits and devices can be modified online.

Online visualization allows to observe and to document the current values of selected measurement positions in the form of tables or plots. Eight diagrams with six curves each can be displayed as graphs. This means that altogether 48 measurement channels can be selected and displayed online during the course of the experiment.

The data of the main data acquisition system and of the mass spectrometers were stored on different computers. Both computers were synchronized by radio-controlled clocks.

The data of the main acquisition system were stored at different frequencies according to the test phases as shown below:

0 s	1 Hz
11528 s	5 Hz
13740 s	1 Hz

The mass spectrometer data were recorded at a frequency of 0.6 Hz during the entire test.

## 6 Test Conduct and Pertinent Results

In summary the QUENCH-10 test was conducted with the following test phases.

	Heatup to ~873 K.
Phase I	Stabilization at ~873 K. Facility checks.
Phase II	Heatup with ~0.3-0.6 K/s to ~1620 K for ~32 min (first transient).
Phase III	<b>Pre-oxidation</b> of the test bundle in a flow of 3 g/s of superheated steam and 3 g/s argon for ~113 min at relatively constant temperature of ~1620-1690 K.
Phase IV	<b>Intermediate cooling</b> from ~1690 to 1190 K in a flow of 3 g/s of superheated steam and 3 g/s argon for ~38 min.
Phase V	<b>Air ingress</b> and transient heatup from ~1190 to 2200 K with an initial heating rate of ~0.3 K/s in a flow of 1 g/s of air for ~30 min (superheated steam flow turned off).
Phase VI	<b>Quenching</b> of the bundle by a flow of 50 g/s of water.

The test conduct is illustrated in [Figs. 22 and 23](#), and the sequence of events is listed in [Table 7](#). In addition, [Fig. 23](#) provides heating rates for the air ingress phase. Temperature histories for the entire test are provided for bundle ([Fig. 24](#)), shroud ([Fig. 25](#)), fluid ([Fig. 26](#)), cooling jacket ([Fig. 27](#)), gas feed-in pipe ([Fig. 28](#)), and off-gas pipe ([Fig. 29](#)).

As in previous QUENCH experiments, the bundle was heated by a series of stepwise increases of electrical power from room temperature to ~873 K in an atmosphere of flowing argon (3 g/s) and preheated steam (3 g/s). The bundle was stabilized at this temperature, the electrical power being ~4 kW. During this time the operation of the various systems was checked.

In a first transient, the bundle was heated by power increase to about 1620 K. This marked the start of the pre-oxidation phase to achieve a cladding oxidation of up to 500  $\mu\text{m}$ . The power was controlled to maintain a more or less constant hydrogen production rate of about 5 mg/s after the peak value of 16 mg/s, caused by the previous heat-up. This procedure led to a slow increase in temperature to 1690 K. This phase lasted ~6800 s. Since the oxide thickness could not be measured online, it was estimated on the basis of pre-test calculations and online monitoring of hydrogen release.

To achieve an adequate duration of the subsequent air ingress phase, the bundle was then cooled to a temperature of about 1190 K (axial maximum). This was done by decreasing the electrical power abruptly from 13.2 to 6.9 kW. The temperature was reached after 2300 s. Hydrogen generation dropped rather quickly to about 0.4 mg/s due to this cooling so that nearly no further oxidation occurred. Towards the end of this phase, corner rod B was extracted from the test bundle for later determination of the oxide thickness axial distribution ([Figs. 51-53, 55](#)).

In the subsequent air ingress phase (see [Fig. 30](#)), the steam flow of 3 g/s was replaced by 1 g/s of air, but with unchanged argon flow and electric power. This change in flow conditions had the immediate effect of reducing the heat transfer so that the temperatures began to rise again. The temperature increase (heating rate 0.3 K/s between 1190 and 1500 K; see also

Fig. 23) and oxidation were somewhat slower than expected, and therefore the electrical power was increased in a stepwise manner from 6.9 to 8 kW (heating rate: 0.9 K/s between 1500 and 2000 K). Due to this procedure, oxidation increased such that the additional heat eventually drove the temperatures beyond the final target value of 2073 K. The duration of this phase was 1767 s. Complete consumption of oxygen and partial consumption of nitrogen (about 0.1 g/s) were observed toward the end of this phase. At the end of the air ingress phase about 0.3 g of hydrogen were released, i.e. approximately at the time when oxygen starvation and nitrogen consumption were observed. Also at the end of air ingress a second corner rod, i.e. corner rod D, was removed. An inspection of the two withdrawn corner rods indicated that pre-oxidation was as desired, i.e. the maximum oxide layer thickness prior to quenching amounted to ~600  $\mu\text{m}$  (see Figs. 54 and 55).

The maximum measured test bundle and shroud temperatures evaluated for some elevations are given in Table 8.

Then reflood was initiated by turning off the air flow, switching the argon injection to the top of the bundle, rapidly filling the lower plenum of the test section and injecting 50 g/s of water.

The power was reduced to 4 kW after a further 10 s to simulate decay heat. Right at the beginning of reflood, there was indication of a short and mild temperature excursion in the upper part of the bundle, leading to maximum measured temperatures of about 2200 K at 950 mm elevation and to ~1400 K at the levels above the heated zone. However, cooling was established almost immediately, and complete quenching of the bundle was achieved after about 150 s (see also Fig. 31). In Fig. 32 the steam flow rate measured by the mass spectrometer is compared to the injected quench water mass flow (F 104). The accumulated data in this figure show a mean evaporation rate of ~15 g/s in the beginning of the quench phase. Toward the end of the quench phase there is a growing difference between injected water and measured steam in the off-gas tube. The water/steam balance for the quench phase is also listed in Table 11.

The progressions of the water front and of the boundary between saturated and superheated steam are given in Fig. 33 and Tables 9 and 10 (as local wetting points of rod surface thermocouples). A modest release of hydrogen was observed during the early part of the reflood. About 3.5 g or 44 % of the nitrogen previously taken up was released.

Detection of He by the mass spectrometer indicated a first small failure of a fuel rod simulator after 20 min in the pre-oxidation phase and a much larger failure after 13 min in the intermediate cool-down phase. A further increase in the measured helium concentration with quench initiation indicated an extended failure of cladding tubes during this highly transient phase (see three marked times of failures in Fig. 34, bottom). The shroud failed shortly after initiation of reflood (see Fig. 34, top), but steam access to unoxidized outer surfaces of the shroud and the inner cooling jacket should have been prevented by a slight overpressure in the annulus, maintained by flowing argon.

The evaluation of the hydrogen release rates with help of the mass spectrometer data gives 45.7 g up to the end of the pre-oxidation phase, 47.3 g of total hydrogen generation up to the beginning of the air ingress phase. No hydrogen was generated during most of the air

ingress phase. Toward the end of this phase, i.e. at 110 s before the quench phase about 0.3 g of hydrogen were released as is demonstrated in [Fig. 35, top](#). The negligible amount of  $H_2$  is conjectured an indication that oxygen was completely consumed so that residual steam could react again with the Zircaloy cladding. Another explanation for the small amount is that  $H_2$  previously dissolved in the metallic matrix is released during the continued oxidation.

During the quench phase 5.2 g of hydrogen were released, hence about 53 g of  $H_2$  in total ([Fig. 35, bottom](#)).

With respect to mass spectrometer measurements concerning air ingress (in total 302 g of  $O_2$  and 1312 g of  $N_2$  were injected into the test section), the following data were evaluated. The total uptakes of the air supply by Zircaloy were about 84 and 8 g of oxygen and nitrogen, respectively (see [Fig. 36](#)). As indicated above, oxygen from the air injection of 1 g/s was completely consumed towards the end of the air ingress phase. Nitrogen, however, was partially consumed starting from around 13200 s. The partial consumption of nitrogen (8 g,  $\sim 0.1$  g/s), which occurred during the phase of advanced  $O_2$  consumption, indicates the ability of  $N_2$  to react with Zr to form ZrN.

## 7 Results of the Aerosol Measurements

### 7.1 Objective of Aerosol Measurements

Beyond the standard FZK QUENCH instrumentation, AEKI proposed to carry out sampling of aerosols during the QUENCH-10 test. This additional measurement aimed to provide information for the composition and the mass of aerosols released during different periods of the test. The evaluation of the measured data – together with other measurements, like temperatures, flow rates – can extend our understanding of the oxidation and bundle degradation phenomena.

### 7.2 Main Characteristics of the Measuring System

The applied aerosol sampling system was similar to the design used in earlier CODEX experiments [15-19]. The two main components of sampling were:

- Impactor system, with 10 impactors, each of them operated for 1 minute during the test.
- Ni plate installed in off-gas pipe, which collected aerosols during the whole experiment.

The construction of the impactors is shown in [Figs. 16-18](#). Each impactor was identical, with the same number and structure of Si-collectors and quartz fiber filters. The system included 10 samplers, magnetic valves and a pump. The control of the magnetic valves was carried out from a computer, which recorded the opening and closing times of the valves as well. The cascade impactors were fastened to a measurement desk (30 x 60 cm) together with all of supplier equipment:

- pump,
- power supply for pump,
- valve to set up the gas flow,

- power supply for ADAM switching modules,
- ADAM switching modules controlled by PC.

The impactor system was connected to the off-gas pipe of the QUENCH facility at ~ 1 m distance from the bundle (Fig. 19). The measurement desk was connected to the off-gas pipe with 10 mm tube.

The Ni plate was placed in the off-gas pipe, close to the outlet junction from the test section. The arrangement of the Ni plate is shown in Fig. 20.

The impactor valves were opened for 60 seconds and aerosols were collected during this period. Sequential opening of impactors was carried out. The opening time for each impactor is given in Table 12. The times of sampler openings are shown in Fig. 37 together with the rod temperature history. One impactor was applied in the pre-oxidation period, one during the intermediate cool-down phase, four in the air ingress and three in the quenching periods, respectively.

### 7.3 Post-test Examination of Samples

The post-test examination of the aerosol samplers was carried out at AEKI after the test. The impactors were weighted before and after the test and the mass increase is documented in Fig. 38. The average weight gain was 1 mg/sampler. There were relatively small differences between the different samplers. The total weight gain of the Ni plate was 8.1 mg.

The following techniques were applied for the post-test examination of different samples:

- SEM – investigation of morphology, size and shapes of particles (Ni plate, collectors),
- EDX – elemental composition of individual particles (Ni plate, collectors),
- SSMS – elemental composition of samples (Ni plate and filters).

#### 7.3.1 Electron Beam Studies

The aim of the electron beam studies was twofold:

1. To know the *morphology of aerosol particles* deposited on the impactor units.
2. To evaluate the *elemental composition* of the aerosol particles released from the QUENCH-10 experiment.

Direct electron beam studies were performed with aerosol samples collected by ten impactor units. For each of them, aerosols present on two collector plates and on a nickel plate were studied. A few selected quartz fiber filters were investigated, too. Aerosol samples were examined without any evaporated or sputtered layer; however, carbon was sputtered on the quartz fiber filter samples. The following instruments and methods were applied:

- Philips SEM 505 scanning electron microscope (SEM) working at 20 kV and using a beam current of a few nanoamperes. First, the secondary electron images (SEI) was obtained at 10 times of magnification to see the degree of coverage of the collector plates by aerosol particles. Then the samples were studied at higher magnifications and digital SEI or BEI (backscattered electron image) images of typical areas were recorded.
- LINK AN 10/55 S type electron beam micro analyser (EDX) with a ppm detection limit in the elemental range between Na<sup>11</sup> and U<sup>92</sup>. Mostly the EDX measurements were done on individual particles and/or aggregates.
- Oxford INCA EDX system using thin window with a possibility to detect isotopes from B<sup>5</sup> to U<sup>92</sup>. The quantitative EDX studies were performed as well. However, the Si or the Ni peaks which stem partly from the materials of the collector plates were always present. The presence of these peaks was most pronounced for small-sized particles of about 1 µm, or less.

### 7.3.2 Sample Preparation

The collector plates were fixed and a piece from the nickel plate on SEM sample holders by a double-side carbon tape. Numbering of the collector Si-plates was consecutive: from 1 to 10, the second collector plates were designated 2/1 through 2/10. The quartz fiber filters were cut into two pieces. One half of them were used for mass spectrometry, and a quarter of a few filters were placed on SEM holders. The quartz fiber filter samples were marked from Q1 to Q10.

### 7.3.3 Results

#### 7.3.3.1 Aerosol particles deposited on the collector Si-plates

Digital SEI images show the following features:

- There are particles and aggregates on each collector Si-plates with different coverage of the plates. This result is in accordance with the one of the mass increase measurements. The amount of the aerosol particles is generally quite few or medium.
- Elongated needle-like as well as large particles with irregular shapes can be found on the collector plates. The number of them seems to be larger for the first series of collector plates, especially for samples No. 1, 5 and 9.

From SEM studies performed at higher magnifications the information on the particle size of the aerosol samples was obtained. The smallest particle size is between about a few tenths of µm and 1 µm. The average particle size is generally a few µm. The size of the aggregates of particles is larger. It can be several tens of µm. The needle-like particles and the large ones with irregular shape have a length of several hundred µm, even mm, whereas the width of them is several tens of µm. Such large particles can be seen e.g. at sample 5. The shape of the individual particles is various: it can be rounded, slightly elongated, rectangular and irregular, too. Most frequently were to find rounded and slightly elongated particles.

The EDX studies of the aerosol samples give the following results:

1. Sn is present in small sized particles and also in larger ones together with Zr and sometimes with a small amount of Fe. The largest amount of Sn rich particles was detected in Sample 8. In the second series of collector samples Sample 2/9 contains a lot of particles with Zr, Sn and sometimes with Fe content.
2. Zr was present in different samples. The highest amount was found in Sample 2/9. The size of the Zr rich particles extends from about 2  $\mu\text{m}$  to 12  $\mu\text{m}$  (this latter size is the length, the width is 2-5  $\mu\text{m}$ ). The shape of these particles is rounded, rectangular or irregular.
3. For most of the studied aerosol samples, beside the Si-rich particles, the most numerous classes of particles were the ones enriched either in Fe, or Ni and Fe, or Fe, Ni and Cr.
4. In some particles of the various collector samples other elements like Mn and W were also detected.

Figures 39 and 40 show the EDX spectra illustrating the above-mentioned findings. Table 13 summarizes the elements most frequently found in the aerosol samples by EDX.

#### *7.3.3.2 Aerosol particles deposited on the Ni plate*

SEM studies of the Ni plate show that the coverage of the Ni plate by aerosol particles is more pronounced than that of the collector plates. Fig. 41 is a typical SEI image taken at 200 times of magnification.

The size of the aerosol particles is generally between a few tenths of  $\mu\text{m}$  and about 3  $\mu\text{m}$ . However, there are larger particles, too. Particles with needle form have a length of 12  $\mu\text{m}$  and a width of 2-2.5  $\mu\text{m}$ . The shape of the particles can be globular, rectangular or slightly irregular -elongated as for the aerosol particles deposited on the collector plates.

The EDX analysis shows that most of the aerosol particles are Zr rich with some content of O, and sometimes with small amount of Sn. There are also Sn-rich particles, they could be found in form of aggregates together with Zr-rich particles. A digital BEI image and the corresponding two typical EDX spectra are shown in Fig. 42.

#### *7.3.3.3 Aerosol deposited on some quartz fiber filters*

Fig. 43 shows an SEI image for sample Q5. A relatively low amount of aerosol particles was present on the selected pieces of quartz fiber filters No. 5, 7, 8 and 10. The size and the shape of the aerosol particles present on the studied quartz fiber filters were similar to the ones found on the collector plates except that here one could not distinguish the fibers of the filter from some particles (needle like) of the aerosol.

The size of the aerosol particles present on the quartz fiber filters is generally between a few tenths of  $\mu\text{m}$  and a few  $\mu\text{m}$ . Some larger particles or aggregates of them can also be found, but the number of them is small. The shape of the aerosol particles can be globular, slightly elongated or irregular, as for the ones deposited on the collector plates.

By EDX the following elements were detected: Zr, Fe, Cr, Sn and Cu. Sn was detected mainly on sample Q8. Only a few Zr-rich particles were found, mostly on sample Q5 (from

the studied filter samples). One can suppose that Zr deposited mostly on the Ni plate and some amounts of it on collector No. 9. The greatest variability was found for the Fe-containing particles for e.g. sample Q5. There were Fe, Ni-Fe, Ni-Cr-Fe, Fe-Cr-Ni-Cu, Fe-Ti-Mn and Cu-rich particles. Most of these particles are small: between a few tenths of  $\mu\text{m}$  and about 1-2  $\mu\text{m}$ .

### 7.3.4 Analyses by Mass Spectrometric Methods

#### 7.3.4.1 Applied methods and instruments

Pocket content was analyzed by spark source method (MS 702 R type Spark Source Mass Spectrometer SSMS was used in this work) after mixing it with high purity graphite to prepare electrodes for sparking. Collector plate surface impurities were measured by

- Laser Ionisation Mass Spectrometry (LIMS) from the surface and
- SSMS with rolled-up sheet electrodes.

In both cases Ni isotopes were used as inner standards. The sensitivity was below  $\mu\text{g}/\text{cm}^2$ .

#### 7.3.4.2 Results on the nickel plate and the pocket

Table 14 shows some mass data gained for the collector plates and for the pocket. Table 15 summarizes the component elements found in the pocket sample. Table 16 summarizes the amount of elements found on the Ni plate by LIMS and SSMS. As it can be seen from the data, the two most important component elements are Zr and Sn. This corresponds to the results of the EDX analysis.

#### 7.3.4.3 Results gained for the quartz fiber filters by spectrometric method

Fig. 44 shows the results gained for the quartz fiber filters. These filters contain generally smaller particles than the collectors. It is interesting to see that the amount of the Zr is the highest for the beginning and later only smaller maxima can be found. It can also be seen that the highest amount of Fe and Cu could be detected at the air ingress period. The EDX results are similar to the ones found by SSMS. The amounts of elements detected by both methods are in correspondence with each other.

## 7.4 Summary of Aerosol Measurement

In accordance with the results of the SEM+EDX and that of the SSMS, the escaped aerosol contained different elements depending on the phase of the experiment:

- The first sample (taken during the pre-oxidation phase) is dominated by Zr.
- At the high temperature air oxidation stage again Zr, moreover Fe and Sn appeared.
- In the quenching period Zr and Sn rich particles were found by EDX.

The quartz fiber filter collected particles with the smallest sizes: Fe and Cu were found by both EDX and SSMS, the amount of Zr was relatively low by both methods.

The weight gain measured for the collector plates has shown maxima at the cooling stages: i.e. the first maximum was found for collector No. 3, working in the intermediate cool-down stage. Weight gain started to increase from collector No. 7, during the air ingress and had a second maximum for collector No. 9, which was in operation in the quenching period. The precipitation of the collector plates studied by SEM was in accordance with these findings.

## 8 Posttest Examination

### 8.1 QUENCH-10 Posttest Appearance Prior to Bundle Sectioning

After the experiment the QUENCH-10 bundle and its shroud appeared severely damaged, i.e. completely oxidized in the region between 750 and 1000 mm (Figs. 45 and 46). Besides oxidation, the shroud exhibits deformation and formerly molten zones partly due to an interaction with the  $ZrO_2$  fiber insulation. During handling shroud and bundle were additionally damaged when pieces of shroud and bundle components fell off. Parts of the shroud that fell off at around 850 mm elevation are shown in Fig. 47. It can be seen that the inner surface of the shroud exhibits a white oxide layer and some spots where Zr nitride had formed by oxidation in air.

The photographs in Figs. 48 and 49 which were taken by a videoscope system inserted into the bundle from the bottom at the (voided) position of corner rod B demonstrate as well spots of ZrN on the shroud inner surface.

Fig. 50 gives the distribution of particles taken posttest from the off-gas pipe.

The appearance of the two corner rods, i.e. rod B (removed from the bundle at the end of the intermediate test phase) and corner rod D (removed from the bundle at the end of air ingress), are presented as cross-sections in Figs. 51-54. Golden-appearing nitride phases were found at the outer surface of corner rod D which broke during pulling at elevation 865 mm. Details are given in the metallographic examination (section 8.3).

### 8.2 Sectioning of the Test Bundle

The encapsulation of the test bundle was performed in three steps. First, a cap was placed over the bottom of the copper electrodes and a low-melting metal alloy (containing Pb, Bi, Sn, and In; density of  $\sim 10 \text{ kg/dm}^3$ ; melting point of 331 K) was used to seal the bottom of the bundle. Secondly, a small amount of the same resin to be used for the encapsulation of the bundle was placed on top of the metal to generate an interface of around 0.2 m that prevents the metal from being liquefied after starting to epoxy the bundle together with its shroud. The epoxying process generally shows a little heating due to the exothermal heat that develops during the curing stage. The mould for filling the bundle with epoxy resin surrounds the shroud over the entire bundle length and is set up vertically. It is evacuated before charging with the resin to allow filling of pores and cracks. So, the bundle is filled from the bottom with approx. 20 kg of resin and hardener. Scale readings on the mass gain of epoxy resin per cm of filling are given in Table 17. The epoxy system Rütapox 0273 with the hardener

designated LC (manufactured by Bakelite GmbH, Iserlohn) was chosen based on the experience with the CORA test bundles. The shrinkage effect is small. After epoxying the bundle the resin is allowed to harden for one week. To obtain the cross sections a saw with a 2.0 mm-thick diamond blade (mean diamond size 138  $\mu\text{m}$ ) of 350 mm OD is used to cut the slabs at 1300 rpm. The elevations of the cross sections are listed in [Table 18](#).

### 8.3 Metallographic Examination

#### 8.3.1 Investigation Procedures

As already mentioned, corner rod B was withdrawn from the QUENCH-10 bundle at the end of the phase of pre-oxidation in steam. In addition, the trial to remove corner rod D was partly successful. At the end of the air exposure phase the lower part of this rod was withdrawn, whereas the fractured upper part remained in the test section. The extent of oxidation of the withdrawn rods as function of the elevation in the bundle was determined by a non-destructive technique based on the eddy current principle of scale thickness measurement, as well as the scale measurement for polished cross sections of the two rods.

The post-test examination of the whole bundle is based on the metallographic preparation of cross section slabs on one side (generally the top one) by careful grinding and polishing, the visual inspection, and a comprehensive photo documentation. In the evaluation, a selection of the available macrographs and micrographs is used for orientation and illustration. The interpretation of the bundle behavior with respect to different aspects is supported by composed, thematic figures. The final bundle state is thus described as far as possible, and the mechanisms of the physical-chemical interaction of the components and of their oxidation are deduced. The bundle will be described from bottom to top, because the extent of interaction increases with the temperature and thus with increasing elevation.

Special attention was paid to the cladding oxidation and phenomena, related to the air exposure phase and the water quenching. The scale thickness on simulator rod and corner rod surfaces as well as inner and outer shroud surfaces was measured. This was done, if possible, in four directions around rods and shroud, and for all prepared cross sections. The results are illustrated in lateral scale thickness profiles and in axial profiles, given for the different bundle components.

#### 8.3.2 Axial Oxidation Profiles of Corner Rods B and D

[Fig. 55](#) summarizes the results of the metallographic and the eddy current method of scale thickness measurements, plotted against the axial elevation in the bundle. In addition, scale thickness and standard deviation are given in tabulated form. Compared to the profile of the first withdrawn rod B, the second profile, that of the removed part of rod D indicates the contribution of the air exposure phase. This was obviously so strong that fracturing of the rod during pulling occurred, so that no information is available for the upper part of rod D. [Fig. 56](#) combines the macroscopic view of both rods, showing the break of rod D at 866 mm, and micrographs of the scales of both rods from the cross sections at 850 mm. The sound scale of rod B is typical for a formation below 1800 K, whereas that of rod D has seen temperatures above 1800 K, is much thicker, and has been attacked and modified during the

air exposure period. More available micrographs are not used here for a discussion of the phenomena, which will follow on basis of the sectioned bundle.

Figs. 57-59 present an overview of the QUENCH-10 cross sections available. They are described and interpreted in the subsequent sections.

### 8.3.3 Lateral and Axial Oxide Scale Thickness Distribution

At the 500 mm elevation (Fig. 60), the  $ZrO_2$  scale thickness around 20  $\mu m$ , measured for the bundle components, indicates minor oxidation with small scatter. The local result for the shroud at NW direction is related to the axial shroud weld, and this special behavior will be discussed later. At 650 mm elevation (Fig. 61), a rather flat temperature profile across the bundle but considerable local scatter are indicated by thickness values between 50 and 130  $\mu m$ . In addition to the shroud weld, the relocated stub fragment of corner rod D remains out of consideration, since its oxidation state is not typical for its final axial position. At the 750 mm level (Fig. 62), the local peak  $ZrO_2$  scale thickness is 500  $\mu m$ , and the relative scatter does not indicate a systematic deviation from temperature profile flatness.

At 800 mm elevation (Fig. 63), some rod claddings are already totally converted to oxide at some positions. A contribution of internal oxidation by oxygen transfer from the fuel pellet simulators has become more important due to the improved contact after melting of the cladding matrix residues. Further, the atmosphere had access to the inner side of fractured cladding. As far as available, the shroud was included into the scale thickness determination at the inner and outer surface. At 850 mm elevation (Fig. 64) the bundle degradation did not allow meaningful systematic measurements any longer. Most gathered values correspond to total oxidation of the locally available cladding and cladding melt, others indicate some cladding thinning in the course of melt loss. The continued oxidation of the much thicker shroud after cladding total conversion is reflected by rather high shroud thickness values. The external shroud oxidation after perforation and the oxidation of "secondary" shroud surfaces, formed by splitting and pocket formation, is included as well. The relocated corner rod fragment in addition to corner rod C is not taken into account. At the 950 mm level (Fig. 65) no rod cladding remained, so that measurements covered only the inner shroud surface and the corner rods A and C, the latter being the above mentioned relocated fragment. At the electrode zone elevation 1080 mm (Fig. 66) the bundle oxidation corresponds to the comparatively moderate temperatures during most phases of the experiment.

The results for the lateral scale thickness profiles at the reported elevations are combined into the axial profile. Fig. 67 consists of the separate profiles for simulator rods, corner rods, and shroud (top), and the average profile of the simulator rods together with the standard deviation range (bottom). The cladding is almost completely oxidized within the elevation range 800 to 1000 mm.

### 8.3.4 Documentation and Interpretation of the Bundle Status

#### Cross section QUE-10-2, bundle elevation 500 mm

The central elevation (500 and 485 mm, top and bottom of the slab) is depicted in [Fig. 68](#), in which the bottom macrograph is shown mirror inverted for easier comparison. This overview shows some sideward movement of the central rod versus the quite regular arrangement of the surrounding rods and the shroud. Note the absence of corner rods B and D, removed (D only as part) during test conduct. More detailed microscopic inspection of the rather moderate rod oxidation did not identify special aspects worth to be depicted. However, shroud inspection identified the following local deviations from growth of sound and protective  $ZrO_2$  scale:

The axial shroud weld at NW direction is covered by especially thick inner surface scale, presented in [Fig. 69](#). By higher magnification a repeated lateral cracking of the scale is identified, which is typical for the well-known breakaway effect, observed in the course of long-term steam oxidation [20]. The post-transition scale is understood to form new crack systems during further growth, by which accumulated internal mechanical growth stress is periodically relieved. In total, reduced protection compared to sound scale gives rise to a growth rate with linear time dependence. Consequently, the importance of the breakaway transition increases with the time spent within this growth regime. It is mentioned that the critical scale growth increment until crack formation increases with the temperature. But even with this information it is not simple to deduce the history of the observed local oxidation behavior. The interim cooling phase in the experiment will have favored the crack formation as well, and the air ingress phase has played some role as well: The micrograph at bottom, right of [Fig. 69](#) shows some particles of zirconium nitride phase embedded by zirconia within the inner part of the scale. Nitrogen penetration and reaction in competition to the scale growth is interpreted to have taken place in gaseous form via the pre-existent crack systems.

Similar special behavior at a few shroud positions is related to or even caused by axially elongated scratches, which gave rise to splitting or spalling and bulging of bright colored oxide, as identified by the endoscopic inspection of the bundle, reported in the previous chapter. The cross section evaluation allows to confirm the spalling of a top layer of the scale. The bright color is interpreted by the stoichiometry of this very compact sub-layer. [Fig. 70](#) is more dedicated to the scale below this top layer. It consists of laterally cracked oxide, from which some flakes with brighter tint may have separated, and of an inner part, typically composed of aggregates of oxide and nitride phase, which most actively have promoted the reaction with the underlying metal by locally advanced penetration. In total, top layer growth within a pre-transition phase, top layer separation related to surface defects, post-transitional scale growth and cracking, and air typical reaction products formation are reasonable consequences of the test condition history. But the reasons for the only localized response remains to be explained.

#### Cross section QUE-10-3, bundle elevation 650 mm

[Fig. 71](#) gives the overview for this elevation and the slab bottom (635 mm). The bundle arrangement is intact, the corner rods A and C show their instrumentation tube section. The presence of corner rod D is the result of the downward pulling of this rod towards the end of the heat-up phase in air, during which it broke. The oxidation state of this remaining fragment is consequently not typical for its final position. A quite large number of rubble fragments are

found, which may have fallen downward during or after the experiment. Pieces of strongly oxidized or completely converted cladding and of annular ZrO<sub>2</sub> pellets can be distinguished.

A closer look on the bundle periphery is given in [Fig. 72](#). The moderate extent of oxidation at this elevation is shown for the empty tubular section of the corner rods A and C (SE and NW directions), as well as the depicted rods 15 and 21 (SW and NE directions). The shroud shows more advanced oxidation only towards NW, at the weld (bottom/right micrograph). The non-typical oxidation extent of the partially shown corner rod D (bottom/left) results from the initial elevation of this fragment. The rubble particles, fragments of fuel simulator pellets and of partially to fully oxidized cladding can be used only as qualitative information source, since the relocation times and previous positions may vary. The macrographs of some rods of the inner ring, as given in [Fig. 73](#), do not show a cladding interaction with the simulator pellets.

Closer views on the central rod ([Fig. 74](#)) and rod 11 ([Fig. 75](#)) show quite comparable pre-transition scale on a relatively thick  $\alpha$ -Zr(O) sub-layer, which is seen in better contrast in polarized light (micrographs at bottom/left). The loss of some pieces of the brittle  $\alpha$ -Zr(O), which was favored by the presence of cracks within this layer, is a specimen preparation artifact. Those cracks will have formed during the cooldown phase, which explains that the scale growth morphology is normal: Columnar grain growth is locally retarded by small lateral flaws, below which a scalloped scale interface is formed. Those features can be interpreted as the result of an ongoing phase transformation from metastable tetragonal to stable monoclinic ZrO<sub>2</sub> [20]. [Fig. 75](#) shows the local effect of partial scale spalling, which is visible due to the brighter color of a still adhering scale flake.

Restricted to some N to NW region, the shroud shows already post-transition scale morphology, as documented in [Fig. 76](#) and [Fig. 77](#). The layered scale on the shroud weld tends to split into partial layers, following the lateral direction of crack systems ([Fig. 76](#)). The  $\alpha$ -Zr(O) layer is comparatively thin, indicating fast scale growth. The exposed outer scale sub-layers tend towards stoichiometry. An innermost scale sub-layer contains clouds of zirconium nitride phase particles, which indicates the influence of the air ingress period. However, the absence of ZrN phase in the adjacent scale is no proof for formation in steam, since the nitride is known to convert continuously to oxide as long as oxygen supply is provided, whereas the released nitrogen is free for continuing nitride formation below. Thus, the history of steam to air transition cannot be deduced from the final oxidation state. The scale morphology of the shroud base material at N orientation ([Fig. 77](#)) confirms the given interpretation fully. In addition, the brightness of the outer scale in the bottom/left micrograph indicates the continuing scale degradation by internal cracking into small pieces, but without loss of coherence.

#### Cross section QUE-08-04, bundle elevation 750 mm

The overview, given in [Fig. 78](#), shows an essentially intact bundle geometry according to a first glance. The more advanced rod cladding and shroud oxidation is more obvious in [Fig. 79](#), which depicts a choice of macrographs of fuel rod simulators. Their variation in the area of contact to the pellet is typical, and some other features of local conditions will be mentioned later. [Fig. 80](#) is concentrated to the corner rods A and C (SE and NW), since the cross section of corner rod D (NE) is not typical for the described elevation, as already mentioned. The tubular section of both instrumented rods is found completely filled with

internally relocated metallic melt, which is embedding the thermocouples. Comparison to Fig. 78, slab bottom, shows, that the filling is not complete there.

The more detailed documentation of the cladding oxidation of simulator rod 9 is given in [Fig. 81](#). This rod shows two scale cracks of wedge shape, which should, as usual, have some axial length, allowing some tube bending vs. flattening during partial release of scale growth stress. This is an initial phase of the “flowering effect”, leading to tube splitting and atmosphere ingress. This was not the case here, but some small volumes below the wedge and within the scale of the bottom/left micrograph have indicated some effect of air consumption reaction, which is not illustrated in more detail. The cladding matrix, converted to  $\alpha$ -Zr(O), was close to complete melting during the experiment. [Fig. 82](#) is focused on scale growth anomalies and uses the scattering of polarized light illumination compared to non-polarized light for comparison and detection. Scale weakness is related to surface crack formation and proceeds towards  $ZrO_2$  stoichiometry, as indicated by the absence of  $\alpha$ -Zr(O) precipitates in the inner scale sublayer (see micrograph at bottom/right). In variance to the two previous figures, rod 16, depicted in [Fig. 83](#) shows an inner cladding scale in the region below the accelerated scale growth, initiated by the crack. It is plausible to conclude that limited steam/air ingress took place through some slit, and was consumed by scale formation. The scale morphology indicates involvement of air, but it is not possible to distinguish the history more precisely.

[Fig. 84](#) compares the internal shroud oxidation for two positions (base material and weld) and by polarized light contrast. Compared to protective scale and an  $\alpha$ -Zr(O) sub-layer of similar thickness (left side, base material), less protective scale growth is faster and the  $\alpha$ -Zr(O) growth cannot follow (right side, weld). The final state of  $\alpha$ -Zr(O) precipitation from the scales during cooldown indicates that the defective scale is closer to stoichiometry and therefore more embrittled.

#### Cross section QUE-10-8, bundle elevation 800 mm

The sectioned bundle slab from 833 mm (top) to 800 mm (bottom) was polished and inspected at the bottom side. This is why the top section is given as smaller insert in [Fig. 85](#), and why the mirror inverted bottom section is the main interest. Advanced oxidation was accompanied by considerable rod cladding damage, which was initiated by expansion under scale growth stress, bending, and axial splitting. The loss of scale segments is much more pronounced at the top elevation, where fractured annular pellet simulators have contributed to rod disintegration as well. Pieces of cladding and pellet rubble are found distributed between the rods, forming a partial rubble bed. The thermocouples of the corner rods A and C are glued to the tube walls, indicating internal melt relocation within the tubes. Melting of the massive metallic shroud after formation of a thick internal scale and some later occurring external oxidation facilitated the observed shroud splitting and bending. The loss of brittle shroud pieces gave rise to the formation of the pocket at W direction, which got filled by rubble. The missing shroud half shell towards W at top elevation was removed together with the zirconia fiber insulation pack during bundle dismantling.

The closer view on some typical fuel rod simulators, given in [Fig. 86](#), confirms the expansion of the almost oxidized cladding, local split formation and related tube flattening. At positions where contact to the pellet was supported by cladding melt formation and accumulation, some previous cladding melt and pellet interaction product layer are still partially metallic, obviously protected from ingress of the atmosphere. Before other rods will be shown for

special details, [Fig. 87](#) documents the already mentioned corner rod melt relocation and the typical shroud oxidation at SE and NW directions.

The central rod, depicted in [Fig. 88](#) shows cladding melt relocation within the instrumented pellet bore hole. The main interest of the figure is a deeper insight into the oxidation history: Facilitated by comparison of the bright-field illumination with polarized light, a scalloped scale transformation front is seen, behind which the scale is internally cracked into small pieces, giving rise to the light scattering in polarization. The effect of the air exposure will become more obvious with the next figures, since no zirconium nitride phase is found here, and since the non-oxidized residues at the pellet gap (bottom, left) are not considered. [Fig. 89](#) shows in corresponding representation of rod 2 the influence of air oxidation, in this case with identification of remaining ZrN: Air attack on the scale took place via a wedge shaped scale crack, and the interior side of the cladding was reached by the reactive nitrogen. The volumes of ZrN phase formation and partial retention are fine-grained. [Fig. 90](#) as the next piece of the puzzle, confirms the air ingress into the scale of rod 6 via some existing scale defect, and even the reaction of nitrogen with the zirconia pellet, here within a pellet crack. Nitrogen can have been only a competitive reaction partner under the condition of local oxygen starvation, since otherwise the pellet would have been stable.

The focus of [Figs. 91 to 93](#) is on the effect of air exposure of pre-existent cladding scale. It is plausible to interpret, that an attack is only possible for heavily oxygen starved conditions. Nitrogen enrichment is assumed to allow scale transformation to nitride and release of oxygen or oxygen consumption elsewhere. Obviously, the nitride formation can penetrate into the scale and form a scalloped reaction front (e.g. [Fig. 91](#), top, right), because free oxygen is absent here. Behind the reaction zone any available oxygen will again transform nitride into oxide, combined with the release of nitrogen. [Fig. 91](#), bottom, right, shows in high magnification that the re-oxidation proceeds by preferential nitride grain boundary oxidation. Residual nitride phase is retained during the cooldown phase of the experiment, protected by the surrounding oxide. [Fig. 92](#) confirms the given interpretation of ZrN formation and oxidation for a position of rod 13, at which the rod is in close contact to a scale fragment of the shroud. In this case, the oxidation front of ongoing ZrN consumption seems to proceed along periodic lateral crack systems. [Fig. 93](#) shows a position of rod 20, at which the pellet gap is filled with cladding melt. The irregular thickness of the oxidized interaction layer is seen in the top, right micrograph. Further, this picture and the details given below illustrate again the described cladding scale nitridation and re-oxidation.

The morphology of the scale transformation caused by air ingress seems to indicate almost catalytic activity of nitrogen under oxygen depleted local conditions, since nitrogen is continuously involved, but subsequently released for repeated activity deeper in the scale. In this sense, an ongoing nitrogen supply from the atmosphere might not be necessary after an incubation phase, so that the air-induced scale transformation might have continued even during the cooldown phase. This aspect should be studied separately, because of the essential importance of the consequences on steam oxidation after an air ingress phase.

#### Cross section QUE-10-5, bundle elevation 850 mm

The regular rod arrangement, depicted in [Fig. 94](#), contrasts to the advanced rod brittleness, having led to fragmentation of cladding and even some pellets. Relocation and agglomeration of fragments have formed a bed of loose rubble. Corner rod A is intact only up

to the slab bottom elevation, whereas for corner rod C the slab shows a second, obviously relocated fragment in addition. Only the eastern part of the shroud is kept in original position.

Details of individual rods are only given for a few positions, for which the degradation can be traced back. Fig. 95 shows a region of rod 4, for which air penetration into a cladding crack and presence of air within the pellet gap can be demonstrated by the identification of zones of zirconium nitride phase, formed as reaction product. Confirming the interpretation given in the previous section, Fig. 96 shows the scale conversion from the surface during the air ingress period for the cladding of rod 12. Note in addition the oxidative conversion of the tin-enriched grains at two thirds of the cladding scale depth in the bottom, left micrograph, indicating a contribution of internal cladding oxidation. Fig. 97, continuing the description of rod 12, is focused on the close region of internal air oxidation, identified by the presence of ZrN phase in the state of partial re-oxidation, as described for the previous elevation. In total, the sequence of events may be complex. For the considered rod, oxygen transfer from pellet to cladding, steam penetration, air penetration, oxygen consumption, nitride formation, and ZrN oxidation, may have contributed to the final state of the internal cladding oxidation.

Fig. 98 is to give the impression, that the shroud has experienced oxidation conditions similar to those of the rods. The internal shroud scale shows a top layer of conversion to nitride and re-conversion to oxide. Nitride phase is present at the conversion front. The through-wall crack formation was obviously a late effect.

#### Cross section QUE-10-6, bundle elevation 950 mm

Fig. 99 shows that all fuel rod simulators have lost their oxidized cladding, which fell down in pieces without any remaining ones. Some rods have lost their pellet partly or completely. The collapse of the central rod above this elevation gave rise to the observed accumulation of central rod pellets, found in upright, oblique, or horizontal orientation within the bundle center. The presence of the central rod stub below must have prevented further axial movement of those pellets. Due to the predominance of oxidation at the given elevation, melting of the rod cladding matrix could not take place before complete conversion. This is why any gluing to the pellets did not occur for the surrounding simulator rods as well. Consequently, collapsing of those rods was only prevented by the tungsten heater rods. A reactor core under comparable conditions might have formed a large void after pellet stack instability and rubble downward relocation onto the residual stubs.

The essentially retained shroud is divided by through-wall cracks and distorted by bending. A closer look on the inner surface oxidation reveals the features of scale modification, caused by the air ingress phase, as already described for the lower elevations. Fig. 100 illustrates at north orientation the two-fold conversion of a scale partial layer into cracked, stoichiometric  $ZrO_2$ , proceeding via ZrN phase formation and re-conversion to oxide. Next, the scalloped band of ZrN is visible, containing periodic crack systems. Below the ZrN growth front the scale shows its non-influenced usual microstructure. Obviously, through-wall cracks have formed later. At the shroud weld towards NW, the converted partial layer of the scale is found spalled from the non-converted scale (Fig. 101). ZrN-phase mainly adheres to the spalled part and indicates due to missing oxidation that spalling was a late event as well.

#### Cross section QUE-10-7, bundle elevation 1080 mm

The bundle shows the fairly well arranged molybdenum electrode section of the rods, surrounding the intact central rod (Fig. 102). The rods of the first ring have lost their cladding

almost completely at the slab bottom elevation, whereas intact to fractured or fragmented cladding is seen at the further described top level. The shroud and the corner rods A and C are intact. A selection of rods, which do not show fracturing is depicted in [Fig. 103](#). Compared to those, [Fig. 104](#) presents macrographs of fractured or fragmented rod cladding. Local through-wall oxidation and through-wall cracking can be distinguished. The fragmentation is to be seen mainly as effect of the air exposure period, according to the above given discussion and the following illustrations.

Starting with the mildest form of irregular scale morphology, speculated to be related to air exposure, [Fig. 105](#) shows a spot at which the scale of the central rod has grown a bit faster than around, and for which polarized light indicates the range of crack penetration. [Fig. 106](#) compares sound scale for rods 20 and 5. Rod 20 has seen a peak temperature below 1800 K according to the absence of  $\alpha$ -Zr(O) phase precipitates, whereas their presence in the innermost part of the scale of rod 5 indicates a peak above 1800 K, interpreting the higher scale thickness. The cladding failures of rod 5 at two other positions are described in [Fig. 107](#). Columnar scale growth was followed by non-oriented growth of defective scale, seen in different depth of penetration, and by some internal cladding oxidation. As identified in higher magnification, embedded clouds of remaining ZrN phase indicate the contribution of the air exposure to this kind of fragmentation, which has been already described for lower elevations. The finally given illustration, [Fig. 108](#), compares the shroud oxidation for a typical position and the weld towards NW. Based on the critical scale thickness, a formation temperature around 1300 K is deduced for both positions. The enhanced oxidation of the re-solidified material condition is again documented.

### 8.3.5 Supporting SEM Inspection and EDX Analysis

More necessary information on the bundle status was gained by scanning electron microscopy (SEM), in support of the light-optical (LM) investigation. Concerning the presence of the zirconium nitride phase at certain positions, the energy dispersive X-ray (EDX) analysis is a decisive identification method. It turned out that the secondary electron (SE) image contrast and especially the back scattered electron (BSE) image contrast are instead sufficient to distinguish the ZrN phase from metallic Zr(O) phase:

In microscopic inspection it is simple to distinguish the more reflective metallic phase from the less reflective ceramic phase, e.g. the bright metallic Zr(O) from the gray ZrO<sub>2</sub>. Typical for ZrN phase is a bright, yellowish golden tint in direct microscopic view. This color contrast becomes generally much fainter in micrographs, in which Zr(O) may have a yellowish tint as well. The contrasts in SEM micrographs are different: A BSE image depicts ZrO<sub>2</sub> and ZrN in quite similar gray tone, compared to a much lighter gray for Zr(O). Specimen topography contrasts give the impression of oblique illumination and corresponding shadows. An SE image can be described to be similar with respect to the missing contrast between ZrO<sub>2</sub> and ZrN, and a weak contrast of both compared to the lighter Zr(O). It is mentioned that oblique surface details give bright topography contrast, and that edges and cavity defects are indicated by bright contrast as well. Nevertheless, the SE electrons are used for the recording of EDX spectra, and a small acceleration voltage is applied for the detection of the light element nitrogen.

Many EDX spectra have been recorded for the levels QUE-10-5 and QUE-10-6 (elevations 850 and 950 mm elevation, respectively), in order to identify the nitrogen peak or to exclude the presence of ZrN phase. A few of them are documented in the following, and reference to others allows the given discussion. Some BSE images are also included in illustrations, to be compared with the LM contrast of ZrN phase. The SE images contain the positions / areas of recorded EDX spectra.

At 850 mm elevation (QUE-10-5) rod 4, already illustrated in Fig. 95, was analyzed by SEM. Fig. 109 allows the comparison of the LM bright field image with the SEM BSE image, which indicates the presence of ZrN phase in form of a particle cloud embedded into the ZrO<sub>2</sub> of the oxidized cladding at southward orientation. The SE image gives the position (Pos. 2) of the depicted EDX spectrum, containing the N peak, whereas the omitted spectrum of Pos. 1 did not show such a peak. The contrasts of the BSE image alone are sufficient to confirm that ZrN phase is also found at the inner border of the scale and in contact to the pellet.

With reference to the previous illustrations of rod 12 at 850 mm elevation, namely Fig. 96, the SEM analysis of a zone of massive ZrN phase and the surrounding ZrO<sub>2</sub> is depicted in Fig. 110. This figure includes an LM micrograph, the magnified field in SE contrast with EDX analysis positions, and two of the spectra. At Pos. 1 ZrN phase is confirmed, at Pos. 2 the re-oxidation of the previously present ZrN during its further inward penetration. The spectrum of Pos. 3, not shown, is similar to Pos. 2. Concerning another cross section area of rod 12, it is mentioned that the interpretation of Fig. 97 has been confirmed by four element spectra in total.

An SEM investigation of the internal shroud oxidation at the 850 mm level was performed for the position depicted in Fig. 98. The BSE contrast between scale and shroud matrix was sufficient to identify the  $\alpha$ -Zr(O) phase precipitation at the grain boundaries of the innermost scale during the cooling from a temperature above 1800 K (prior cubic sub-layer). The suspected seam of ZrN phase, remaining after the air exposure period at penetration position, showed very faint BSE contrast compared to the scale, and the EDX spectrum in comparison to spectra of the oxide behind and before this zone gave the clear confirmation (Fig. 111).

At 950 mm elevation the massive shroud scale modification was studied at two positions. Northward in the bundle (compare to Fig. 100), a scalloped penetration front of ZrN phase was confirmed by SEM investigation mainly by the presence of the nitrogen peak in the respective spectrum and the absence of N at three other positions behind and before this transformation / re-oxidation zone (Fig. 112). Finally, SEM results are depicted in Fig. 113 for the shroud weld towards NW (compare to Fig. 101). Besides overviews by LM and in BSE contrast, BSE images show the spalled outer scale sub-layer and the inner part of the scale. The LM contrast of bright zones of the outer layer and the absence of such a contrast in the BSE image is sufficient to identify those zones as ZrN phase. The system of lateral cracks might have facilitated the spalling. The grain boundary contrast of the inner layer is sufficient to confirm the precipitation of  $\alpha$ -Zr(O) phase, formed during decay of the cubic ZrO<sub>2</sub> modification.

### 8.3.6 Summary and Conclusions

The results of the comprehensive metallographic post-test evaluation of the QUENCH-10 bundle and of the scale thickness measurements are given and discussed on basis of the observed degradation phenomena. Special attention was paid to the cladding oxidation during the air exposure phase and the bundle response to quenching.

The two corner rods, withdrawn during the experiment (rod B, after the steam pre-oxidation phase, and the lower part of rod D, withdrawn towards the end of the transient phase of air exposure) were inspected in addition to the examination of several bundle cross sections. The surplus oxidation of rod D during air exposure was the reason for rod fracturing during pulling. Axial scale profiles and summarizing illustrations are given for both rods. The results fit to the measured values and metallographic observations obtained for the bulk bundle. The lateral scale thickness distribution for the cross sections and the thus determined axial profiles for the oxidation extent of the bundle components gave rather flat lateral profiles with large local scatter, and pronounced axial profiles. At 800 mm elevation some of the rods show complete cladding conversion after fast external oxidation of the molten cladding matrix and internal oxygen transfer from the pellets. Above this level only local thickness results can be given, at 950 mm all claddings are lost after fragmentation and relocation. Within this elevation range the oxidation of the shroud is seen to have continued, including the surfaces of secondary cavities. Above the 1000 mm level the extent of bundle oxidation is decreasing.

The shroud examination at the 500 and 650 mm elevations, performed complementary to the videoscope inspection, comprised the observed discolored and partially spalled spots of scale and the axially extended stripes of similar appearance. The axial weld seam of the shroud at NW is covered by thick post-transition scale, characterized by breakaway-related lateral crack system formation. The presence of zirconium nitride phase embedded within the internal sub-layer indicates the contribution of the air exposure. Similarly localized shroud scale morphology, assumed to be related to scratches or local defects, is interpreted as top layer growth and eventual separation, post-transitional scale growth and embrittlement, and air typical interaction products formation. At 650 mm a number of relocated and accumulated cladding and pellet fragments is observed within the bundle. The detailed documentation of the rods revealed the rather moderate cladding oxidation by growth of protective smooth or scalloped pre-transitional scale.

At the 750 mm level the more advanced rod cladding oxidation is accompanied by local defect formation: Scale cracking, axial crack expansion to wedge form, the related trends towards scale stoichiometry and tube deformation, all of them initiating mechanisms of the "flowering effect", facilitate the observed local air reaction product formation and air penetration through the cladding. At 800 and 850 mm the degradation of the rods is more advanced or even serious, respectively: Deformation of cladding contours, axial splitting and expansion have exposed the interior to the atmosphere, and the disintegration of fractured annular pellet simulators is mentioned. Locally, metallic cladding melt residues remain between scale and pellet, due to limited atmosphere access. At both levels a bed of relocated rubble fragments has been accumulated.

The most striking and repeatedly documented interaction of air with pre-oxidized cladding is the formation of nitride phase as top layer under consumption of oxide. The observations resulting not only from the inspection of the 800 and 850 mm elevations can be interpreted

by the following steps: Inward expansion of the ZrN zone proceeds, whereas the re-oxidation of nitride to oxide is initiated at the free surface, and is penetrating inward as well. The re-oxidation product seems to be porous, or at least more fragile than the original scale, which allows to distinguish between both forms. The nitride growth front may proceed regularly, develop a scalloped contour, or divide into spots. Observed exhaustion of the process should be due to nitrogen losses. The fact that at least some of the originally formed ZrN phase has survived during quenching should be due to the protected position within scale. Those tentative interpretations are based on considering the thermodynamic phase stabilities: Accordingly, the phenomenon should be restricted to scale/metallic matrix diffusion couples, in order to explain the consumption of the oxygen, released during oxide conversion, by the underlying metal. Serious oxygen starvation in the atmosphere should be the other condition for the effect.

At the 950 mm elevation all fuel rod simulators have lost their cladding and some of them pellet fragments as well. Predominance of oxidation and absence of cladding melt/pellet reaction have led to the collapse of the central rod, whereas the surrounding ones were only stabilized by the tungsten rods. The shroud shows the above described air exposure related reaction sequence at the whole internal surface.

The inspection of the electrode section of the bundle at 1080 mm elevation allowed to study the air exposure related fragmentation of the cladding from the initiating features, and thus the reasons for the earlier mentioned relocation of coarse cladding fragments: Locally advanced cladding consumption and cracking, supported by nitride phase formation, promote local wall penetration of cladding, which is only partly converted elsewhere. It is plausible to assume that stress concentration to those weak regions has caused the splitting into fragments.

The described air specific aspects of the bundle oxidation have required special efforts for the doubtless determination of ZrN phase distinguished from Zr(O) phase. By optical microscopy ZrN shows golden color, compared to the yellowish tint of Zr(O) and the gray tone of ZrO<sub>2</sub>. Scanning electron microscopy (SEM) gives good contrast between the lighter gray of Zr(O) and the darker gray of ZrO<sub>2</sub> and ZrN for a back scattered electron (BSE) image, and slightly less distinct contrast of the same kind for the secondary electron (SE) image. The energy dispersive X-ray (EDX) analysis (using SE illumination) is the decisive method for the determination or exclusion of nitrogen in an element spectrum. All critical interpretations of microstructures have been checked for reliability and consistence of the deduced degradation mechanisms, related to oxygen starvation conditions or the total air exposure phase.

#### **8.4 Hydrogen Absorption by Zircaloy**

The hydrogen absorbed could not be analyzed for this test bundle as there was no remaining Zircaloy-4 metal in the rod claddings of the hot zone.

## 9 Computational Support

### 9.1 Analytical Work for Test Preparation by FZK/IRS and PSI with Help of the SCDAP/RELAP5 mod 3.1irs and MELCOR Codes

Preparation of the test is based on common analytical work at Forschungszentrum Karlsruhe and Paul Scherrer Institut (PSI), Villigen, Switzerland [11], mainly with the severe accident codes SCDAP/RELAP5 (S/R5) and MELCOR, to derive the protocol for the essential test phases, namely pre-oxidation, air ingress, and quench phase. For issues that could not be tackled by this computational work, suggestions for the test conduct were made and applied during the test. Furthermore, improvements of the experimental set-up and the test conduct were suggested and largely applied.

In S/R5 a programming error was found concerning the output value of the oxide scale thickness for advanced oxidation. Its relevance was not only assessed by comparison of the QUENCH-10 predictions with MELCOR results from PSI, but also by comparison with SVECHA results (see next section) and with SET, both performed at FZK/IMF. The SVECHA calculations are based on temperature histories, predicted by S/R5 for the central rod. For the aims of the test preparation, its consequences could therefore be taken into account appropriately.

### 9.2 Modeling of the Central Rod Oxidation with the SVECHA Code

According to the scenario of the test QUENCH-10 the maximum oxide layer thickness of ~600  $\mu\text{m}$  before the air ingress phase should be obtained. The accurate duration of the corresponding test phases was needed to run the test properly. Most of the integral computer codes, based on empirical kinetics of the oxide layer growth, were verified for relatively thin (less of 300  $\mu\text{m}$ ) oxide scales. Therefore it was decided to additionally use the mechanistic code SVECHA/QUENCH [21]. The oxidation module of the SVECHA code is based on solutions of differential equations with help of diffusion coefficients for oxygen, achieved from the experimental work of Pawel and Cathcart and as well of Leistikow and Schanz. The code was developed for the single rod tests with inductive rod heating and therefore needs as input data either a heat source inside the cladding or a temperature history of the cladding surface. To avoid the problem of heat sources the “unheated” central rod of the QUENCH-10 bundle was chosen for modelling.

The temperature history was based on the temperature profiles, achieved with the integral code SCDAP/RELAP 5 [14]. The rod was divided into 18 axial meshes within the heated zone of the bundle using steps of 50 mm for the twelve lower meshes and of 100 mm for the six upper meshes. The mesh steps correspond to the SCDAP/RELAP 5 data. [Fig. 114](#) shows some of the used temperature profiles for different bundle elevations.

The following input parameters were applied, which were obtained by converting bundle integral values to the one rod channel:

- Steam flow rate:  $0.9 \cdot 10^{-4}$  kg/s
- Argon flow rate:  $0.98 \cdot 10^{-4}$  kg/s

- Channel pressure:  $2.2 \cdot 10^5$  Pa.

The calculated hydrogen mass, generated during oxidation, was extrapolated to the whole bundle. For the extrapolation a multiplier of 30.674 was used, corresponding to the ratio between the perimeter of all Zircaloy elements (shroud, 21 rod simulators, 4 corner rods) and the perimeter of a single rod simulator. [Fig. 115](#) shows the evolution of hydrogen generation for the single rod and for the whole bundle.

[Fig. 116](#) shows the changes of the phases of the cladding with the time for the elevations 675 mm, 925 mm, and 1250 mm. One can see that the thickness of the oxide layer at the hottest bundle elevation (925 mm) reaches the value of 600  $\mu\text{m}$  after pre-oxidation during  $\sim 6200$  s.

### 9.3 Investigation of Oxidation and Hydrogen Behavior with the CALUMO Code

As QUENCH-10 is a new type of test (air ingress) in the frame of the QUENCH program, some improvement in the framework of models implemented in the CALUMO code had to be done. The main features of this work will be discussed in the following without going too much into details.

In a first step the thermo-physical data of air (thermal conductivity, heat capacity, viscosity, mass density, and diffusivity) had to be implemented. Based on the data taken from ref. [22] simple correlations were established. These correlations are needed for the model of convective heat transfer into the fluid and for the diffusivity limit for the oxidation rate of Zry. The properties of gas mixtures are calculated in CALUMO with the help of the model of Wilke [23].

In order to simulate the oxidation of Zry in air a new simple model was developed based on the data given in ref. [24]. It should be noted that these data were for tests under steady-state conditions done in a furnace at IMF. In this new model it is assumed that the evolution of the scale  $\delta_{\text{ox}}$  can be described with parabolic-linear time dependence as follows:

$$\text{for } t \leq t_f : \delta_{\text{ox}}^2(t) = k_p^{\text{par}} \cdot t \quad (1)$$

$$\text{for } t \geq t_f : \delta_{\text{ox}}(t) = a^{\text{lin}} \cdot (t - t_f) + \delta_{\text{ox}}(t_f) \quad (2)$$

In this way, the phenomenon of break-away oxidation could be dealt with. Thus, the newly developed model depends on three empirical parameters, namely the parabolic rate constant  $k_p^{\text{par}}$ , the linear rate parameter  $a^{\text{lin}}$ , and the time of break-away  $t_f$ . These parameters depend all on the temperature  $T$ . Simple correlations have been determined with the help of the data given in [24] and implemented in the CALUMO code.

In order to account for the varying temperature conditions in a QUENCH test a failure parameter  $f$  is defined in the form of a life fraction rule:

$$f(t) = \sum_i \frac{\Delta t_i}{t_f(T)} \quad (3)$$

The summation in eq. (3) goes over all  $\Delta t_i$  up to a certain time  $t$ . It should be noted that the calculation in CALUMO proceeds via time steps.

The basic idea behind such a definition of a failure parameter is the fundamental concept of flaw size in fracture mechanics. The flaw size in the scale increases with time due to vacancy migration and we think that a life fraction rule is best suited to describe this in a simple way.

If the failure parameter  $f$  reaches the value 1, the break-away regime commences (by definition). For each subgroup of fuel rods in the bundle (for definition of the subgroups see ref. [25]) and for the shroud values of the failure parameter are calculated in each axial mesh as is done for the temperatures, for example.

The situation in the test QUENCH-10 is more complicated than that of the oxidation tests reported in [24], as there is a foregoing period of oxidation under steam, which has eventually led to the formation of stable oxide scales. For temperatures below 1100 K there is also a break-away regime in case of steam oxidation. Thus, we can also define a failure parameter in the same way as done in eq. (3) by using the experimental data on  $t_f$  for steam oxidation also given in [24]. Thus, at the onset of the air oxidation the failure parameter  $f$  has well-defined values in the different axial meshes. The question how we can do the switch to the treatment of air oxidation can only be decided on a physical basis.

The situation is clear if the break-away regime is already reached under steam oxidation. Then we can simply continue with the break-away regime under air. If at the end of the steam oxidation period we are still in the parabolic regime, one can estimate the time needed for the nitrogen to migrate through the oxide scale with help of the following expression:

$$\Delta t_{diff}^N = \frac{\delta_{ox}^2}{\Pi \cdot D^N} \quad (4)$$

$D^N$  : nitrogen diffusion coefficient in  $ZrO_2$

No values for the nitrogen diffusion coefficient in  $ZrO_2$  were found in the literature. But in order to estimate the effect we can take the oxygen diffusion coefficient instead. Depending on the oxide scale thickness at the end of steam oxidation phase we have estimated that it can take more than 2000 s before nitrogen reaches the metallic substrate.

On this reason it was decided that in case of a stable oxide scale oxygen is the only species contributing to the corrosion under air. It is known that for oxidation of Zry under oxygen one can use the same correlations as under steam. Of course, it is possible that by the presence

of nitrogen short-circuit paths are formed in the oxide scale and then the expression (4) would no longer be relevant.

There is one special feature in QUENCH-10, namely the intermediate decrease of the temperatures due to a reduction of the electric power. In the oxide scale through-wall cracks can be formed if  $ZrO_2$  undergoes a phase transition from the tetragonal to the monoclinic modification (see for example [26]). This effect occurs for oxide scales above a certain thickness (about 200  $\mu m$  [27]). For the calculations of QUENCH-10 with CALUMO the number of through-wall cracks and the axial zone is specified explicitly in order to simplify the treatment.

In the frame of the pre-calculations for QUENCH-10 it was found that the code could not simulate correctly the long lasting nearly steady-state pre-oxidation phase under steam. From about 5000 s onwards there was an upward drift of the bundle temperatures ending in a temperature escalation. In the post test calculation campaign it was found that this problem of the code could be solved by replacing the model for convective heat transfer into the fluid. We have now implemented the heat transfer model of McAdams for superheated steam [28] as given in [29] for bundles with square lattices:

$$Nu = 0.0214 \cdot Re^{0.8} \cdot Pr^{1/3} \cdot \left(1 + \frac{2.3}{x/d_{hyd}}\right) \quad (5)$$

Nu : Nusselt number    Re : Reynolds number    Pr : Prandtl number

x : axial distance from the inlet     $d_{hyd}$  : hydraulic diameter

The characteristic dimensionless numbers of the fluid are calculated with the help of the thermo-physical values of the gas mixture in the coolant channel. The newly developed models were implemented in most advanced version of the CALUMO code, namely CALUMOf and the calculations for QUENCH-10 were done with this version.

In [Fig. 117](#) are shown evolutions of the failure parameter  $f$  for the claddings of the inner row of heated fuel rod simulators at different axial locations. At the beginning of the air ingress phase the maximum values are about 0.6. During the air ingress phase the failure parameter crosses the failure threshold ( $f = 1$ ) at two axial locations. Failure of the oxide scale means that cracks are formed and therefore short-circuit paths for the gas transport. The scale is no longer protective and eq. (4) becomes obsolete. The results shown in [Fig. 117](#) suggest that the break-away condition was probably reached in a certain axial region and in view of the uncertainties in the data may be even at the very beginning of the air ingress phase. This could have led to the observed temperature escalations.

The real case calculations with CALUMO were done before the results of post test examinations were available. Thus, we have made the assumption on through-wall cracks in the oxide scale as the cause of the observed temperature escalations in the air ingress phase. But an assumption on break-away oxidation would have led to similar results.

On the basis of Figs. 118 to 122 we are now going to discuss some results of the CALUMO code in comparison to the respective data of the test instrumentation concerning the temperature evolutions between 150 and 1250 mm, the axial profiles of oxide scale thickness for the fuel rod simulators and the shroud, and the results on hydrogen production (rates and time-integrated production).

Figs. 118 and 119 show the mean temperature in the outer ring of fuel rod simulators "tsurz", that of the inner cluster of 8 fuel rod simulators "tcenz", that of the central rod "tcrz", and the mean shroud temperature "tshrz". They are compared to the available thermocouple readings at different axial positions between 150 and 1250 mm.

As a general remark we can state that the characteristic features of the temperature evolution in the considered part of the test section are on the whole relatively well simulated. There is some upswing of the calculated temperatures during the first half of the pre-oxidation phase most probably caused by the heat release due to the oxidation process and the coupling with the heat release by the electrodes. This phenomenon is not seen by the thermocouples. The upswing does not lead to a temperature escalation, as has occurred for the pre-calculations of QUENCH-10. We think that this is due to the new model of convective heat transfer. In the second part of the steam pre-oxidation phase the slope of calculated temperatures matches that of the thermocouple readings fairly well, especially in the heated part of the test section.

The thermal behavior of the test section as shown by the thermocouple readings is rather well simulated by the code during the phase of reduced power. All the essential characteristic features are relatively well met (downward slopes, period of thermal equilibrium). During this phase oxidation is not important and it is only the electric heat release, which determines the thermal behavior of the test section. Such a situation is rather well described by the code, a fact which is now well established.

All the periods with significant temperature changes caused by power changes or caused by the switch from steam/argon to air/argon gas mixture are fairly well simulated. Only for the second drop of electric power in the steam pre-oxidation phase the thermocouple readings show a behavior rather different from the calculated temperatures, with a slight decrease reflecting the drop of electric power, whereas the calculated temperatures continue with their increase for some time.

The absolute level of the calculated temperatures in comparison to the level of thermocouple readings needs some comment. The calculated temperatures show a spread of roughly 200 K with the lowest temperature given by the shroud and the highest by that of the inner rod bundle. The levels of the thermocouple readings are often near to the calculated shroud temperature or at some axial levels (550 and 650 mm) distinctly below this. It should be noted that the code calculates mean temperatures, whereas the thermocouples are mostly located at the outside. On geometrical reasons the thermocouples do not even measure exactly the clad or shroud outer temperature, but a temperature being somewhat lower, as there is a temperature gradient from the convective heat transfer. The TIT thermocouples in the corner rods, on the other hand, are at locations in the bundle, where the temperatures are relatively low. But astonishingly enough TIT C/12 indicates a higher

temperature than TCRC 12. The temperatures in the test section determine the oxidation and hydrogen production. As we can see in the following both are relatively well simulated by the CALUMO code. This would not be the case with temperatures as given by the thermocouple readings. Of course, this statement is based on the fact that we use the oxidation correlation of Leistikow [30].

The temperature escalations towards the air ingress phase between 650 and 850 mm calculated by the code are due to the assumption of through-wall crack formation at the period of reduced electric power. Similar temperature escalations can probably be obtained with the assumption of break-away oxidation. Without such assumptions the code would not give temperature escalations and the temperatures would not rise above 1650 K. As is suggested by the thermocouple readings and by the hydrogen measurement by the mass spectrometer these temperature escalations are real. It could not be found out why the code does not calculate an important temperature escalation at 950 mm as given by the thermocouple readings. For completeness we have also plotted in Fig. 120 axial profiles of the central rod temperature for different times into the air ingress phase. This gives a good overview on the evolution of the temperature escalation. The maximum temperature reached during the escalation depends on the modelling and on the assumptions having been taken.

There is a problem in quench module of the CALUMO code, which didn't appear in earlier calculations of QUENCH tests, namely the temperatures do not fall below 400 K as suggested by the thermocouple readings but stay at a level fairly above. This is not a serious problem for the QUENCH-10 calculations as this occurs towards the end, but this problem must be solved for forthcoming tests. May be that it is due to axial heat flow in the electrodes modelled in the code.

A comparison of calculated hydrogen values (rate and time integrated hydrogen) with experimental data from the mass spectrometer are to be seen in Fig. 121. Hydrogen production of QUENCH-10 is in an acceptable way simulated by the code. There is one peak in the measured hydrogen production rate at about 2600 s (early steam pre-oxidation phase with high electric power). The calculated curve shows a small peak at the same time and a second higher peak about a 1000 s later with a height similar to the experimental one. The second peak is due to the upswing of the temperatures.

At about 13400 s (air ingress phase) there appears an important as-calculated hydrogen peak due to the temperature escalation. The mass spectrometer sees several events, but the first steep increase of the hydrogen signal coincides with that in the calculated curve. Total calculated hydrogen production is nearly 52 g, whereas the mass spectrometer gives about 53 g. These are very encouraging results.

The calculated axial profiles of the oxide scale thickness at the time, when the corner rods were withdrawn and when the calculation was stopped are plotted in Fig. 122 together with experimental values from post test examinations, with "doxi" denoting the oxide scales of the inner cluster of 9 heated fuel rods, „ doxc „ that of the central rod, "doxa" that of the outer ring of 12 heated fuel rods and "doxsh" the oxide scale of the shroud. The values of outer ring of heated rods are considered to be representative for the corner rods.

The maximum value of calculated oxide scale thickness compares in all cases rather well with the measured values and the width of the profiles is similar. But there is one problem with the code results. All the calculated profiles are shifted downwards by 100 to 200 mm. This problem was encountered for all QUENCH tests and we have not yet found an explanation for it. The results having been found for the oxidation confirm that for the hydrogen production, especially the satisfactory agreement between measured and calculated values.

## 10 References

- [1] J.M. Broughton, P. Kuan, and D.A. Petti, "A Scenario of the Three Mile Island Unit 2 Accident," *Nuclear Technology*, 87, 34, 1989.
- [2] P. Hofmann, S. Hagen, V. Noack, G. Schanz, L. Sepold, "Chemical-Physical Behavior of Light Water Reactor Core Components Tested under Severe Reactor Accident Conditions in the CORA Facility," *Nuclear Technology*, vol. 118, 1997, p. 200.
- [3] S. Hagen, P. Hofmann, V. Noack, L. Sepold, G. Schanz, G. Schumacher, "Comparison of the Quench Experiments CORA-12, CORA-13, CORA-17," FZKA 5679, Forschungszentrum Karlsruhe, 1996.
- [4] S.M. Modro and M.L. Carboneau, "The LP-FP-2 Severe Fuel Damage Scenario; Discussion of the Relative Influence of the Transient and Reflood Phase in Affecting the Final Condition of the Bundle," OECD/LOFT Final Event, ISBN 92-64-03339-4, 1991, p. 388.
- [5] B. Clement, N. Hanniet-Girault, G. Repetto, D. Jacquemain, A.V. Jones, M.P. Kissane, P. von der Hardt, "LWR Severe Accident Simulation: Synthesis of the Results and Interpretation of the First Phebus FP Experiment FPT0," *Nuclear Engineering and Design*, 226, (Spec. Iss.) 5-82, 2003.
- [6] L. Sepold, A. Miassoedov, G. Schanz, U. Stegmaier, M. Steinbrück, J. Stuckert, C. Homann, "Hydrogen Generation in Reflooding Experiments with LWR-type Rod Bundles (QUENCH Program)," *Journal Nuclear Technology*, Vol. 147, Aug. 2004, pp. 202-214.
- [7] P. Hofmann, V. Noack, M.S. Veshchunov, A.V. Berdyshev, A.V. Boldyrev, L.V. Matweev, A.V. Palagin, V.E. Shestak, "Physico-Chemical Behavior of Zircaloy Fuel Rod Cladding Tubes During LWR Severe Accident Reflood," FZKA 5846, Forschungszentrum Karlsruhe, 1997.
- [8] P. Hofmann, A. Miassoedov, L. Steinbock, M. Steinbrück, M. Veshchunov et al., "Quench Behavior of Zircaloy Fuel Rod Cladding Tubes. Small-Scale Experiments and Modeling of the Quench Phenomena," FZKA 6208, Forschungszentrum Karlsruhe, 1999
- [9] J. Stuckert, M. Steinbrück, U. Stegmaier, "Single Rod Quench Tests with Zr-1Nb. Comparison with Zircaloy-4 Cladding Tests and Modelling," FZKA 6604, Forschungszentrum Karlsruhe, 2001

- [10] A. Miassoedov et al., "Large Scale Experiments on Core Degradation, Melt Retention and Coolability (LACOMERA)," FISA-2003: EU Research in Reactor Safety, Luxembourg, Nov. 10-13, 2003, Proc., p. 373-378.
- [11] Z. Hózer, G. Gyenes, G. Ézsöl, P. Vértes, "Level 2 Probabilistic Safety Assessment of the Paks Nuclear Power Plant; Calculation of the Source Term for the Failure of the Fuel Stored in the Spent Fuel Storage Pool, Revision № 2," AEKI intern. report, 2003.
- [12] M. Steinbrück, P. Severloh, U. Stegmaier, T. Ziegler. „Oxidation of Zircaloy in prototypic air-steam mixtures”. 11th International QUENCH Workshop at Forschungszentrum Karlsruhe, Oct. 25-27, 2005, Proceedings CD-ROM, Forschungszentrum Karlsruhe, 2005.
- [13] M. Steinbrück, A. Miassoedov, G. Schanz, L. Sepold, U. Stegmaier, J. Stuckert, "Experiments on Air Ingress during Severe Accidents," 13th International Conference on Nuclear Engineering, Beijing, China, May 16-20, 2005 (ICONE13-50080), 2005 (CD ROM).
- [14] Ch. Homann, W. Hering, J. Birchley, T. Haste, "Analytical Support for the Preparation of Bundle Test QUENCH-10 on Air Ingress," FZKA 7086 (SAM-LACOMERA-D01) 2005.
- [15] Z. Hózer, P. Windberg, I. Nagy, L. Maróti, L. Matus, M. Horváth, A. Pintér, A. Czitrovsky, P. Jani, "CODEX-AIT-1 Experiment: Core Degradation Test under Air Ingress," KFKI-2002-02/G, KFKI, 2002.
- [16] Z. Hózer, P. Windberg, I. Nagy, L. Maróti, L. Matus, M. Horváth, A. Pintér, A. Griger, M. Balaskó, B. Alföldy, A. Czitrovsky, P. Jani, "CODEX-AIT-2 Experiment: Core Degradation Test with Steam Oxidation and Air Ingress," KFKI-2002-03/G, KFKI, 2002.
- [17] Z. Hózer, I. Nagy, P. Windberg, M. Balaskó, L. Matus, O. Prokopiev, A. Pintér, M. Horváth, Gy. Gyenes, A. Czitrovsky, A. Nagy, P. Jani, "CODEX B4C Experiment: Core Degradation Test with Boron Carbide Control Rod," KFKI-2003-01/G, KFKI, 2003.
- [18] Z. Hózer, P. Windberg, I. Nagy, L. Maróti, L. Matus, M. Horváth, A. Pintér, M. Balaskó, A. Czitrovsky, P. Jani, "Interaction of Failed Fuel Rods under Air Ingress Conditions," *Nucl. Technology*, **141**, pp. 244, 2003.
- [19] A. Pintér, Csordás, L. Matus, A. Czitrovsky, P. Jani, L. Maróti, Z. Hózer, P. Windberg, R. Hummel, "Investigation of Aerosols Released at High Temperature from Nuclear Reactor Core Models," *J. Nucl. Materials*, **282**, ISS 2-3, pp. 205, 2000.
- [20] G. Schanz, S. Leistikow, "ZrO<sub>2</sub>-Scale Degradation During Zircaloy-4 High Temperature Steam Exposure; Microstructural Mechanisms and Consequences for PWR Safety Analysis," ANS/ENS Topical Meeting on Reactor Safety Aspects of Fuel Behaviour, Aug. 2-6, 1981, Sun Valley, ID, USA, Proc. Vol II, p.342.
- [21] A. V. Berdyshev, A. V. Boldyrev, A. V. Palagin, V. E. Shestak, and M. S. Veshchunov, "SVECHA/QUENCH Code for the Modeling of Reflooding Phenomena in Severe Accidents Conditions," Proc. 9th Int. Top. Mtg. Nuclear Reactor Thermal Hydraulics (NURETH-9), San Francisco, California, October 3-8, 1999, American Nuclear Society, 1999 (CD-ROM).

- [22] Verein Deutscher Ingenieure, VDI-Wärmeatlas, "Berechnungsblätter für den Wärmeübergang," 8. Auflage, Springer Verlag Heidelberg, 1997.
- [23] C.R. Wilke, J. Chem. Phys. 18, p. 517, 1950.
- [24] S. Leistikow, unpublished results, 1981.
- [25] H. Steiner, M. Heck, "Calculations of QUENCH Tests with the FZK Bundle Code CALUMO," FZKA 7192, Forschungszentrum Karlsruhe, 2005.
- [26] H. Steiner, M. Heck, "Stresses in an Oxidized Zircaloy Cladding Under Quench Conditions: Recalculation of Single-Rod Quench Tests," Nucl. Techn. 123, pp. 209-221, 1998.
- [27] L. Steinbock, J. Stuckert, "Determination of the crack pattern of quenched Zircaloy tubes," FZKA 6013, Forschungszentrum Karlsruhe, 1997.
- [28] W.H. McAdams, W.E. Kennel, and J.N. Emmons, "Heat transfer to superheated steam at high pressures addendum," Trans. ASME 72, p. 421, 1950.
- [29] N.E. Toraus, M.S. Kazimi, "Nuclear Systems I Thermal Hydraulic Fundamentals," Hemisphere Publishing Corporation N. Y., 1990.
- [30] S. Leistikow, et al., "Kinetik und Morphologie der isothermen Dampfoxidation von Zircaloy-4 bei 700° bis 1300°C," KFK 2587, Forschungszentrum Karlsruhe, 1978.

## Acknowledgments

Test QUENCH-10 (QUENCH-L1) was performed and co-financed in the frame of the LACOMERA Project FIR1-CT-2002-40158 of the EU 5th Framework Program. Thanks are due to Dr. A. Miassoedov, FZK/IKET, who initiated this project within the Karlsruhe Research Center. In general, at the Karlsruhe Research Center the broad support needed for preparation, execution, and evaluation of the experiment is gratefully acknowledged. In particular, the authors would like to thank Messrs. L. Anselment and S. Horn for the assembly of the heated test rods, Mr. J. Moch for the assembly of the entire test section and the various support, and Mrs. J. Laier for processing the test data.

The determination of the test conduct was based on numerous pre-test calculations with SCDAP/RELAP5, MELCOR, and SVECHA/Q performed in collaboration of Forschungszentrum Karlsruhe (Drs. C. Homann and W. Hering) and PSI (Drs. J. Birchley and T. Haste). Good agreement with the experimental results for the various phases of the test demonstrates the quality of modelling the facility with the codes. This also holds well for the computation of the maximum oxide layer thickness.

**Table 1: QUENCH Test Matrix**

Test	Quench medium	Injection rate	Temp. at onset of flooding <sup>1)</sup>	Max. ZrO <sub>2</sub> before flooding <sup>2)</sup>	Max. ZrO <sub>2</sub> layer thickness <sup>3)</sup>	H <sub>2</sub> production before / during cooldown	Remarks, objectives
<b>QUENCH-00</b> Oct. 9 - 16, 97	Water	80 g/s	≈ 1800 K		≈ 500 μm		COBE Project; commissioning tests.
<b>QUENCH-01</b> February 26, 98	Water	52 g/s	≈ 1830 K	312 μm	≈ 610 μm	36 / 3	COBE Project; partial fragmentation of pre-oxidized cladding.
<b>QUENCH-02</b> July 7, 98	Water	47 g/s	≈ 2440 K		completely oxidized	20 / 140	COBE Project; no additional pre-oxidation; quenching from high temperatures.
<b>QUENCH-03</b> January 20, 99	Water	40 g/s	≈ 2450 K		completely oxidized	18 / 120	No additional pre-oxidation, quenching from high temperatures.
<b>QUENCH-04</b> June 30, 99	Steam	50 g/s	≈ 2160 K	82 μm	≈ 360 μm	10 / 2	Cool-down behavior of slightly pre-oxidized cladding by cold steam injection.
<b>QUENCH-05</b> March 29, 2000	Steam	48 g/s	≈ 2020 K	160 μm	≈ 400 μm	25 / 2	Cool-down behavior of pre-oxidized cladding by cold steam injection.
<b>QUENCH-06</b> Dec. 13 2000	Water	42 g/s	≈ 2060 K	207 μm	≈ 660 μm	32 / 4	OECD-ISP 45; prediction of H <sub>2</sub> source term by different code systems.
<b>QUENCH-07</b> July 25, 2001	Steam	15 g/s	≈ 2100 K	230 μm	completely oxidized	66 / 120	COLOSS Project; impact of B <sub>4</sub> C absorber rod failure on H <sub>2</sub> , CO, CO <sub>2</sub> , and CH <sub>4</sub> generation.

Test	Quench medium	Injection rate	Temp. at onset of flooding <sup>1)</sup>	Max. ZrO <sub>2</sub> before flooding <sup>2)</sup>	Max. ZrO <sub>2</sub> layer thickness <sup>3)</sup>	H <sub>2</sub> production before / during cooldown	Remarks, objectives
<b>QUENCH-09</b> July 3, 2002	Steam	49 g/s	≈ 2100 K		completely oxidized	60 / 400	As QUENCH-07, steam-starved conditions prior to cooldown.
<b>QUENCH-08</b> July 24, 2003	Steam	15 g/s	≈ 2090 K	274 μm	completely oxidized	46 / 38	As QUENCH-07, no absorber rod
<b>QUENCH-10</b> July 21, 2004	Water	50 g/s	≈ 2200 K	514 μm	completely oxidized	48 / 5	LACOMERA Project; Air ingress.
<b>QUENCH-11</b> Dec 08, 2005	Water	18 g/s	≈ 2040 K	170 μm	t.b.d.	9 / 141	LACOMERA Project; Boil-off.

<sup>1)</sup> Maximum measured bundle temperature at 950 mm elevation.

<sup>2)</sup> Measured at the corner rod withdrawn from the bundle.

<sup>3)</sup> Measured posttest.

**Table 2: Design Characteristics of the QUENCH-10 Test Bundle**

Bundle type		PWR
Bundle size		21 rods
Number of heated rods		20
Number of unheated rods		1
Pitch		14.3 mm
Rod outside diameter		10.75 mm
Cladding material		Zircaloy-4
Cladding thickness		0.725 mm
Rod length	heated rod (levels) unheated rod (levels)	2480 mm (-690 mm to 1790 mm) 2842 mm (-827 mm to 2015 mm, incl. extension piece)
Heater material		Tungsten (W)
Heater length		1024 mm
Heater diameter		6 mm
Annular pellet	material heated rod unheated rod	ZrO <sub>2</sub> ;Y <sub>2</sub> O <sub>3</sub> -stabilized Ø 9.15/6.15 mm; L=11 mm Ø 9.15/2.5 mm; L=11 mm
Pellet stack	heated rod unheated rod	0 mm to ~ 1020 mm 0 mm to 1553 mm
Corner rod (4)	material instrumented uninstrument. (solid)	Zircaloy-4 tube Ø 6x0.9 (bottom: -1140 mm), rod Ø 6 mm (top: +1300 mm) rod Ø 6 mm (-1350 to +1155 mm)
Grid spacer	material length location of lower edge	Zircaloy-4, Inconel 718 Zry 42 mm, Inc 38 mm -200 mm Inconel 50 mm Zircaloy-4 550 mm Zircaloy-4 1050 mm Zircaloy-4 1410 mm Zircaloy-4
Shroud	material wall thickness outside diameter length (extension)	Zircaloy-4 2.38 mm 84.76 mm 1600 mm (-300 mm to 1300 mm)
Shroud insulation	material insulation thickness elevation	ZrO <sub>2</sub> fiber ~ 37 mm -300 mm to ~1000 mm
Molybdenum-copper electrodes	length of upper electrodes length of lower electrodes diameter of electrodes: - prior to coating - after coating with ZrO <sub>2</sub>	766 mm (576 Mo, 190 mm Cu) 690 mm (300 Mo, 390 mm Cu)  8.6 mm 9.0 mm
Cooling jacket	Material: inner/outer tube inner tube outer tube	Inconel 600 (2.4816)/SS (1.4571) Ø 158.3 / 168.3 mm Ø 181.7 / 193.7 mm

10/2005

**Table 3: Diameters of the Materials Used for the QUENCH High-Temperature Thermocouples**

Material	Dimensions as-received, mm	Final dimensions, mm
W/Re wires	0.254	
HfO <sub>2</sub> insulation OD (see drawing below)	1.1	
Ta tube OD / ID	2.15 / 1.65	1.4 / 0.94
Zr tube OD / ID	2.35 / 1.65 ± 0.013	2.1 / 1.4

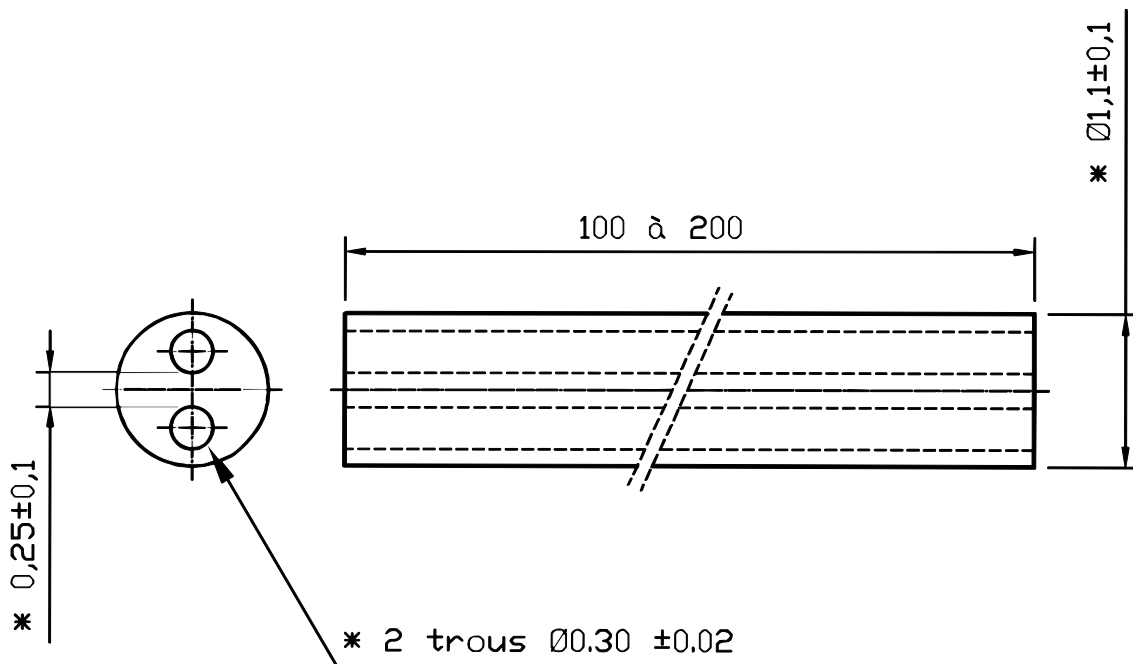


**Table 4: List of Instrumentation for the QUENCH-10 Test**

Channel	Designation	Instrument, location	Output in
:		Reserve	
2	TSH 9/0 I	TC (W/Re) shroud outer surface, 550 mm, 26°, TC cable routed outside ZrO <sub>2</sub> insulation	K
3	TFS 2/15	TC (W/Re) fuel rod simulator 4 (type 2), 1150 mm, 315°	K
4	TFS 2/17 F	TC (W/Re) fuel rod simulator 6 (type 2), 1350 mm. 45°, fluid temperature	K
5	TSH 15/180 I	TC (W/Re) shroud outer surface, 1150 mm, 206°, TC cable routed outside ZrO <sub>2</sub> insulation	K
6	TFS 5/11	TC (W/Re) fuel rod simulator 13 (type 5), 750 mm, 45°	K
7		Reserve	
8	TFS 3/13	TC (W/Re) fuel rod simulator 3 (type 3), 950 mm, 315°	K
9	TFS 3/14	TC (W/Re) fuel rod simulator 5 (type 3), 1050 mm, 45°	K
10		Reserve	
11	TFS 4/13	TC (W/Re) fuel rod simulator 20 (type 4), 950 mm, 135°	K
12	TFS 5/10	TC (W/Re) fuel rod simulator 12 (type 5), 650 mm, 225°	K
:		Reserve	
15	TSH 10/90 I	TC (W/Re) shroud outer surface, 650 mm, 26°, TC cable routed outside ZrO <sub>2</sub> insulation	K
16	TFS 5/14	TC (W/Re) fuel rod simulator 18 (type 5), 1050 mm, 45°	K
17	TSH 16/180 I	TC (W/Re) shroud outer surface, 1250 mm, 206°, TC cable routed outside ZrO <sub>2</sub> insulation	K
18	TSH 13/90 I	TC (W/Re) shroud outer surface, 950 mm, 116°, TC cable routed outside ZrO <sub>2</sub> insulation	K
19	TSH 14/90 I	TC (W/Re) shroud outer surface, 1050 mm, 116°, TC cable routed outside ZrO <sub>2</sub> insulation	K
20	TSH 11/0 I	TC (W/Re) shroud outer surface, 750 mm, 26°, TC cable routed outside ZrO <sub>2</sub> insulation	K
21	TSH 12/0 I	TC (W/Re) shroud outer surface, 850 mm, 26°, TC cable routed outside ZrO <sub>2</sub> insulation	K
22	TFS 2/5	TC (NiCr/Ni) fuel rod simulator 2 (type 2), 150 mm, 225°	K
23	TFS 2/7	TC (NiCr/Ni) fuel rod simulator 6 (type 2), 350 mm, 45°	K
24	F 902	Off-gas flow rate downstream condenser, upstream Caldos	Nm <sup>3</sup> /h

Channel	Designation	Instrument, location	Output in
25	FM 401	Argon gas mass flow rate	g/s
:		Reserve	
32	TIT A/13	TC (W/Re) corner rod A, center, 950 mm	K
33	TCRC 13	TC (W/Re) central rod, center, 950 mm	K
34	TFS 4/9	TC (W/Re) fuel rod simulator 17 (type 4), 550 mm, 135°	K
35	TSH 9/90	TC (NiCr/Ni) shroud outer surface, 550 mm, 116°	K
36	TSH 9/270	TC (NiCr/Ni) shroud outer surface, 550 mm, 296°	K
37	TFS 3/16	TC (W/Re) fuel rod simulator 7 (type 3), 1250 mm, 135°	K
38	TFS 5/9	TC (NiCr/Ni) fuel rod simulator 10 (type 5), 550 mm, 315°	K
39	TFS 2/9	TC (NiCr/Ni) fuel rod simulator 8 (type 2), 550 mm, 135°	K
40	TIT C/12	TC (W/Re) corner rod C, center, 850 mm	K
:		Reserve	
42	TFS 5/8	TC (NiCr/Ni) fuel rod simulator 21 (type 5), 450 mm, 135°	K
43	TFS 3/8	TC (NiCr/Ni) fuel rod simulator 5 (type 3), 450 mm, 45°	K
44	T003	Cooling water off-gas tube, outlet	K
45	T 304	TC (NiCr/Ni) outer surface of pipe downstream V302	K
:		Reserve	
47	TFS 5/15	TC (W/Re) fuel rod simulator 19 (type 5), 1150 mm, 225°	K
48	TFS 5/16	TC (W/Re) fuel rod simulator 21 (type 5), 1250 mm, 135°	K
49	TFS 5/17	TC (W/Re) fuel rod simulator 10 (type 5), 1350 mm, 315°	K
50	TCRC 12	TC (W/Re) central rod, center, 850 mm	K
51	TFS 2/11	TC (W/Re) fuel rod simulator 8 (type 2), 750 mm, 135°, feed through at the bottom	K
52	TSH 13/270 I	TC (W/Re) shroud outer surface, 950 mm, 296°, TC cable routed outside ZrO <sub>2</sub> insulation	K
53	TSH 14/270 I	TC (W/Re) shroud outer surface, 1050 mm, 270°, TC cable routed outside ZrO <sub>2</sub> insulation	K
54	TSH 11/180 I	TC (W/Re) shroud outer surface, 750 mm, 206°, TC cable routed outside ZrO <sub>2</sub> insulation	K
55	TSH 12/180 I	TC (W/Re) shroud outer surface, 850 mm, 206°, TC cable routed outside ZrO <sub>2</sub> insulation	K
:		Reserve	

Channel	Designation	Instrument, location	Output in
61	T 206	Temperature upstream steam flow instrument location, 1 g/s	K
62	P 206	Pressure at steam flow instrumentation location, 1 g/s	bar
63	R 001 air	Flow rate air, 1 g/s	g/s
64	T 402 b	Temperature of the tube surface downstream gas heater	K
:		Reserve	
66	TSH 15/0 I	TC (W/Re) shroud outer surface, 1150 mm, 26°, TC cable routed outside ZrO <sub>2</sub> insulation	K
67	TSH 16/0 I	TC (W/Re) shroud outer surface, 1250 mm, 26°, TC cable routed outside ZrO <sub>2</sub> insulation	K
68	T 512	Gas temperature at bundle outlet	K
:		Reserve	
71	Ref. T 01	Reference temperature 1	K
72	TFS 2/1 F	TC (NiCr/Ni) fuel rod simulator 4 (type 2), -250 mm, 315°, fluid temperature	K
73		Reserve	K
74	TFS 2/3	TC (NiCr/Ni) fuel rod simulator 8 (type 2), -50 mm, 135°	K
75	TCR 7	TC (NiCr/Ni) fuel rod simulator 1 (type 1), 350 mm, 135°	K
76	TFS 2/6 F	TC (NiCr/Ni) fuel rod simulator 4 (type 2), 250 mm, 315°, fluid temperature	K
77	TCR 9	TC (NiCr/Ni) fuel rod simulator 1 (type 1), 550 mm, 135°	K
78	TFS 5/4/0 F	TC (NiCr/Ni) fuel rod simulator 15 (type 5), 50 mm, 315°, fluid temperature	K
79	TFS 5/4/180	TC (NiCr/Ni) fuel rod simulator 21 (type 5), 50 mm, 135°	K
:		Reserve	K
81	TFS 5/6	TC (NiCr/Ni) fuel rod simulator 18 (type 5), 250 mm, 45°	K
82	TFS 5/7	TC (NiCr/Ni) fuel rod simulator 19 (type 5), 350 mm, 225°	K
83	TSH 4/270	TC (NiCr/Ni) shroud outer surface, 50 mm, 296°	K
84	TSH 3/180	TC (NiCr/Ni) shroud outer surface, -50 mm, 206°	K
85	TSH 4/180	TC (NiCr/Ni) shroud outer surface, 50 mm. 206°	K
86	TSH 7/180	TC (NiCr/Ni) shroud outer surface, 350 mm, 206°	K
87	TSH 4/90	TC (NiCr/Ni) shroud outer surface, 50 mm, 116°	K
88	TSH 1/0	TC (NiCr/Ni) shroud outer surface, -250 mm, 26°	K

Channel	Designation	Instrument, location	Output in
89	TSH 4/0	TC (NiCr/Ni) shroud outer surface, 50 mm, 26°	K
90	TSH 7/0	TC (NiCr/Ni) shroud outer surface, 350 mm, 26°	K
91	TCI 9/270	TC (NiCr/Ni) cooling jacket inner tube wall, 550 mm, 270°	K
92	TCI 10/270	TC (NiCr/Ni) cooling jacket inner tube wall, 650 mm, 270°	K
93	TCI 11/270	TC (NiCr/Ni) cooling jacket inner tube wall, 750 mm, 270°	K
94	TCI 13/270	TC (NiCr/Ni) cooling jacket inner tube wall, 950 mm, 270°	K
95		Reserve	
96	TCI 1/180	TC (NiCr/Ni) cooling jacket inner tube wall, -250 mm, 180°	K
97	TCI 4/180	TC (NiCr/Ni) cooling jacket inner tube wall, 50 mm, 180°	K
98	TCI 7/180	TC (NiCr/Ni) cooling jacket inner tube wall, 350 mm, 180°	K
99	TCI 11/180	TC (NiCr/Ni) cooling jacket inner tube wall, 750 mm, 180°	K
100	TCI 12/180	TC (NiCr/Ni) cooling jacket inner tube wall, 850 mm, 180°	K
101	TCI 13/180	TC (NiCr/Ni) cooling jacket inner tube wall, 950 mm, 180°	K
102	TCI 15/180	TC (NiCr/Ni) cooling jacket inner tube wall, 1150 mm, 180°	K
103	T002 inlet	Cooling water off-gas tube, inlet	K
104	TCI 9/90	TC (NiCr/Ni) cooling jacket inner tube wall, 550 mm, 90°	K
105	TCI 10/90	TC (NiCr/Ni) cooling jacket inner tube wall, 650 mm, 90°	K
106	TCI 11/90	TC (NiCr/Ni) cooling jacket inner tube wall, 750 mm, 90°	K
107	TCI 13/90	TC (NiCr/Ni) cooling jacket inner tube wall, 950 mm, 90°	K
108	T 305 flange	TC (NiCr/Ni) bundle inlet flange	K
109	TCI 1/0	TC (NiCr/Ni) cooling jacket inner tube wall, -250 mm, 0°	K
110	TCI 4/0	TC (NiCr/Ni) cooling jacket inner tube wall, 50 mm, 0°	K
111	TCI 7/0	TC (NiCr/Ni) cooling jacket inner tube wall, 350 mm, 0°	K
112	TCI 11/0	TC (NiCr/Ni) cooling jacket inner tube wall, 750 mm, 0°	K
113	TCI 12/0	TC (NiCr/Ni) cooling jacket inner tube wall, 850 mm, 0°	K
114	TCI 13/0	TC (NiCr/Ni) cooling jacket inner tube wall, 950 mm, 0°	K
115	TCI 15/0	TC (NiCr/Ni) cooling jacket inner tube wall, 1150 mm, 0°	K
:		Reserve	
119	T 306 foot	TC (NiCr/Ni) outer surface of bundle foot	K
120	TCO 1/0	TC (NiCr/Ni) cooling jacket outer tube surface, -250 mm, 0°	K
121	TCO 7/0	TC (NiCr/Ni) cooling jacket outer tube surface, 350 mm, 0°	K

Channel	Designation	Instrument, location	Output in
122	TCO 13/0	TC (NiCr/Ni) cooling jacket outer tube surface, 950 mm, 0°	K
123	T 601	Temperature upstream off-gas flow instrument (orifice) F 601	K
:		Reserve	
126	T 307 offgas	TC (NiCr/Ni) inner surface of inlet of off-gas pipe	K
:		Reserve	
128	T 104	Temperature quench water	K
129	T 201	Temperature steam generator heating pipe	K
130	T 204	Temperature upstream steam flow instrument location, 50 g/s	K
131	T 205	Temperature upstream steam flow instrument location, 10 g/s	K
132	T 301A	Temperature downstream superheater	K
133	T 302	Temperature heating pipe of superheater	K
134	T 303	Temperature upstream total flow instrument (orifice) location	K
135	T 401	Temperature upstream gas flow instrument (orifice) location	K
136	T 403	Argon temperature at inlet cooling jacket	K
137	T 404	Argon temperature at outlet cooling jacket	K
138	T 501 cont-t	Temperature in containment (close to bundle head)	K
139	T 502	Temperature at outer surface of containment, 0°, 2.4 m	K
140	T 503	Temperature at outer surface of containment, 270°, 2.2 m	K
141	T 504	Temperature at outer surface of containment, 270°, 3.2 m	K
142	T 505	Temperature at outer surface of containment, 90°, 3.2 m	K
143	T 506	Temperature at outer surface of containment, 270°, 3.6 m	K
144	T 507	Temperature at outer surface of containment, 90°, 3.6 m	K
145	T 508	Temperature at outer surface of containment, 180°, 4.0 m	K
146	T 509	Temperature at outer surface of containment, 0°, 4.2 m; defect	K
147	T 510	Temperature at outer surface of containment, 270°, 4.4 m	K
148	T 511	Gas temperature at bundle inlet	K
149	T 901	Temperature upstream off-gas flow instrument F 901	K

Channel	Designation	Instrument, location	Output in
:		Reserve	
151	Ref. T 02	Reference temperature 2	K
152	P 201	Pressure steam generator	bar
153	P 204	Pressure at steam flow instrument location, 50 g/s	bar
154	P 205	Pressure at steam flow instrument location, 10 g/s	bar
155	P 303	Pressure downstream F 303 flow instrument (orifice) location	bar
156	P 401	Pressure downstream gas flow instrument location	bar
157	P 511	Pressure at bundle inlet	bar
158	P 512	Pressure at bundle outlet	bar
159	P 601	Pressure downstream offgas flow instrument (orifice) F 601	bar
160	P 901	Pressure downstream offgas flow instrument F 901	bar
161	L 201	Liquid level of steam generator	mm
162	L 501	Collapsed quenching water level inside the test bundle	mm
163	L 701	Liquid level in condensate collector	mm
164	Q 901	H <sub>2</sub> concentration (Caldos)	% H <sub>2</sub>
165	P 411	Pressure He supply	bar
166	P 403	Argon pressure inside annulus of cooling jacket	bar
167	P 406	Pressure inside annulus shroud/ cooling jacket	bar
168	F 104	Flow rate quench water	l/h
169	F 204	Flow rate steam, 50 g/s	g/s
170	F 205	Flow rate steam, 10 g/s	g/s
171	F 303	Flow rate at bundle inlet (steam + argon), orifice	mbar
172	F 401	Argon gas flow rate	Nm <sup>3</sup> /h
173	F 403	Flow rate cooling gas	Nm <sup>3</sup> /h
174	F 601	Flow rate in offgas pipe (orifice)	mbar
175	F 901	Offgas flow rate downstream condenser and upstream Caldos	m <sup>3</sup> /h
176	E 201	Electric current of steam generator	A
177	E 301	Electric current of superheater	A
178	E 501	Electric current of inner ring of fuel rod simulators	A
179	E 502	Electric current of outer ring of fuel rod simulators	A

Channel	Designation	Instrument, location	Output in
180	E 503	Electric voltage of inner ring of fuel rod simulators	V
181	E 504	Electric voltage of outer ring of fuel rod simulators	V
182	Hub_V302	Gas supply valve lift	%
183	Ref. T 03	Reference temperature 3	K
:		Reserve	
250	E 505	Electric power inner ring of fuel rod simulators	W
251	E 506	Electric power outer ring of fuel rod simulators	W

Note: Tips of thermocouples TFS 2/1, TFS 5/4/0, TFS 2/6, TFS 2/17 were bent into flow channel to measure fluid temperature.

**Table 5: QUENCH-10; Failure of Thermocouples**

Thermocouple	Elevation [mm]	Time at failure [s]	Failure temperature [K]
TFS 5/10	650	pretest	-
TFS 3/13	950	3419	1682
TFS 4/13	950	3560	1590
TFS 3/14	1050	5970...11369*)	1455
TFS 5/11	750	9439	1384
TFS 2/15	1150	9883	1187
TFS 5/14	1050	11369	925
TFS 3/16	1250	11645...13486*)	996
TFS 2/11	750	13226	1533
TSH 12/0 I	850	13408	2169

\*) The first number is considered as starting time of unreliable data. The second number indicates the final time of the thermocouple readings provided within the “reduced data set” which is made available to partner institutions.

**Table 6: QUENCH-10; Change in Contact Between Thermocouple and Cladding**

Thermocouple	Elevation [mm]	Time [s]	Temperature [K]
TFS 5/14	1050	6800 - 6881	1439→1480
TFS 5/14	1050	6881 - 6900	1480→1379
TFS 2/15	1150	6912 - 6918	1397→1340
TFS 2/11	750	7094 - 7506	1480→1430→1480
TFS 2/11	750	8420 - 8427	1480→1440

**Table 7: QUENCH-10; Sequence of Events**

Time [s]	Event
0 (10:25:04 h)	Start of data recording, test bundle at 873 K (TIT A/13), data acquisition frequency at 1 Hz. Argon and steam flow at 3.0 g/s (773 K).
581	Start of heatup from 3.85 kW.
2025	12.5 kW electric power reached (TIT A/13 = 1285 K).
2523	End of first transient. Temperature at 1593 K (TIT A/13). End of electric power plateau (~12.5 kW).
3710	First rod failure (He detection).
9319	End of pre-oxidation phase. Electric power reduced from 13.15 kW to 6.9 kW (TIT A/13 = 1695 K).
10113	Subsequent rod failure (P 411; He detection).
11353-11373	Withdrawal of corner rod B (TIT A/13 = 1193 K).
11528	Data acquisition frequency = 5 Hz.
11626	Start of air ingress, steam flow turned off.
11658	Target air flow rate of 1.0 g/s reached.
12470	El. power increase from 6.9 kW to 7.3 kW.
13000	El. power increase from 7.3 kW to 7.7 kW.
13125	El. power increase from 7.7 kW to 8.1 kW.
13275	Withdrawal of corner rod D (increase at TFS 5/9). TIT A/13 = 2085 K .
13393	End of air ingress. Quench initiation (fast injection and quench pump). TIT A/13 = 2196 K; TSH 13/90 I = 2083 K.
13394	Quench water at test section inlet (T 511 drops below saturation temp.).
13397	Shroud failure (P 406, TSH 12/0 I, TCI 12/0).
13404	Start of el. power reduction from 8.1 kW to 3.9 kW (TIT A/13 = 2116 K).
13407	Electric power at 3.9 kW (simulation of decay heat).
13429	Rod failures (P411; He detection).
13488	Water at bundle elevation 1250 mm (local wetting at TFS 5/16).
13712	Electric power shut off.
13713	Quench water shut off (F 104).
13714	Electric power below 0.3 kW.
13731	Quench water flow at zero.
13740	Data acquisition frequency at 1 Hz.
16079.8	End of data recording.

**Table 8: QUENCH-10; Maximum Measured Test Bundle and Shroud Temperatures Evaluated for Some Elevations**

Elevation [mm]	Thermocouple	Time [s]	Maximum temperature [K]
350	TFS 2/7	13391.8	1117
350	TSH 7/180	13391.6	1074
450	TFS 3/8	13392.8	1197
550	TFS 2/9	13392.0	1324
550	TSH 9/90	13392.8	1266
650	TSH 10/90 I	13398.0	1364
750	TSH 11/0 I	13397.6	1995
850	TIT C/12	13397.0	2169
850	TSH 12/180 I	13397.6	2165
950	TIT A/13	13396.2	2209
950	TSH 13/90 I	13398.8	2097
1050	TSH 14/270 I	13401.8	1345
1150	TFS 5/15	13401.0	1406

**Table 9: QUENCH-10; Reaction of Rod Cladding Thermocouples on the Boundary Between Superheated and Saturated Steam**

Elevation [mm]	Thermocouple	Time *) [s]
- 50	TFS 2/3	13397
50	TFS 5/4/180	13398
150	TFS 2/5	13399
250	TFS 5/6	13400
350	TFS 2/7	13409
350	TFS 5/7	13404
450	TFS 3/8	13469
450	TFS 5/8	13464
550	TFS 2/9	13468
550	TFS 4/9	13458
550	TFS 5/9	13486
1150	TFS 5/15	13524
1250	TFS 5/16	13526
1350	TFS 5/17	13635

\*) When saturation temperature level is clearly reached.

**Table 10: QUENCH-10; Reaction of Fluid Thermocouples on the Boundary Between Superheated and Saturated Steam**

Elevation [mm]	Thermocouple	Time *) [s]
	T 511	13394
-250	TFS 2/1 F	13396.4
50	TFS 5/4/0 F	13397.4
250	TFS 2/6 F	13399.8
1350	TFS 2/17 F	13554.4
	T 512	13576

\*) First time at saturation temperature level.

**Table 11: QUENCH-10; Estimation of Water/Steam Balance**

Measurements during the test [g]		Post-test measurements [g]	
Steam during pre-oxidation (flow meter F 205)	34274	Water collected downstream the condenser L 701 <i>thereof during quench phase</i>	40800, ~6400
Pre-injected (fast water injection)	4000	Water in lower plenum	5720
Quench water (flow meter F 104)	15297	Water retained in ZrO <sub>2</sub> fiber insulation	6380
		Water in annulus of upper plenum	170
		Steam consumed by Zr oxidation, on the basis of H <sub>2</sub> generation	475
Total water injected	53571	Total water collected	53545

**Table 12: QUENCH-10; Sequence of Aerosol Sampling**

Impactor	Start (s)	Stop (s)	Duration (s)	Period	Temperature TIT A/13 (°C)	Temperature TCRC 13 (°C)
1*)						
2	6191	6250	60	Pre-oxidation	1430	1354
3	11117	11176	60	Intermediate cool-down	974	935
4	12107	12166	60	Air ingress	1042	1006
5	12806	12865	60	Air ingress	1424	1327
6	13228	13287	60	Air ingress	1765	1605
7	13304	13363	60	Air ingress	1890	1632
8	13411	13470	60	Quenching	1737	1350
9	13474	13533	60	Quenching	1192	601
10	13537	13596	60	Quenching	160	92

\*) Impactor 1 was a service sampler.

**Table 13: QUENCH-10; Results of EDX Investigations**

Mark of the sample	Degree of coverage	Most frequently found elements
Sample 1	Low - medium	Fe, Cr, O, Sn
Sample 2	Low	O, Fe
Sample 3	Medium	O, Fe
Sample 4	Low	Fe, Cr
Sample 5	Medium - larger	Fe, O, Zr
Sample 6	Low	Fe, Cr, Mn, O
Sample 7	Medium - low	Fe, O
Sample 8	Medium - larger	Fe, Zr
Sample 9	Medium - larger	Fe, Mn
Sample 10	Low-medium	Fe, Cr, O
Sample 2/1	Medium	Sn, Zr, O, Fe, W
Sample 2/2	Low-medium	Fe, Cr, Cu, Mn
Sample 2/3	Medium	Fe, Cu, O
Sample 2/4	Low-medium	Fe, Cu, Cr, O
Sample 2/5	Medium - larger	Fe, Cr, Cu, O, Sn, Mo
Sample 2/6	Low	Fe, Ni, Cr, O
Sample 2/7	Low-medium	Fe, O
Sample 2/8	Low - medium	Fe, Sn, O, Cr, Ti
Sample 2/9	Larger	Zr, Sn, Fe, O
Sample 2/10	Medium	Fe, O, Cr

**Table 14: QUENCH-10; Mass Data for the Collector Plates and the Pocket**

Type of weight	Weight (mg)
Total weight gain	6.3
Weight gain of the collector plates	2.8
Weight of powder collected in the pocket	3.5

**Table 15: QUENCH-10; Components Found in the Pocket**

Element	Zr	Fe	Sn	W
Amount ( $\mu\text{g}$ )	2500	60	45	1

**Table 16: QUENCH-10; Components Found on the Ni Plate**

Element	Zr	Sn	Mn	Fe	W	Cr	Hf
Amount ( $\mu\text{g}/\text{cm}^2$ )	70	40	4	1,3	1	0.4	0.25

**Table 17: QUENCH-10; Scale Readings on the Mass Gain of Epoxy Resin During the Filling Process**

Elevation, mm	Mass, g	Scale	Elevation, mm	Mass, g	Scale	Elevation, mm	Mass, g	Scale
270	0		750	260		1050	816	
280	76		760	356		1060	916	
290	155		770	456		1070	1024	
300	475		780	550		1080	1122	
310	559		790	664		1090	1220	
320	648		800	804		1100	1322	
330	745		810	900		1110	1432	
340	845		820	996		1120	1528	
350	945		830	1095		1130	1625	
360	1045	Reset	840	1195	Reset	1140	1725	
370	45		850	64		1150	1828	
380	170		860	164		1160	2026	
390	270		870	265		1170	2118	
400	365		790	664		1180	2218	
410	460		800	804		1190	2320	
420	560		810	900		1200	2418	
430	660		820	996		1210	2516	
440	760		830	1095		1220	-	
450	855		840	1195	Reset	1230	2631	
460	955		850	64		1240	2714	
470	1050		860	164		1250	2814	
480	1148	Reset	870	265		1260	2910	
490	-		790	664		1270	3005	
500	25		800	804		1280	3106	

510	120		810	900		1290	3190	
520	223		820	996		1300	-	
530	316		830	1095		1310	3241	
540	419		840	1195	Reset	1320	3445	
550	510		850	64		1330	3540	
560	610		860	164		1340	3658	
570	698		870	265		1350	3764	
580	790		880	374		1360	3882	
590	880		890	460		1370	3976	
600	970		900	575		1380	4084	
610	1073		910	690		1390	4194	
620	1128	Reset	920	750		1400	4298	
630	40		930	870		1410	4403	
640	120		940	975		1420	4504	
650	200		950	1085		1430	4611	
660	285		960	1195		1440	4699	
670	376		970	1295	Reset	1450	4803	
680	470		980	85		1460	4916	
690	562		990	190		1470	5022	
700	662		1000	295		1480	5129	
710	761		1010	402				
720	862		1020	512				
730	69		1030	624				
740	165		1040	711				

**Table 18: QUENCH-10; Cross Sections for the Metallographic Examination**

23.08.2005

Sample	Sample length (mm)	Axial position		Remarks
		bottom (mm)	top (mm)	
Cut	4	-14	-10	Cut 1 – large machine
QUE-10-a	68	-10	58	
Cut	2	58	60	
Que-10-b	190	60	250	
Cut	4	250	254	Cut 2 – large machine
QUE-10-c + d	229	254	540	
Cut	4	540	544	Cut 3 – large machine
QUE-10-e	89	544	633	
Cut	2	633	635	
QUE-10-3	15	635	<b>650</b>	TC elevation 10, 650 mm polished
Cut	2	650	652	
QUE-10-f	81	652	733	
Cut	2	733	735	
QUE-10-4	15	735	<b>750</b>	TC elevation 11, 750 mm polished
Cut	2	750	752	
QUE-10-g	44	752	796	
Cut	4	796	800	Cut 4 – large machine
QUE-10-8	33	<b>800</b>	833	800 mm polished
Cut	2	833	835	
QUE-10-5	15	835	<b>850</b>	TC elevation 12, 850 mm polished
Cut	2	850	852	
QUE-10-i	83	852	935	
Cut	2	935	937	
QUE-10-6	13	937	<b>950</b>	TC elevation 13, 950 mm polished
Cut	2	950	952	
QUE-10-j	98	952	1050	
Cut	2	1050	1052	
QUE-10-7	28	1052	<b>1080</b>	1080 mm polished
Cut	4	1080	1084	Cut 5 – large machine
QUE-10-l	282	1084	1366	
Cut	4	1366	1370	Cut 6 – large machine
QUE-10-m	176	1370	1546	
Cut	4	1546	1550	Cut 7 – large machine
		1550		Upper remnant

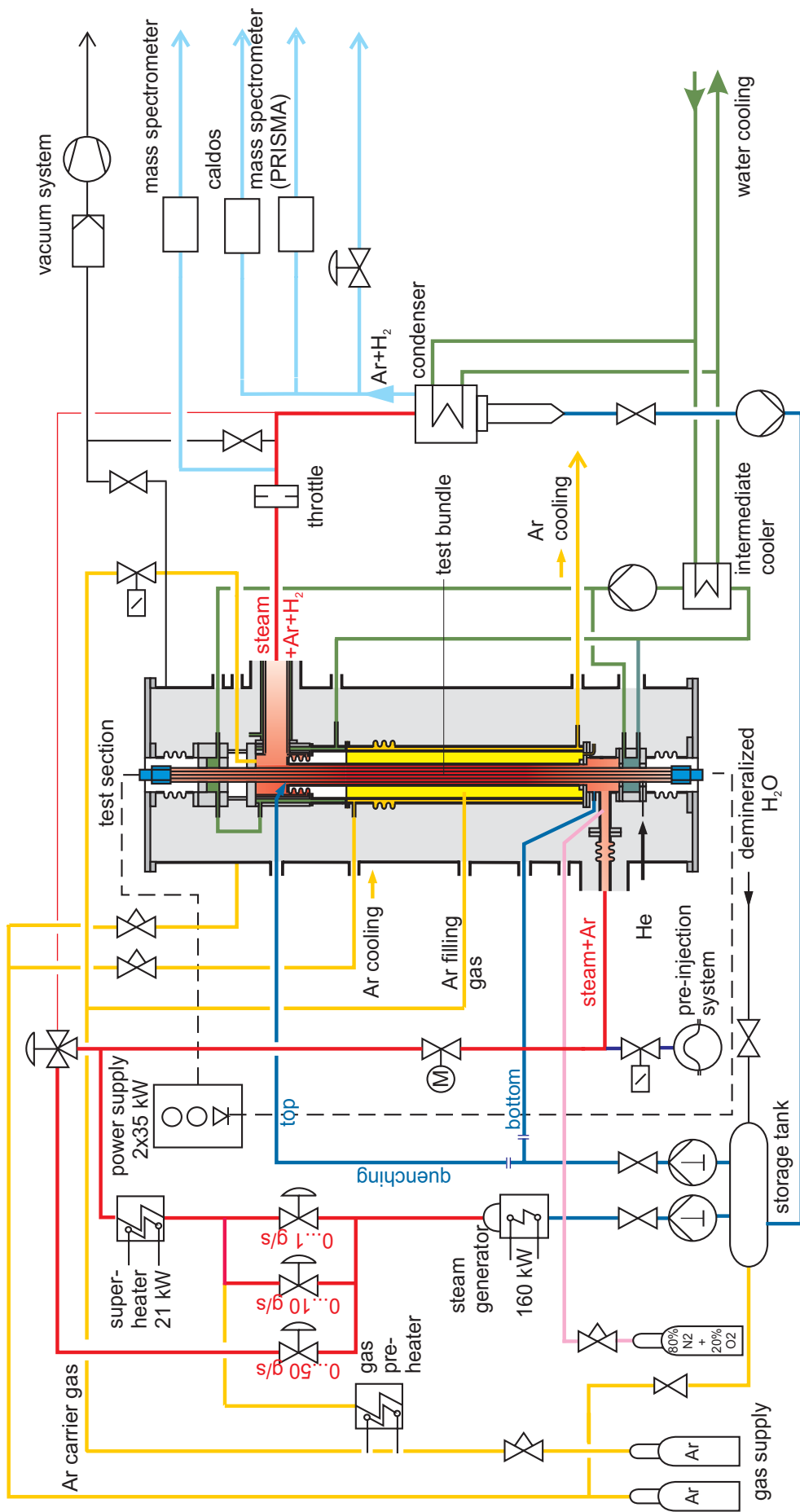


Fig.1-QUE10-Flow diagram.cdr  
15.09.04 - IMF

Fig. 1: Flow diagram of the QUENCH test facility.

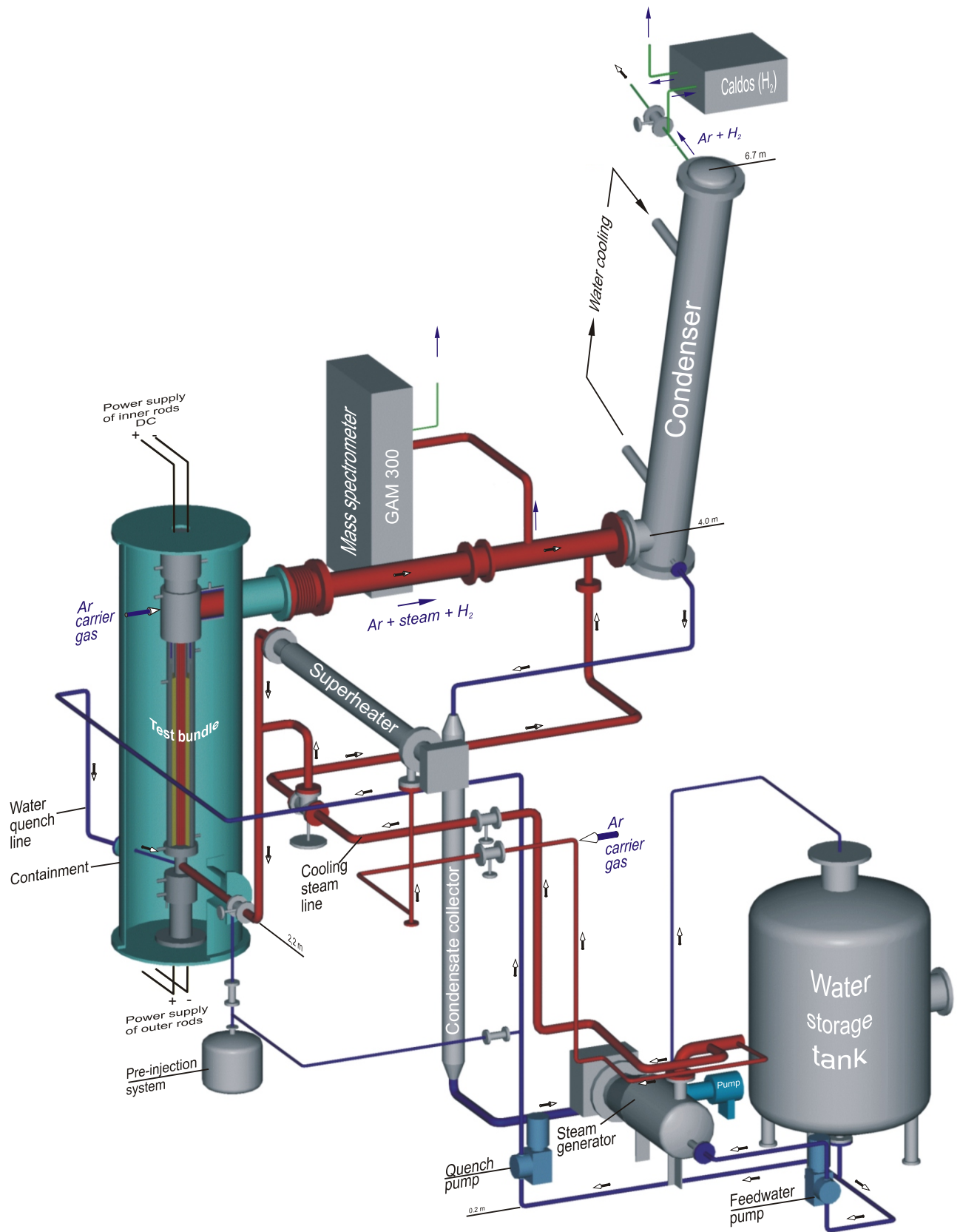


Fig.2-QUE10-Gesamtanlage.cdr  
03.06.04 - IMF

Fig. 2: QUENCH Facility - Main components.

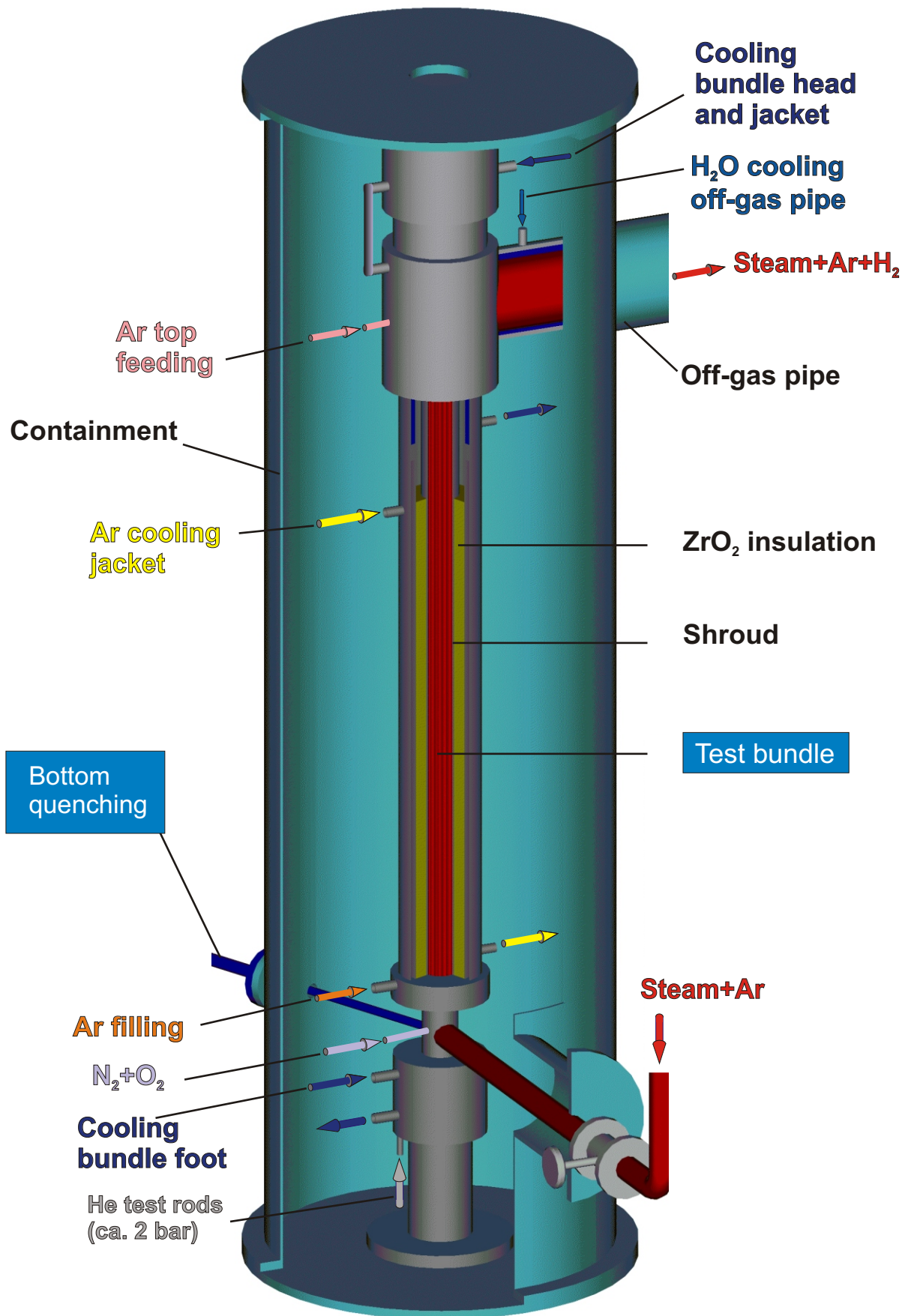


Fig.3-QUE10 Containment 3D.cdr  
15.07.05 - IMF

Fig. 3: QUENCH Facility; Containment and test section.

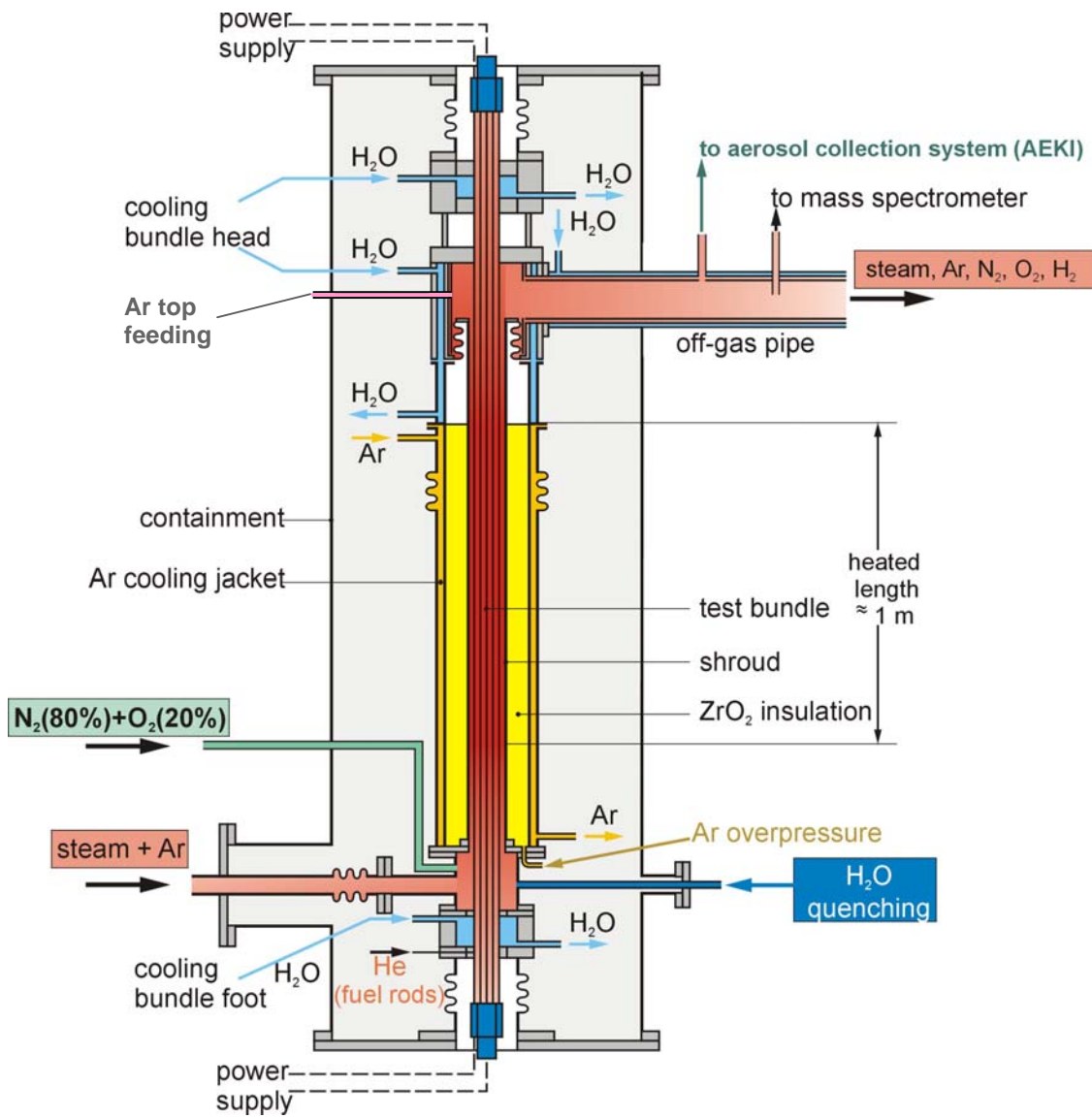


Fig. 4: QUENCH-10; Test section with flow lines.

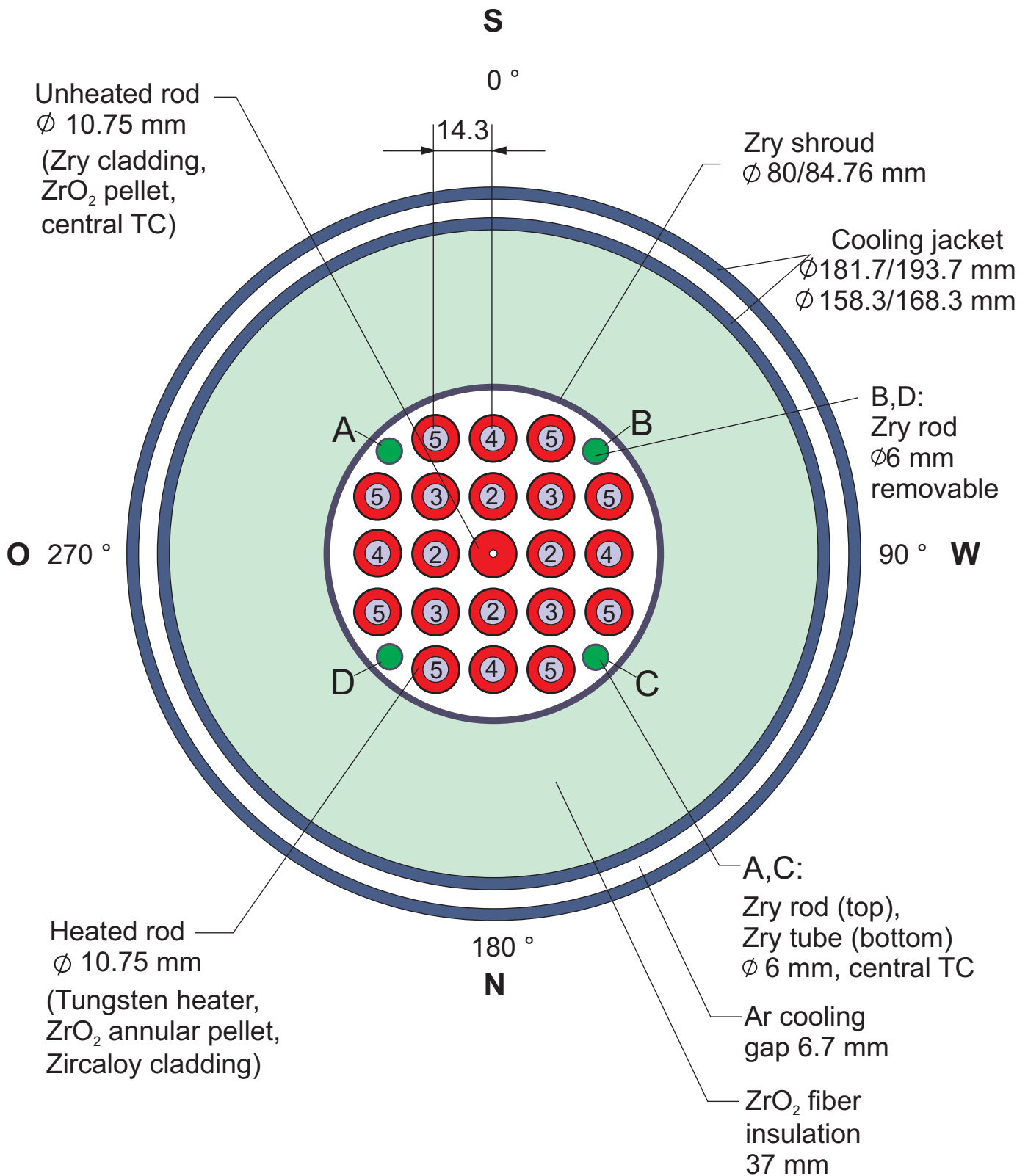


Fig.5-QUE10 Cross section.cdr  
11.04.06 - IMF

Fig. 5: QUENCH-10; Fuel rod simulator bundle (cross section, top view) including rod type indications.

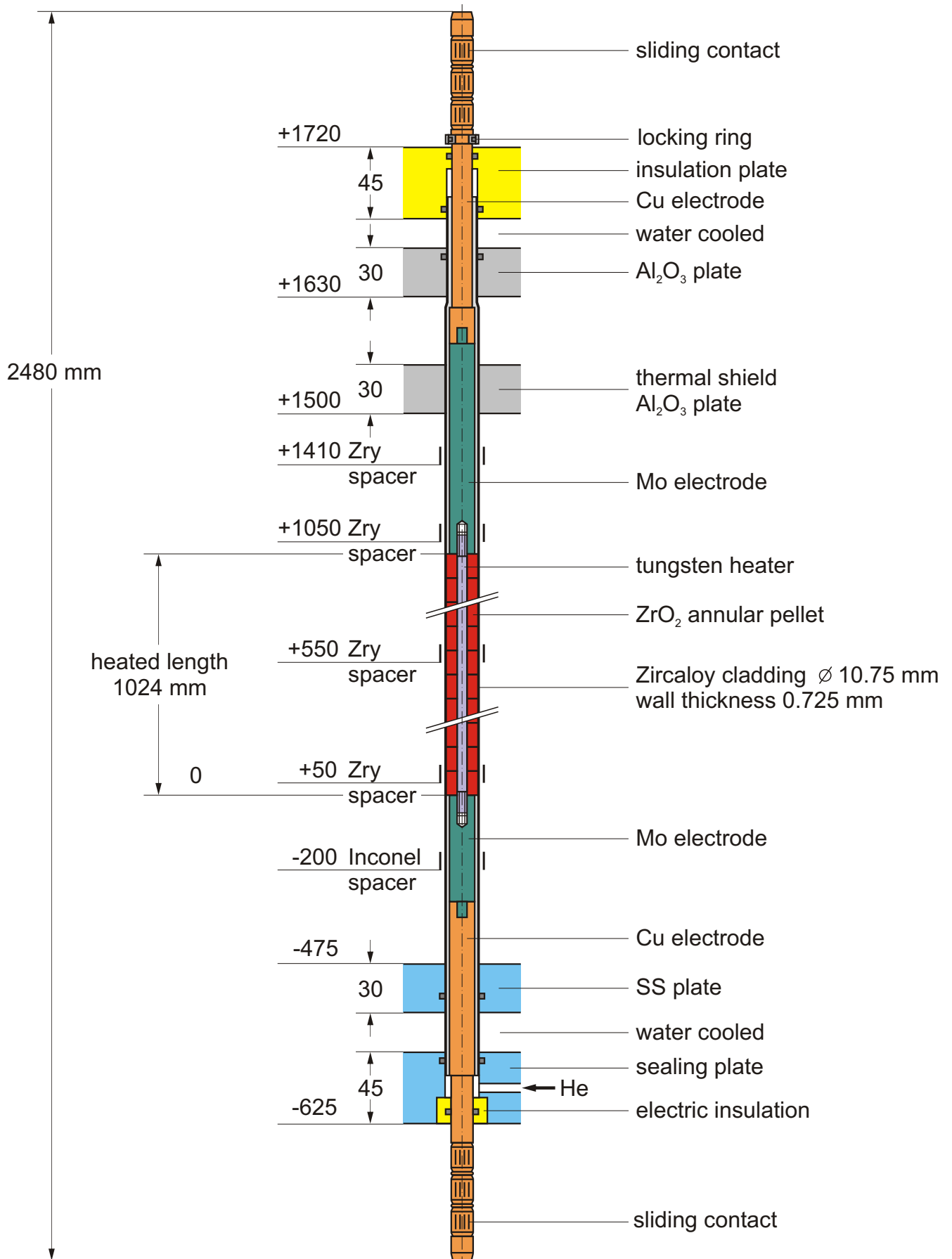


Fig.6-QUE10-Heated fuel rod sim.cdr  
08.06.04 - IMF

Fig. 6: Heated fuel rod simulator.

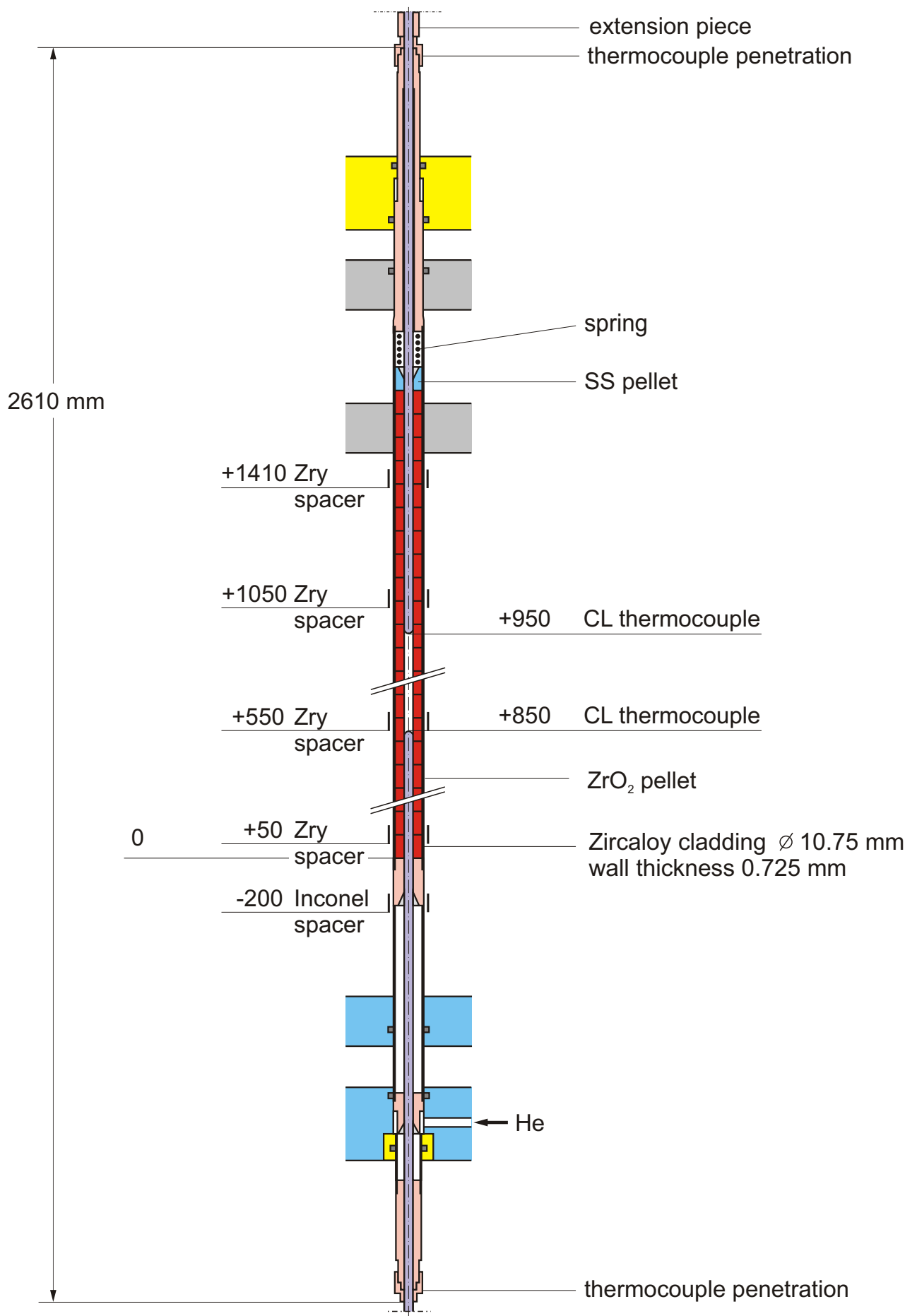


Fig. 7 : Unheated fuel rod simulator.

Fig. 7-QUE10 Unheated fuel rod sim.cdr  
02.06.04 - IMF

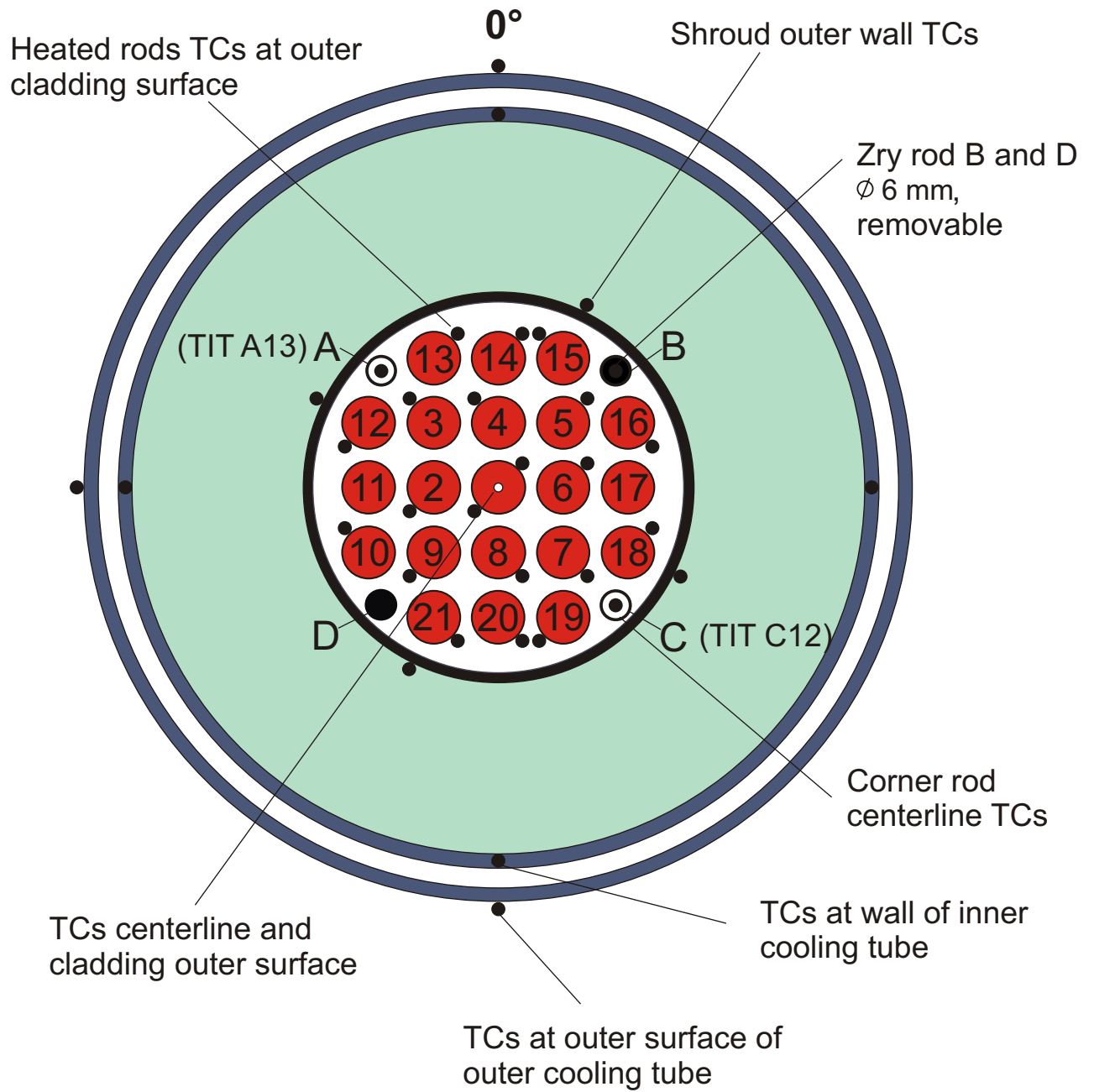


Fig.8-QUE10 TC instr.cdr  
 05.04.05 - IMF

Fig. 8: QUENCH-10; Test bundle; TC instrumentation and rod designation (top view).

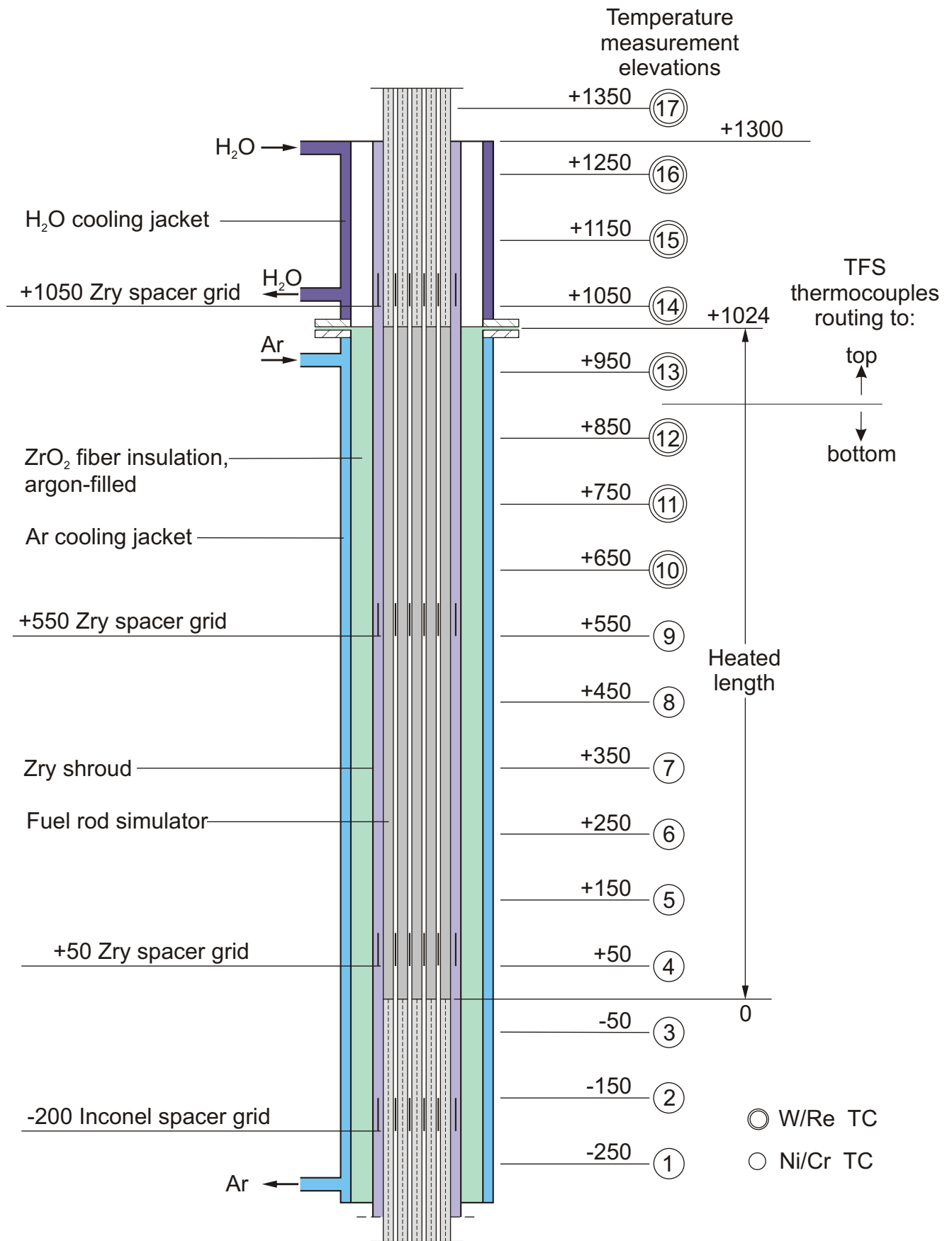
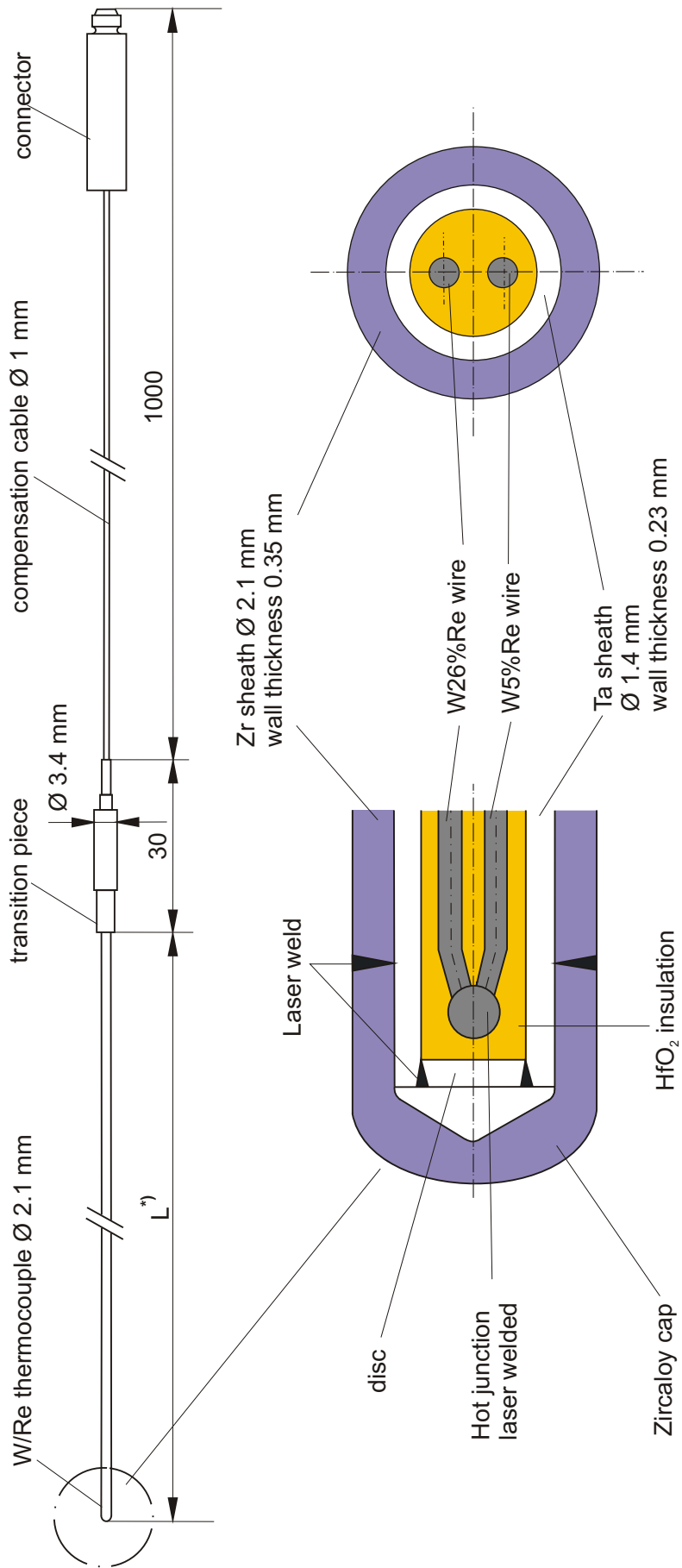


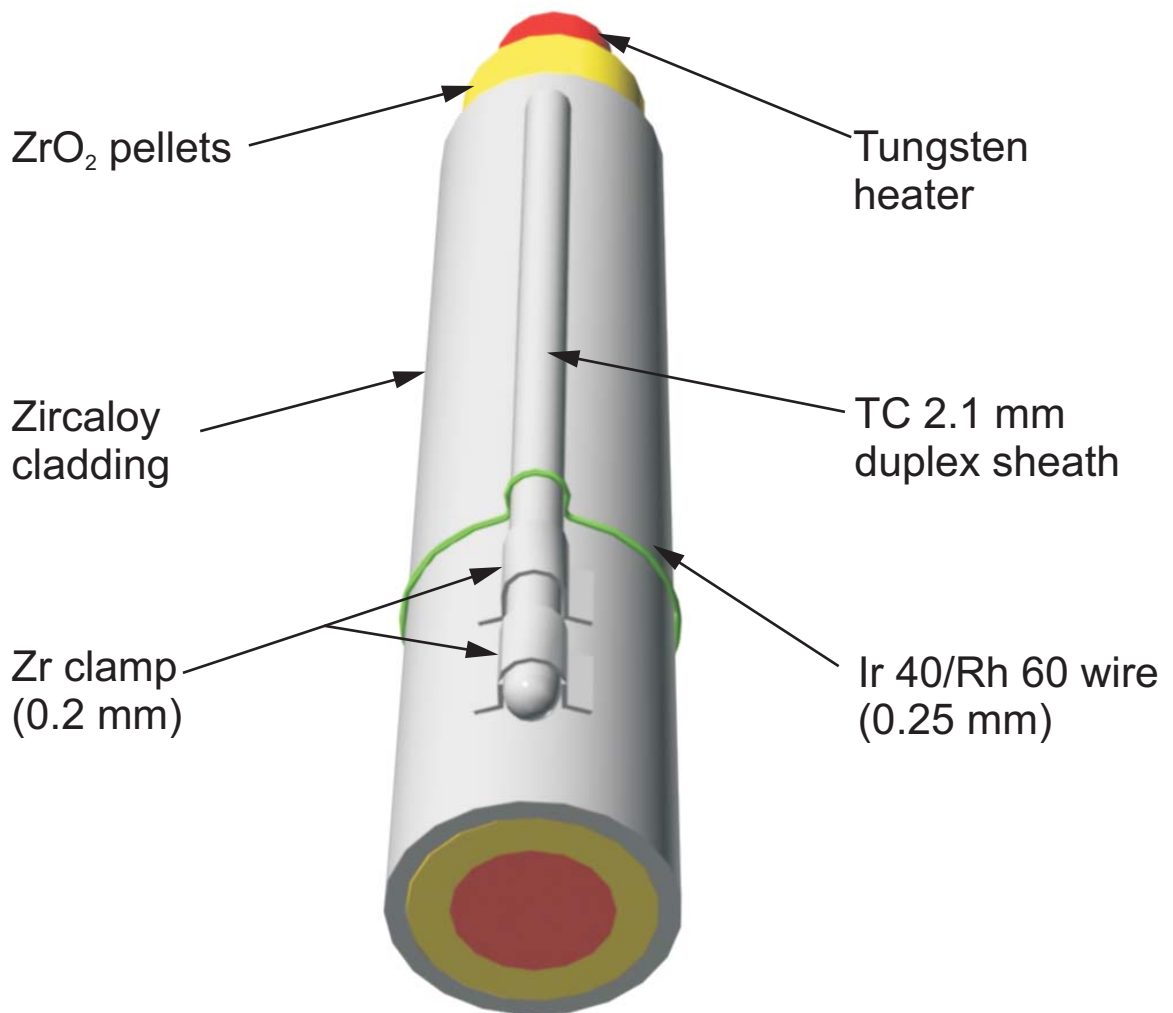
Fig.9-QUE10-TC elevations.cdr  
01.12.04 - IMF

Fig. 9: Axial temperature measurement locations in the QUENCH test section.



\*) L: high-temperature section length dependent on the TC position in the test bundle 500 mm - 1700 mm

Fig. 10: QUENCH; High-temperature thermocouple.

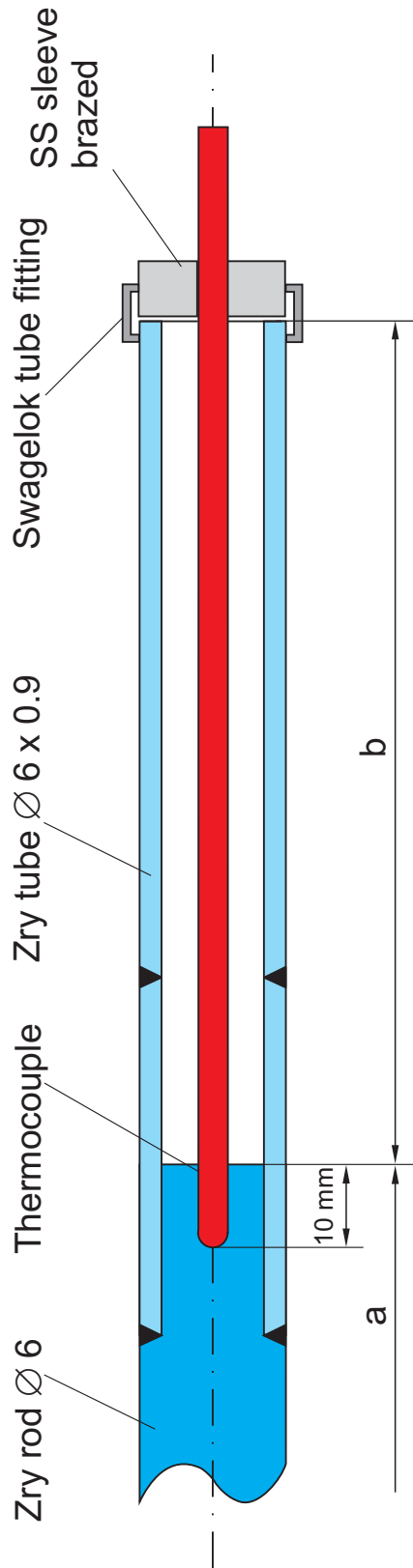


Tests with pre-oxidation: Zr clamp + wire

Tests without pre-oxidation: Zr clamp

Fig. 11: QUENCH-10; Concept for TC fastening at the test rod.

(TIT A13, TIT C12)



Rod A: TIT A13 (950 mm), W/Re, Ø 2.1 mm, a = 360 mm, b = 2080 mm  
 Rod C: TIT C12 (850 mm), W/Re, Ø 2.1 mm, a = 460 mm, b = 1980 mm  
 (Rod B, D: Zry-4 rod, Ø 6 mm, removable)

Fig 12-QUE10-TC in Zry-rod.cdr  
 08.09.05 - IMF

Fig. 12: QUENCH-10; Arrangement of the thermocouples inside the corner rods.

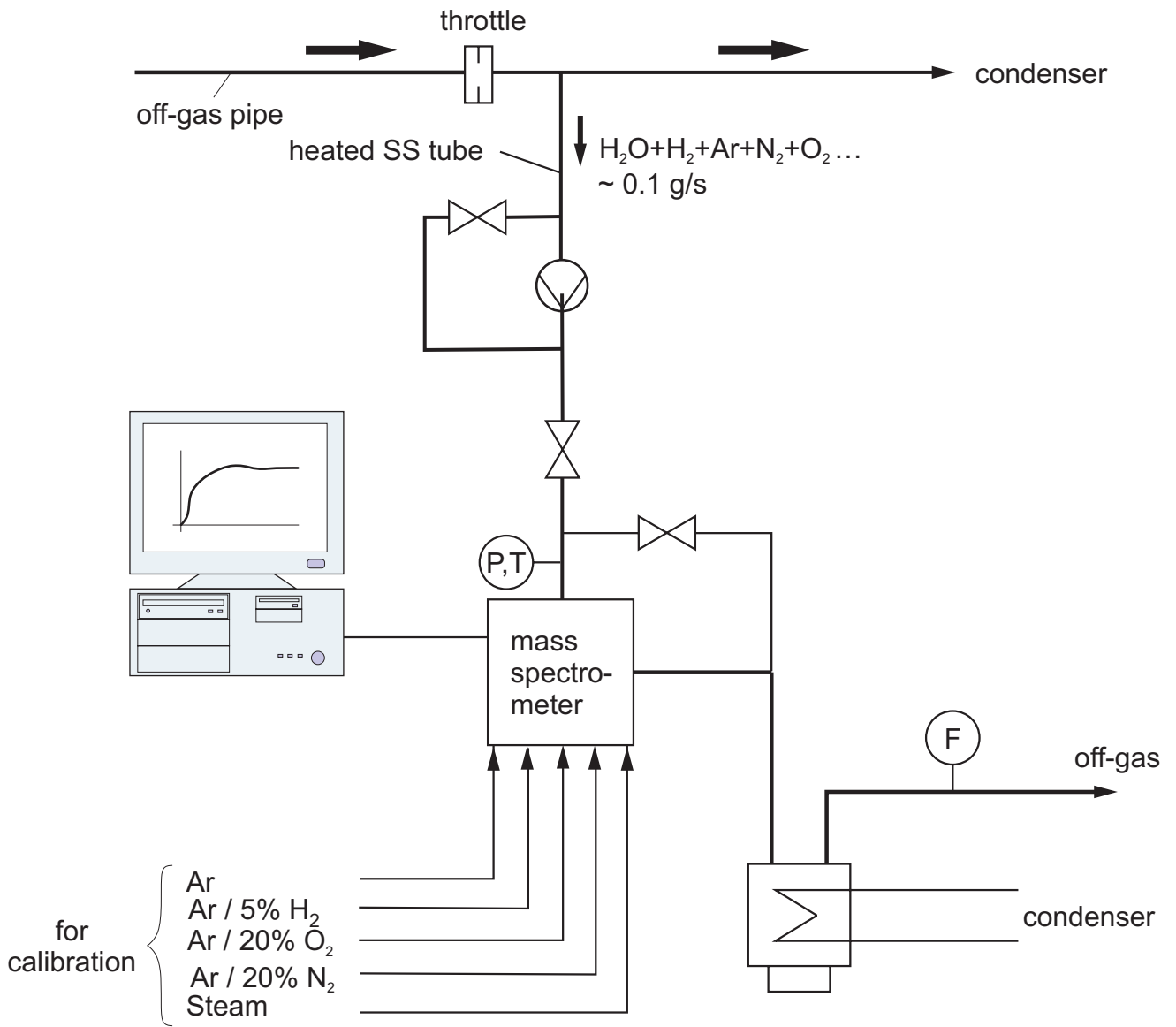


Fig.13-QUE10-MS Quench facility.cdr  
 21.04.06 - IMF

Fig. 13: QUENCH Facility;  $\text{H}_2$  measurement with the GAM 300 mass spectrometer.

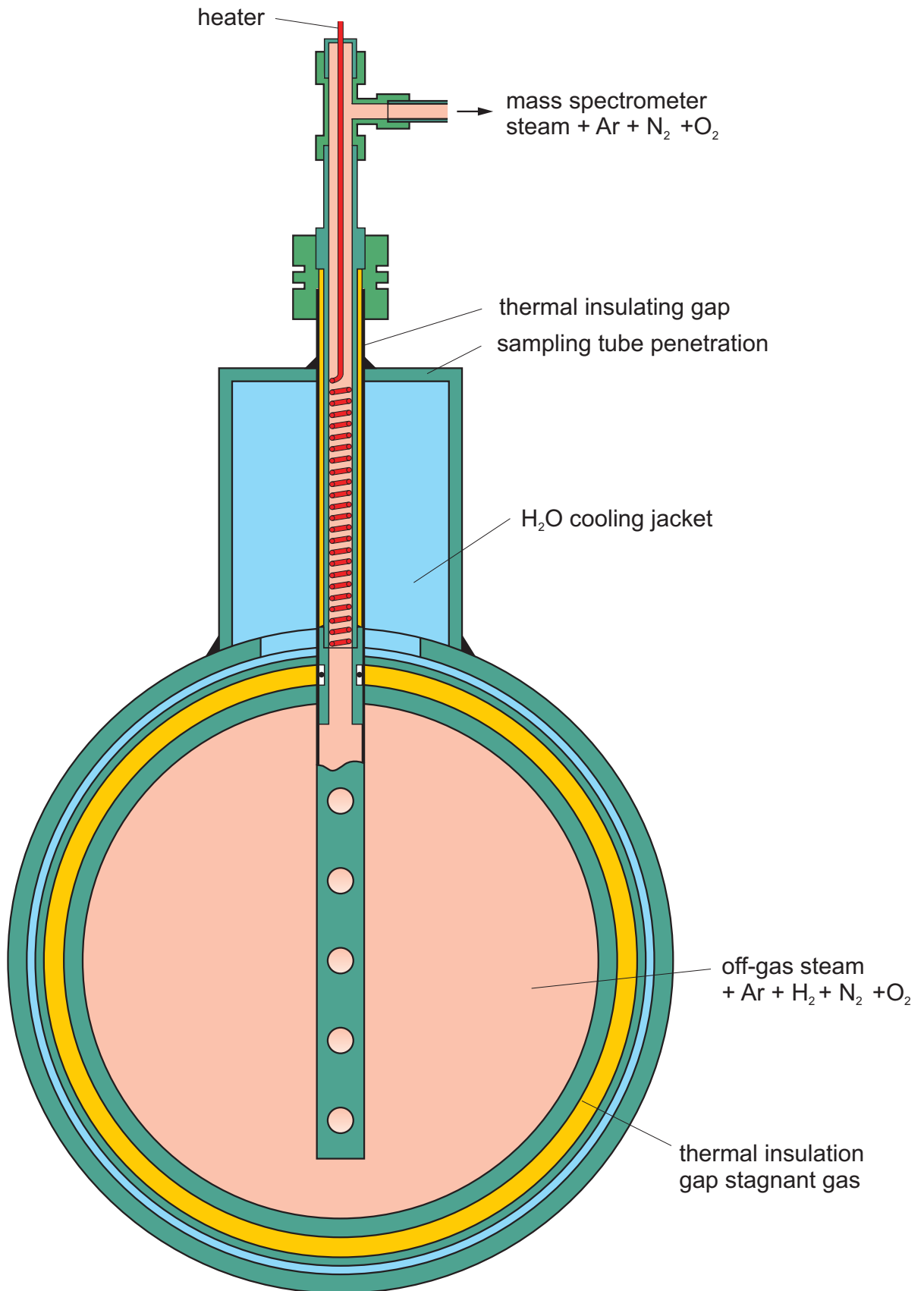


Fig 14 QUE10 MS sampling position new.cdr  
07.09.05 - IMF

Fig.14: Mass spectrometer sampling position at the off-gas pipe of the QUENCH test facility.

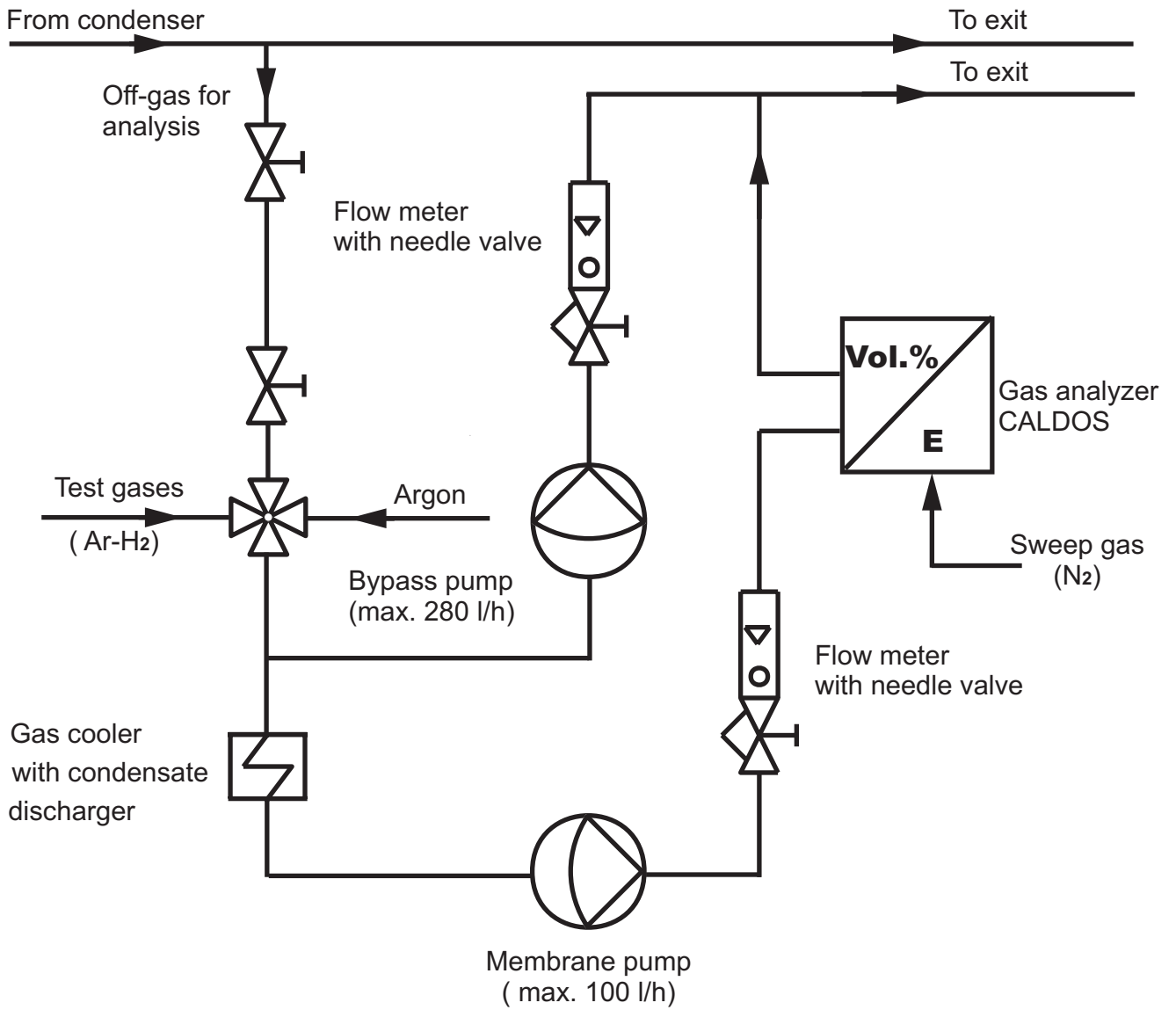


Fig 15 QUE10 Caldos Schema (ab QUE04).cdr  
07.09.05 - IMF

Fig.15: Hydrogen measurement with the CALDOS analyzer connected to the exhaust gas pipe of the QUENCH facility.

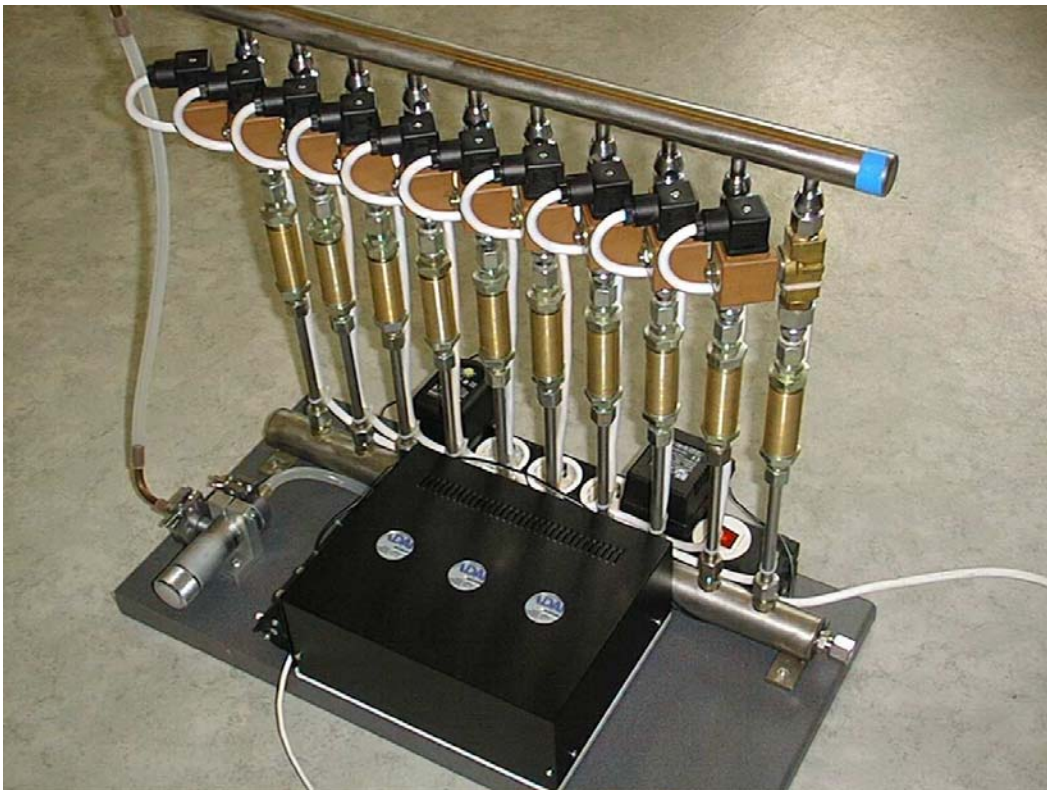


Fig. 16: QUENCH-10; Aerosol sampling system.

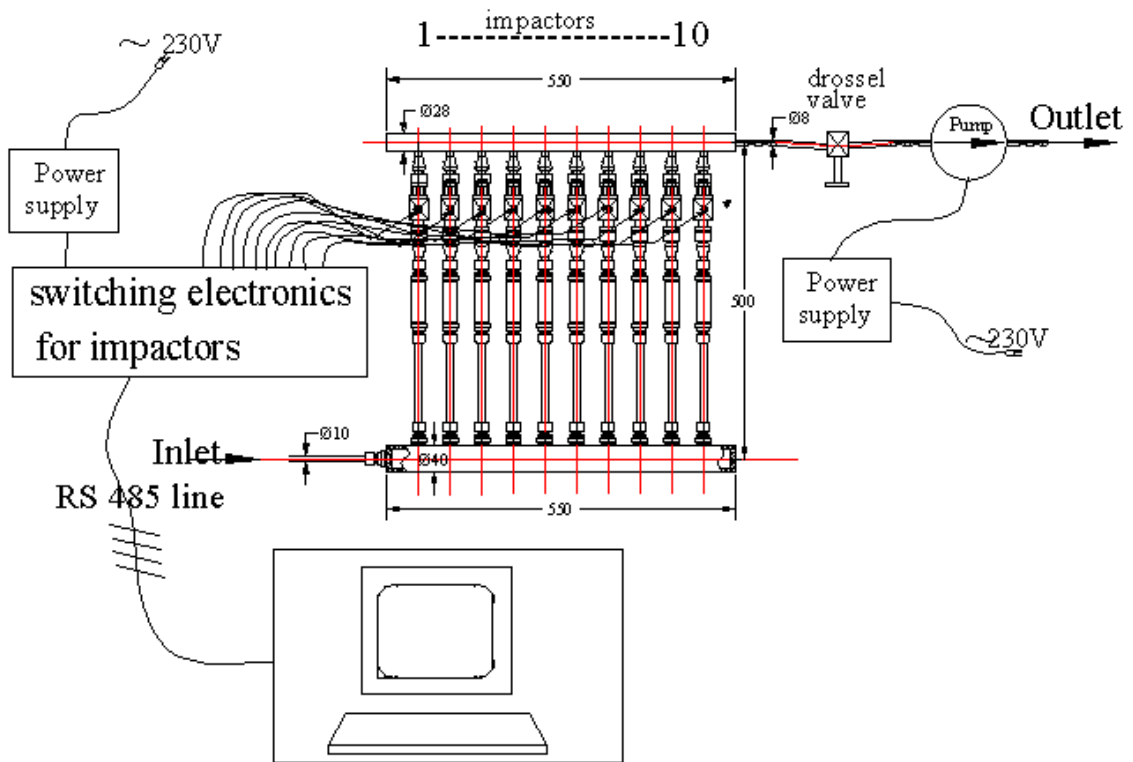
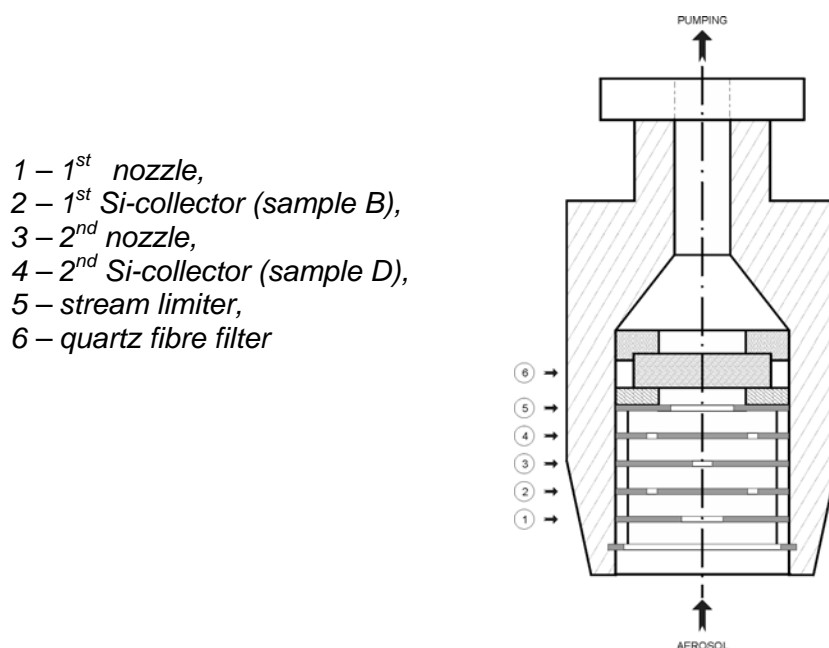
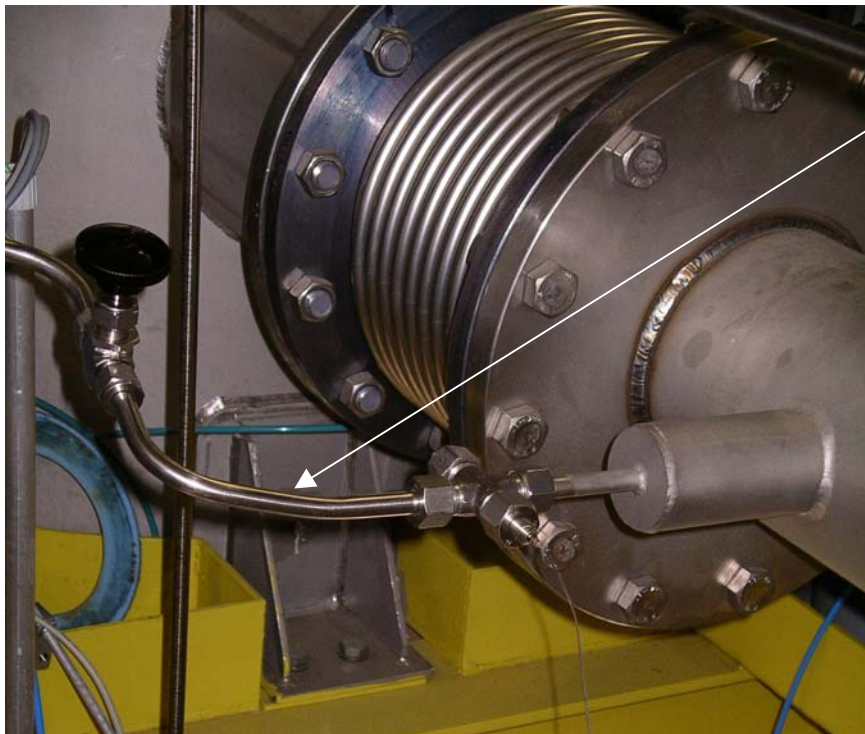
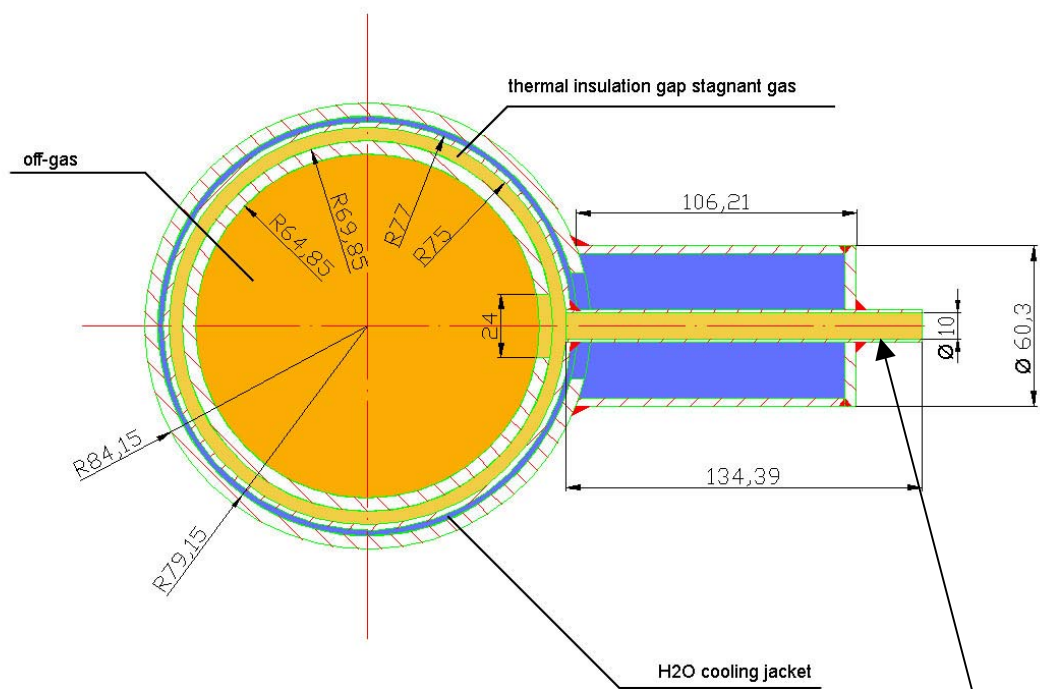


Fig. 17: QUENCH-10; Main components of the aerosol sampling system.



- 1 – 1<sup>st</sup> nozzle,
- 2 – 1<sup>st</sup> Si-collector (sample B),
- 3 – 2<sup>nd</sup> nozzle,
- 4 – 2<sup>nd</sup> Si-collector (sample D),
- 5 – stream limiter,
- 6 – quartz fibre filter

Fig. 18: QUENCH-10; Scheme of the impactor sampler.



**Aerosol feeding line  
from off-gas pipe to  
sampler**

**(distance from flange  
at test section outlet:  
~106 cm)**

Fig. 19: QUENCH-10; Sampling location at the off-gas pipe for the aerosol sampler, top, Connection of the aerosol sampling device to the off-gas pipe, bottom.

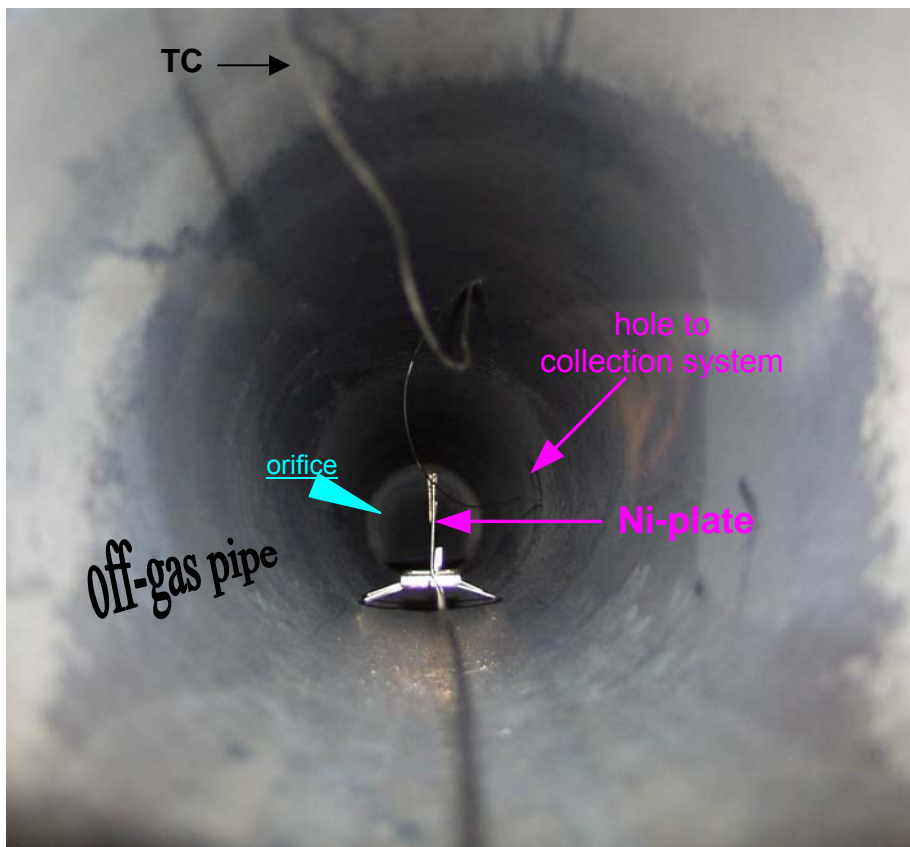
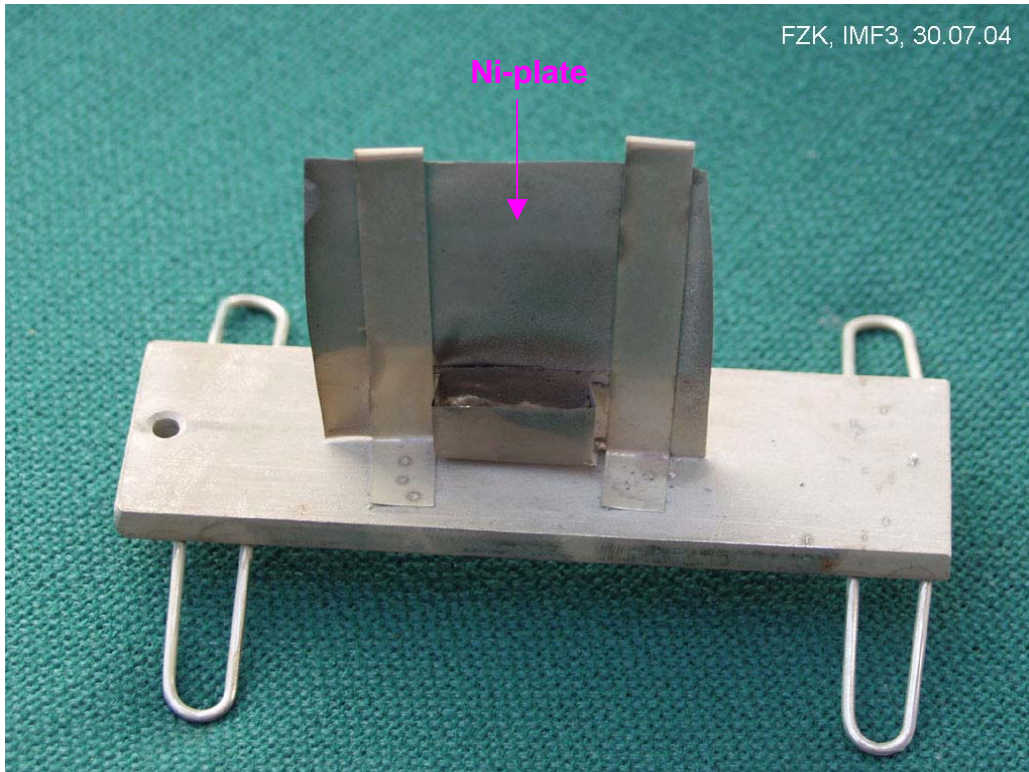


Fig. 20: QUENCH-10; Arrangement to hold the Ni-plate in the off-gas pipe of the QUENCH facility (installed at the bottom of the pipe near the take-up tube for the aerosol collection system).

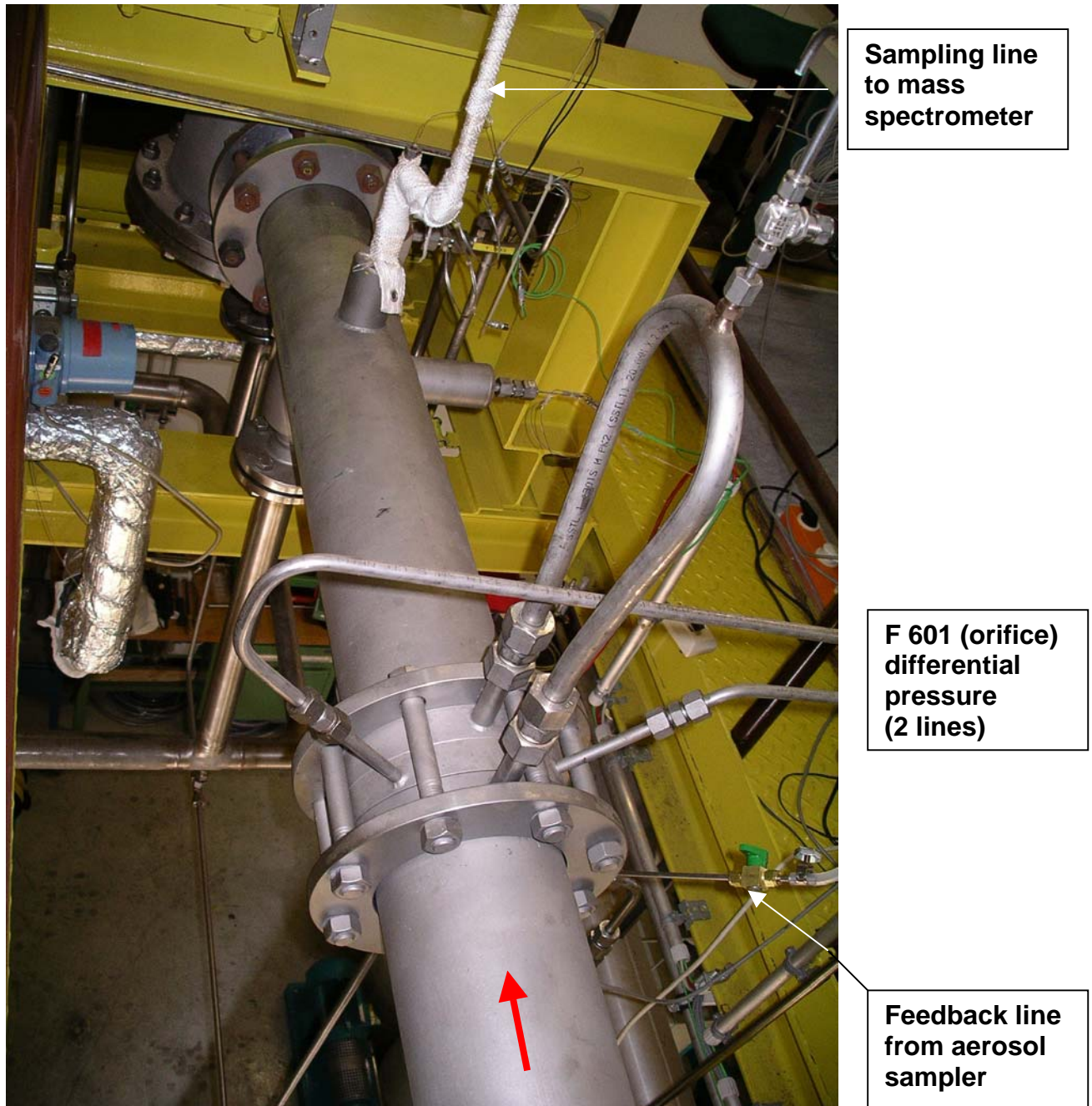


Fig. 21: QUENCH-10; Off-gas pipe (top view). The two flanges in the center of the photograph hold the standard orifice located about 2.70 m downstream the test section outlet.

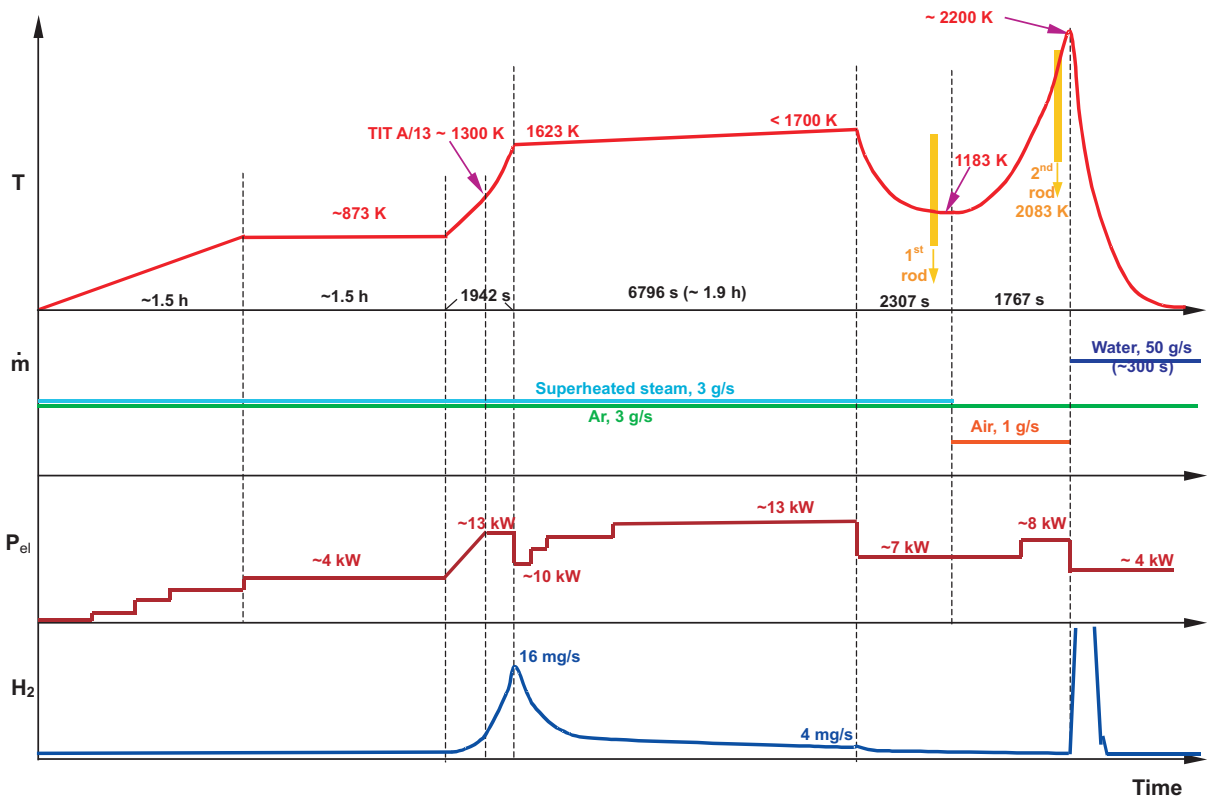
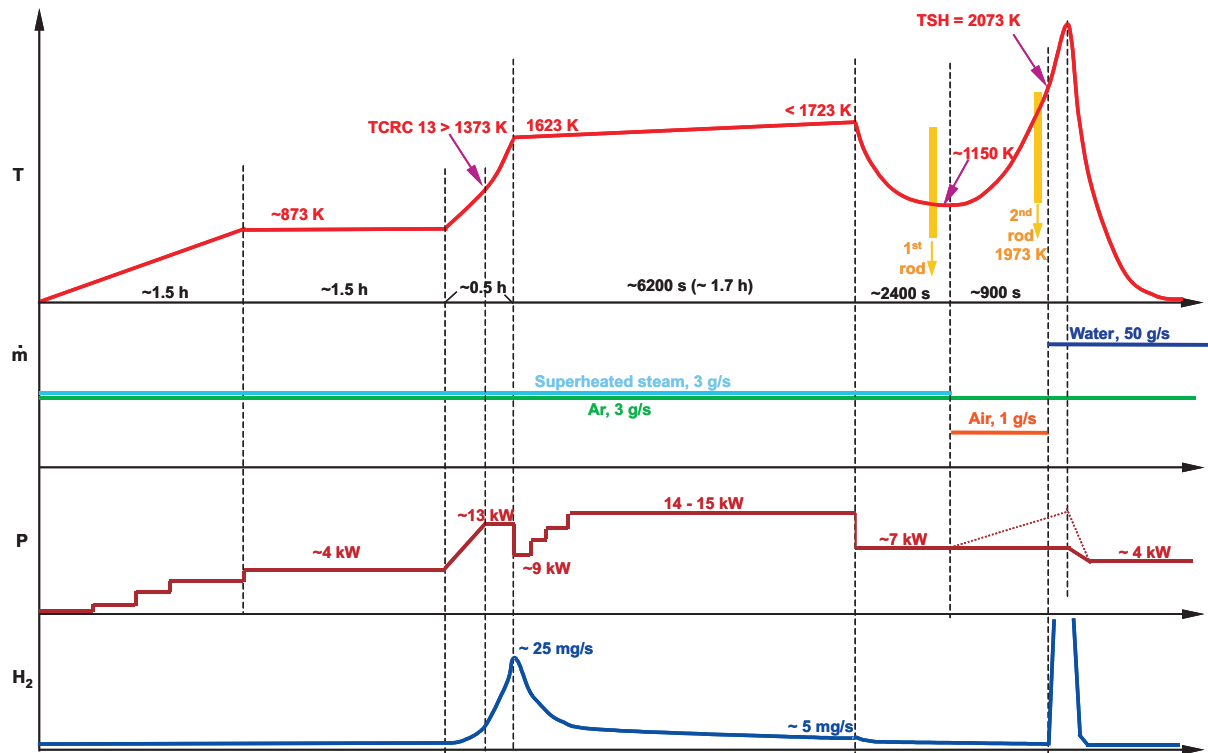


Fig 21 QUE10 test conduct.cdr  
07.04.05 - IMF

Fig. 22: QUENCH-10; Test conduct as planned, top, test as conducted, bottom.

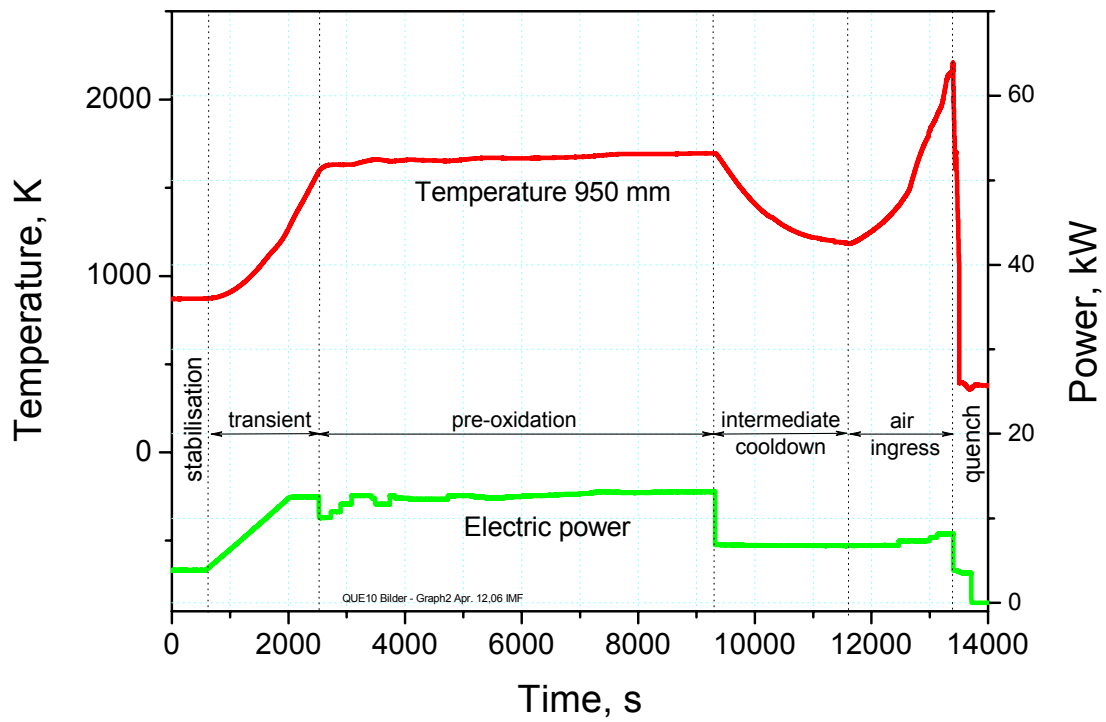


Fig. 23: QUENCH-10; Test phase definitions together with temperature at elevation 950 mm electrical power input and heating rates during the air ingress phase.

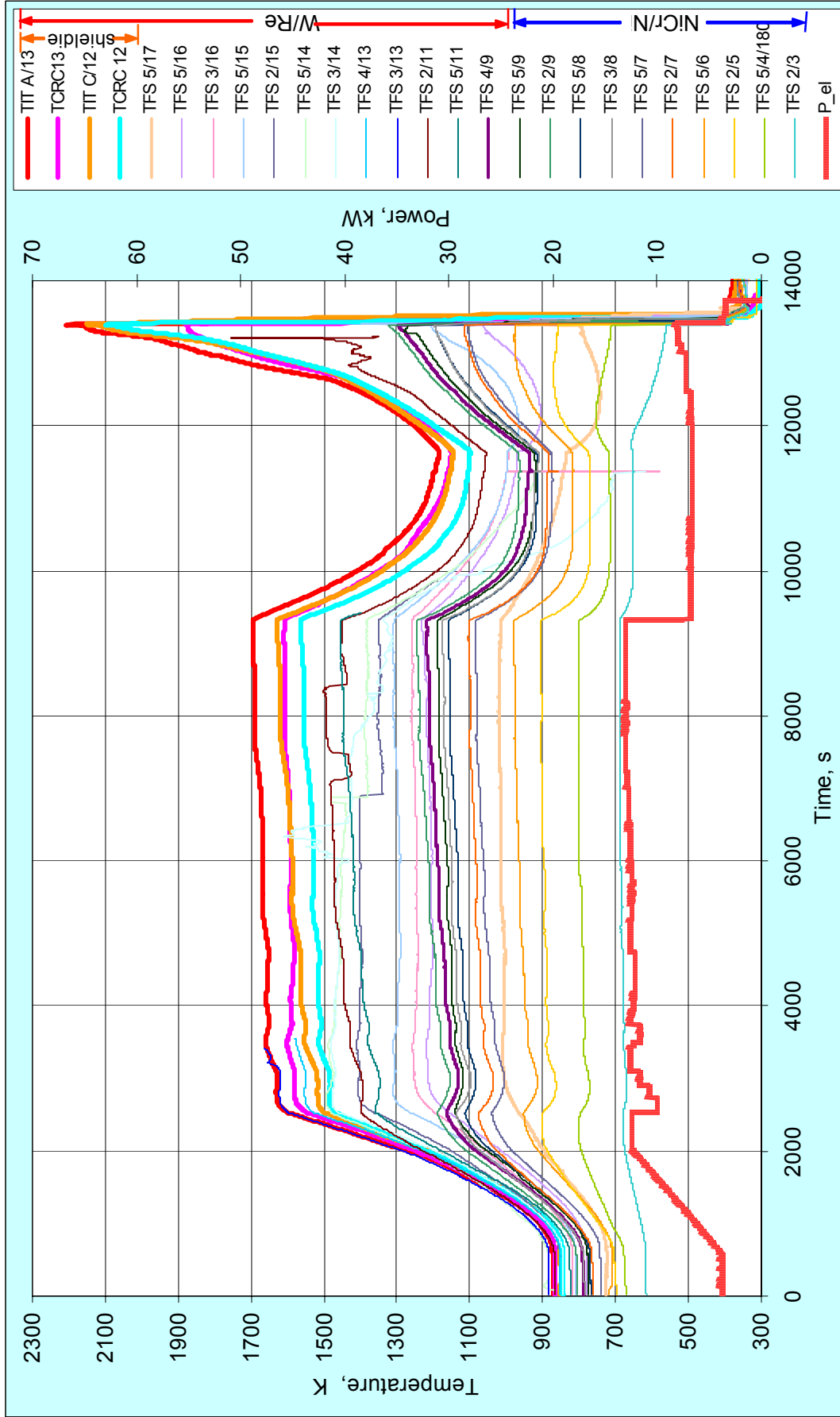


Fig. 24: QUENCH-10; Bundle temperatures during the test

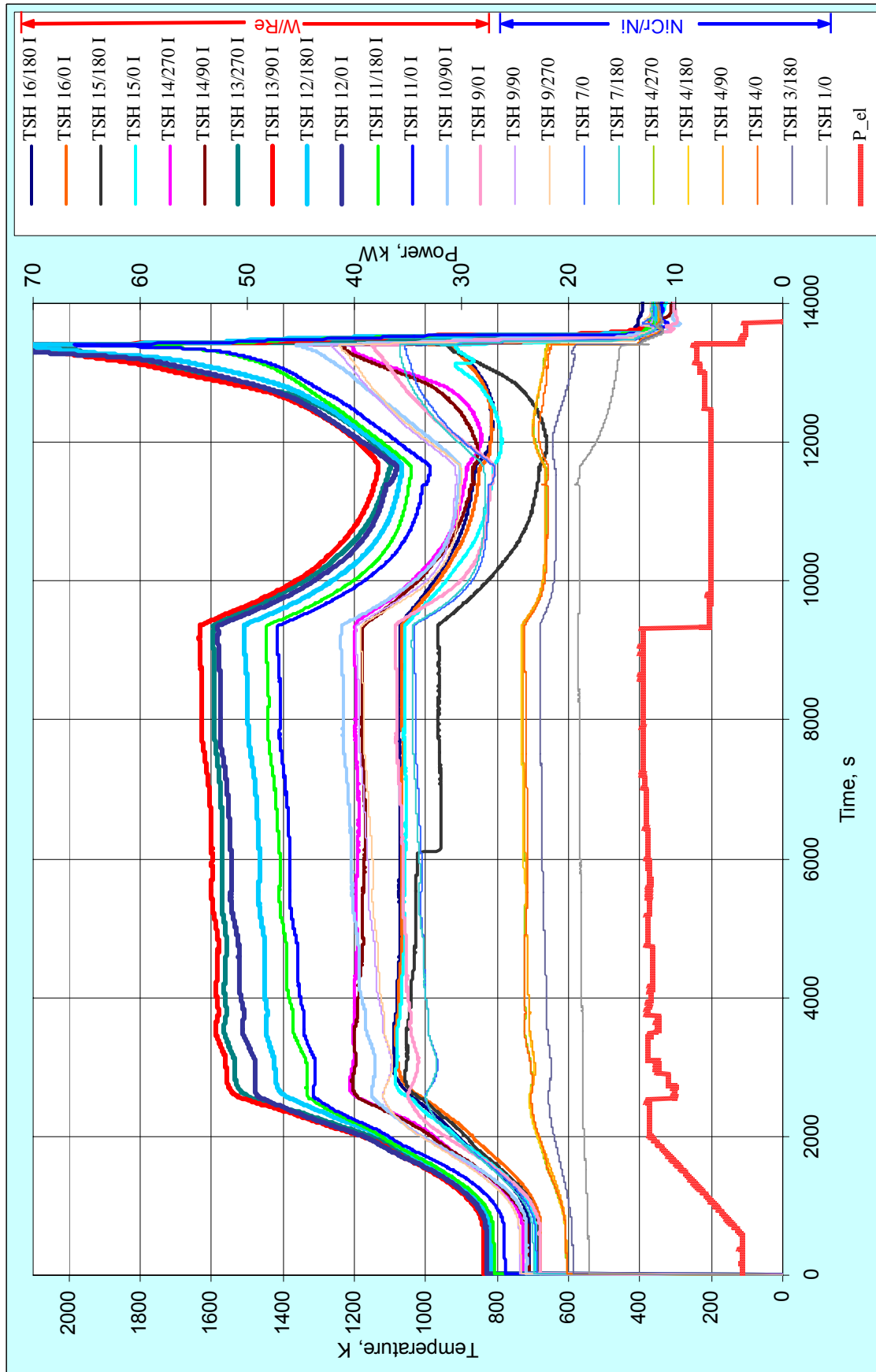


Fig. 25: QUENCH-10; Shroud temperatures during the test

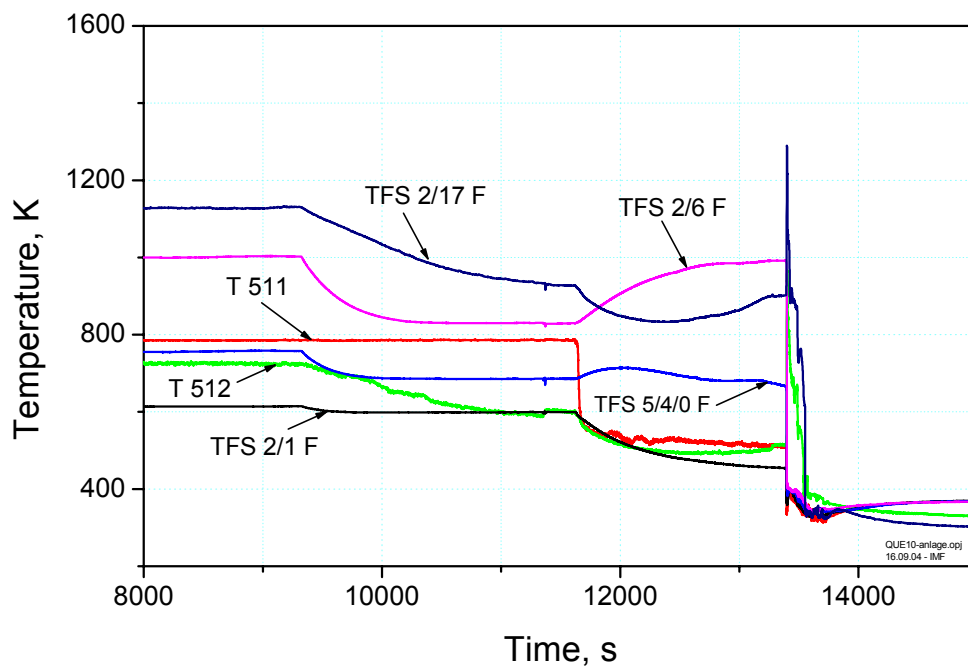


Fig. 26: QUENCH-10; Coolant temperatures T 511 at bundle inlet, TFS 2/1 F at -250 mm, TFS 5/4/0 F at -50 mm, TFS 2/6 F at 250 mm, T 512 at bundle outlet (~1350 mm), and TFS 2/17 F at 1350 mm.

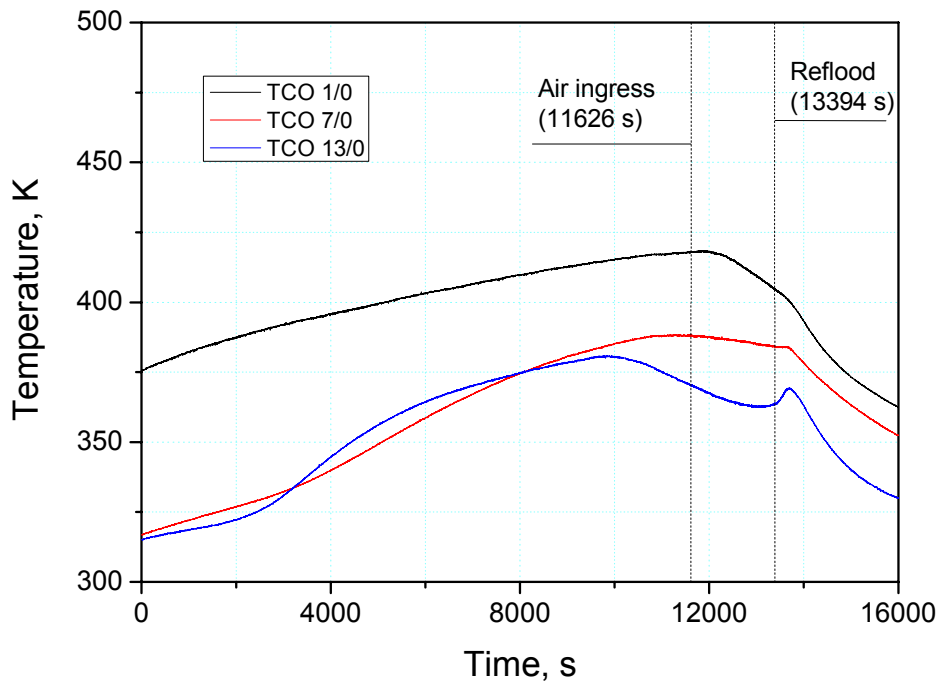
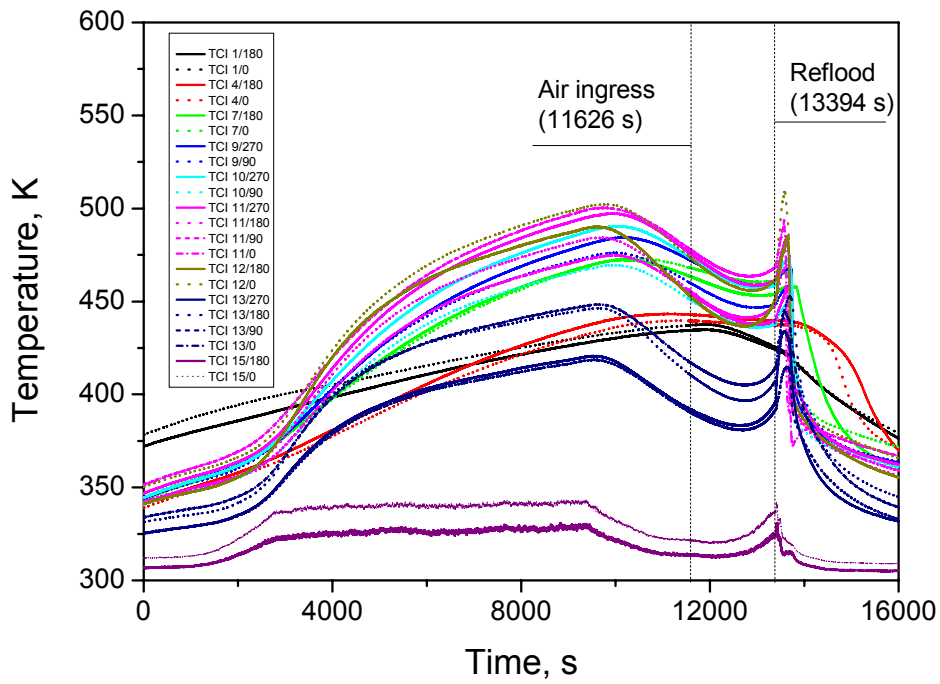


Fig. 27: QUENCH-10; Overview of the TCI (inner cooling jacket), top, and TCO (outer cooling jacket) temperatures, bottom.

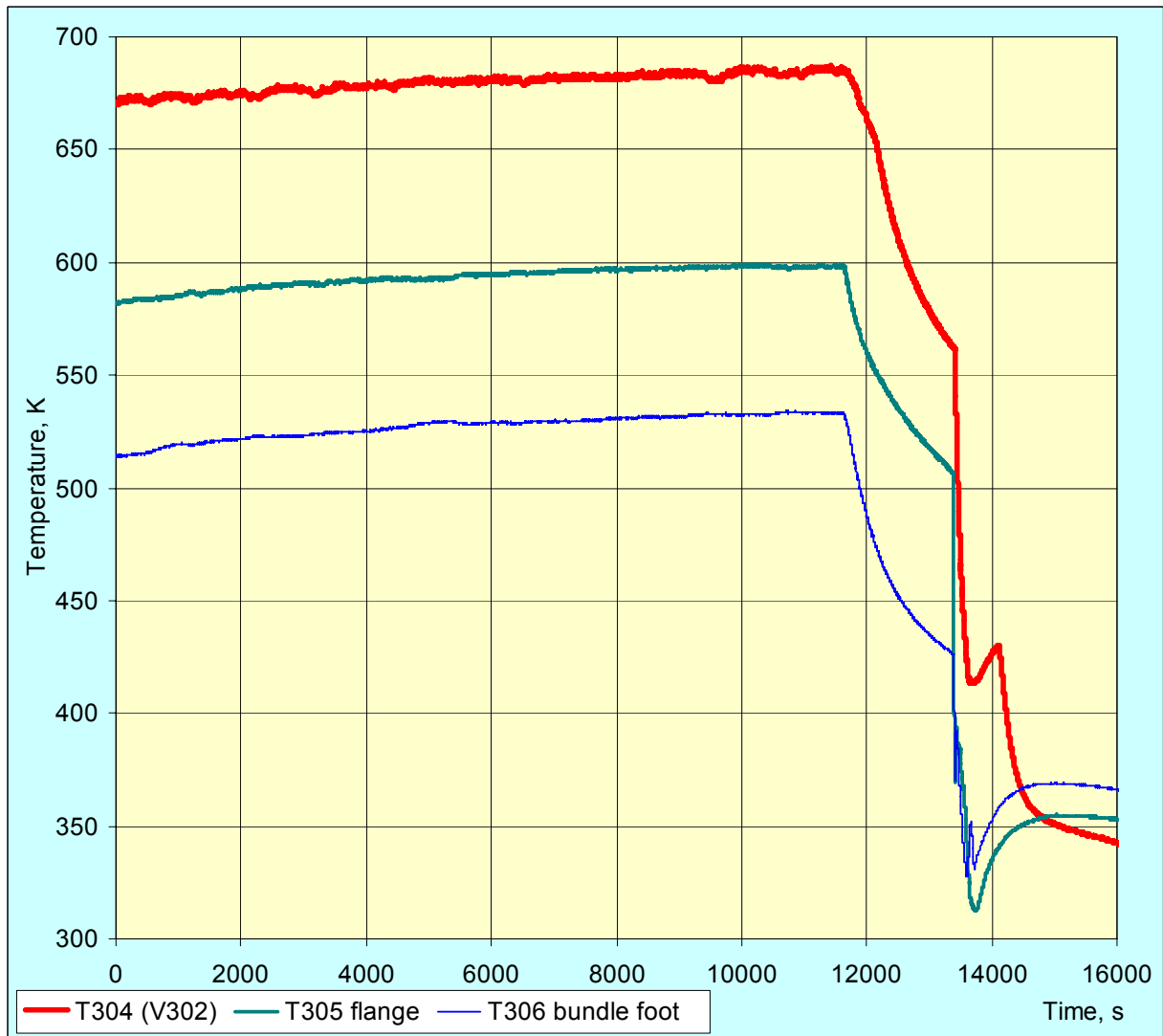


Fig. 28: QUENCH-10; Temperatures measured at different locations of outer pipe surfaces, downstream the test section inlet.

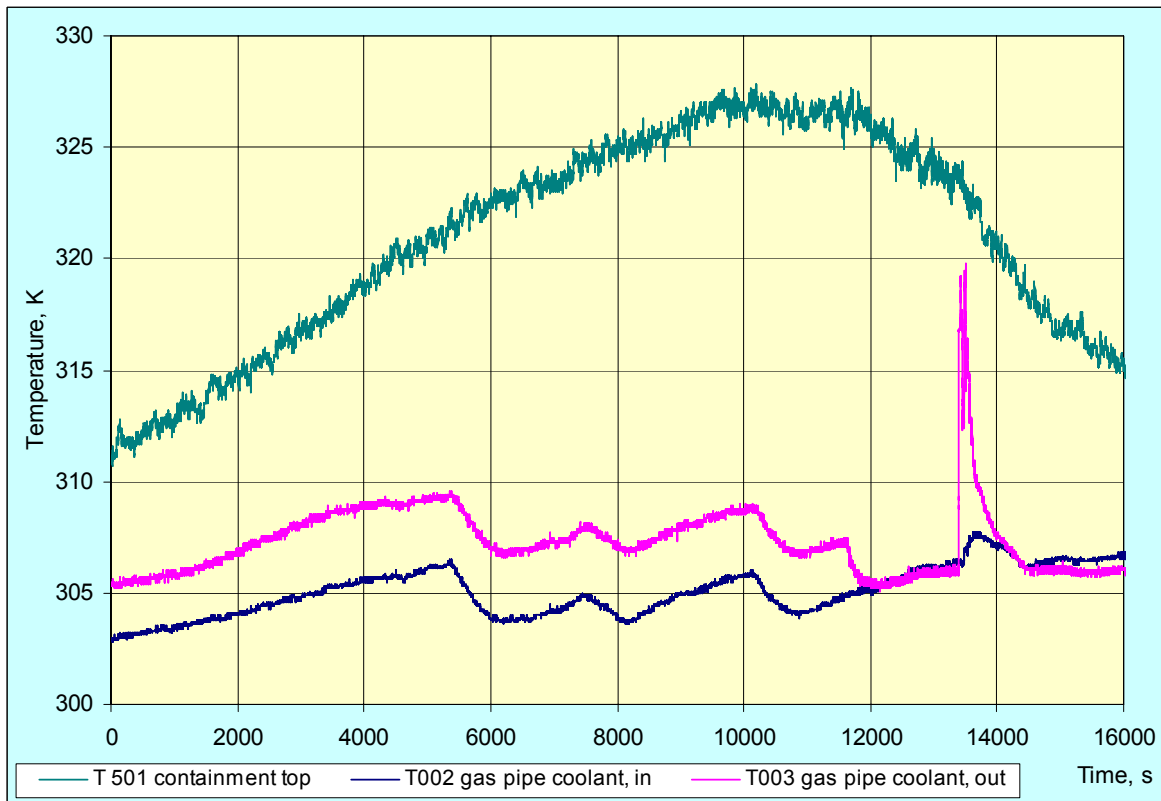
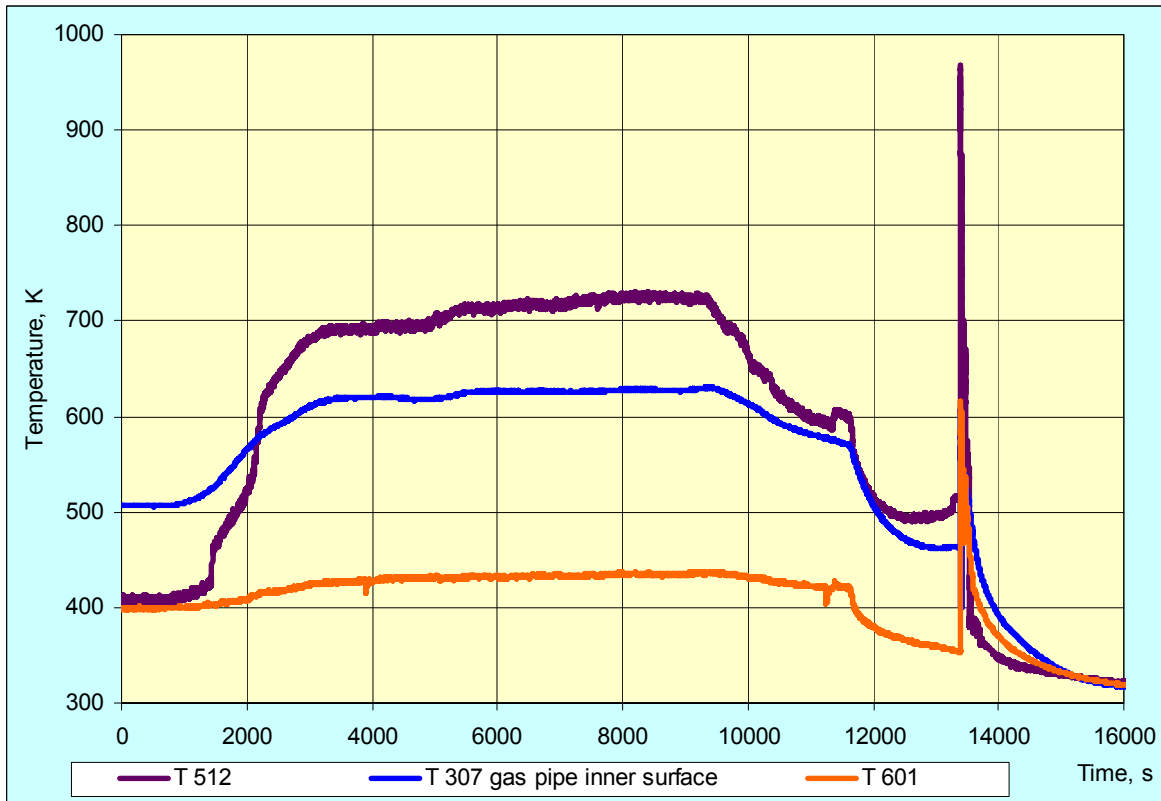


Fig. 29: Temperatures at test section outlet (T 512), at the inner surface of the off-gas pipe (T307) together with gas temperature T 601, top, and central containment temperature at ~1450 mm together with inlet (T 002) and outlet (T 003) temperatures of the water coolant of the off-gas pipe, bottom.

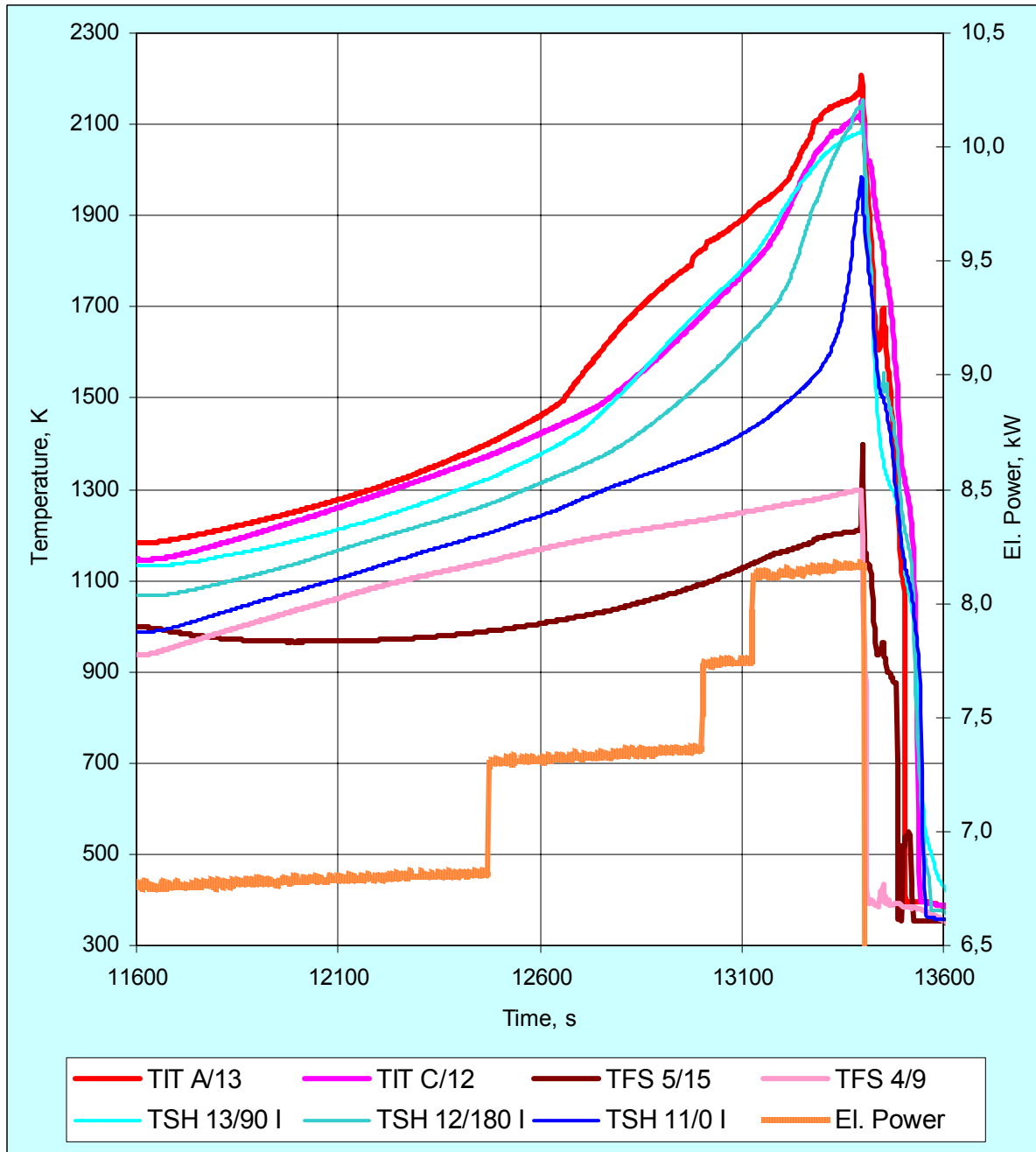


Fig. 30: Bundle and shroud temperatures during the air ingress phase together with the electric power history.

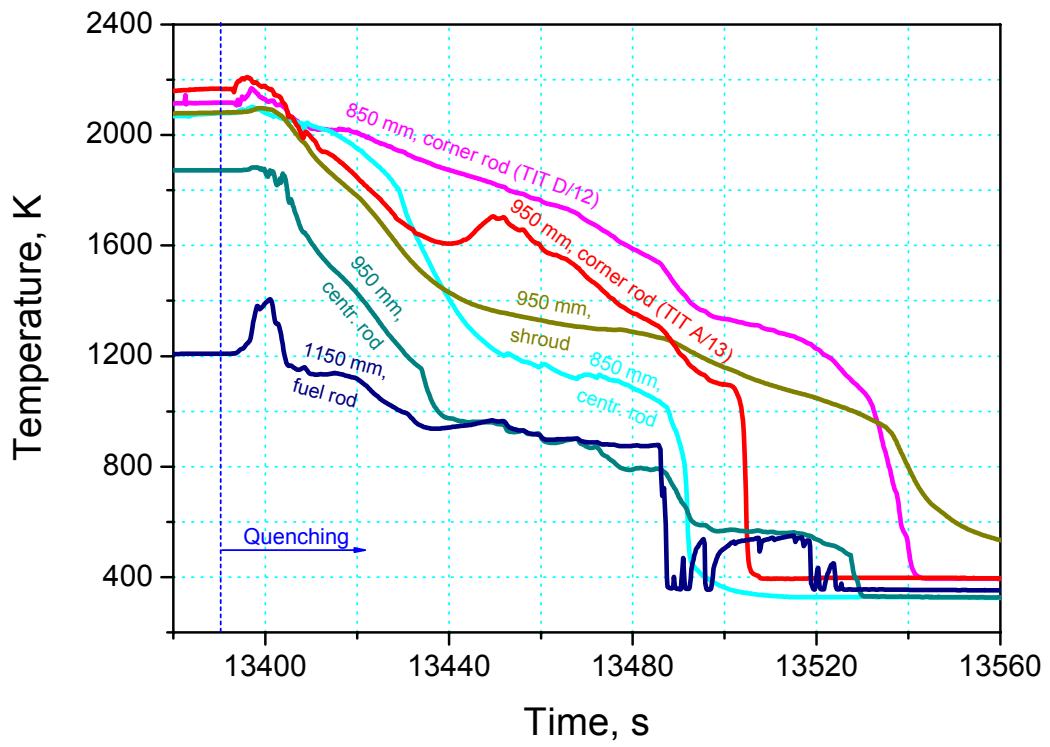


Fig. 31: QUENCH-10; Temperatures during the quenching phase.

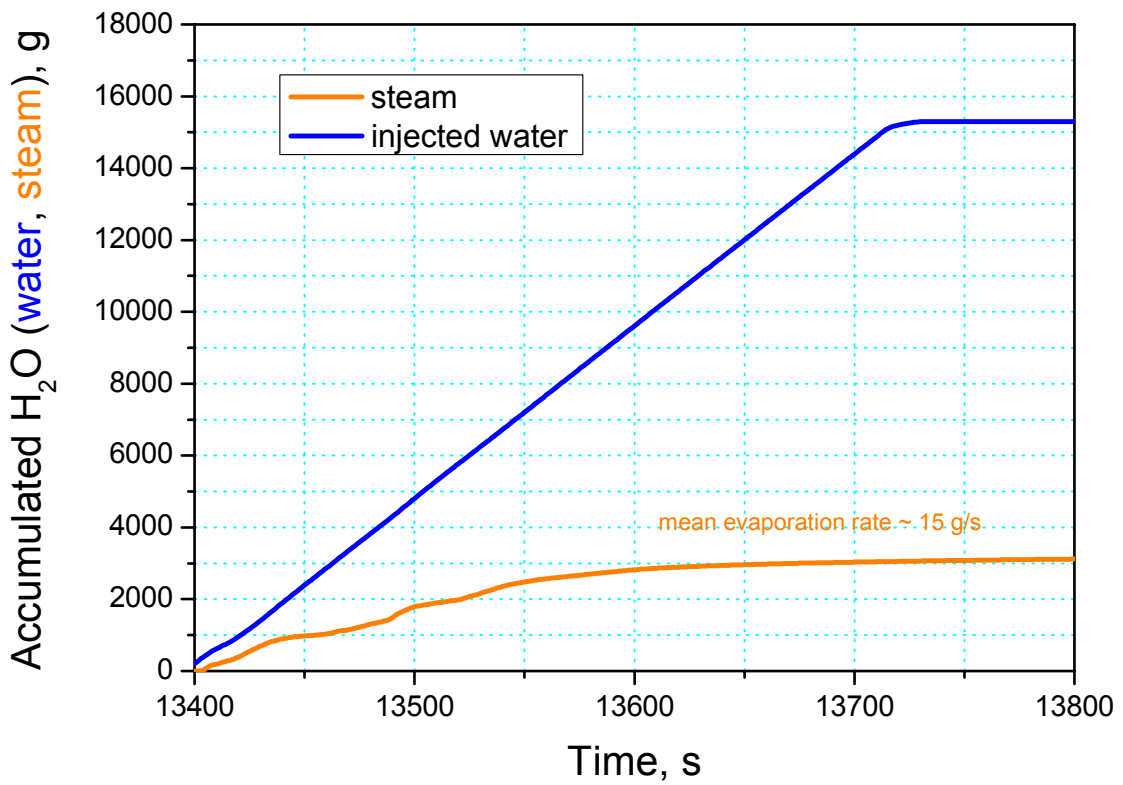
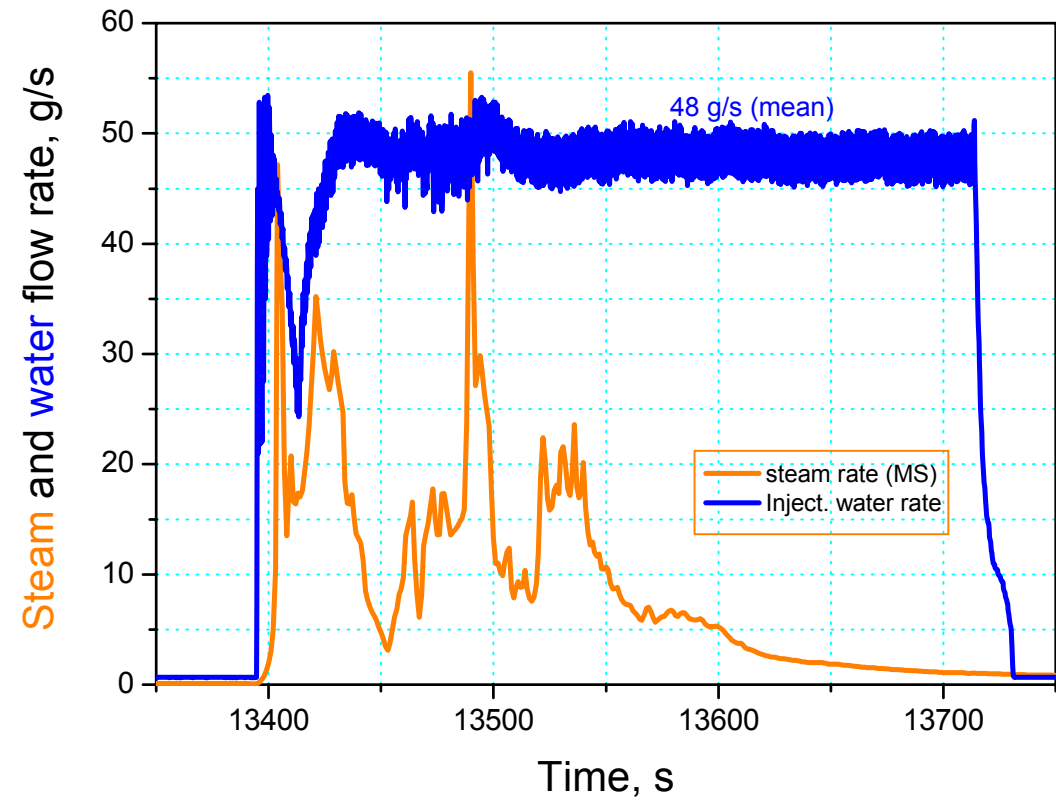


Fig. 32: QUENCH-10; Quench water injection and steam generation.

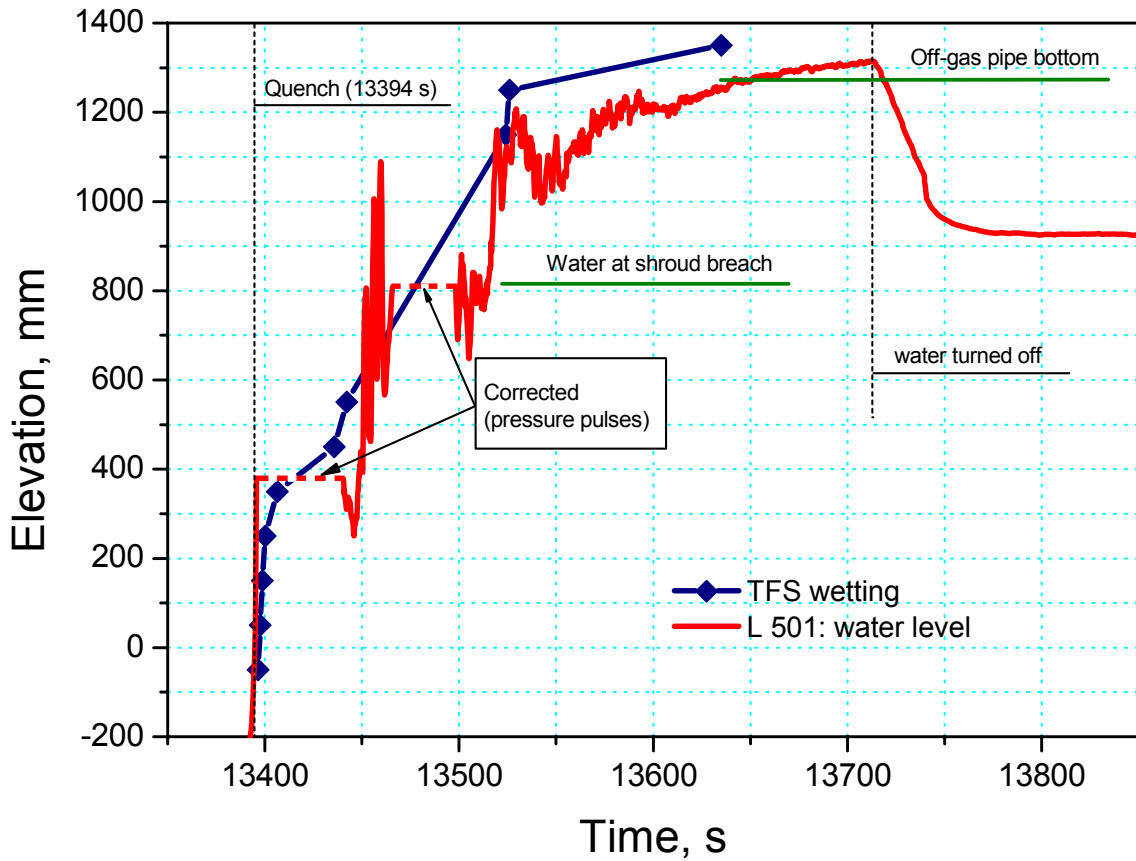


Fig. 33: QUENCH-10; Progression of the wetting front (L 501, red curve) and of the boundary between superheated and saturated steam (blue curve).

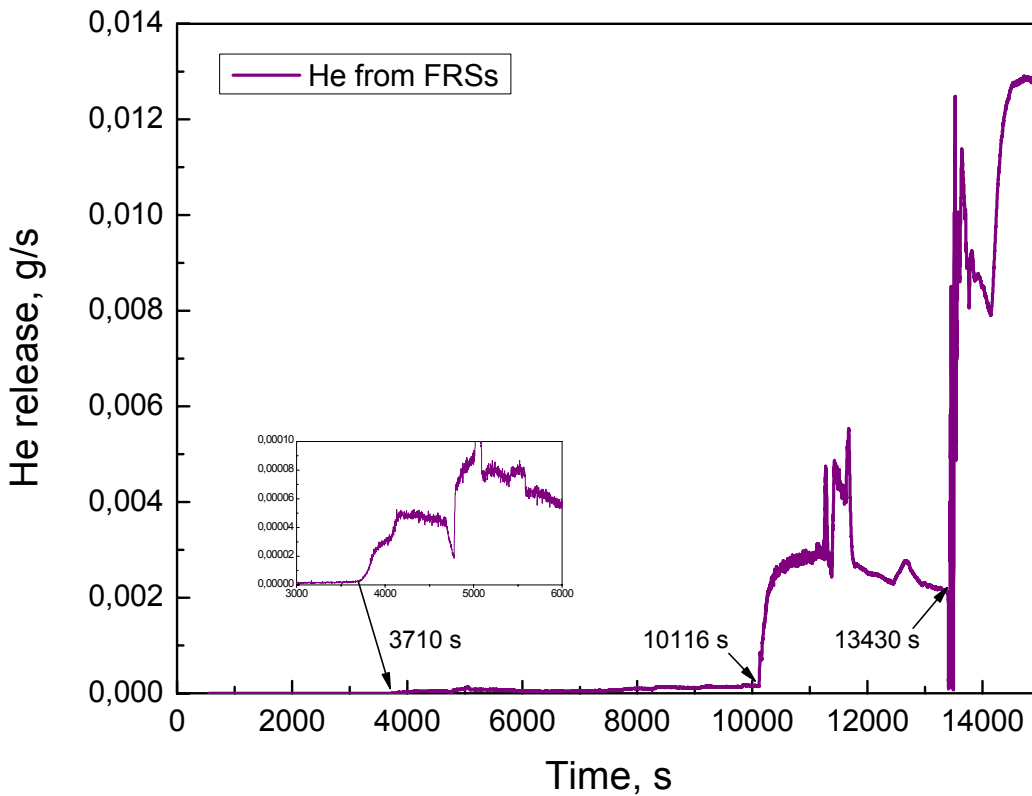
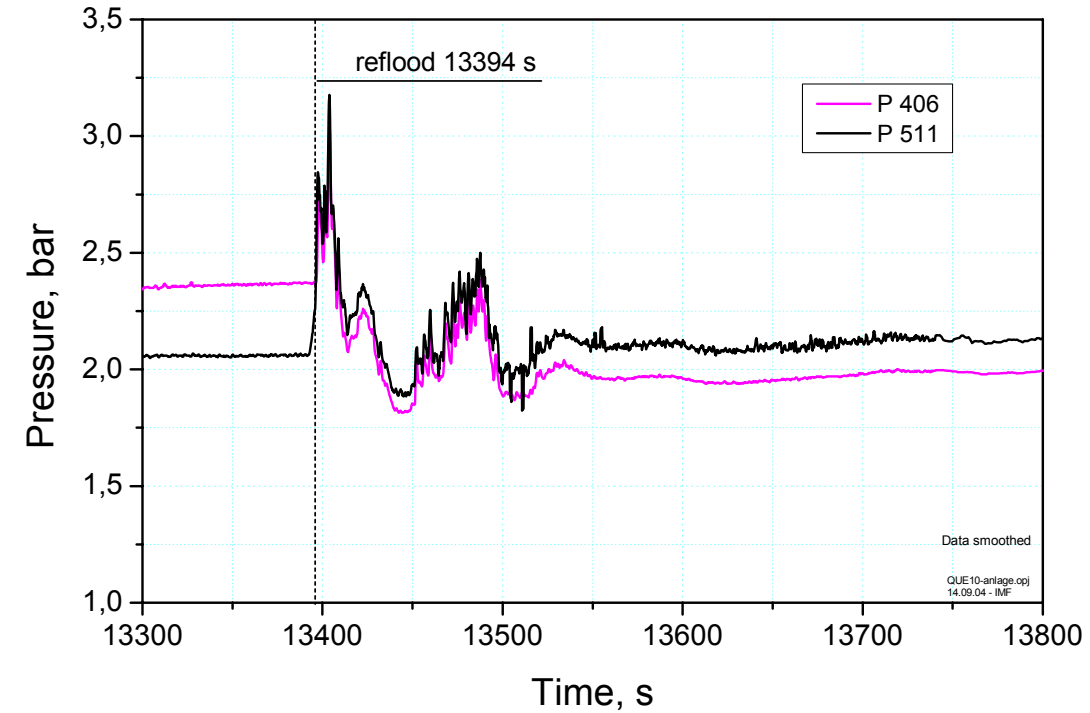


Fig. 34: QUENCH-10; Argon pressure P 406 indicating shroud failure shortly after onset of reflood, i.e. at 13397 s, together with system pressure at the test section inlet (P 511), top, and helium release rate measured by MS, bottom.

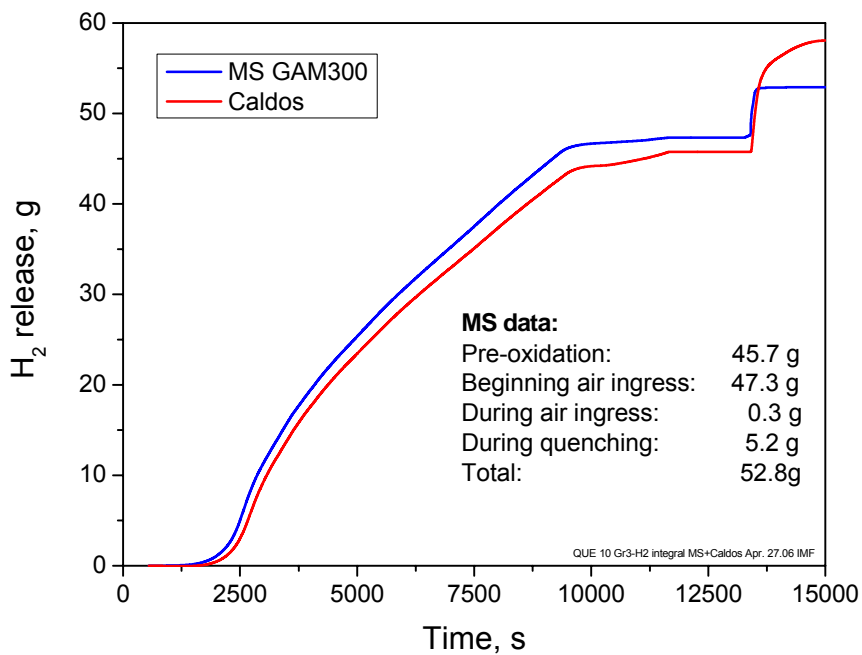
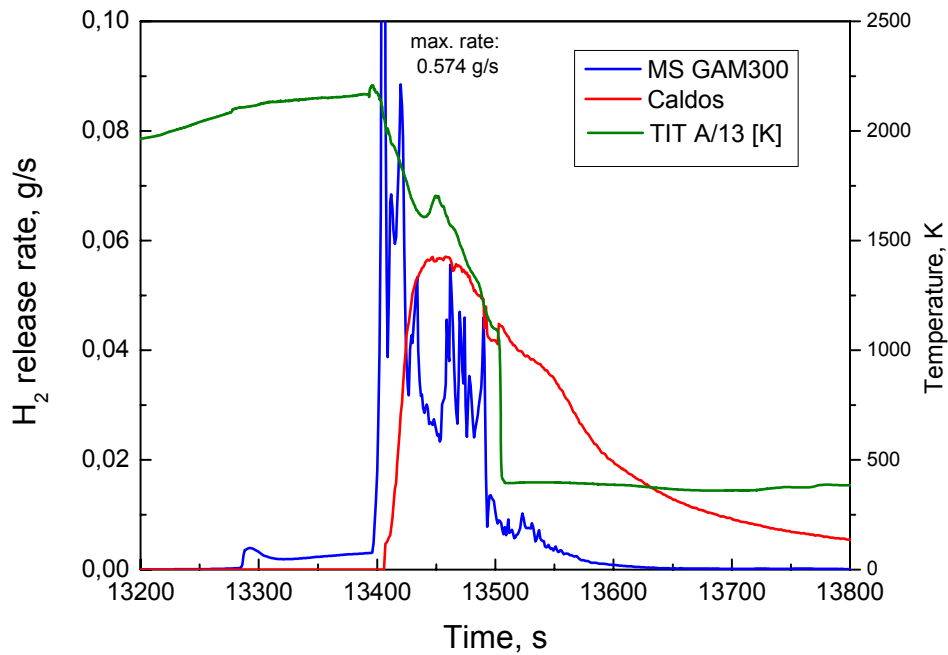


Fig. 35: QUENCH-10; Hydrogen release rates measured by mass spectrometer and Caldos analyzer (Caldos values were set zero during air ingress phase), top. Integral hydrogen release measured by MS and Caldos, bottom.

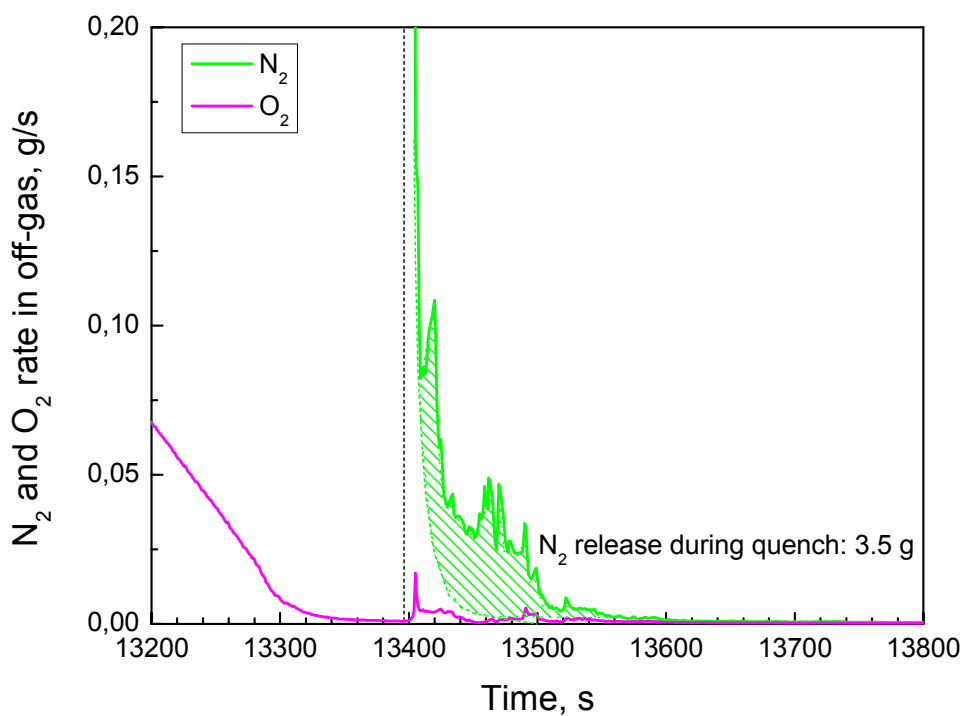
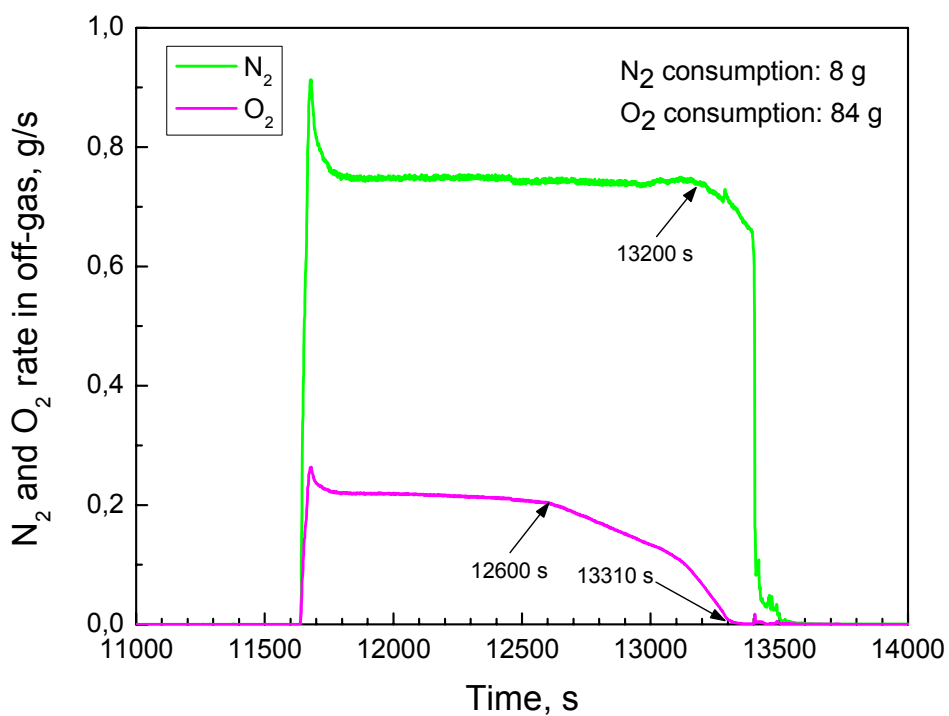


Fig. 36: QUENCH-10; Nitrogen and oxygen rates measured by MS in the off-gas during the air ingress phase, top, and during the quench phase, bottom.

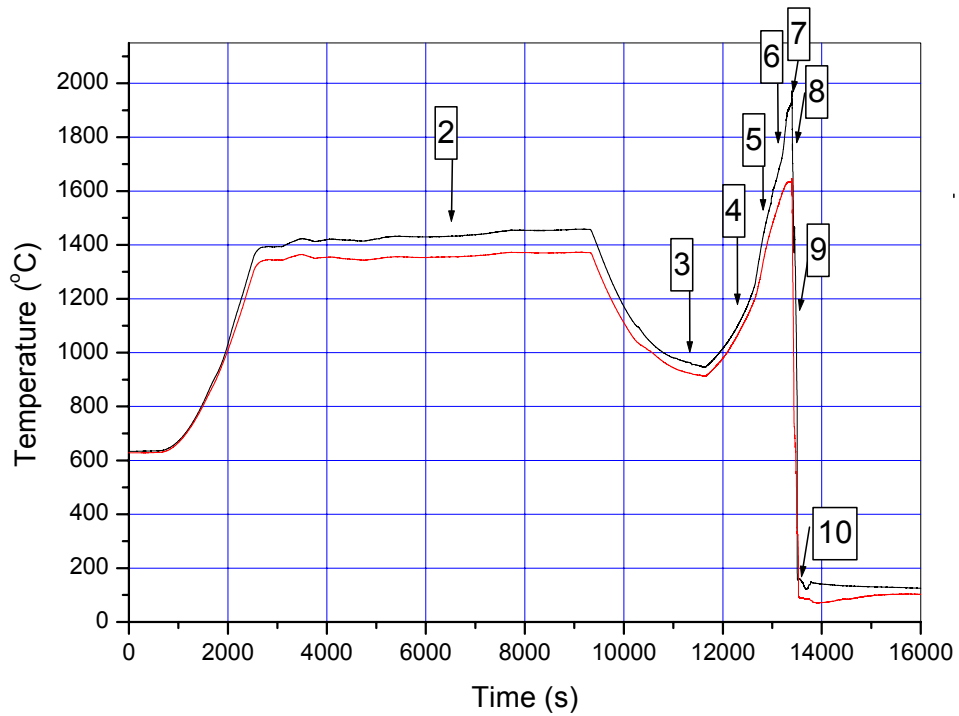


Fig. 37: QUENCH-10; Timing of aerosol sampling.

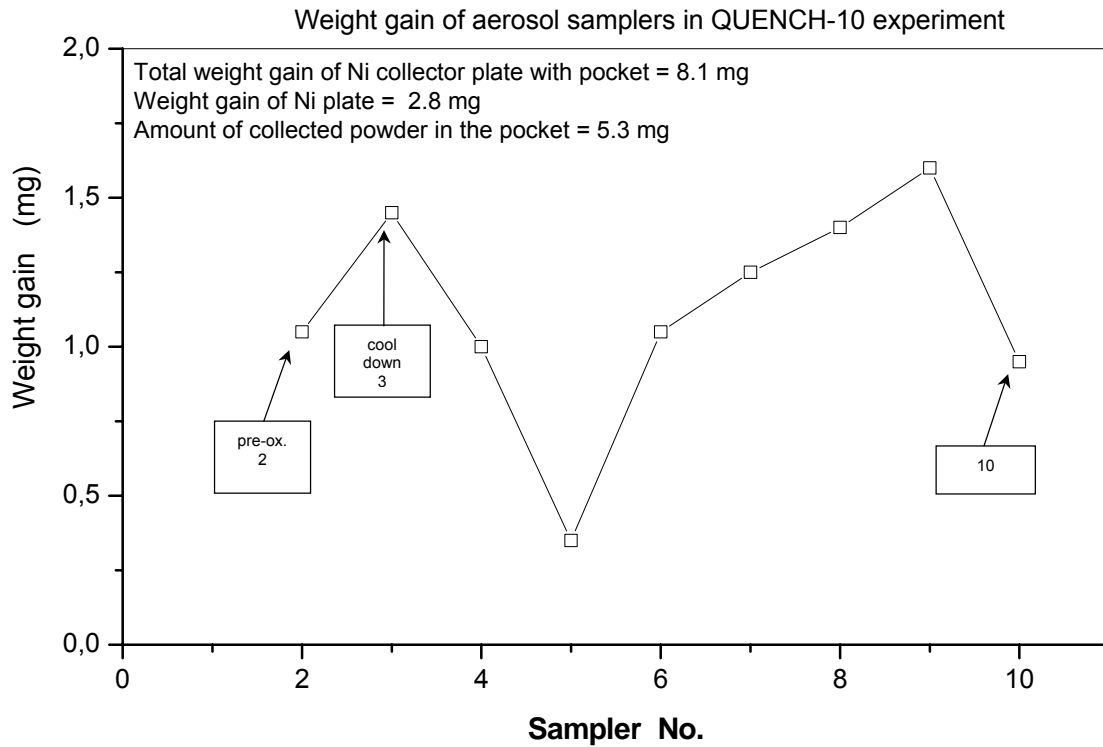


Fig. 38: QUENCH-10; Weight gain from aerosol sampling.

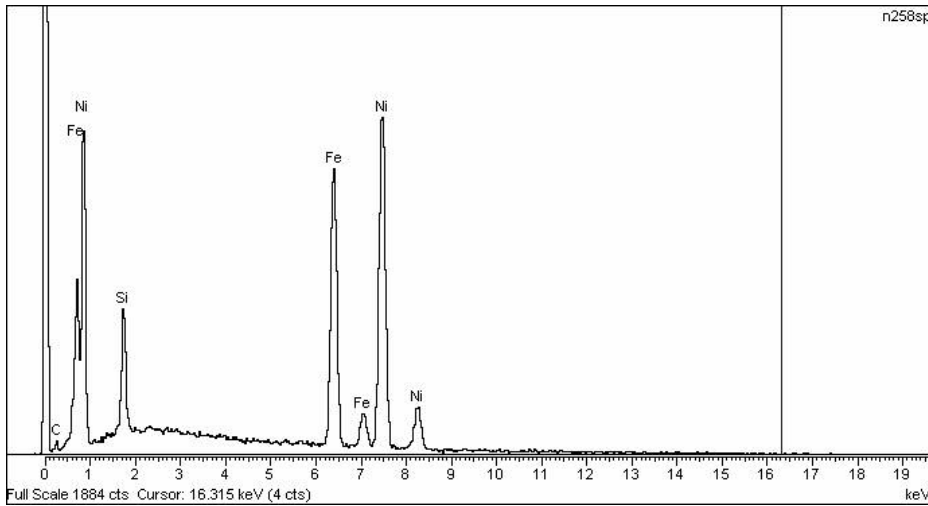
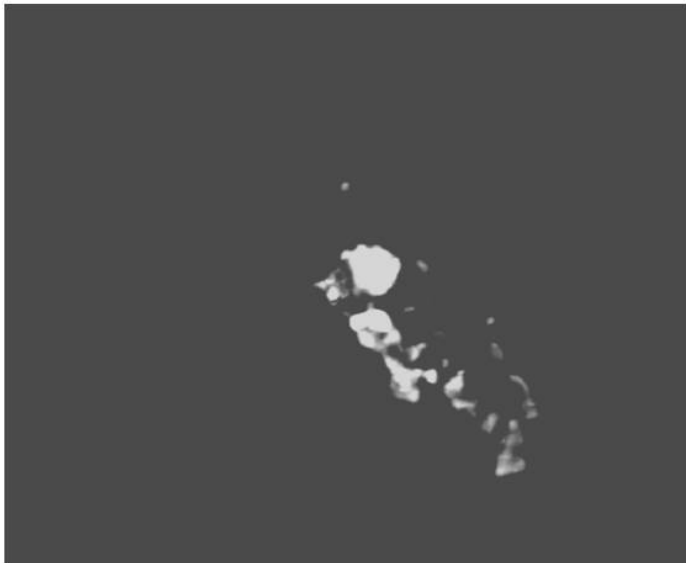


Fig. 39: QUENCH-10; Digital BEI image and some EDX spectra for Sample 2/5 showing various Fe-containing particles.

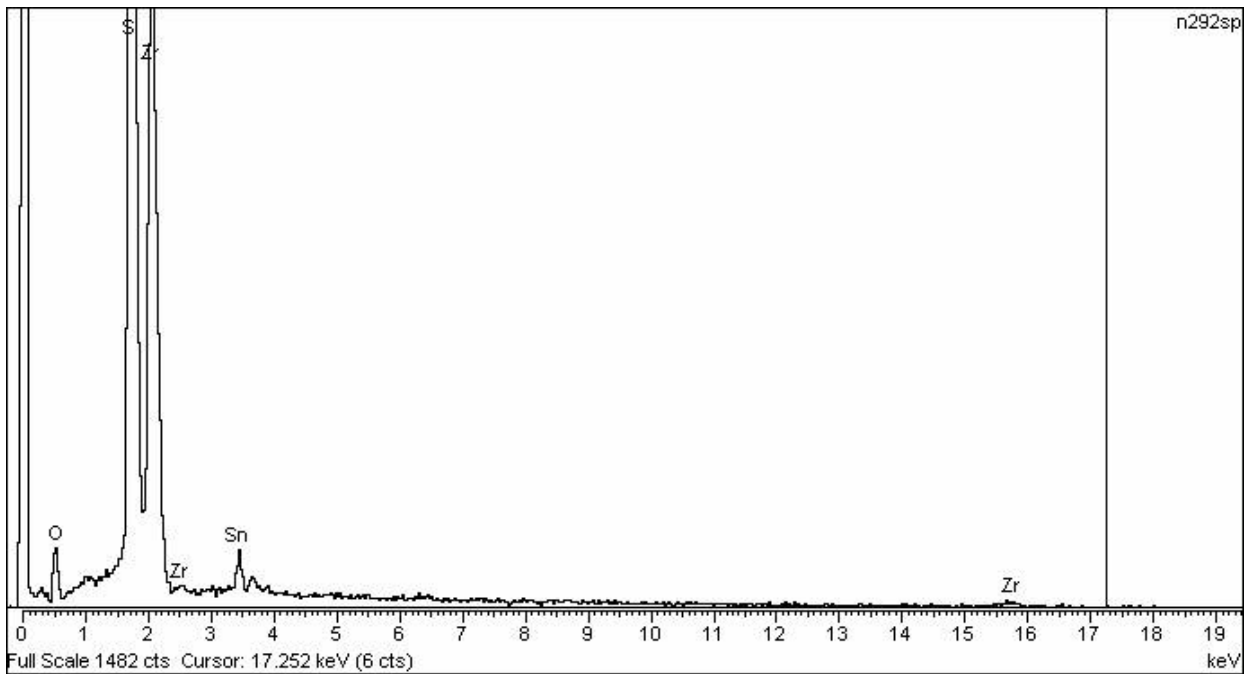
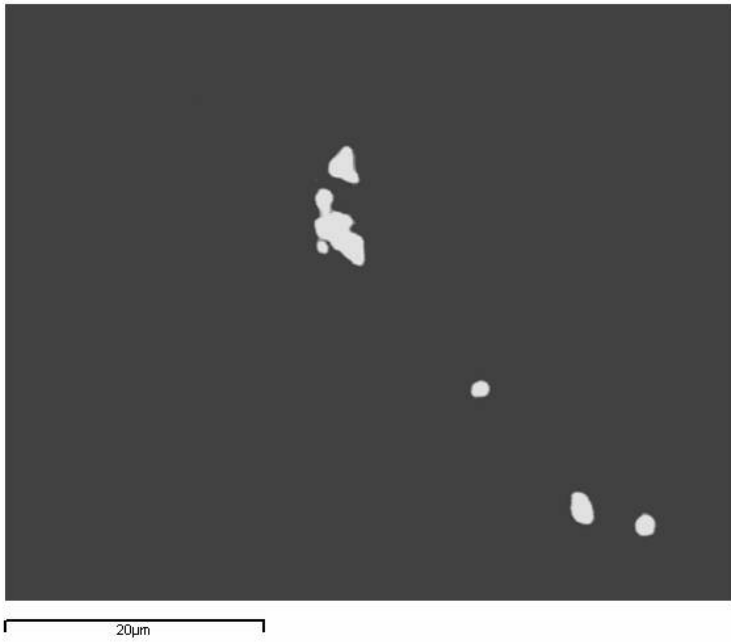


Fig. 40: QUENCH-10; Zr (Sn) containing particles and a typical EDX spectrum for Sample 2/9.

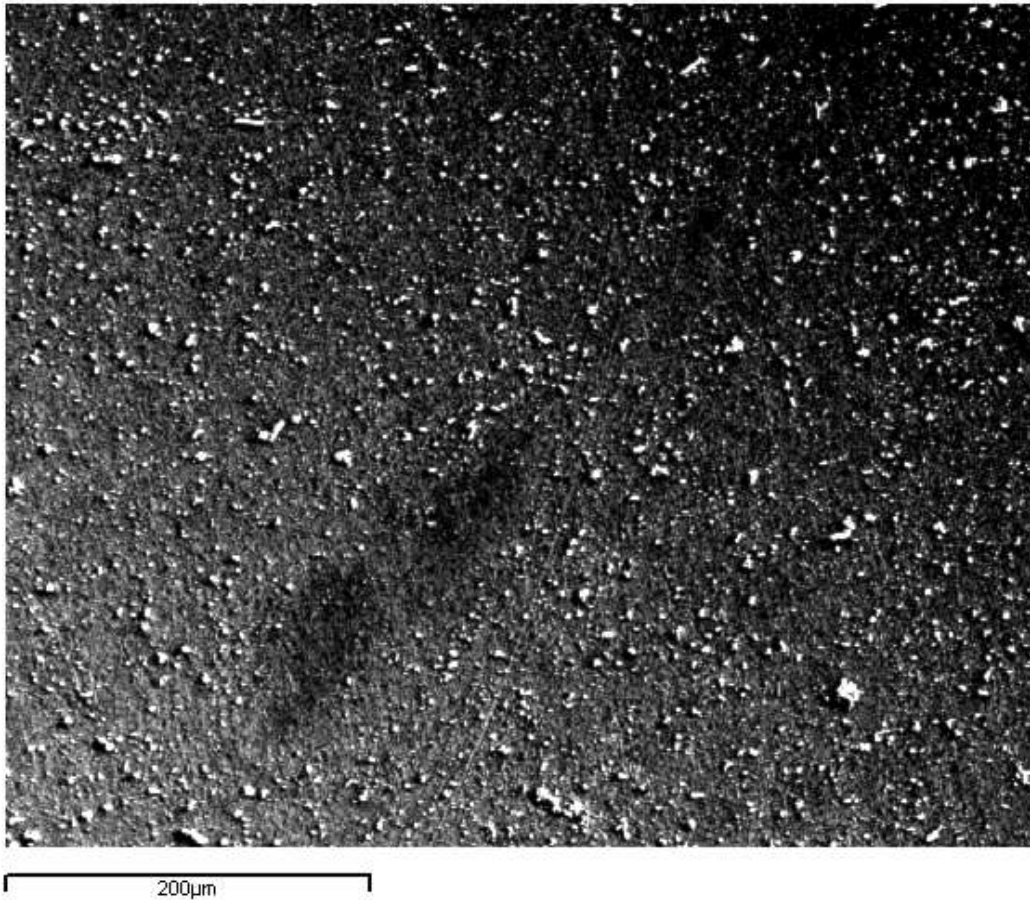


Fig. 41: QUENCH-10; Typical SEI image taken from aerosols deposited on the Ni plate.

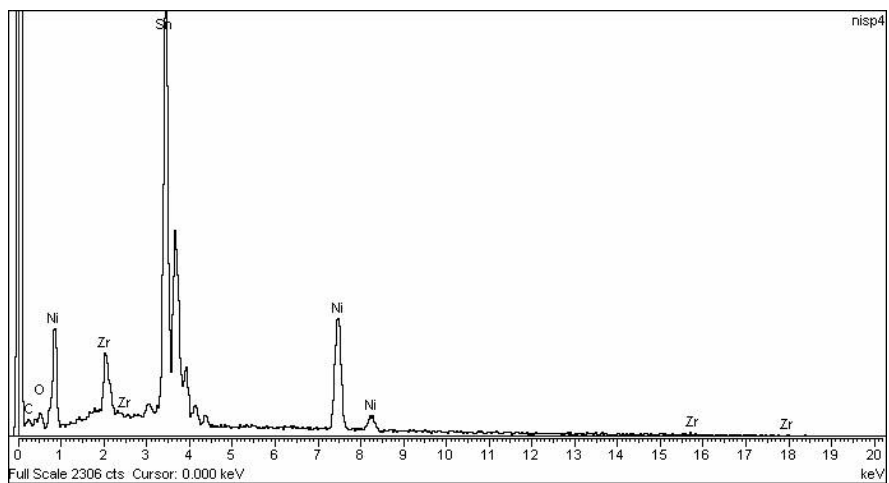
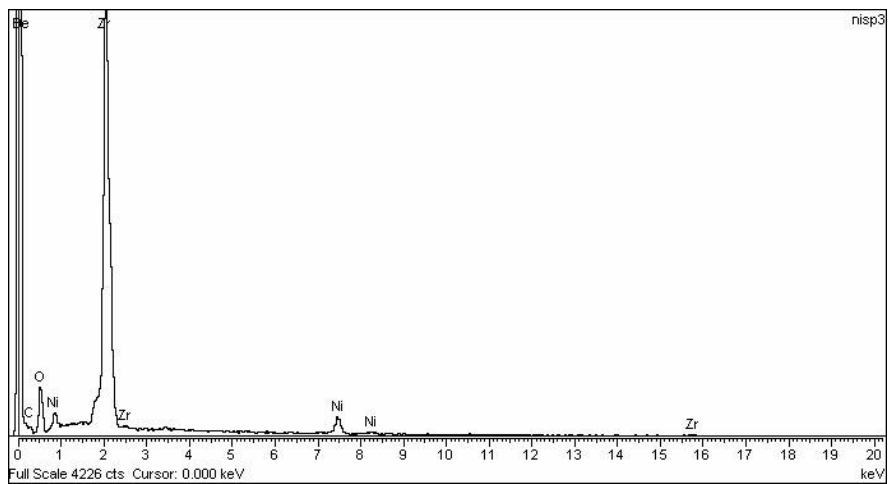
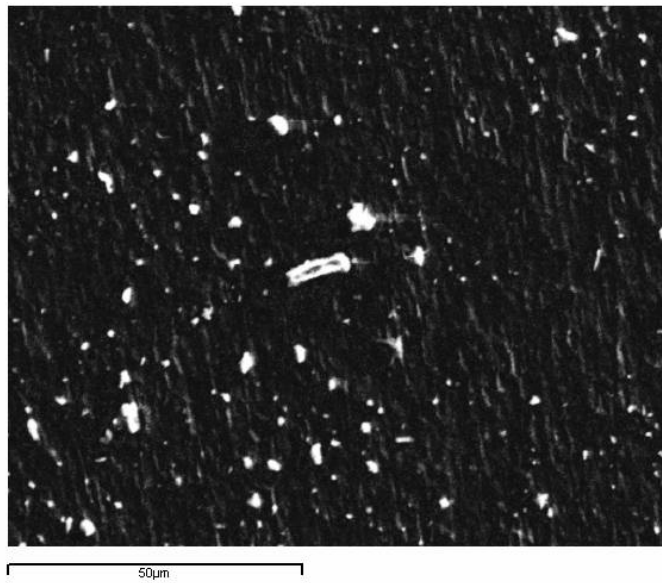


Fig. 42: QUENCH-10; Typical BEI image (magnification 1000 x) and two EDX spectra of aerosols deposited on the Ni plate.

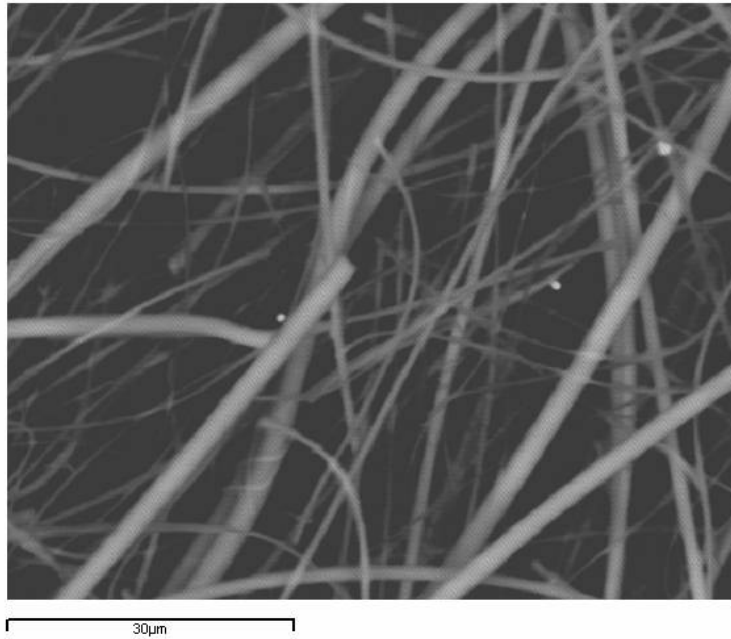


Fig. 43: QUENCH-10; Microscopic image of sample Q5.

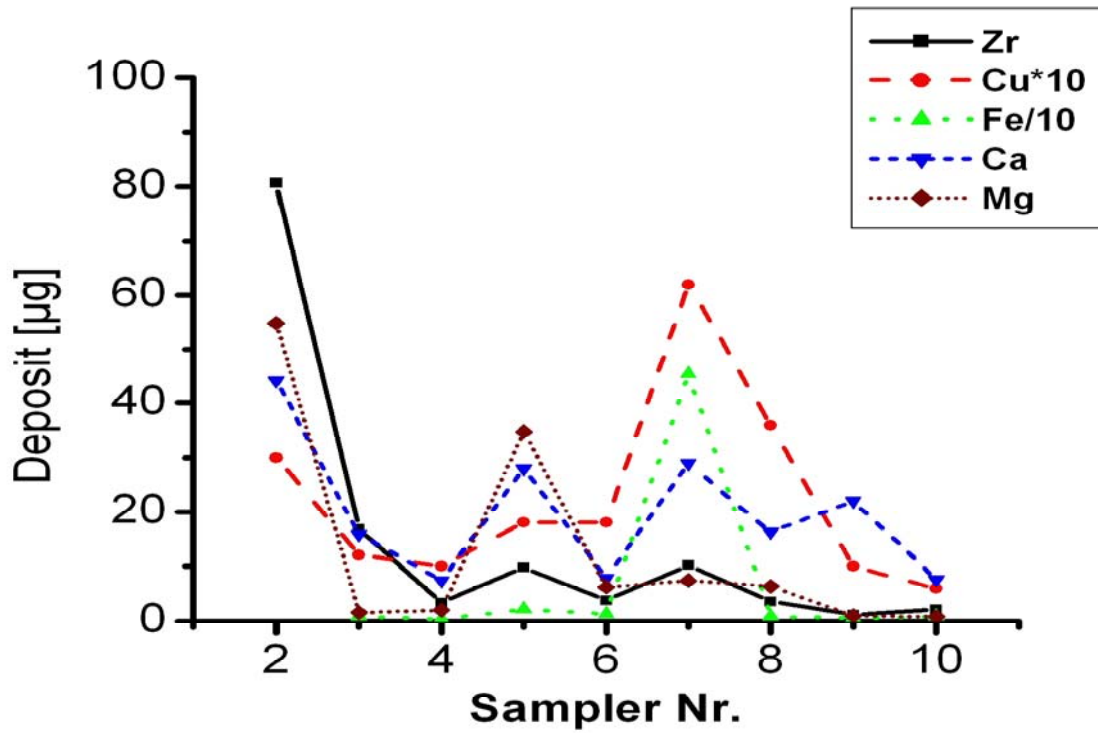


Fig. 44: QUENCH-10; Results of SSMS measurements taken at the quartz fiber filters.



Entire length of the bundle with  $ZrO_2$  fiber insulation at  $315^\circ$  orientation.



View of the hot zone at  $315^\circ$  orientation of the QUENCH-10 bundle after removal of the  $ZrO_2$  fiber insulation.

Fig. 45: QUENCH-10; Posttest view of the QUENCH-10 bundle.



Bundle orientation: 0°



Bundle orientation: 90°



Bundle orientation: 180°



Bundle orientation: 270°

Fig. 46: QUENCH-10; Posttest view of the QUENCH-10 bundle at the elevations of the hot zone (after removal of the shroud insulation). Parts of the shroud fell off during handling.



View of the outer shroud surface which was in contact with the  $ZrO_2$  fiber insulation.



View of the inner side of the shroud. At the fracture surface the  $\alpha$ -Zr(O) metal layer can be recognized. The inner surface is oxidized. There some nitride has formed due to oxidation in air.

Fig. 47: QUENCH-10; Parts of shroud of the QUENCH-10 bundle which fell off during handling (at ~850 mm elevation).



Camera at elevation 900 mm:  
Pellets and debris of failed rods.



Camera at elevation 850 mm:  
Cracks in the shroud and  
cladding of a fuel rod simulator.



Camera at elevation 750 mm:  
Shroud deformation and cracks  
in the cladding.



Camera at elevation 650 mm:  
Spots of zirconium nitride on  
the shroud inner surface.

Fig. 48: QUENCH-10; Photographs taken by a videoscope inserted into the bundle from the bottom, at the (voided) position of extracted corner rod B.



Camera at elevation 450 mm:  
Remnant of corner rod D, axial stripe of zirconium nitride on the shroud inner surface.



Camera lens looking sideways at elevation 150 mm:  
Spots of zirconium nitride on the shroud inner surface.

Fig. 49: QUENCH-10; Photographs taken by a videoscope inserted into the bundle from the bottom, at the empty position of extracted corner rod D.

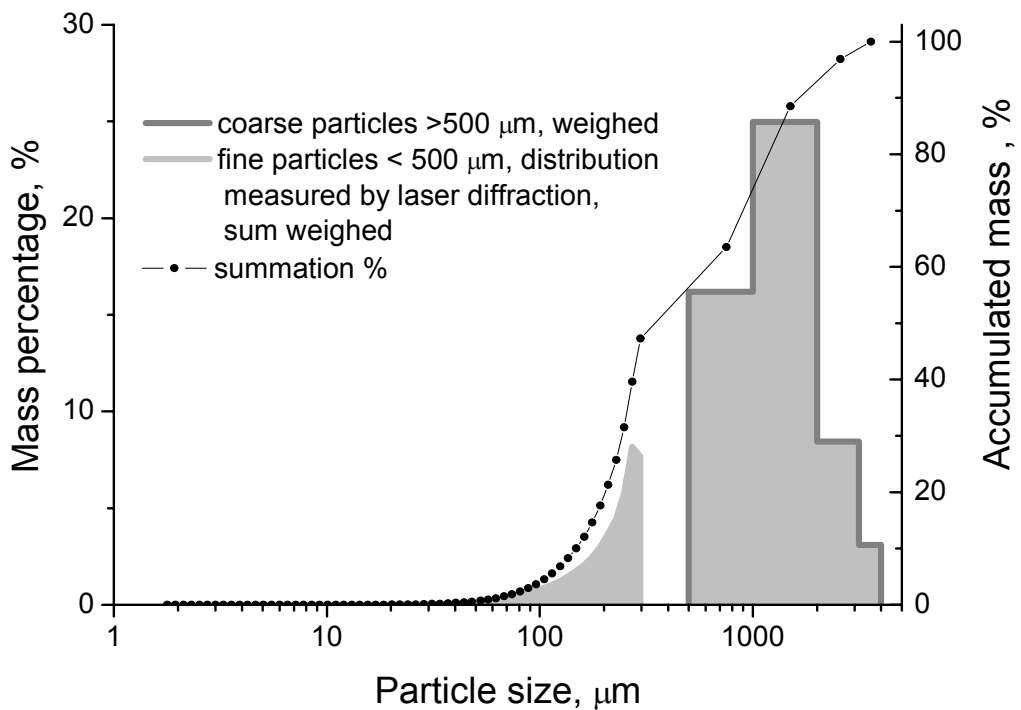
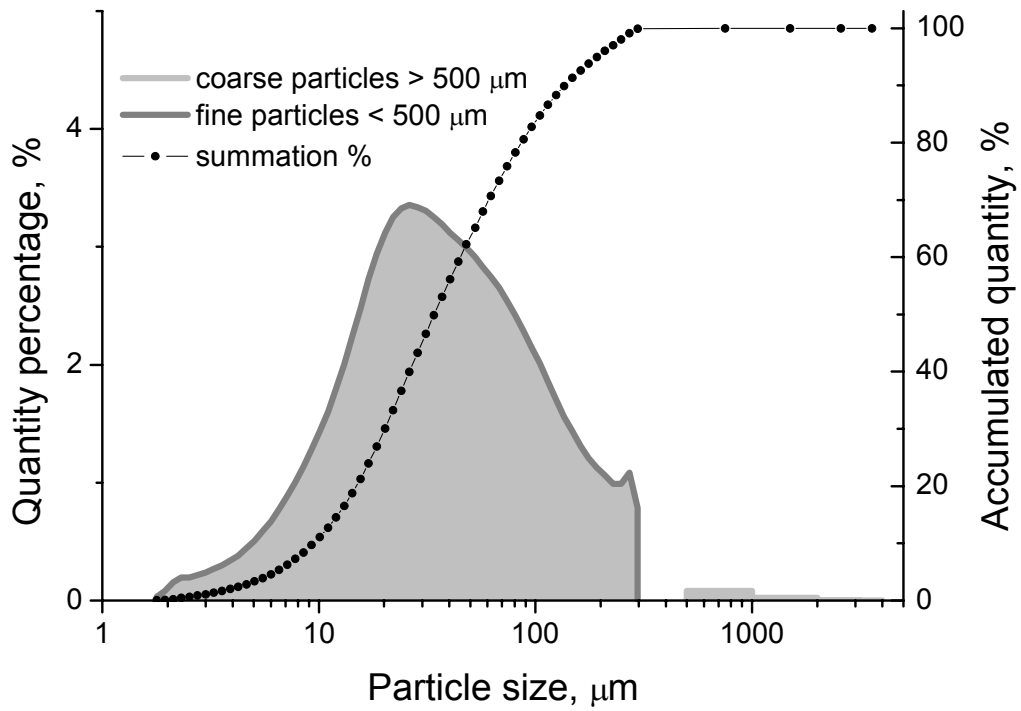
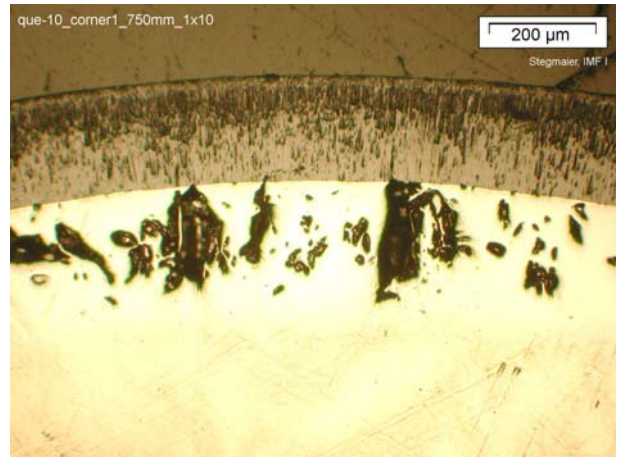
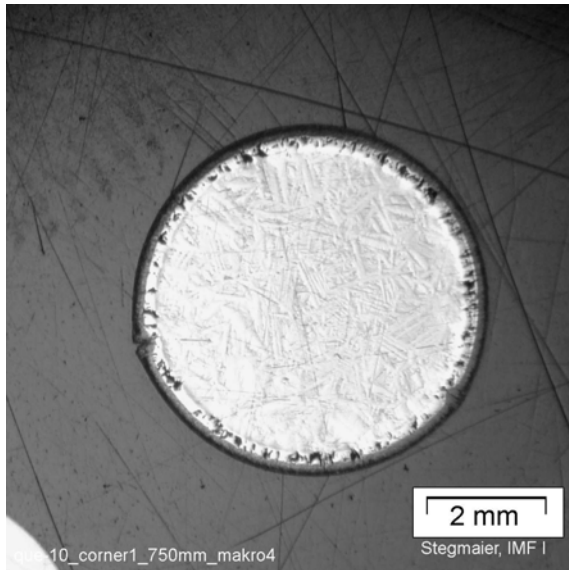
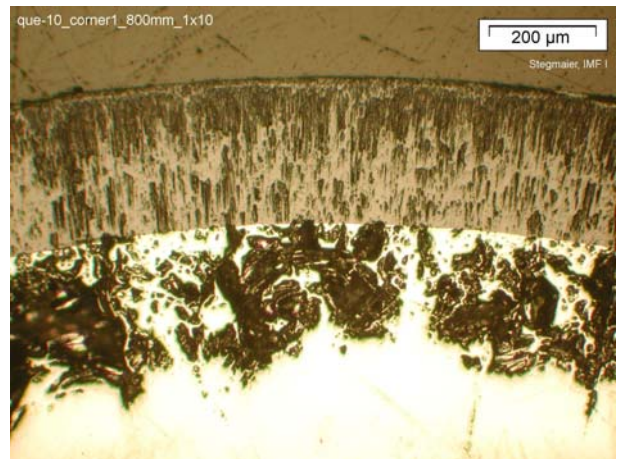
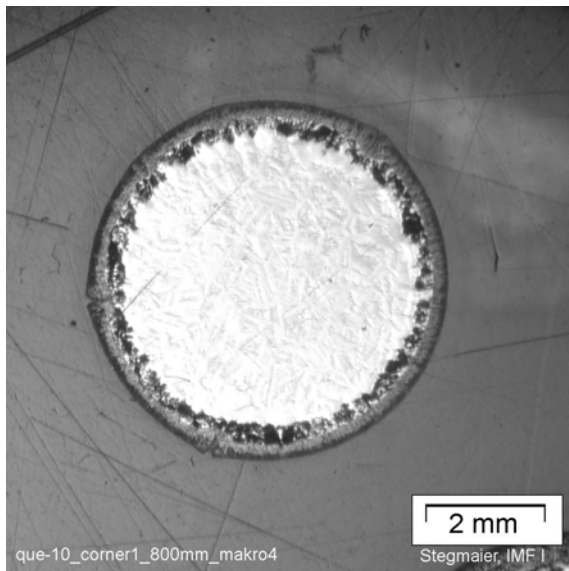


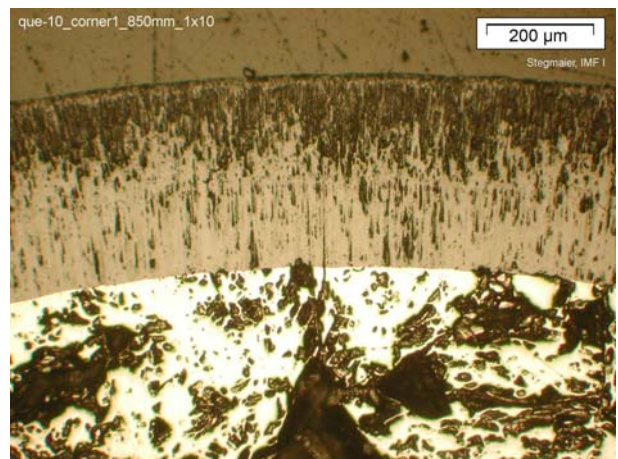
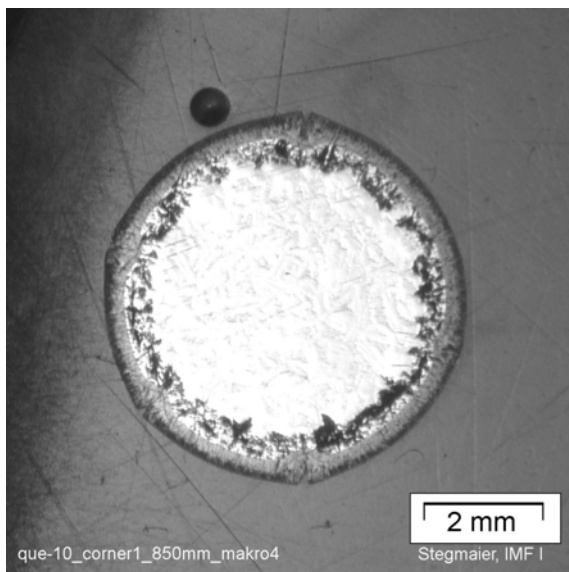
Fig. 50: Distribution of particles taken from the off-gas pipe after the QUENCH-10 experiment; Quantity distribution, top, mass distribution, bottom.



750 mm: oxide scale thickness of ~194 μm

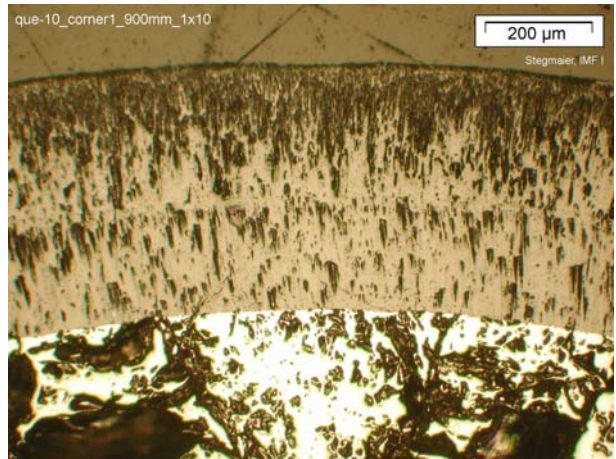
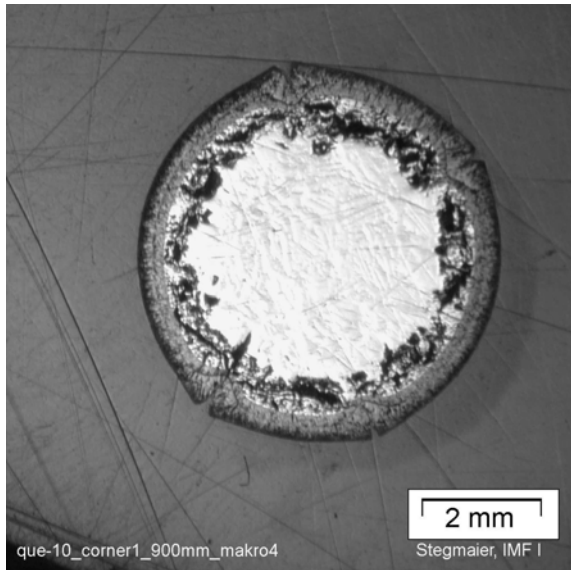


800 mm: oxide scale thickness of ~268 μm

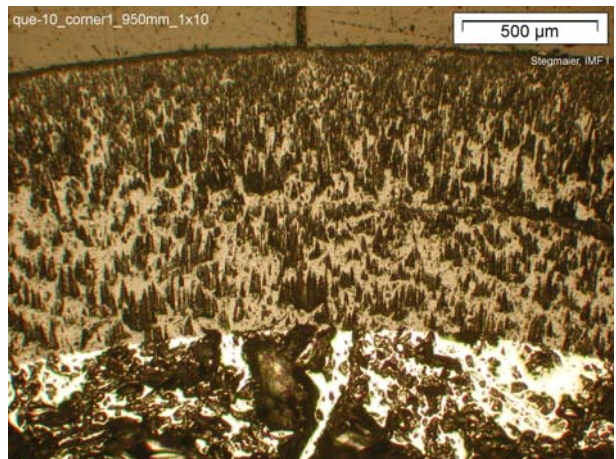
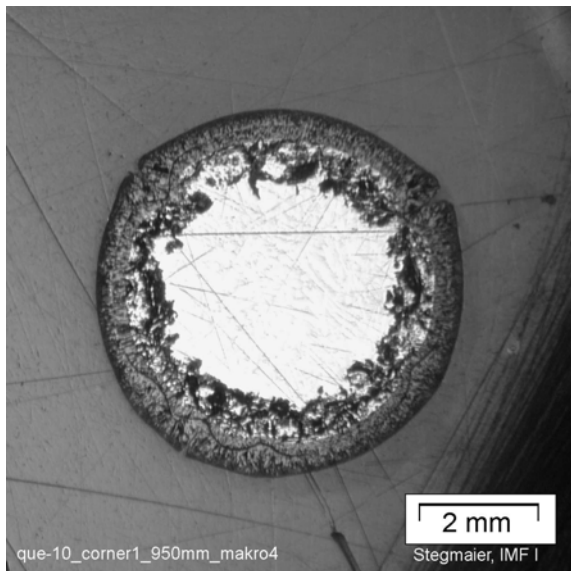


850 mm: oxide scale thickness of ~357 μm

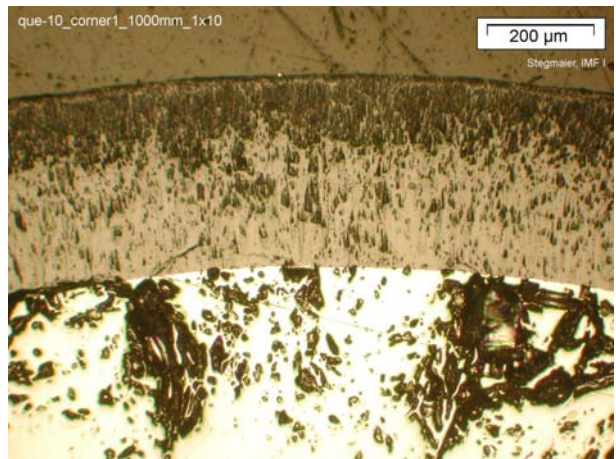
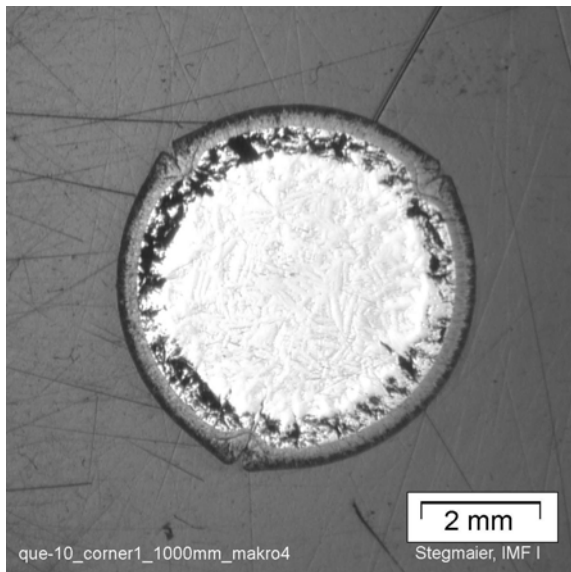
Fig. 51: QUENCH-10; Oxide scale thickness of corner rod B at 750, 800 and 850 mm elevation.



900 mm: oxide scale thickness of ~453 μm

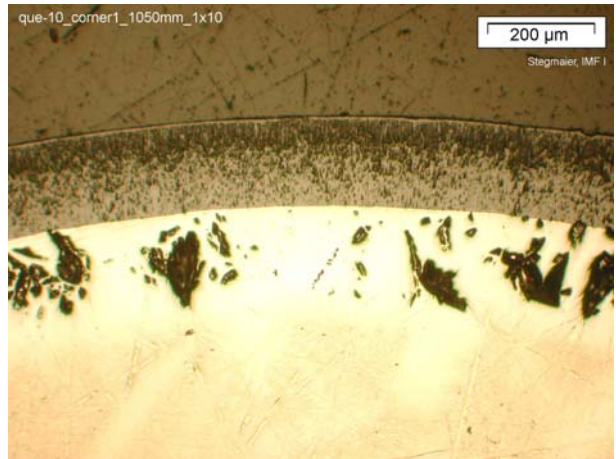
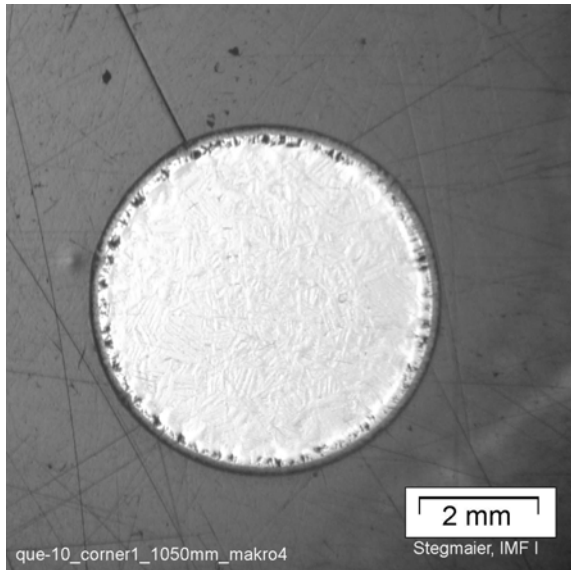


950 mm: oxide scale thickness of ~514 μm

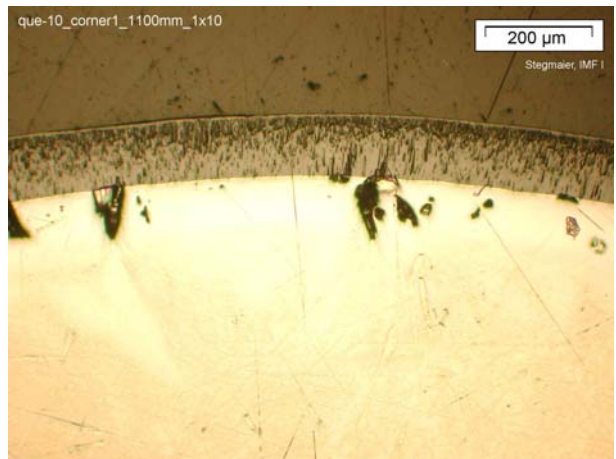
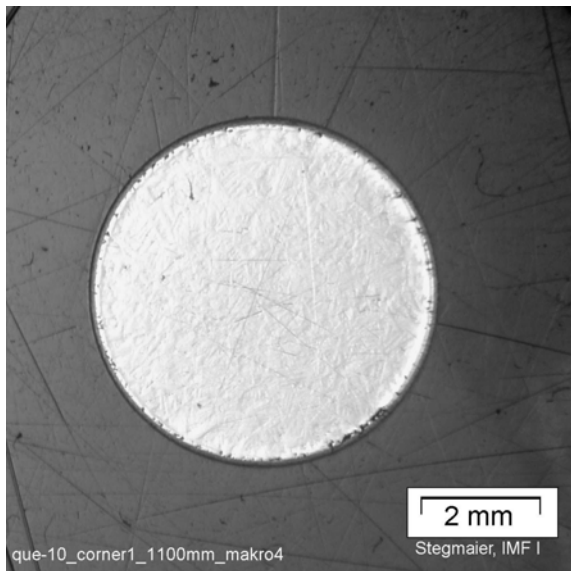


1000 mm: oxide scale thickness of ~358 μm

Fig. 52: QUENCH-10; Oxide scale thickness of corner rod B at 900, 950 and 1000 mm elevation.

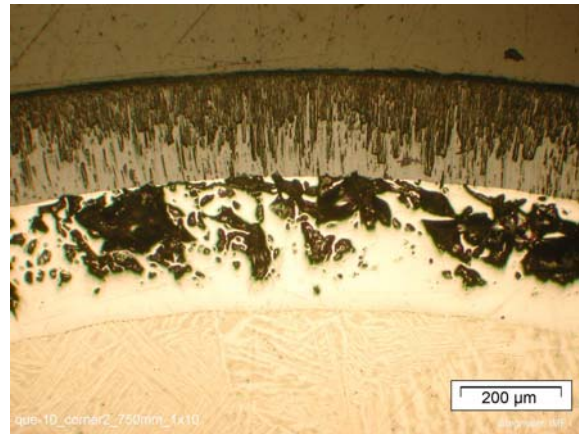
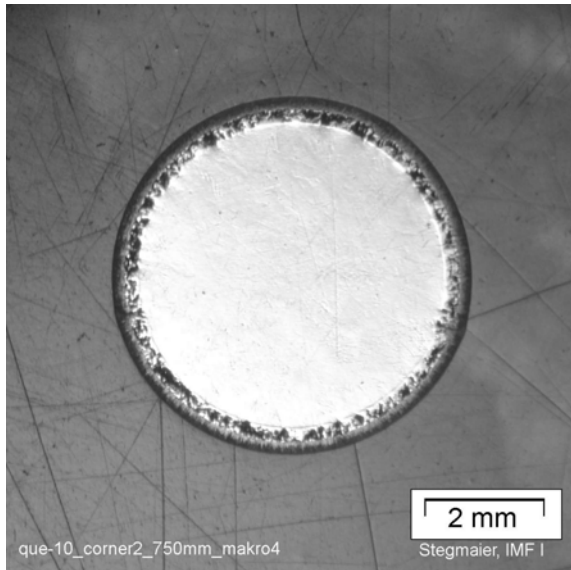


1050 mm: oxide scale thickness of ~172  $\mu\text{m}$

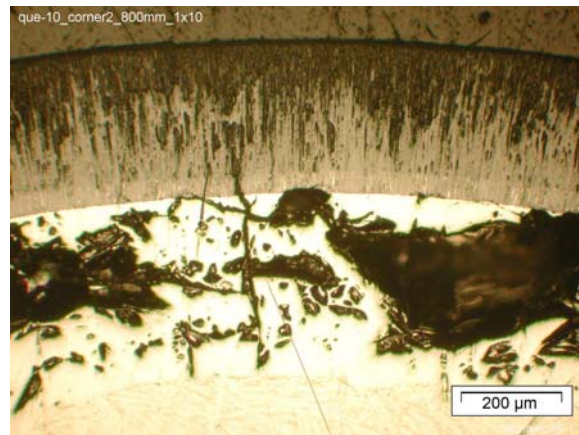
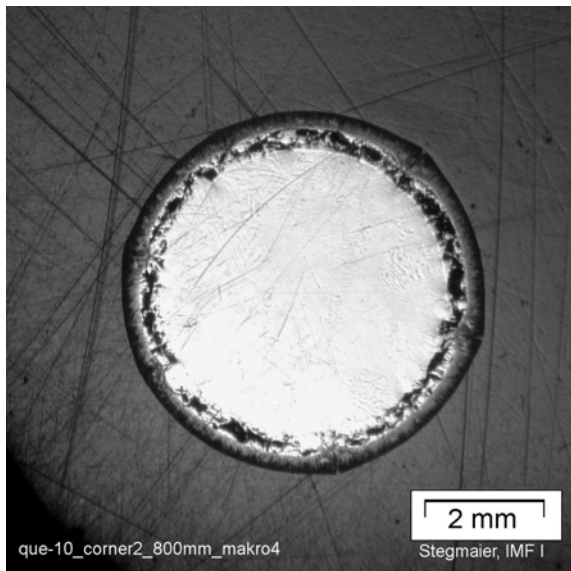


1100 mm: oxide scale thickness of ~108  $\mu\text{m}$

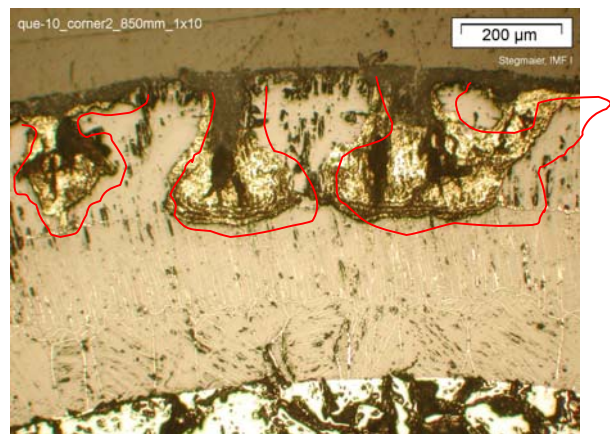
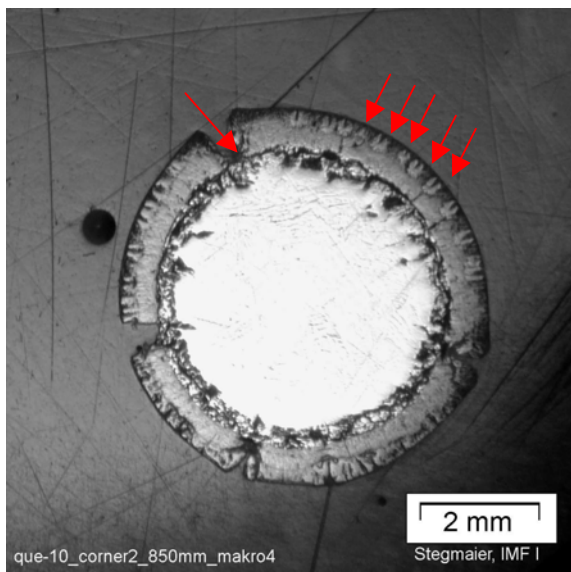
Fig. 53: QUENCH-10; Oxide scale thickness of corner rod B at 1050 and 1100 mm elevation.



750 mm: oxide scale thickness of  $\sim 205 \mu\text{m}$

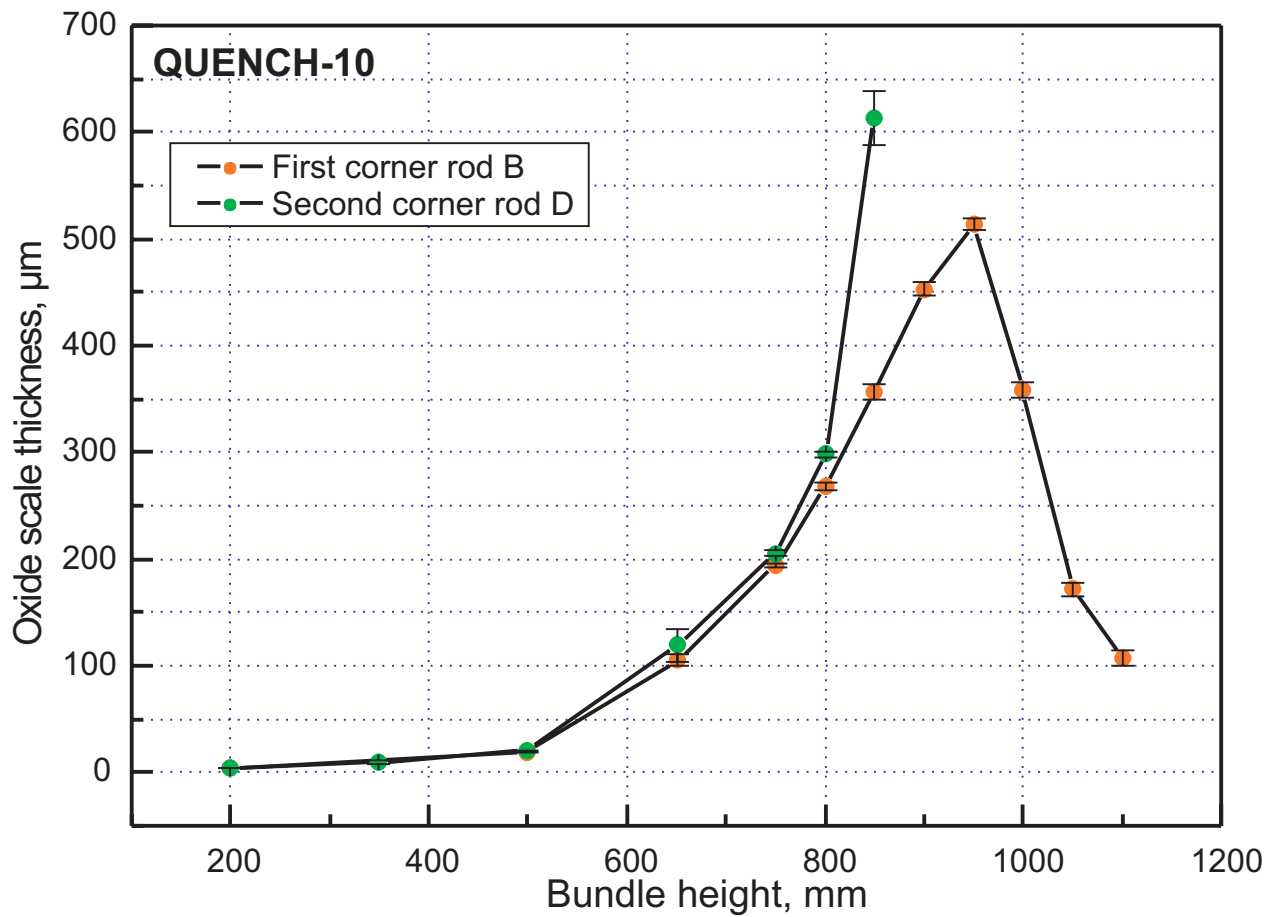


800 mm: oxide scale thickness of  $\sim 298 \mu\text{m}$



850 mm: oxide scale thickness of  $\sim 613 \mu\text{m}$   
 This is the first cross section where we see **nitride** phases along grooves.

Fig. 54: QUENCH-10; Oxide scale thickness of corner rod D at 750, 800 and 850 mm elevation.



<b>Corner rod B</b>			<b>Corner rod D</b>		
Bundle level mm	oxide-layer mean value, µm	st. deviation	Bundle level mm	oxide-layer mean value, µm	st. deviation
200	4	0.5	200	4	0.5
500	19	1	350	10	1.3
650	105	5	500	20	0
750	194	1.8	650	119	14.5
800	268	2.8	750	205	2.8
850	357	7	800	298	2.7
900	453	6.1	850	613	25.4
950	514	5.2			
1000	358	7.5			
1050	172	6.4			
1100	108	7.3			

Fig. 55: QUENCH-10; Corner rods as pulled out of the bundle: rod B (end of steam pre-oxidation) and rod D (end of air oxidation phase).

Top: Side views of the withdrawn corner rod B and the withdrawn part of corner rod D

Bottom, left: 850 mm elevation, cross section of corner rod B, withdrawn before the air ingress phase

Bottom, right: Same elevation, corner rod D, withdrawn after the air ingress phase

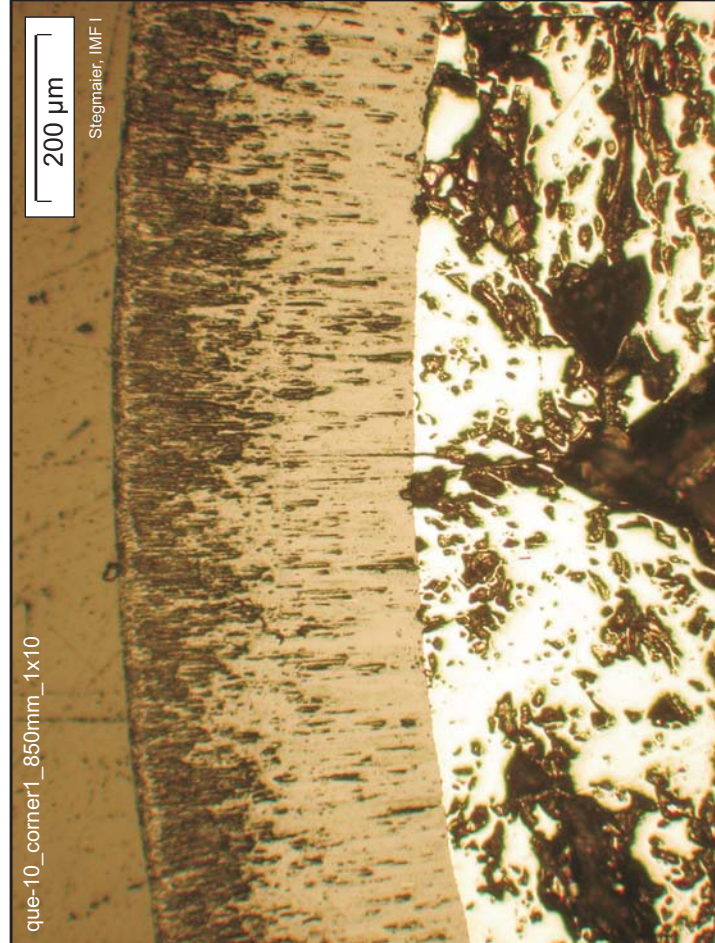


Fig. 56: Overview of the withdrawn corner rods B and D, and comparison of their oxidation at the previous bundle position 850 mm.



QUE-10-3 (635 mm, bottom)



QUE-10-3 (650 mm, top)



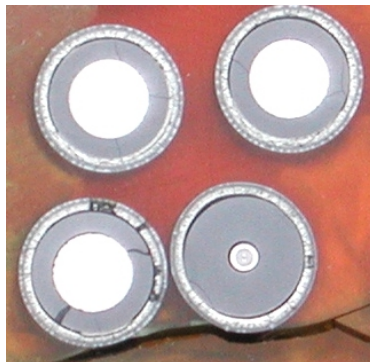
QUE-10-4 (735 mm, bottom)



QUE-10-4 (750 mm, top)



Detail 650 mm



Detail 750 mm

Fig. 57: QUENCH-10; Cross sections at 635 mm, 650 mm, 735 mm, and 750 mm (bottom views: mirror-inverted).



QUE-10-8 (800 mm, bottom)



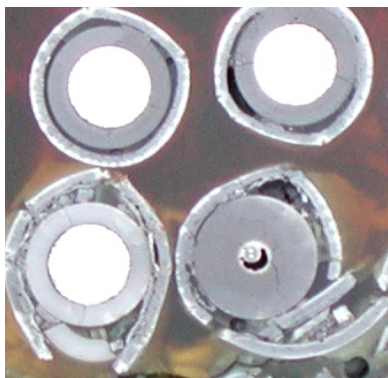
QUE-10-8 (833 mm, top)



QUE-10-5 (835 mm, bottom)



QUE-10-5 (850 mm, top)

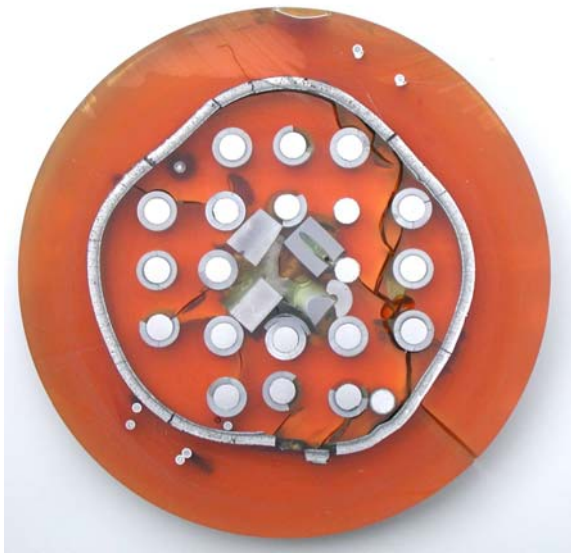


Detail 800 mm



Detail 850 mm

Fig. 58: QUENCH-10; Cross sections at 800 mm, 833 mm, 835 mm, and 850 mm (bottom views: mirror-inverted).



QUE-10-6 (937 mm, bottom)



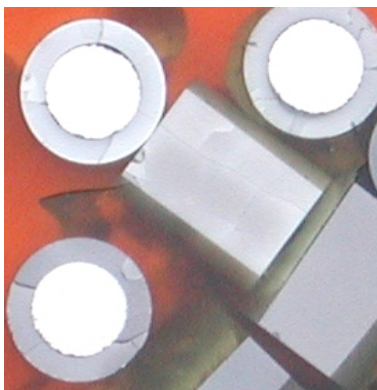
QUE-10-6 (950 mm, top)



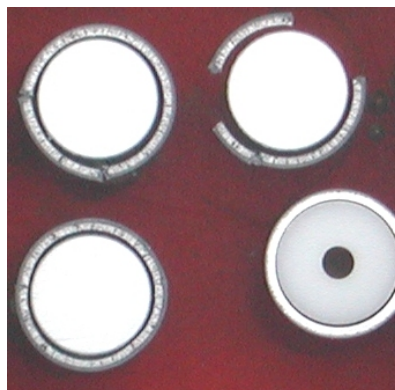
QUE-10-7 (1052 mm, bottom)



QUE-10-7 (1080 mm, top)



Detail 950 mm



Detail 1080 mm

Fig. 59: QUENCH-10; Cross sections at 937 mm, 950 mm, 1052 mm, and 1080 mm (bottom views: mirror-inverted).



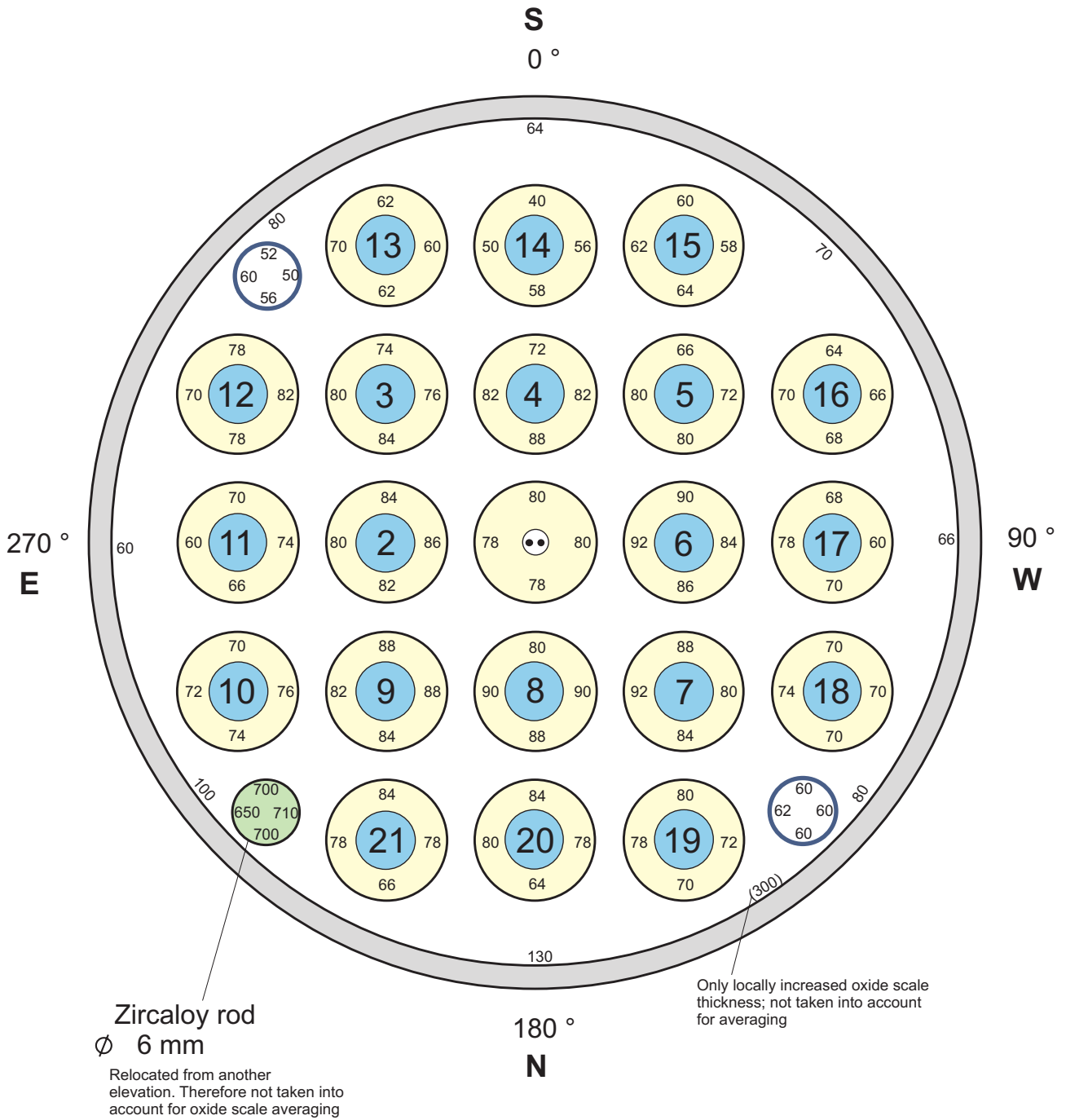


Fig. 61-QUE10 cross section 3.cdr  
09.02.06. - IMF

Fig. 61: QUENCH-10; Oxide layer thickness at bundle elevation 650 mm  
( Cross section QUE-10-3)

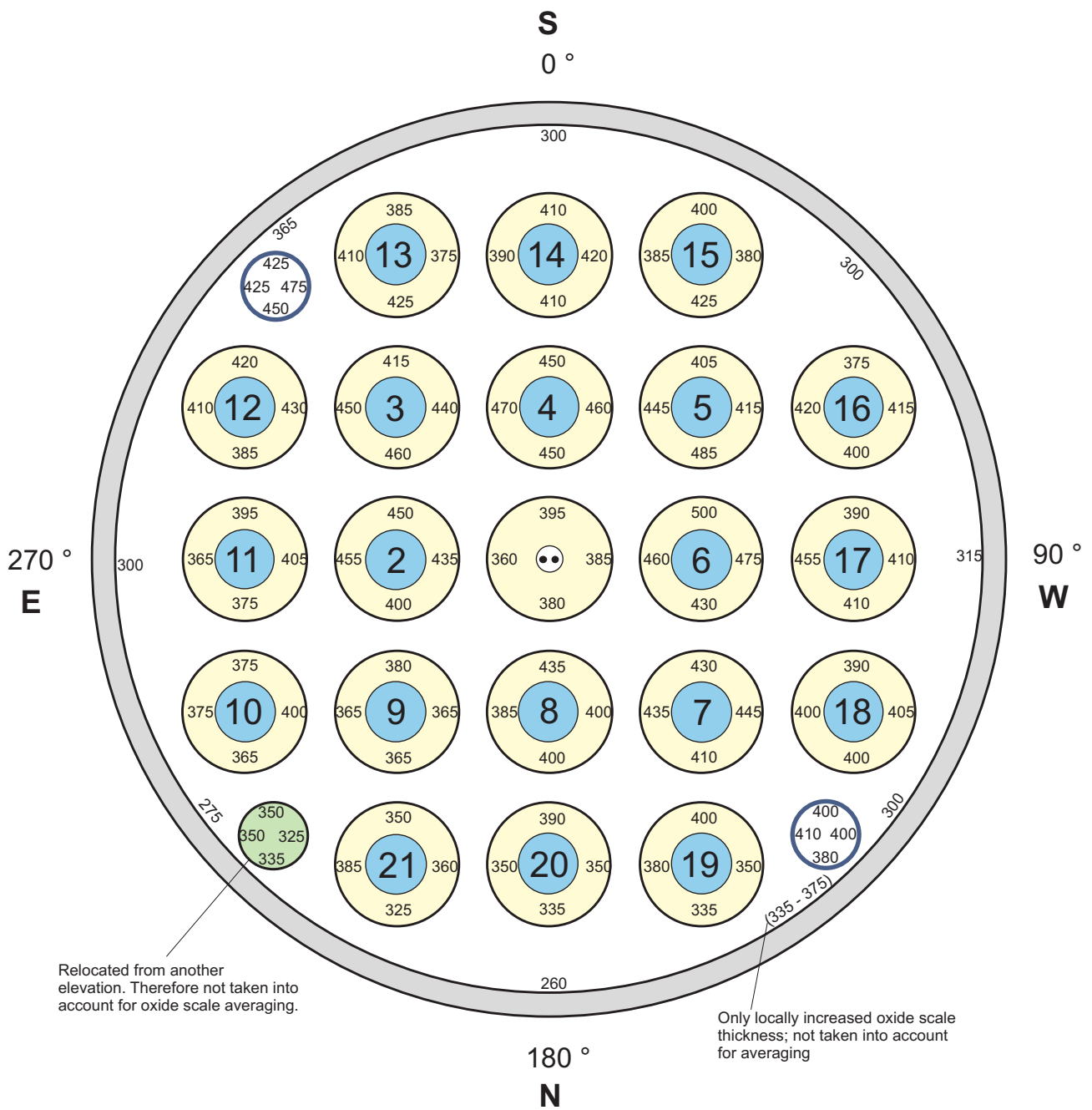


Fig. 62-QUE10 cross section 4.cdr  
09.02.06. - IMF

Fig. 62 : QUENCH-10; Oxide layer thickness at bundle elevation 750 mm  
( Cross section QUE-10-4)

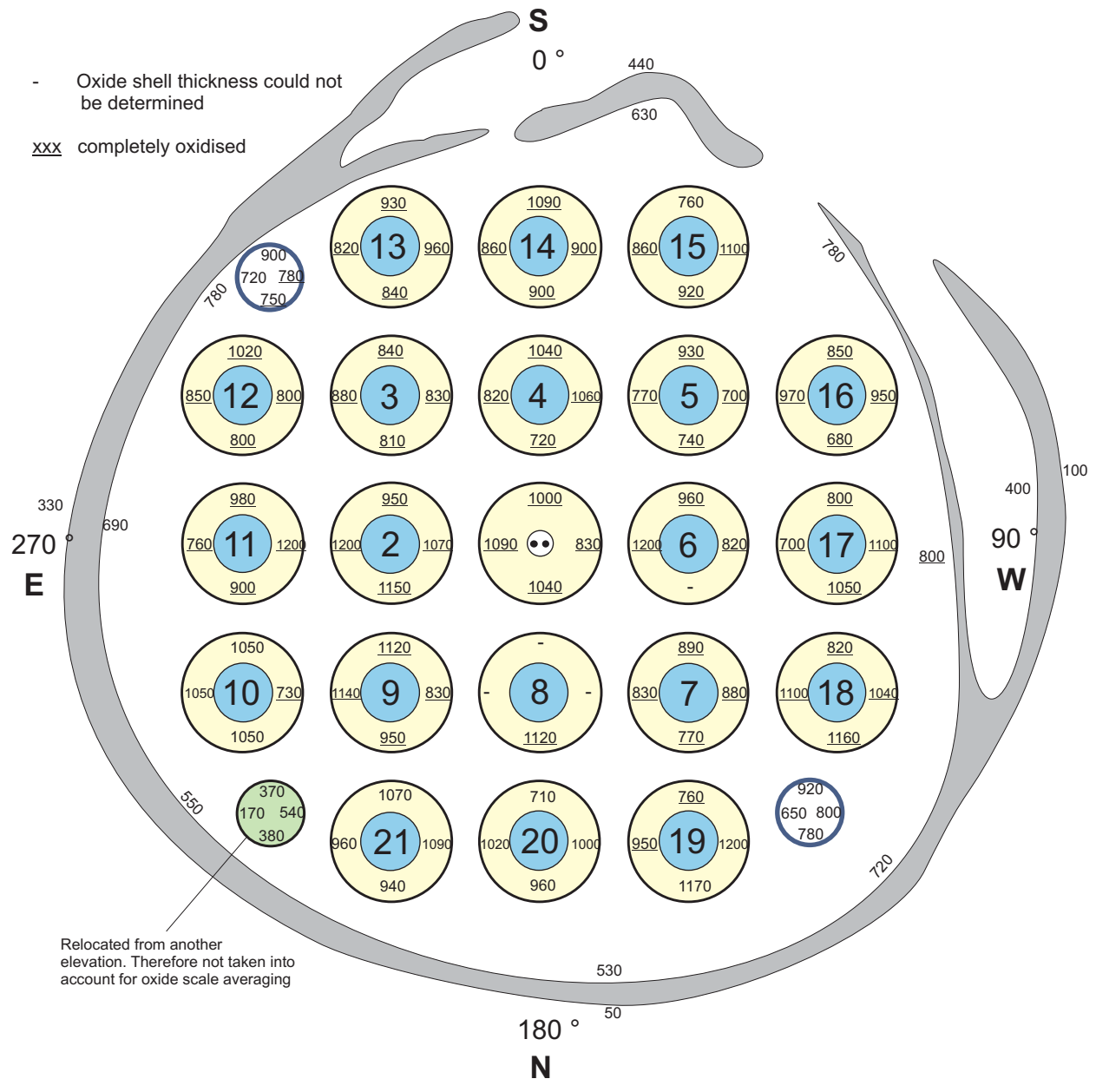


Fig. 63-QUE10 cross section 8.cdr  
09.02.06 - IMF

Fig. 63: QUENCH-10; Oxide layer thickness at bundle elevation 800 mm  
( Cross section QUE-10-8)

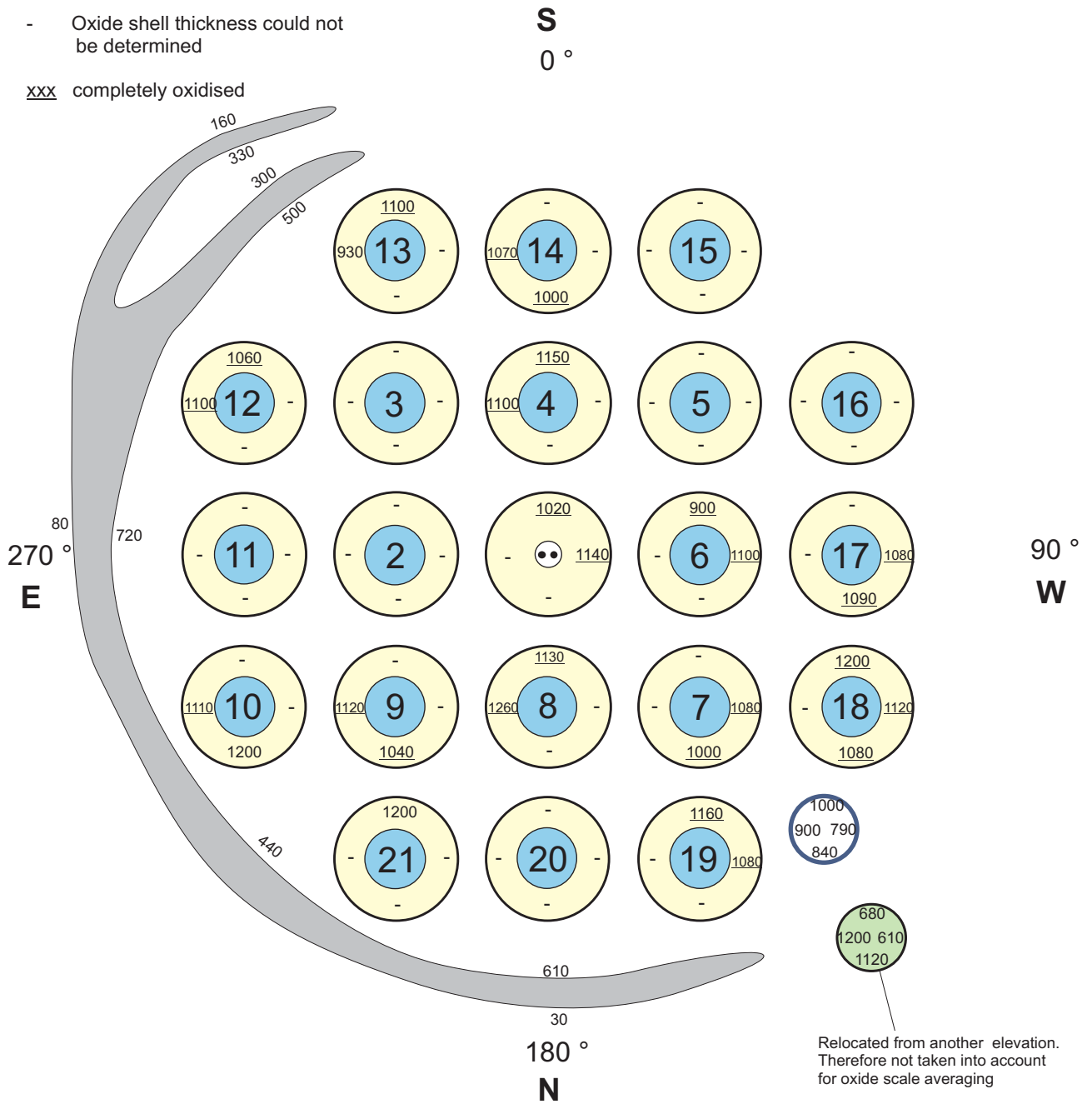


Fig. 64-QUE10 cross section 5.cdr  
09.02.06 - IMF

Fig. 64: QUENCH-10; Oxide layer thickness at bundle elevation 850 mm ( Cross section QUE-10-5)

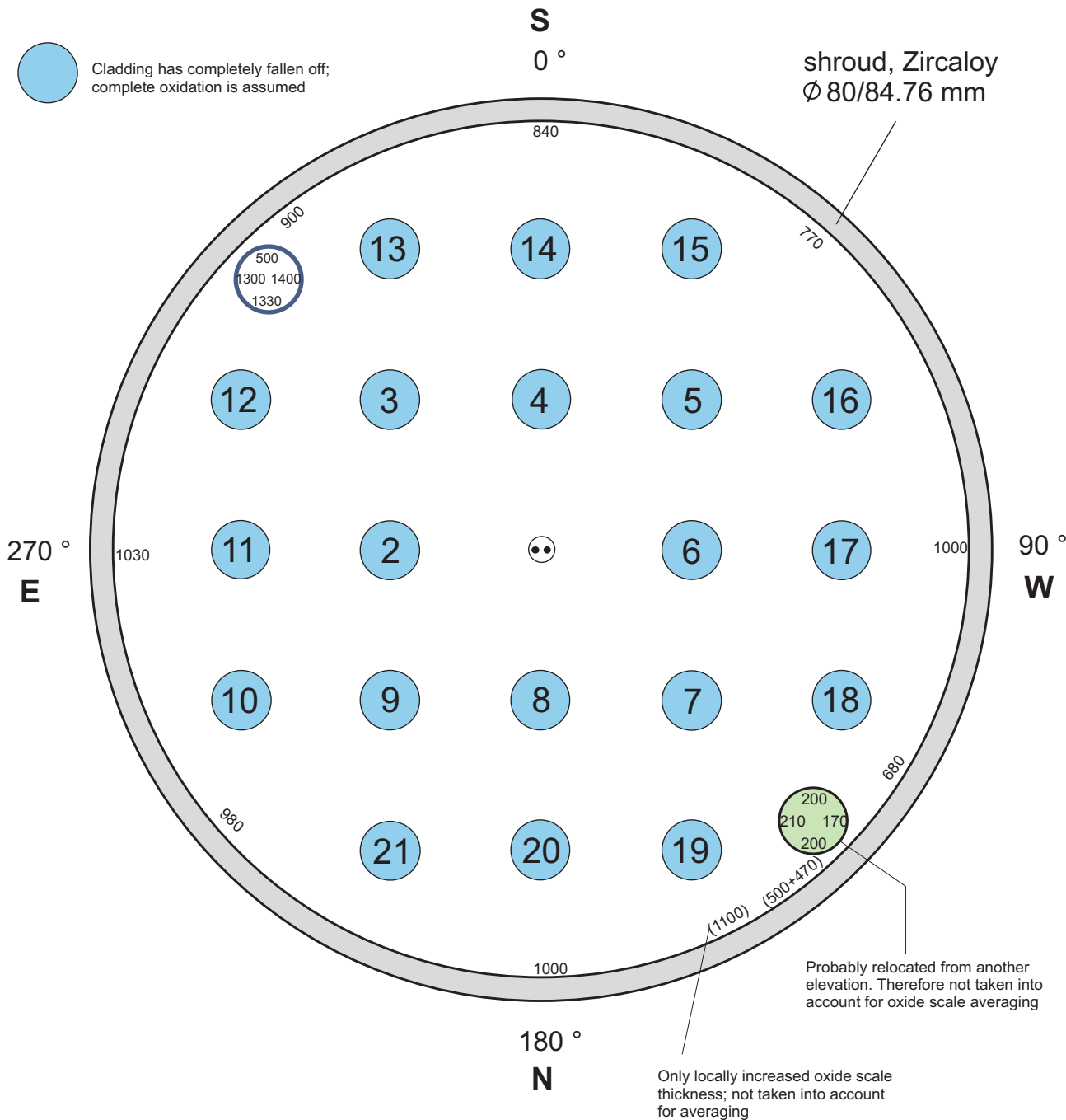


Fig. 65-QUE10 cross section 6.cdr  
 09.02.06 - IMF

Fig. 65 : QUENCH-10; Oxide layer thickness at bundle elevation 950 mm  
 ( Cross section QUE-10-6)

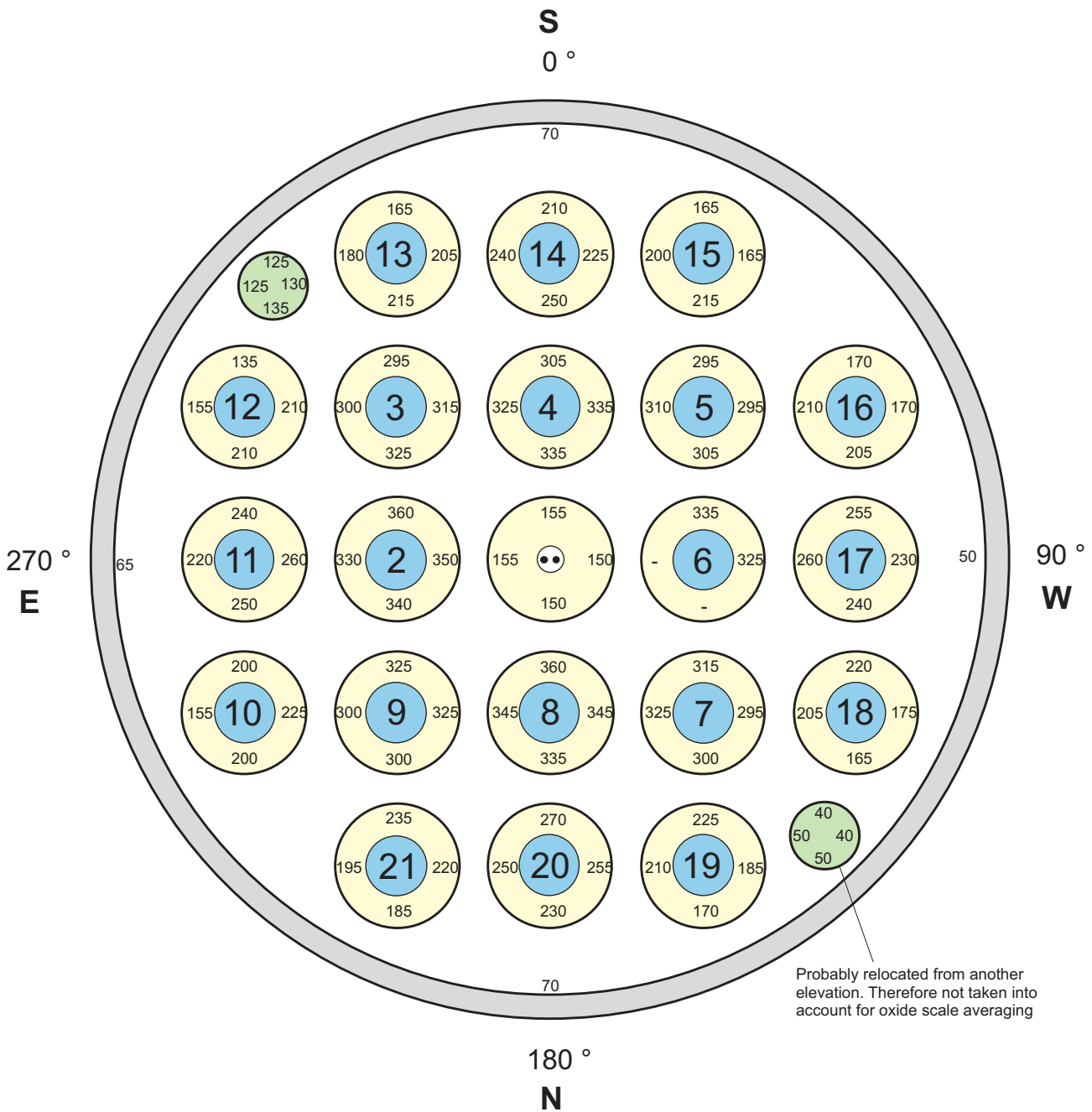


Fig. 66-QUE10 cross section 7.cdr  
09.02.06 - IMF

Fig. 66: QUENCH-10; Oxide layer thickness at bundle elevation 1080 mm ( Cross section QUE-10-7)

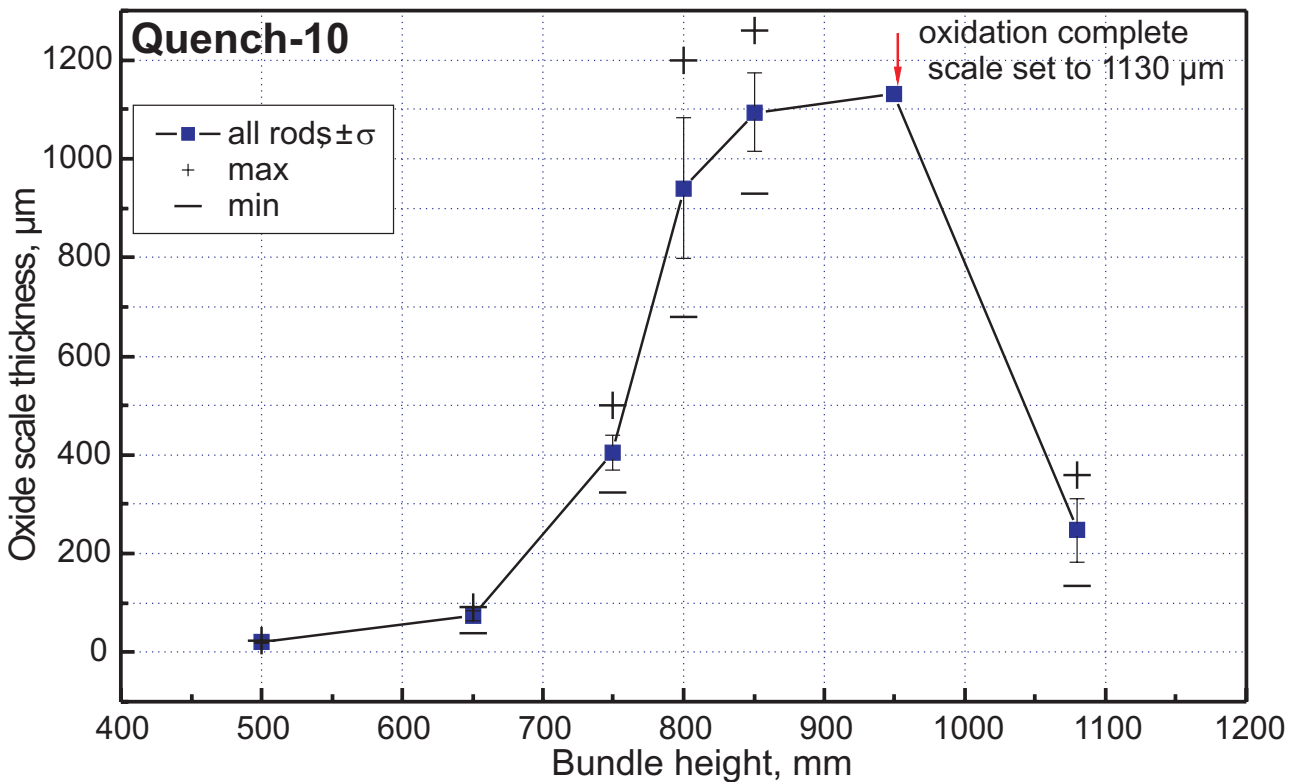
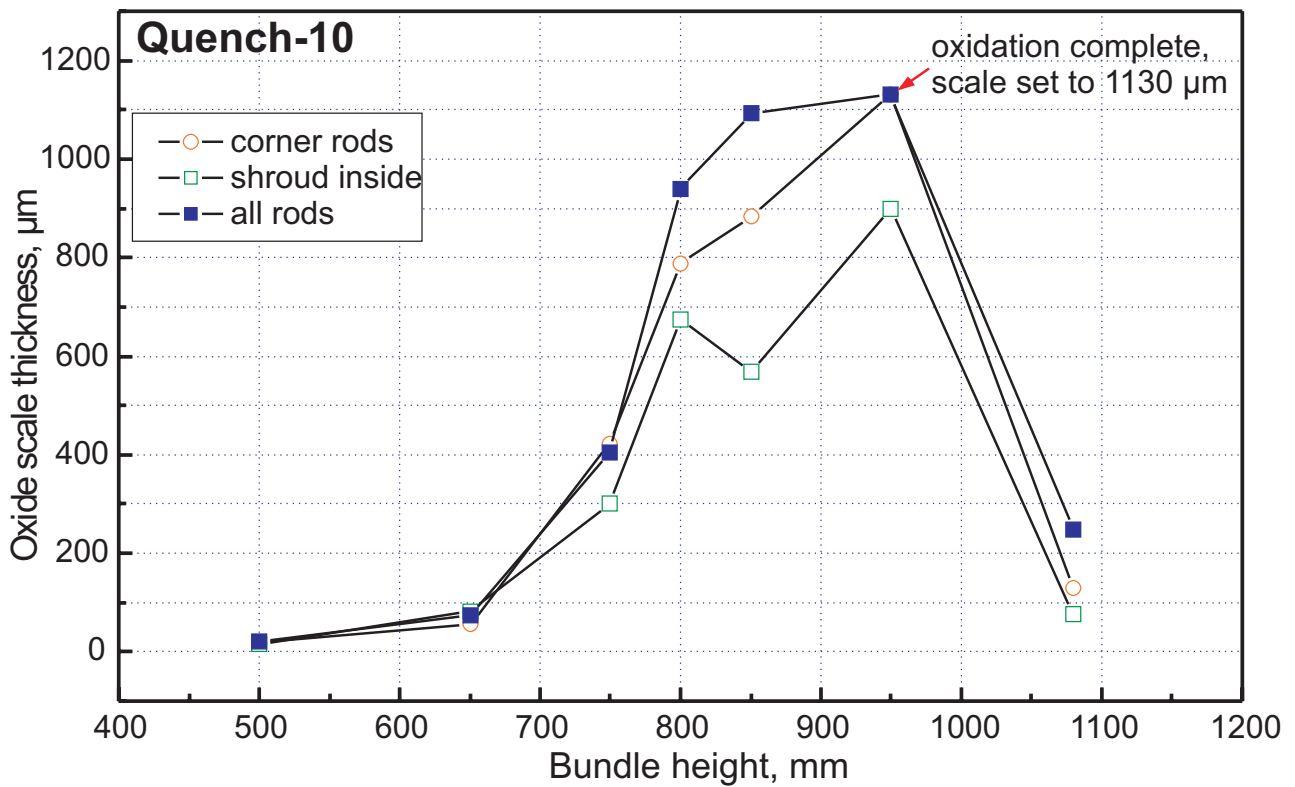
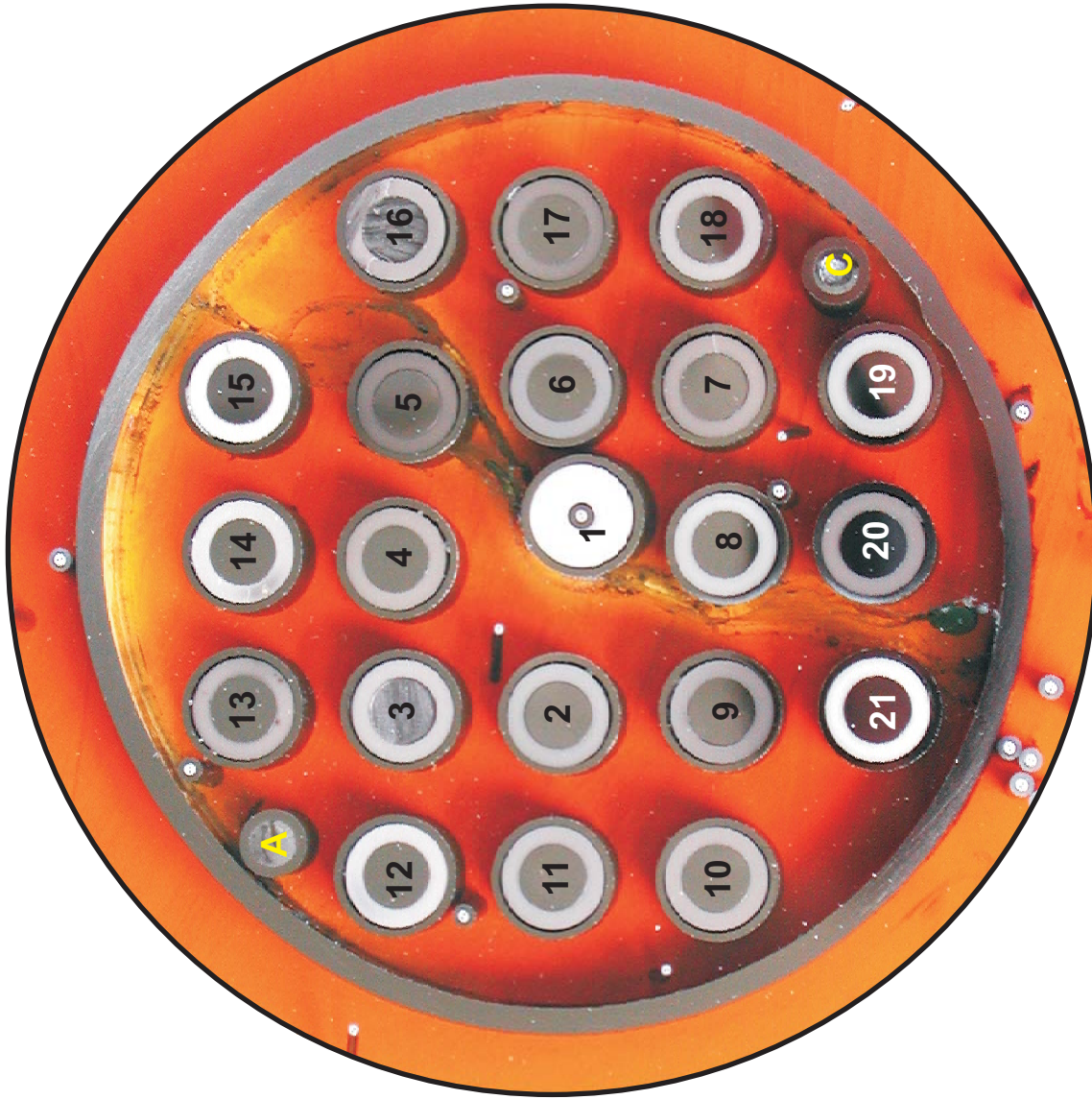


Fig. 67: QUENCH-10; axial profiles of oxide layer thickness, given as mean values for all bundle components (top), average and standard deviation for simulator rods (bottom).



Bottom of cross section slab, 635 mm elevation, inverted to top view

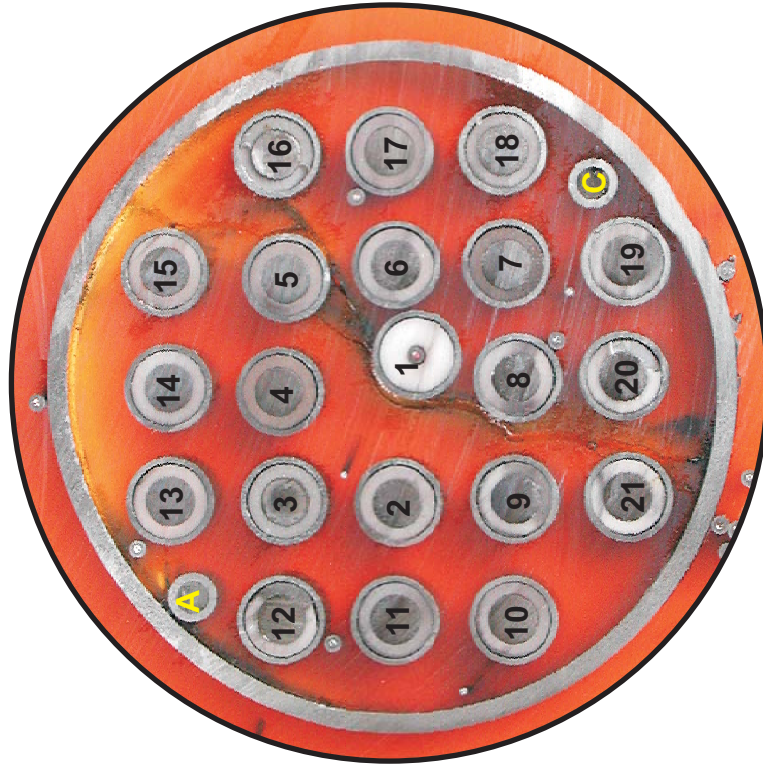
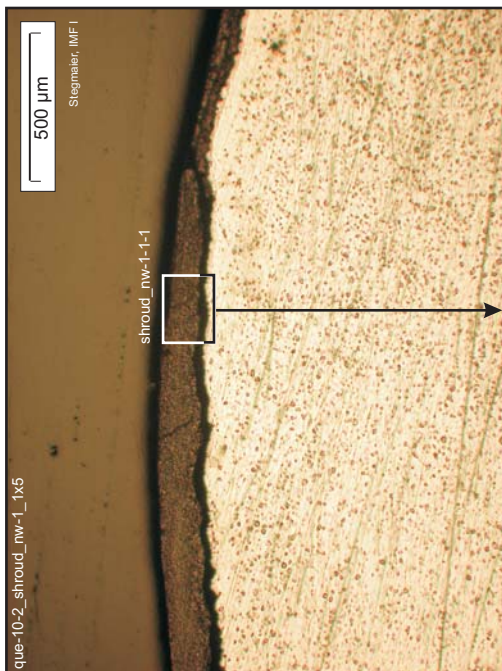


Fig. 68: QUENCH-10; Cross section at 500 mm bundle elevation (QUE-10-2); overview from top.



Positions within the axial shroud weld

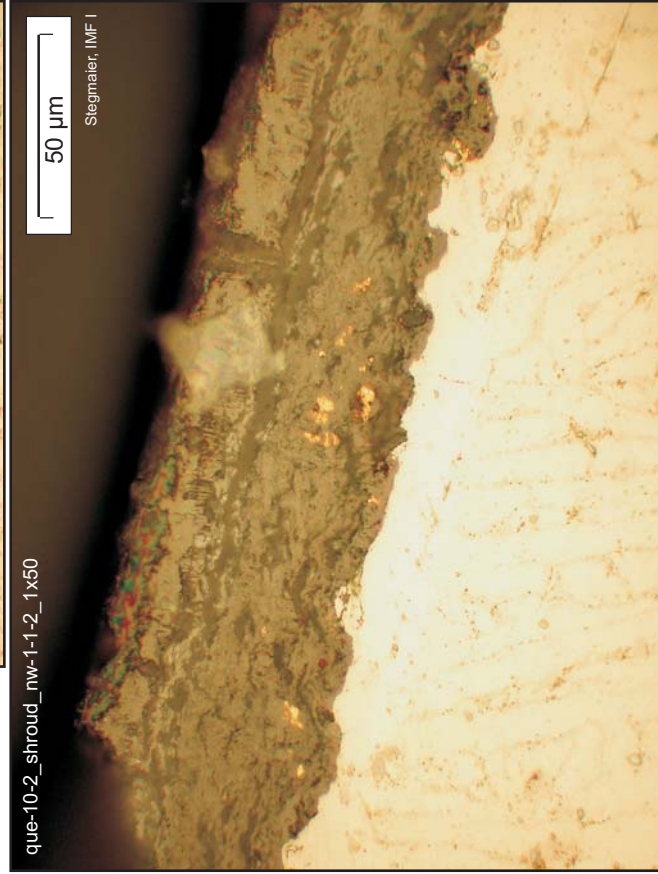
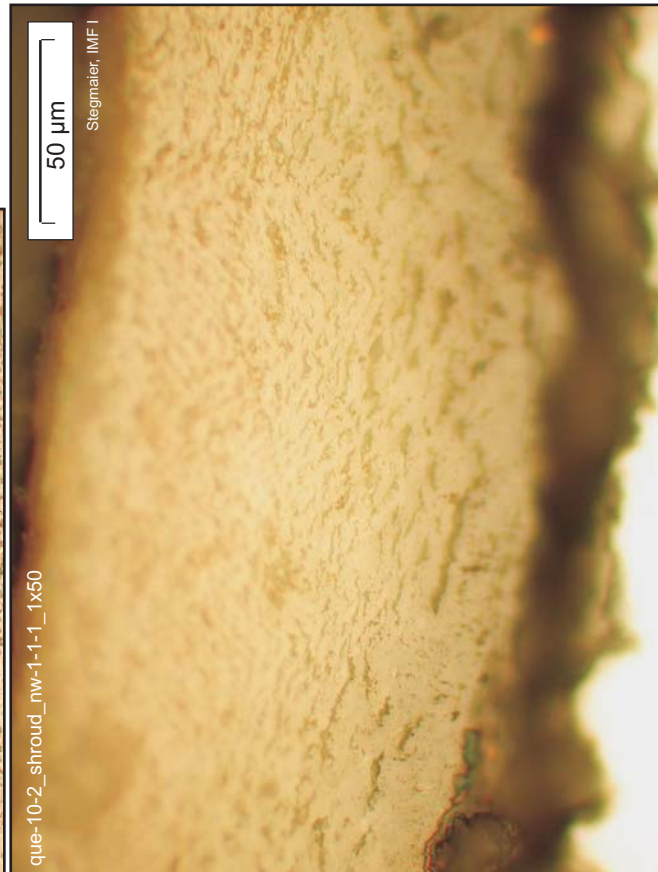
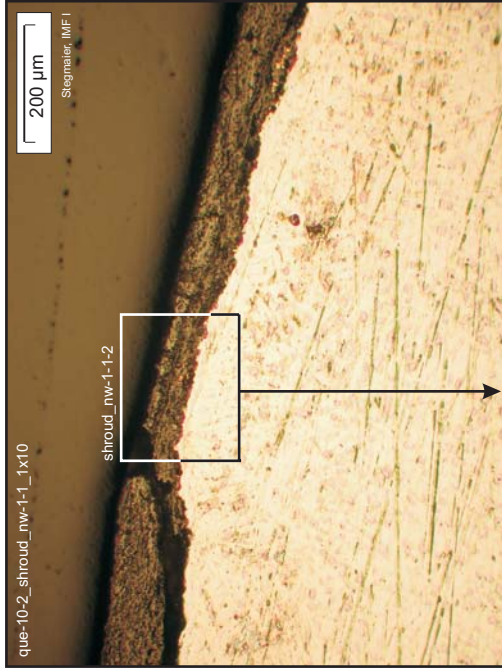


Fig. 69: QUENCH-10; Cross section at 500 μm (QUE-10-2); internal shroud scale at NW, showing post-transitional crack system formation and some embedded zirconium nitride phase (bottom, right).

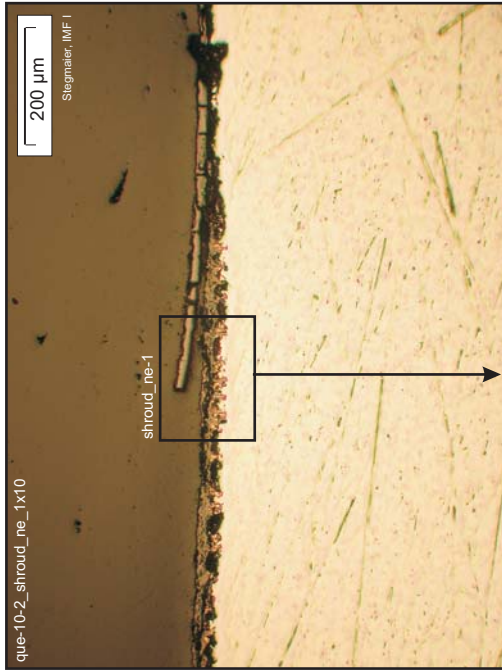
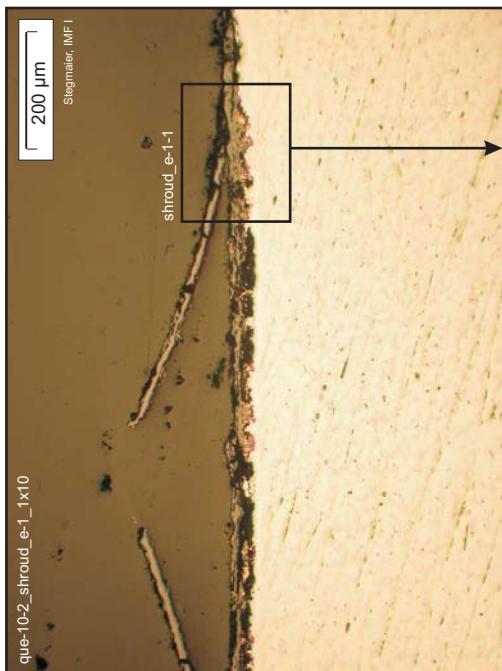


Fig. 70: QUENCH-10; Cross section at 500 mm (QUE-10-2), inner shroud scale at E and NE: Top-layer spalling (initiated by scratches), sub-layers cracking, and zirconia / zirconium nitride penetration.

Bottom of cross section slab, 635 mm elevation, inverted to top view

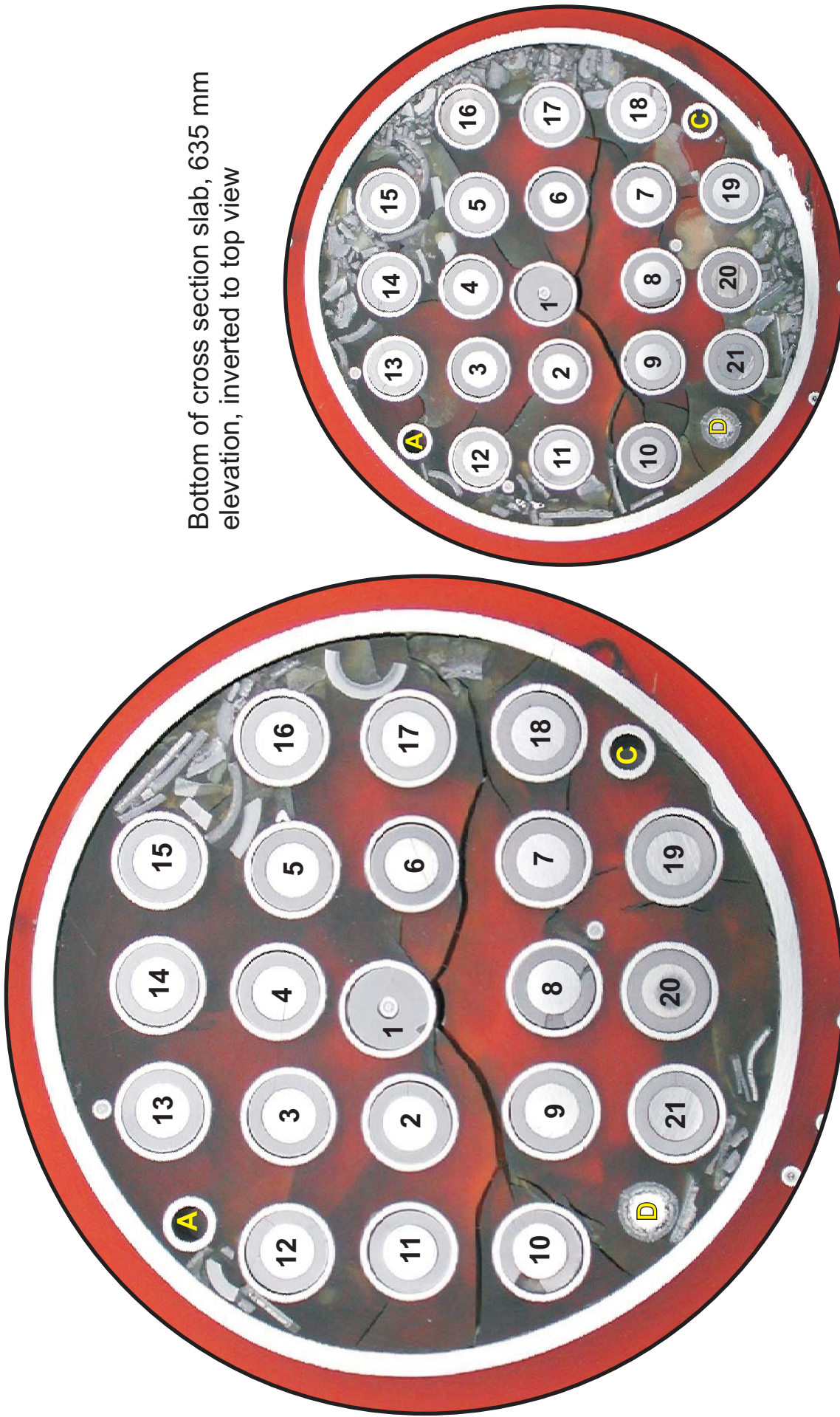


Fig. 71: QUENCH-10; Cross section at 650 mm bundle elevation (QUE-10-3); overview from top.

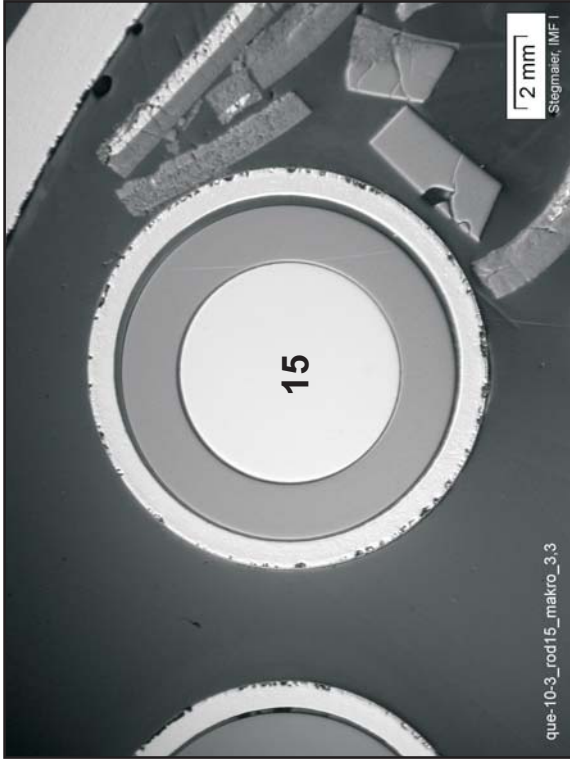
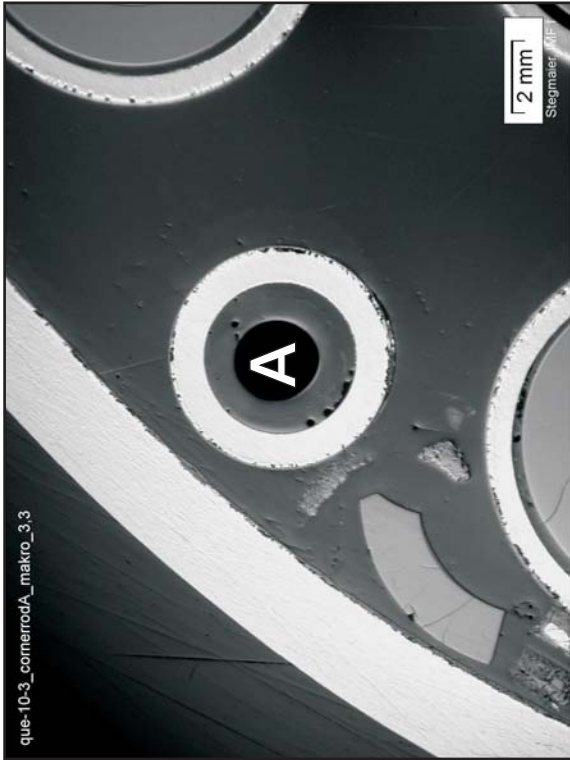


Fig. 72: QUENCH-10; Cross section at 650 mm bundle elevation (QUE-10-3). Macrographs from bundle periphery, showing rod simulators 15 and 21, corner rods A, C, D, shroud, and rubble.

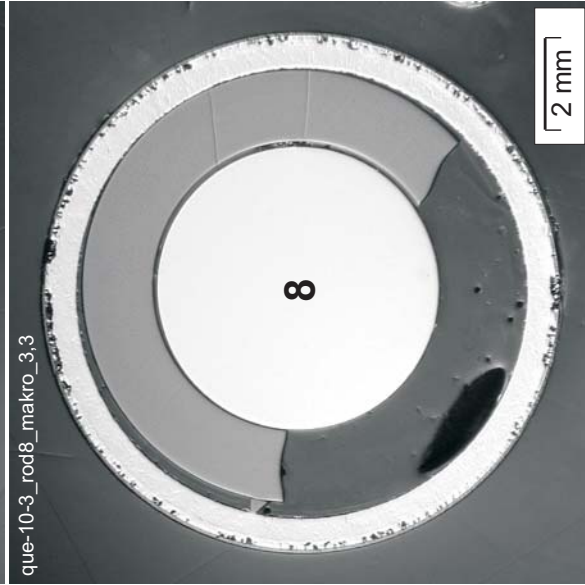


Fig. 73: QUENCH-10; Cross section at 650 mm bundle elevation (QUE-10-3). Macrographs of some rod simulators of the first ring.

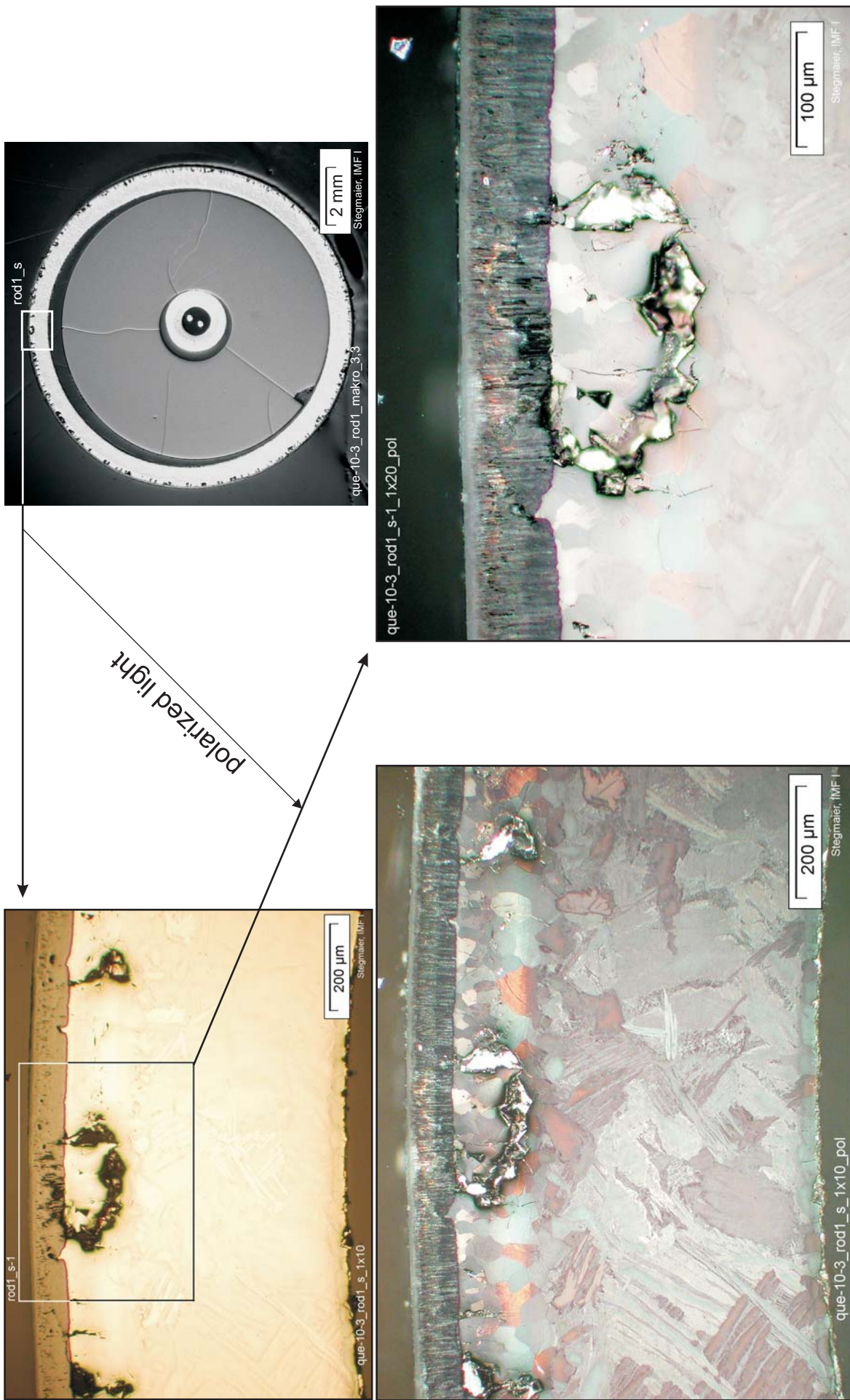


Fig. 74: QUENCH-10; Cross section at 650 mm bundle elevation (QUE-10-3), central rod cladding: Scale with pre-transition morphology, and thick  $\alpha$ -Zr(O) sub-layer which shows some fracturing.

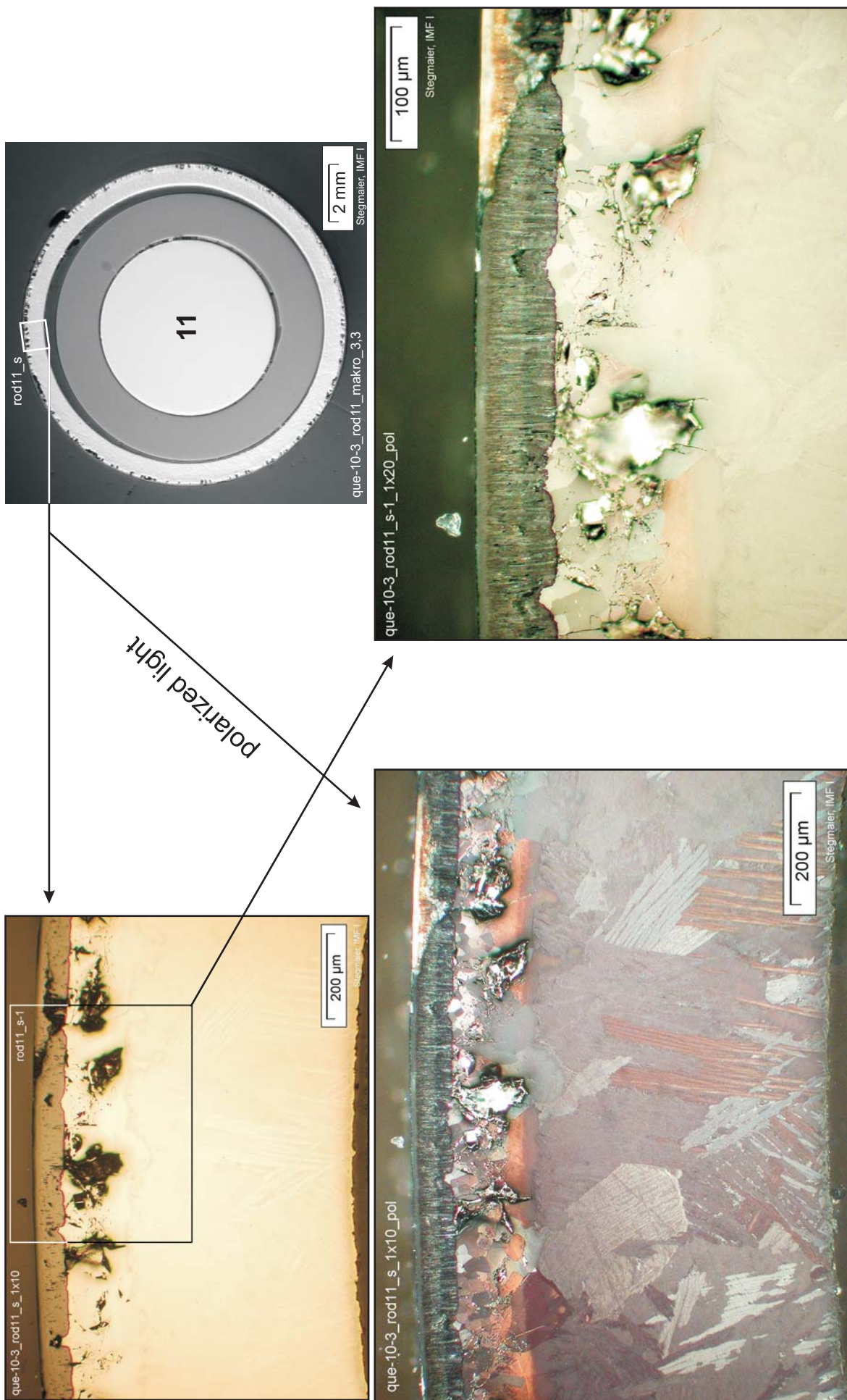


Fig. 75: QUENCH-10; Cross section at 650 mm bundle elevation (QUE-10-3), cladding of rod 11: Scale with pretransition morphology and thick  $\alpha$ -Zr(O) sub-layer, both showing some fracturing.

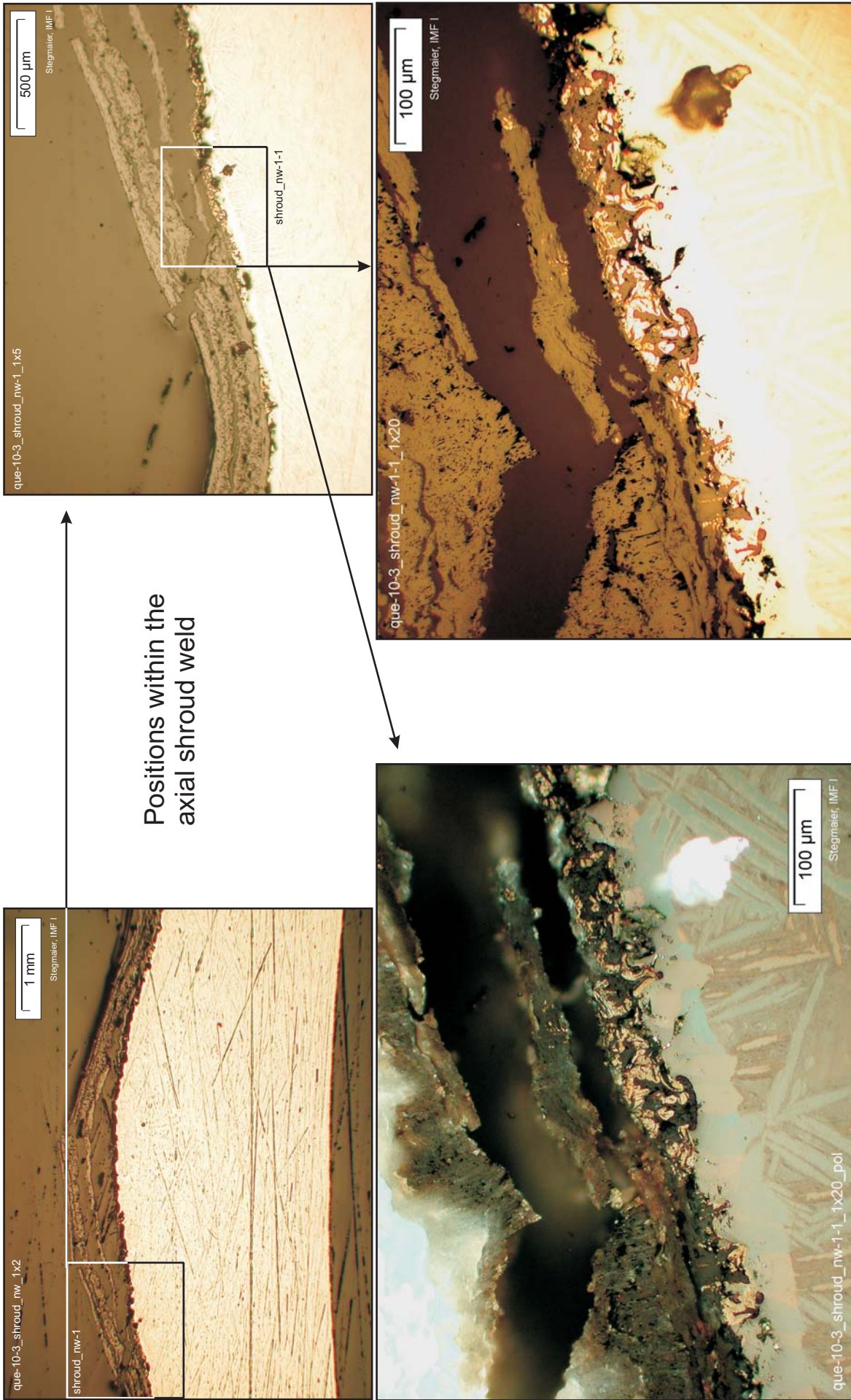
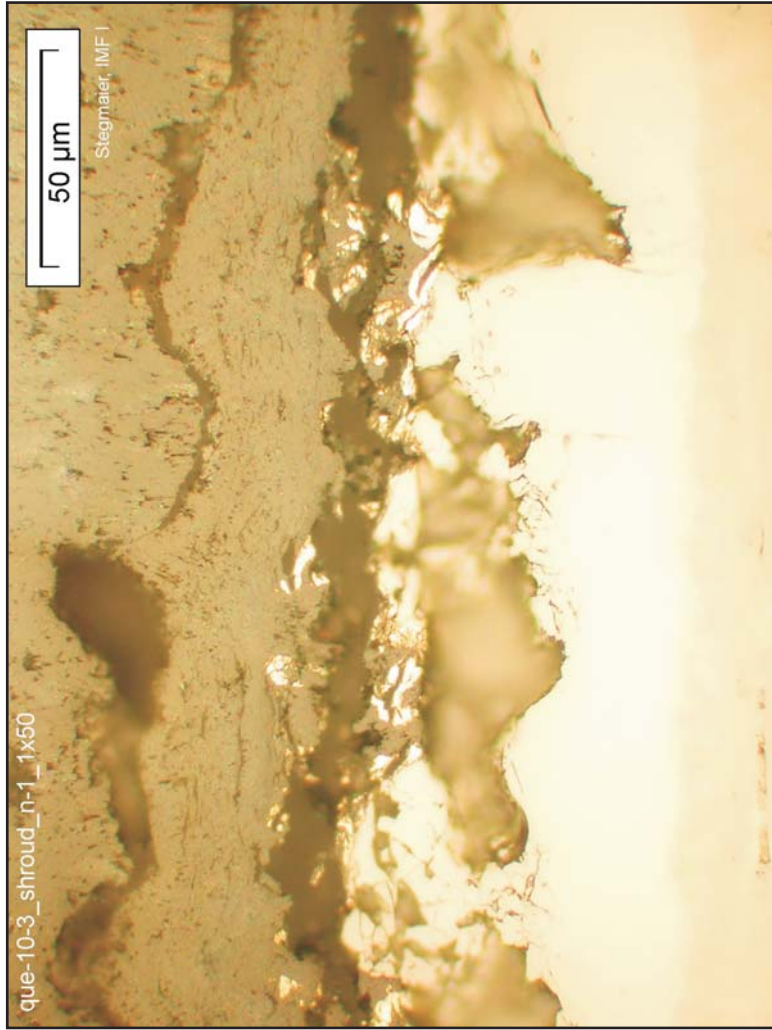
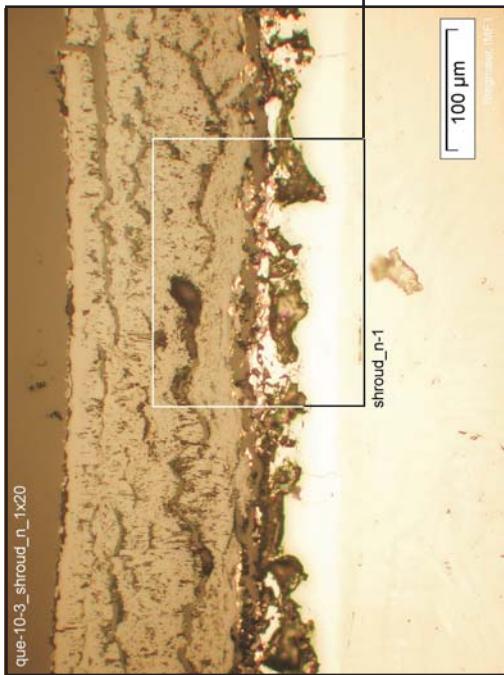
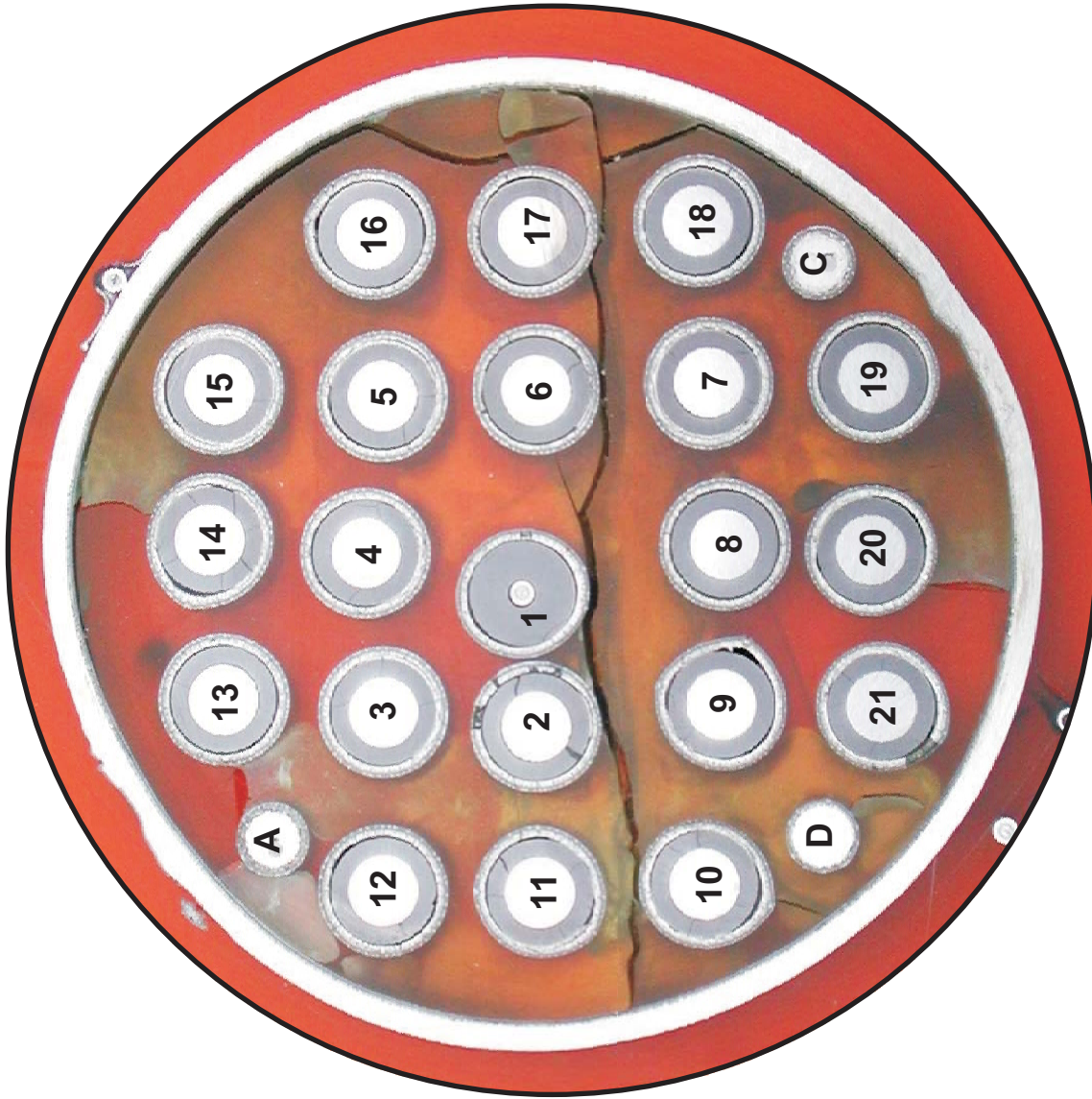


Fig. 76: QUENCH-10; Cross section at 650 mm bundle elevation (QUE-10-3), shroud, inner scale at NW: Cracked and partially spalled sub-layers, and innermost sub-layer of zirconia / zirconium nitride.



Polarized light illumination,  
 same depicted area as bright-  
 field micrograph at top, left

Fig. 77: QUENCH-10; Cross section at 650 mm (QUE-10-3), shroud, internal post-transition scale at N. Inner sub-layer with ZrN (top, right), scattering of polarized light indicates scale degradation (bottom, left).



Bottom of cross section slab, 735 mm elevation, inverted to top view

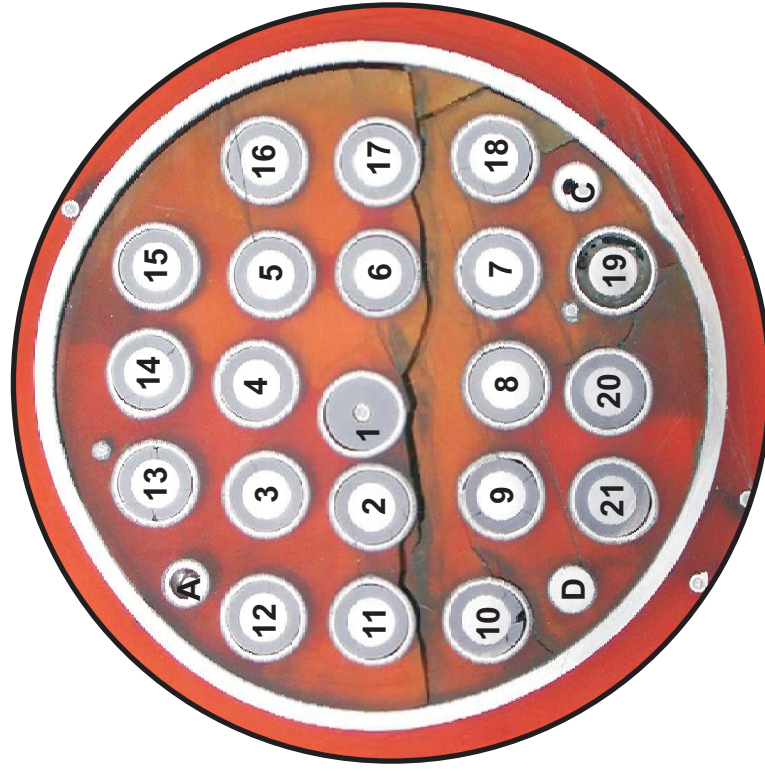


Fig. 78: QUENCH-10; Cross section at 750 mm bundle elevation (QUE-10-4); overview from top.

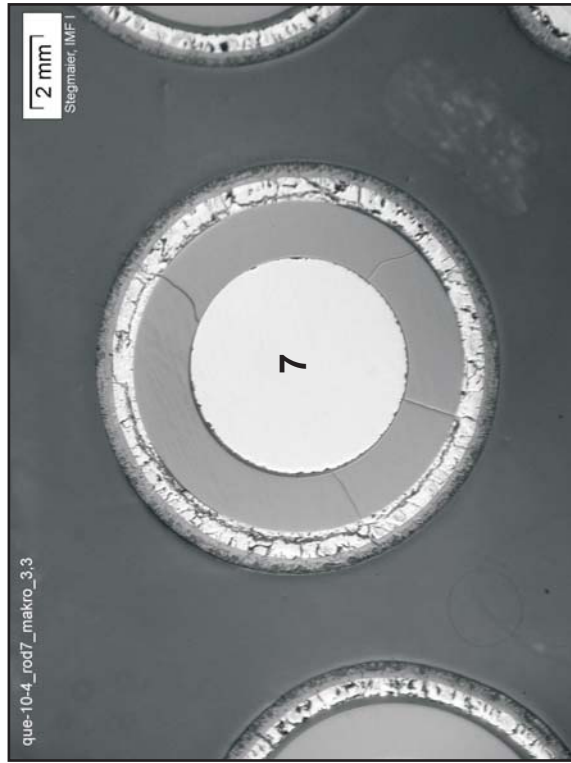
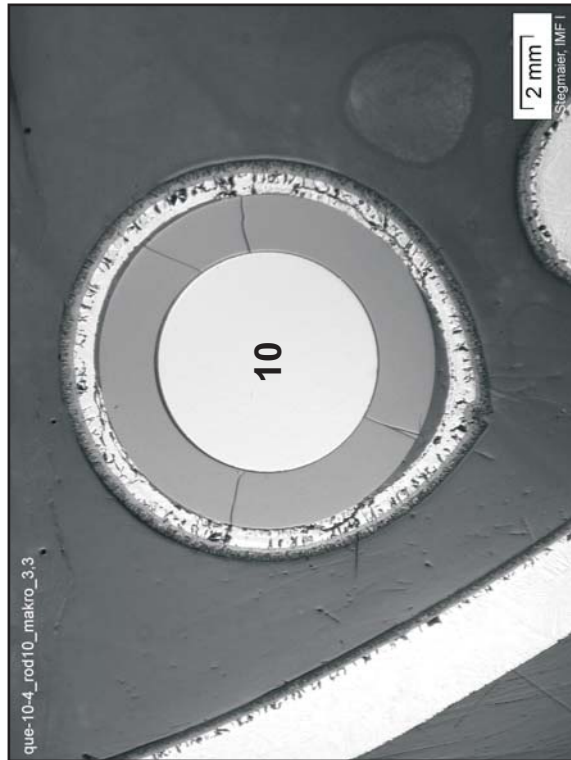
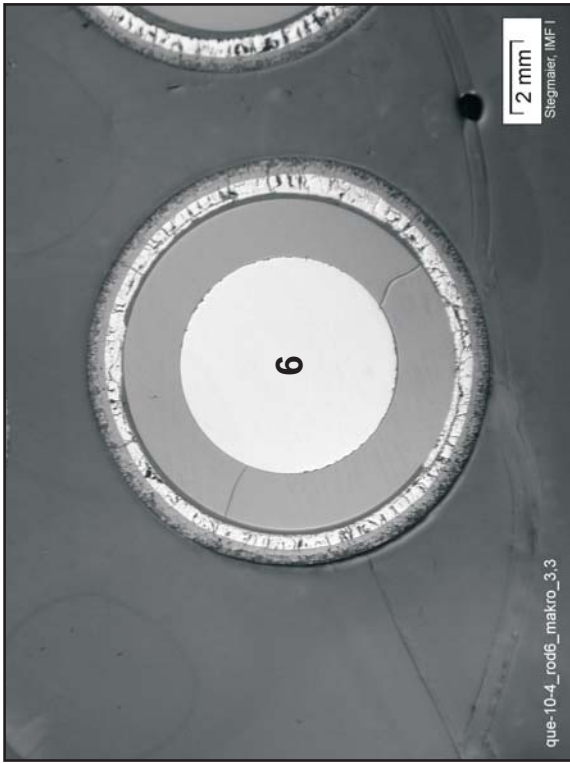
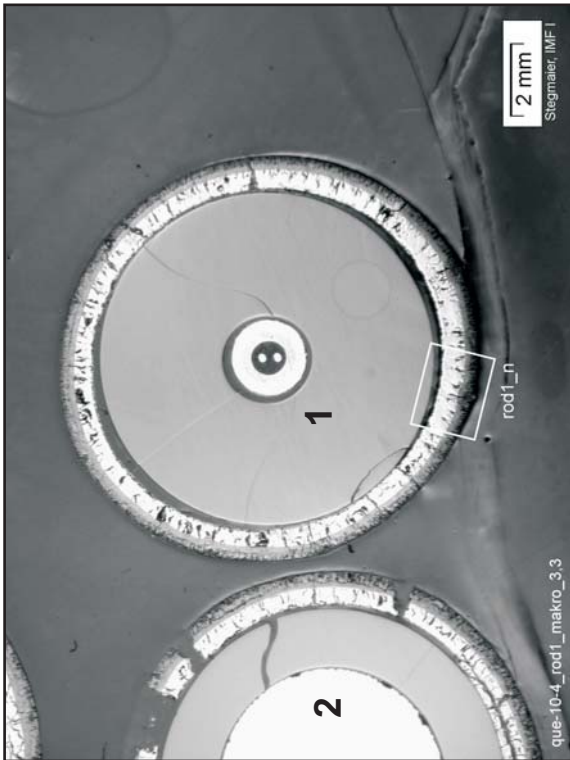
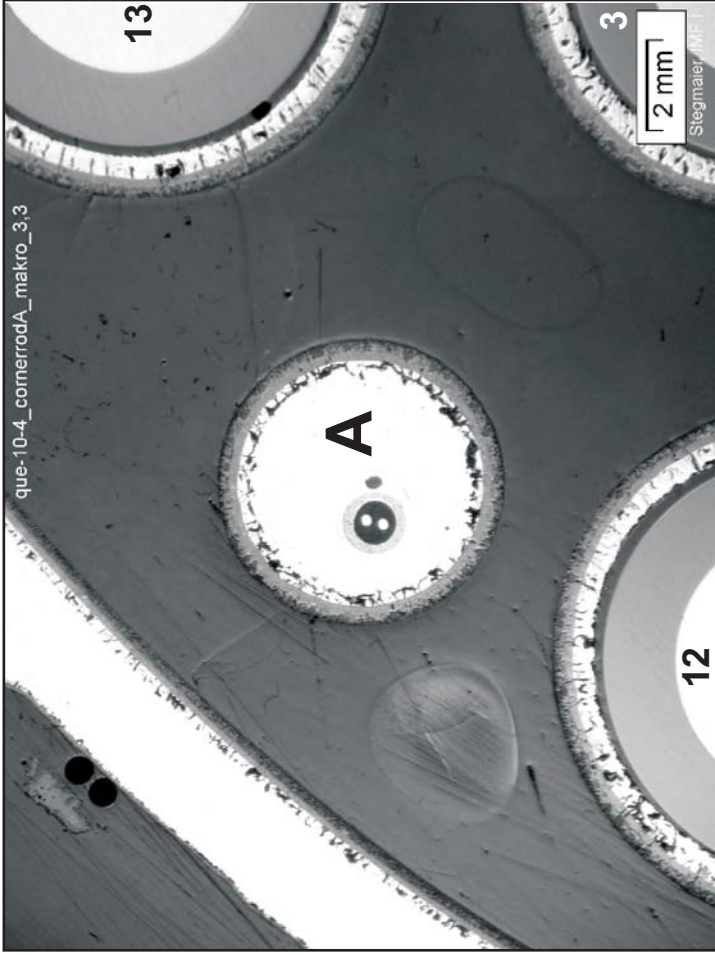


Fig. 79: QUENCH-10; Cross section at 750 mm bundle elevation (QUE-10-4). Macrographs of selected rods, showing typical partial cladding oxidation and different extent of pellet contact.



Bundle corner towards NW



Bundle corner towards SE

Fig. 80: QUENCH-10; Cross section at 750 mm bundle elevation (QUE-10-4). Macrographs of corner rods A and C, showing filling of instrumented tubular section by internally relocated melt.

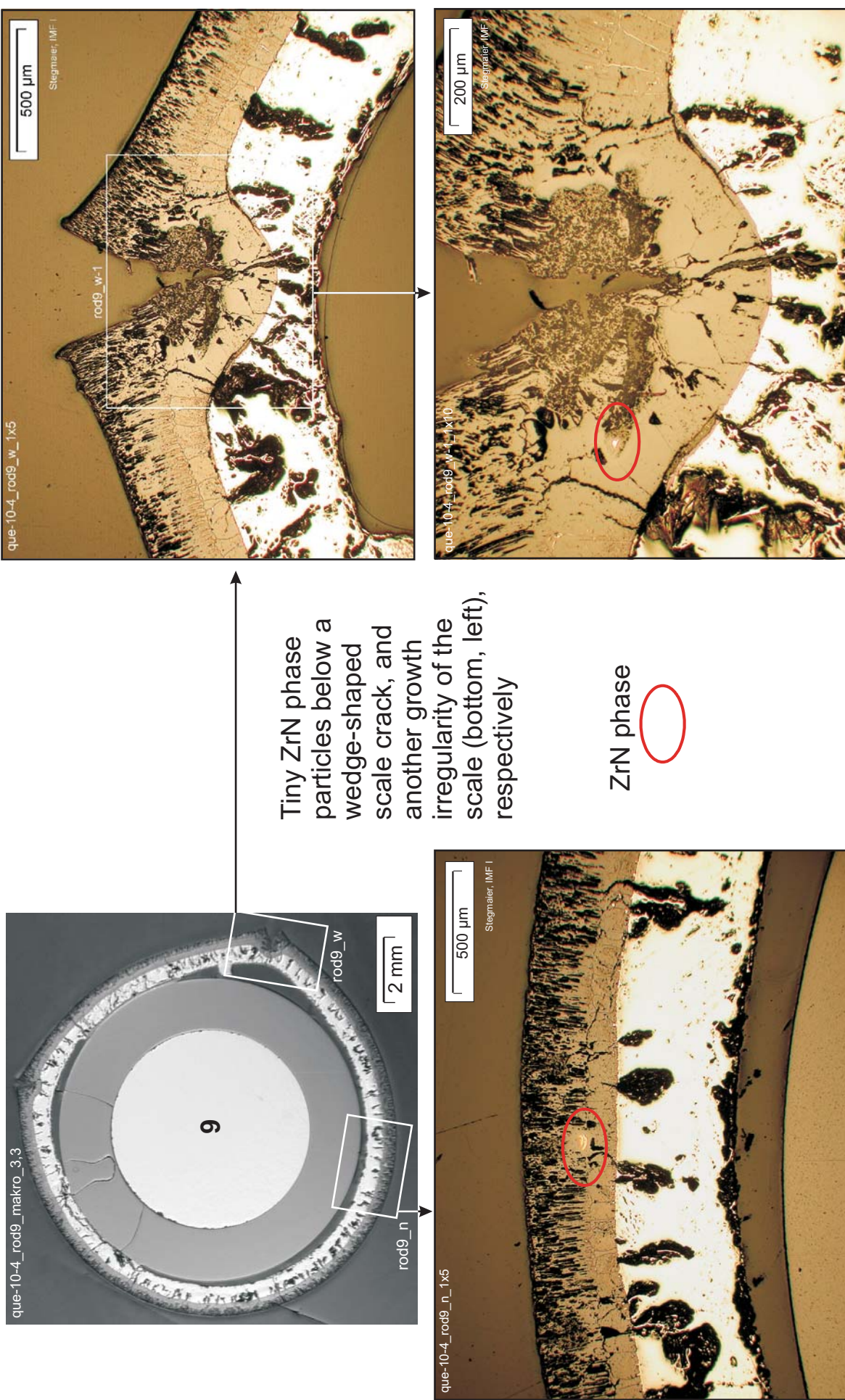


Fig. 81: QUENCH-10; Cross section at 750 mm bundle elevation (QUE-10-4). Details of cladding oxidation of rod 9 at two positions, where some nitrogen penetration took place.

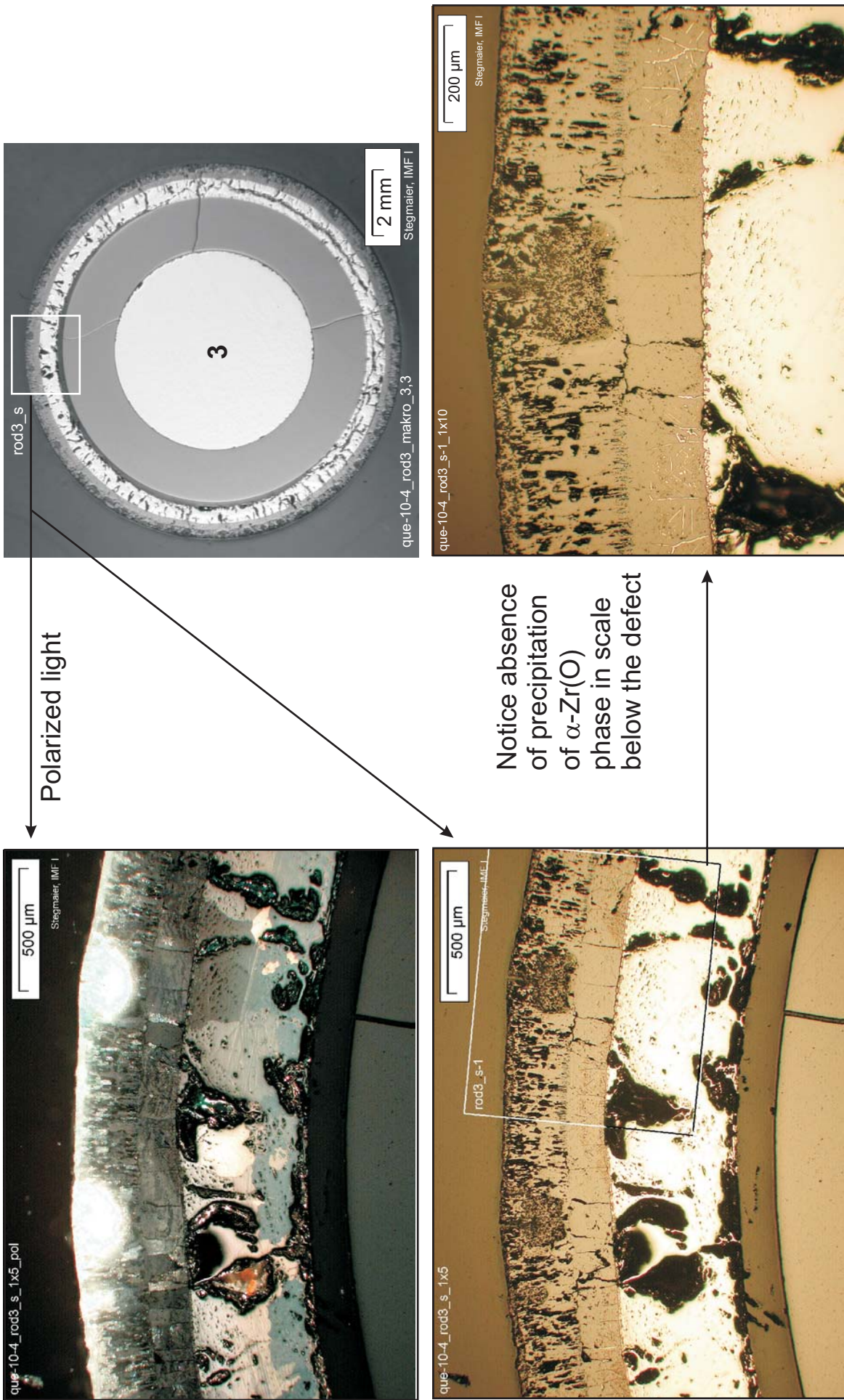
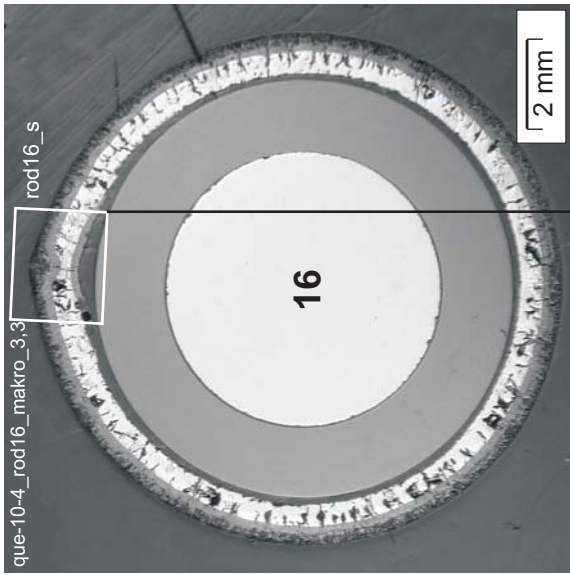


Fig. 82: QUENCH-10; Cross section at 750 mm bundle elevation (QUE-10-4). Details of cladding oxidation of rod 3, illustrating local cladding scale defects and related growth morphology.



Wedge-shaped crack and internal scale

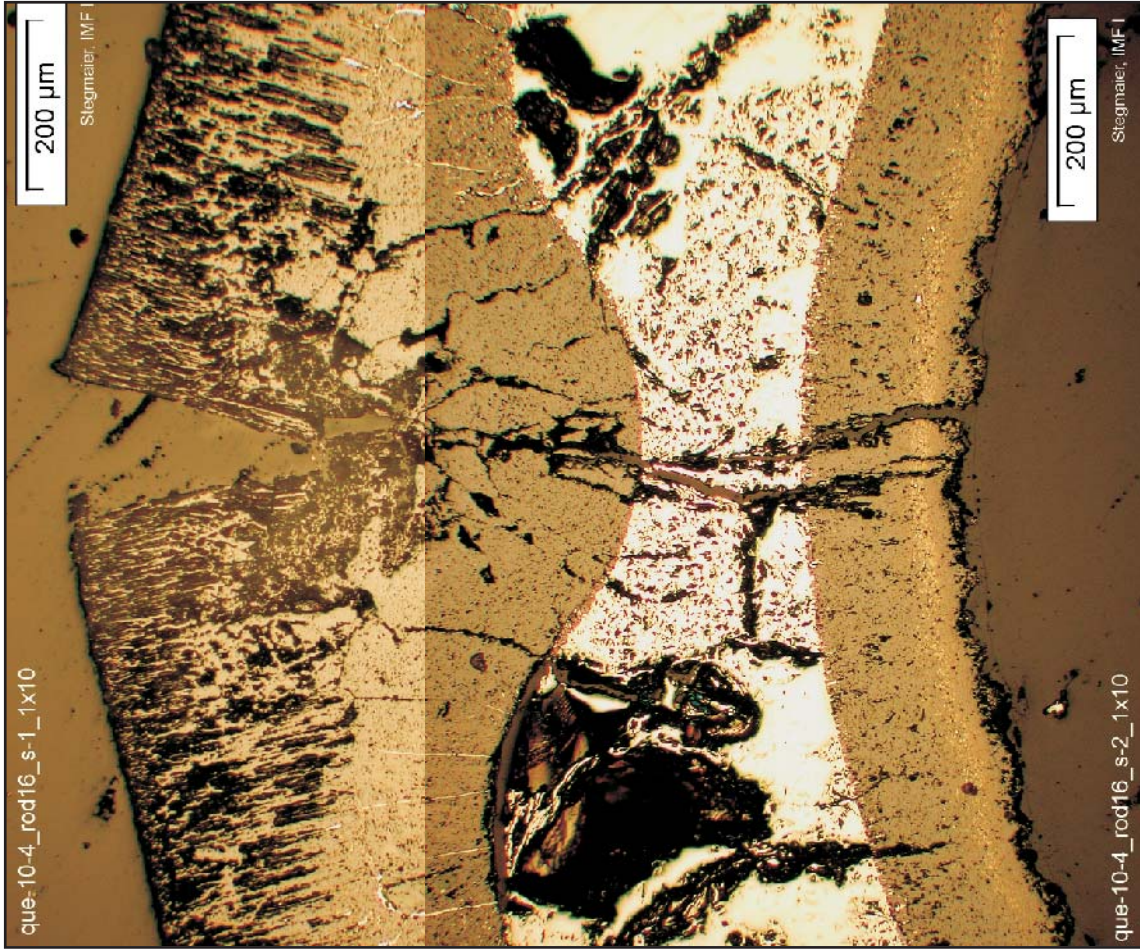
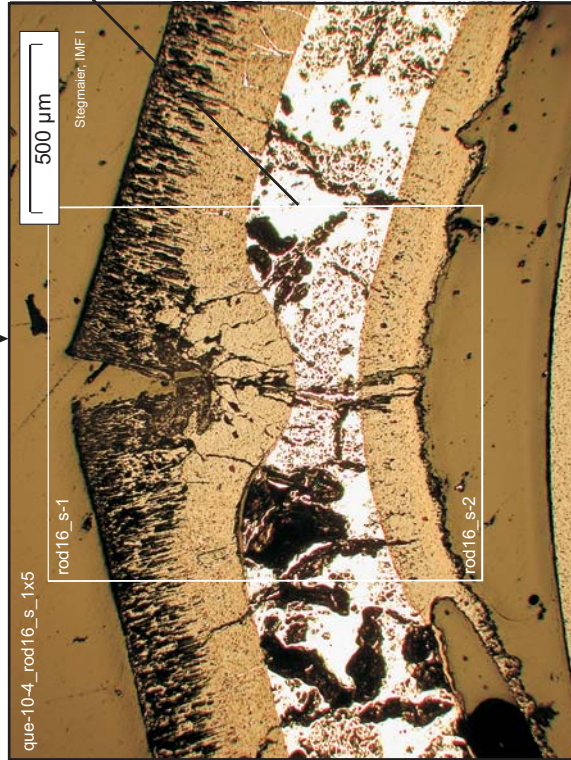
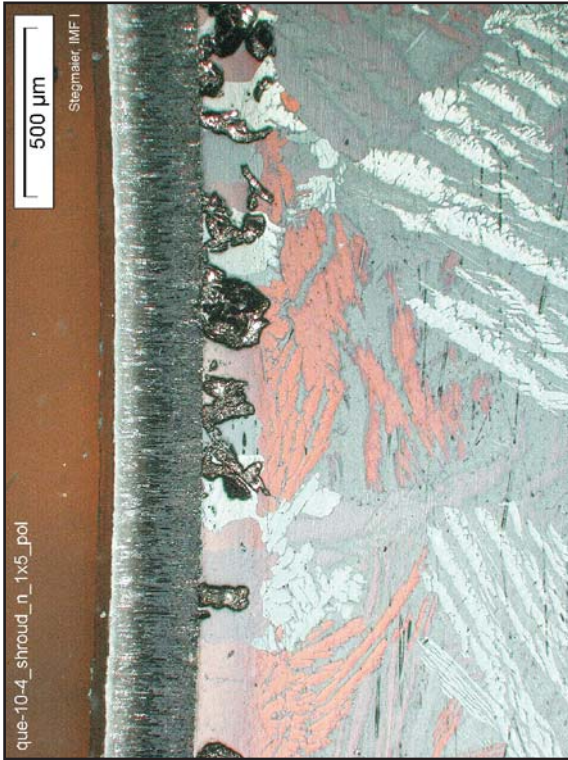
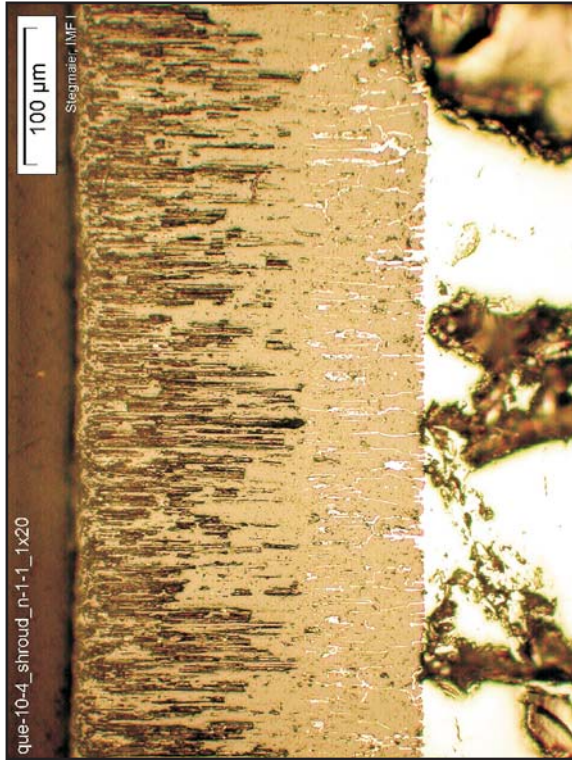


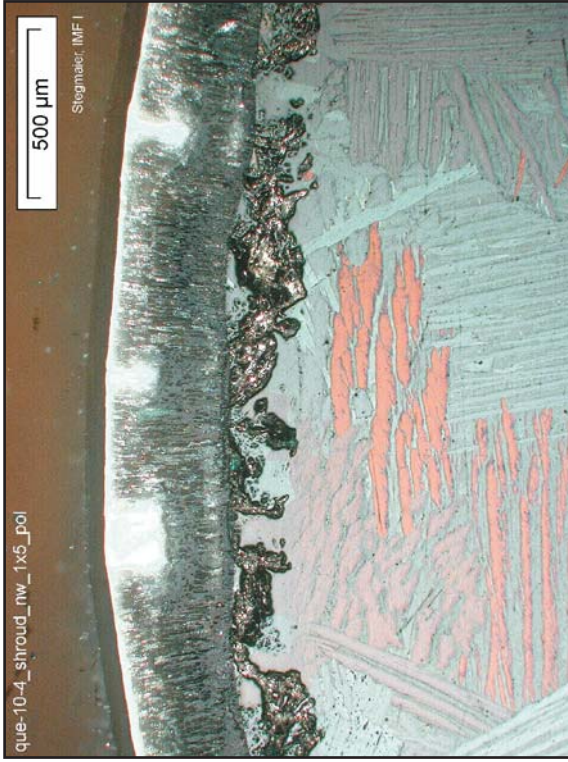
Fig. 83: QUENCH-10; Cross section at 750 mm (QUE-10-4). Cladding of rod 16, showing presence of an inner scale, possibly formed during steam/air ingress through an axially elongated scale crack.



Shroud towards NW, at position NW, at position of weld, non-typical scale



Shroud towards N, typical scale



Note absence of precipitates of  $\alpha$ -Zr(O) phase in scale below defect

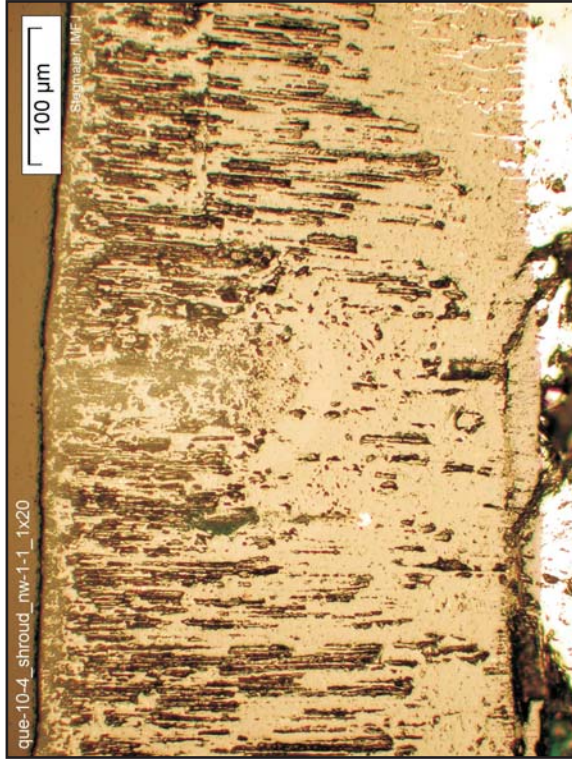
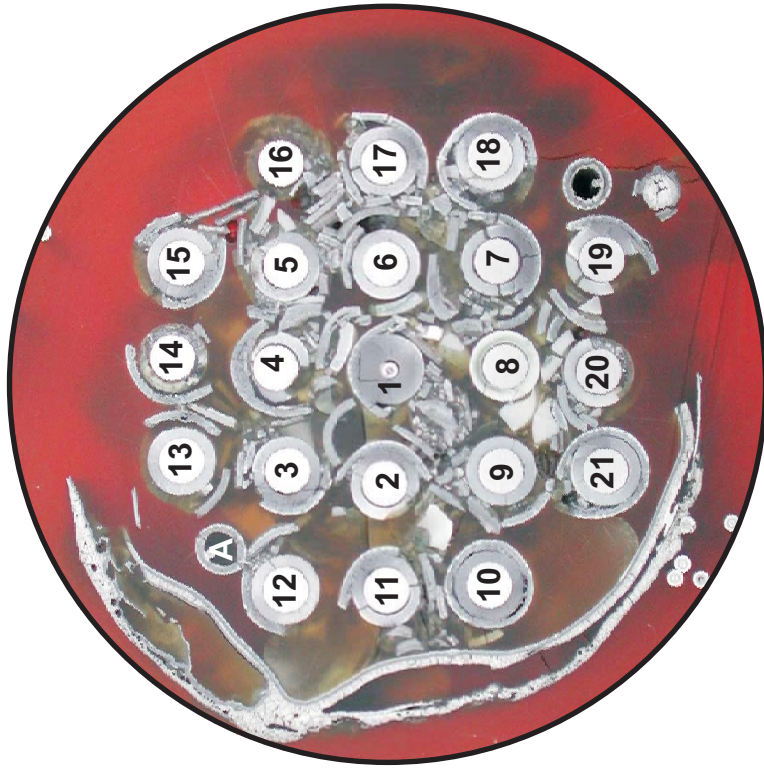
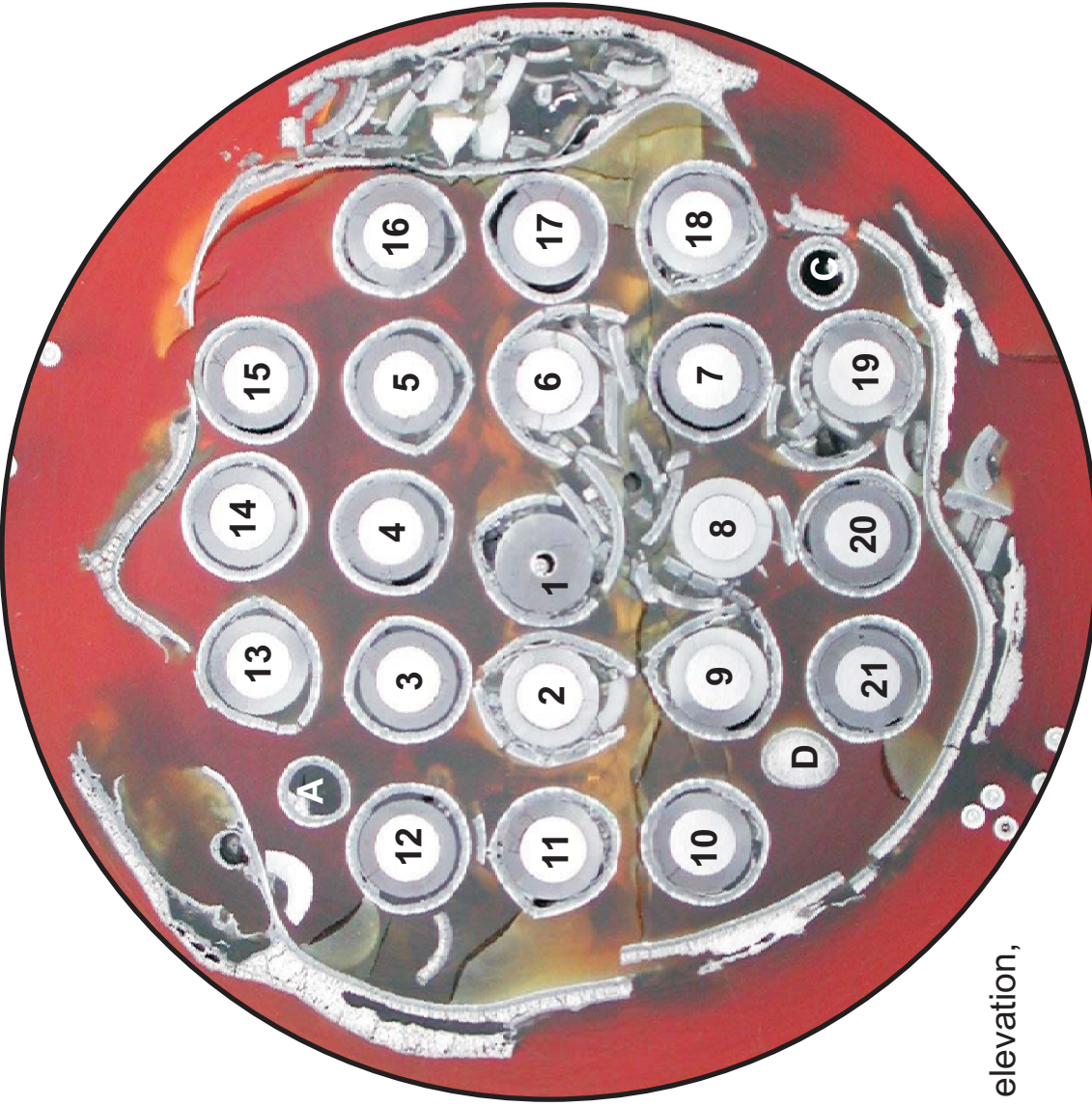


Fig. 84: QUENCH-10; Cross section at 750 mm (QUE-10-4). Shroud at two positions, illustrating sound (left) vs. locally degraded scale, from which no  $\alpha$ -Zr(O) phase precipitates during cooling (right).



Top of cross section slab, 833 mm elevation, shown for comparison



Slab bottom, 800 mm elevation, inverted to top view

Fig. 85: QUENCH-10; Cross section at 800 mm bundle elevation (QUE-10-8); overview from top.

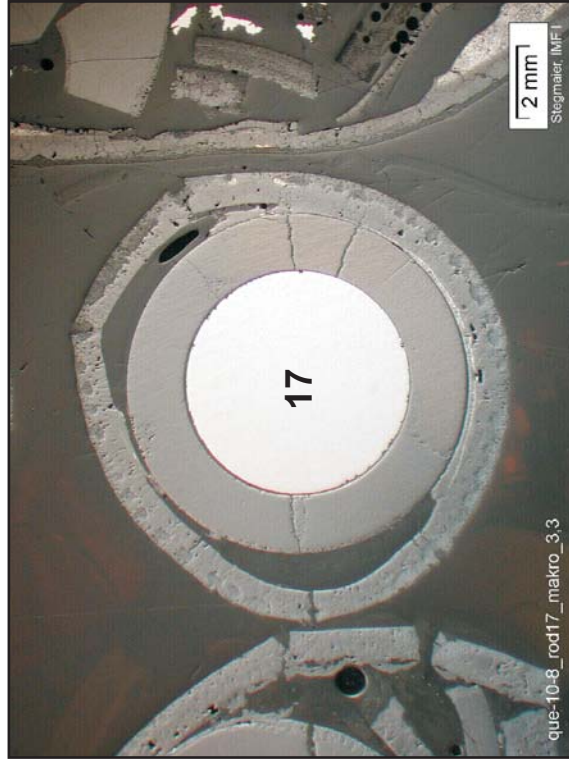
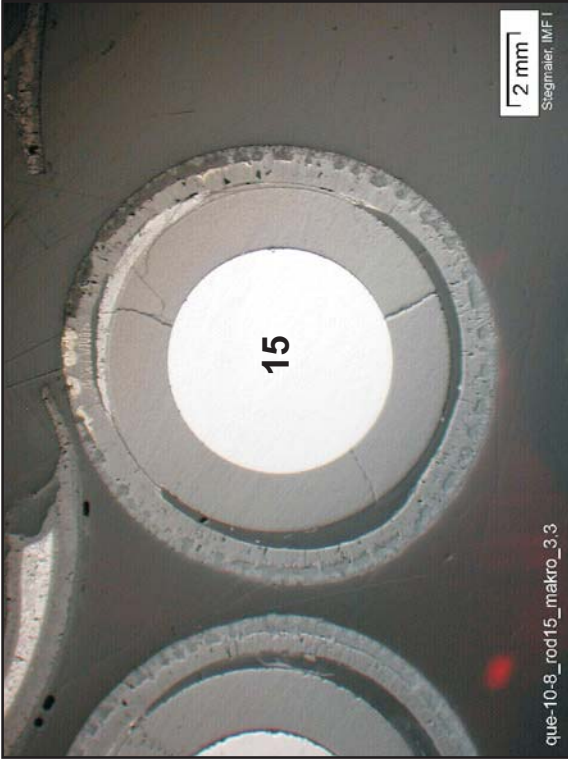
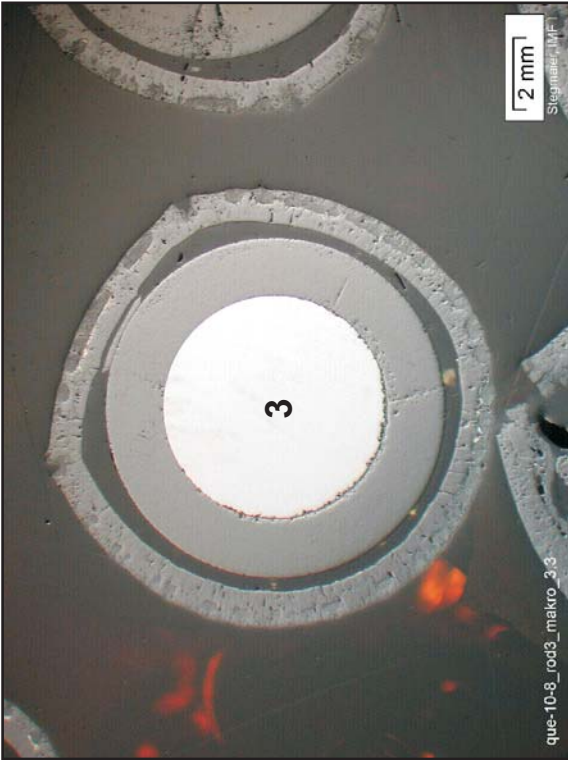


Fig. 86: QUENCH-10; Cross section at 800 mm bundle elevation (QUE-10-8). Macrographs of selected rods, showing the typical almost complete cladding oxidation, and some extent of pellet interaction.

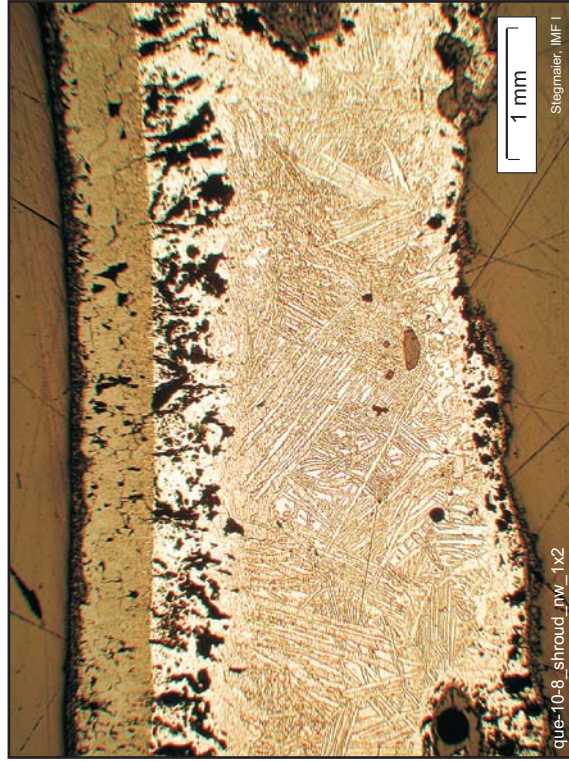
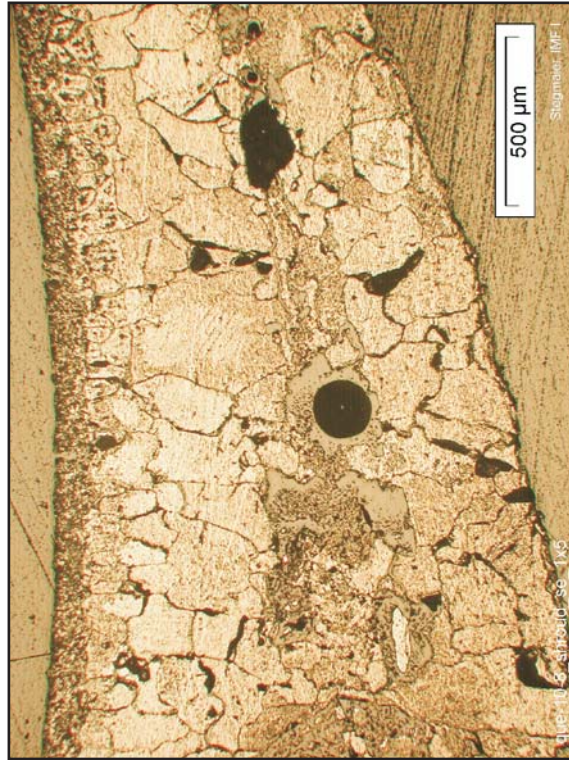
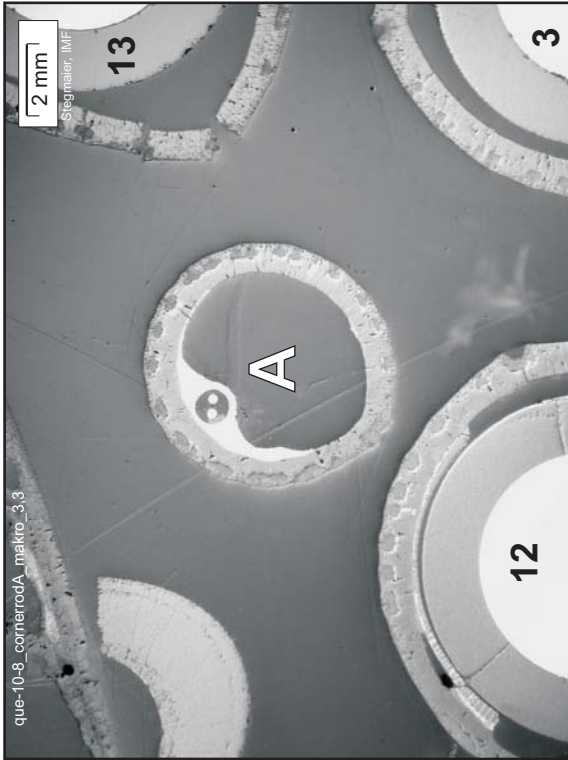


Fig. 87: QUENCH-10; Cross section at 800 mm bundle elevation (QUE-10-8). Corner rod A and shroud at SE (left side), corner rod C and shroud at NW (right side).

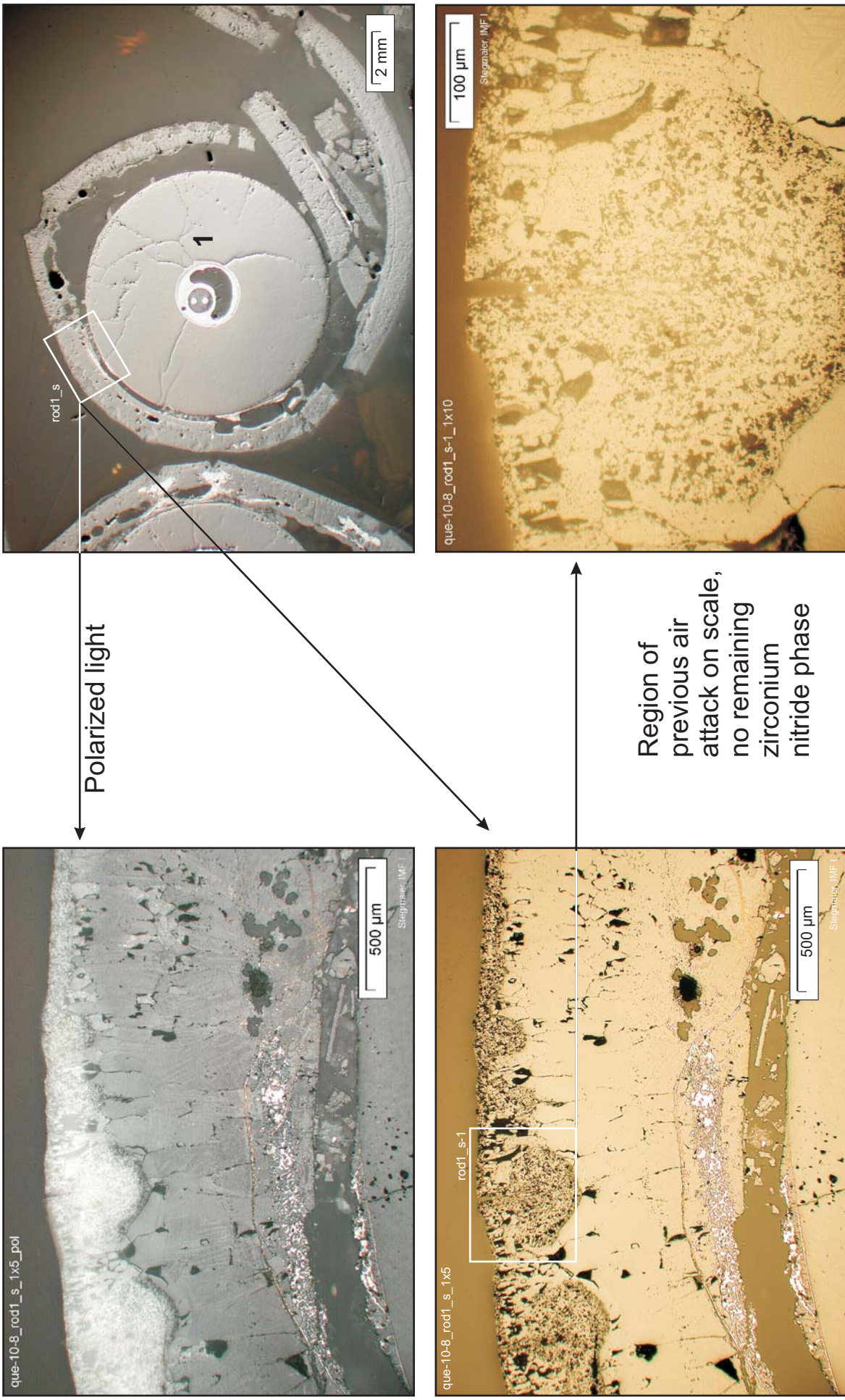


Fig. 88: QUENCH-10; Cross section at 800 mm bundle elevation (QUE-10-8). Mostly oxidized cladding of central rod, showing, in comparison to polarization contrast, localized air-related morphology.

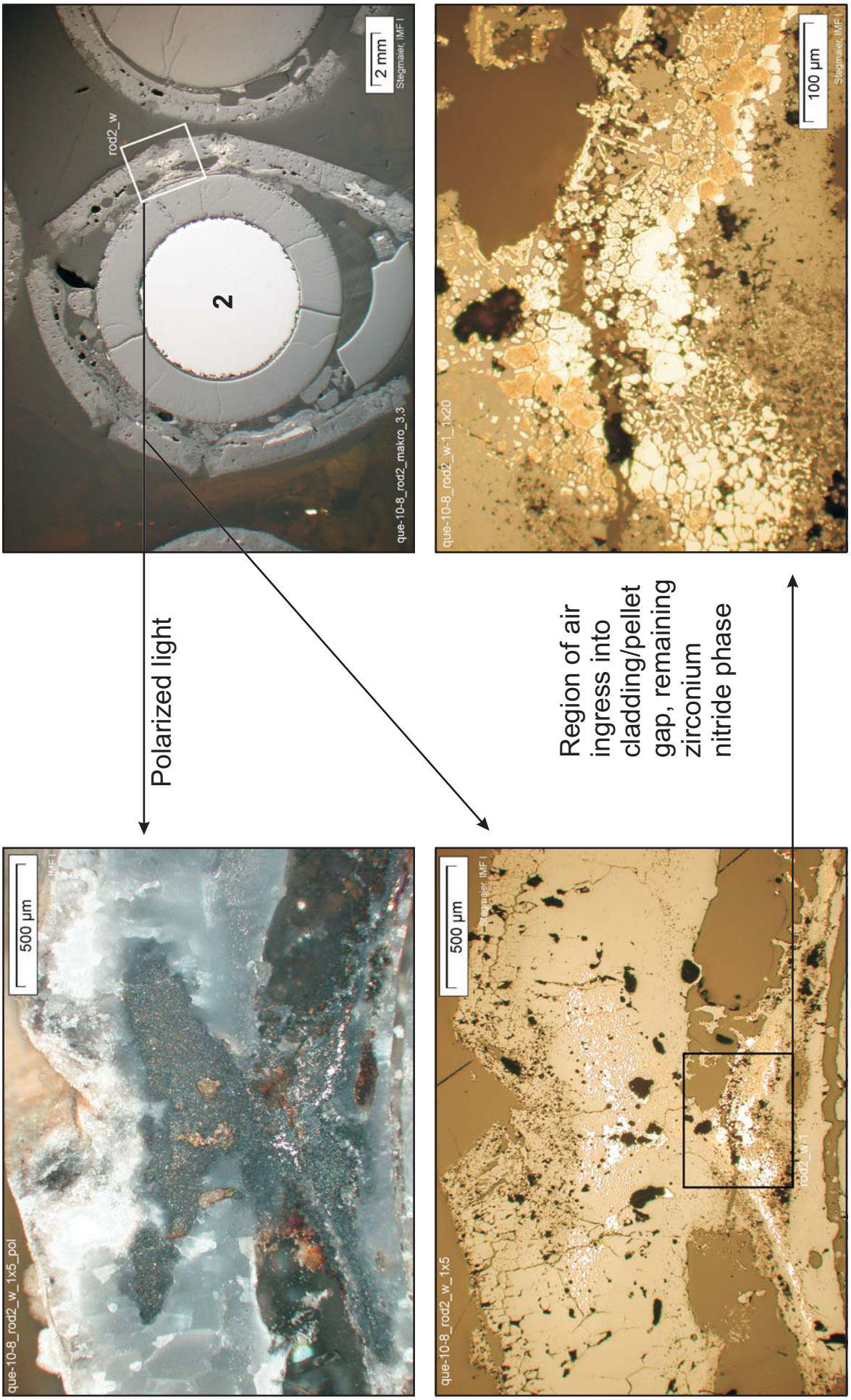
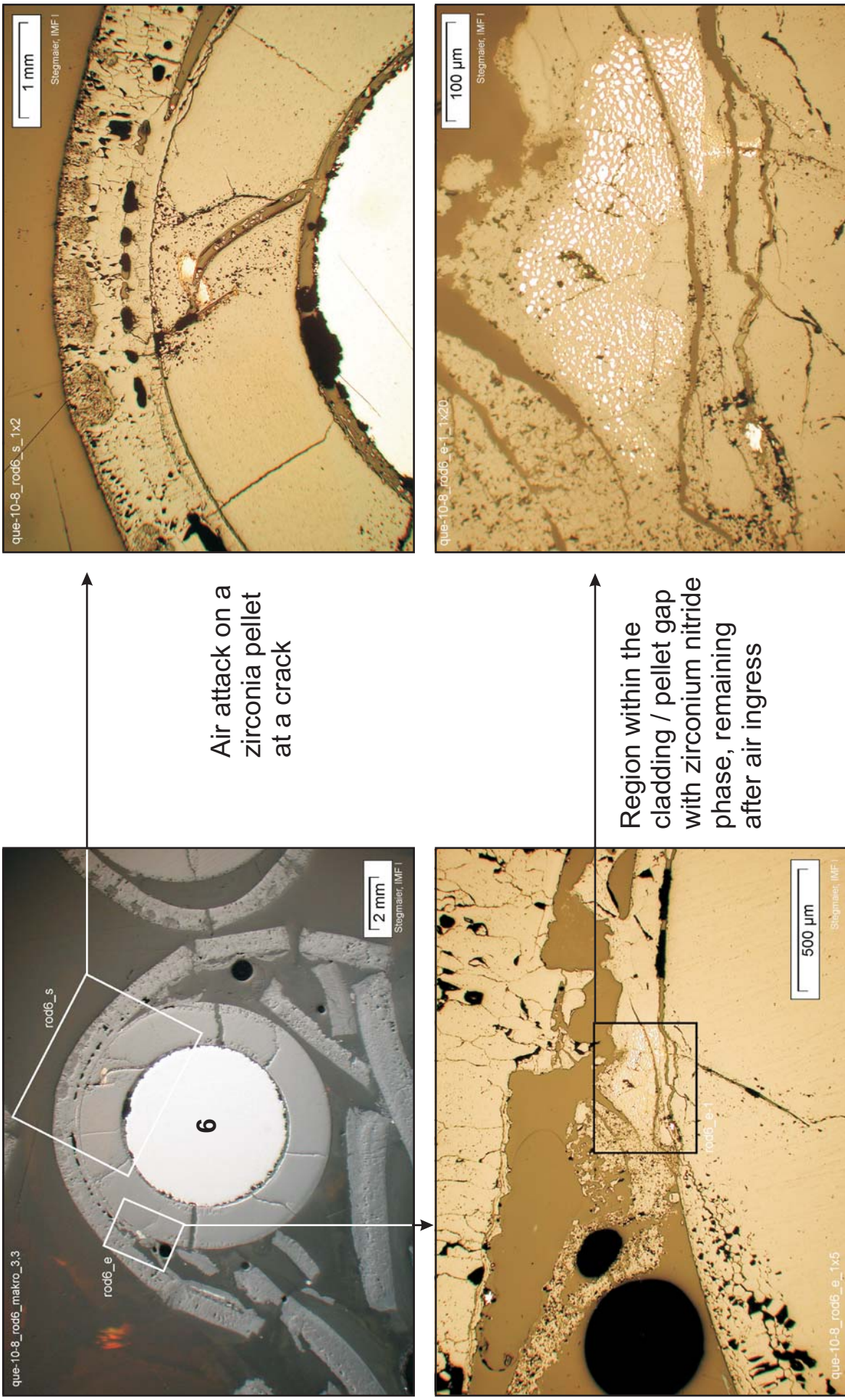


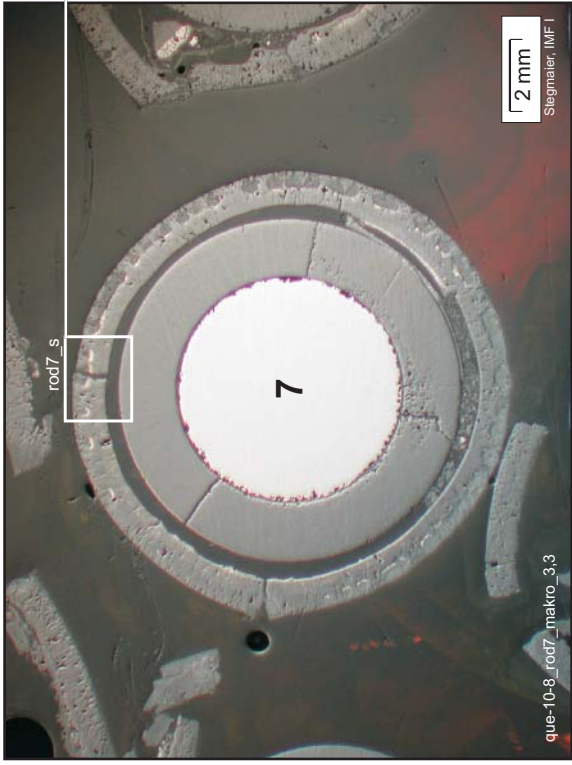
Fig. 89: QUENCH-10; Cross section at 800 mm bundle elevation (QUE-10-8). Mostly oxidized cladding of rod 2, shown in comparison to polarization contrast; air ingress into cladding and pellet gap.



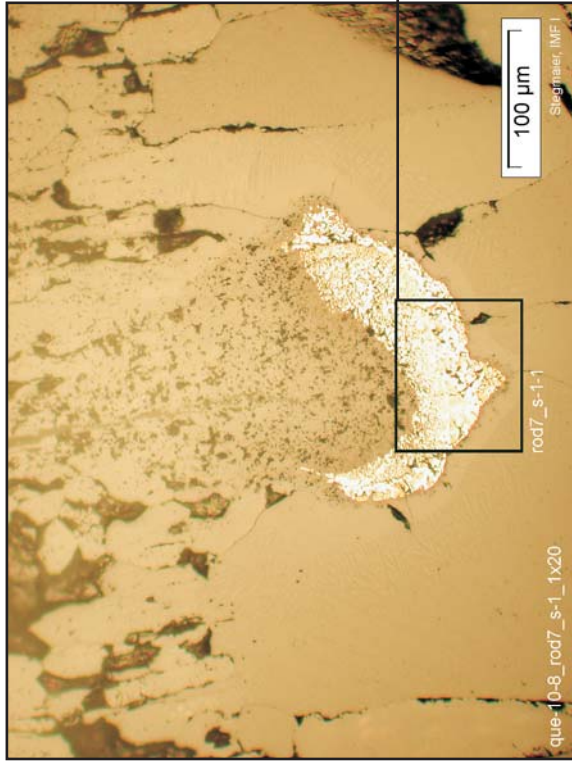
Air attack on a zirconia pellet at a crack

Region within the cladding / pellet gap with zirconium nitride phase, remaining after air ingress

Fig. 90: QUENCH-10; Cross section at 800 mm bundle elevation (QUE-10-8). Finally oxidized cladding of rod 6 after air attack, and indications of air ingress into gap and simulator pellet.



Transformation of fully oxidized cladding under oxygen-starved air exposure: Conversion of oxide to nitride, penetration of ZrN fronts, re-conversion of nitride to oxide



Region of residual zirconium nitride phase, which was protected from steam exposure during quenching

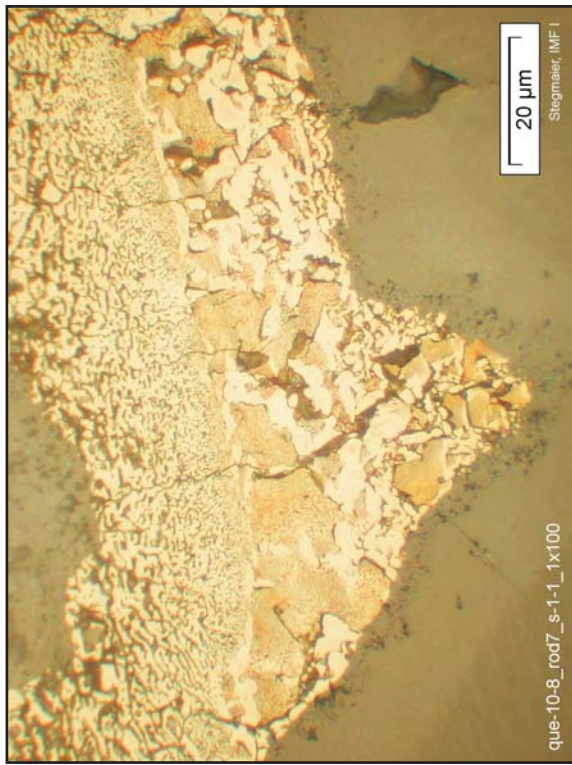


Fig. 91: QUENCH-10; Cross section at 800 mm bundle elevation (QUE-10-8). Attack of the fully oxidized cladding of rod 7 during the air exposure phase of the experiment, resulting in residual ZrN phase.

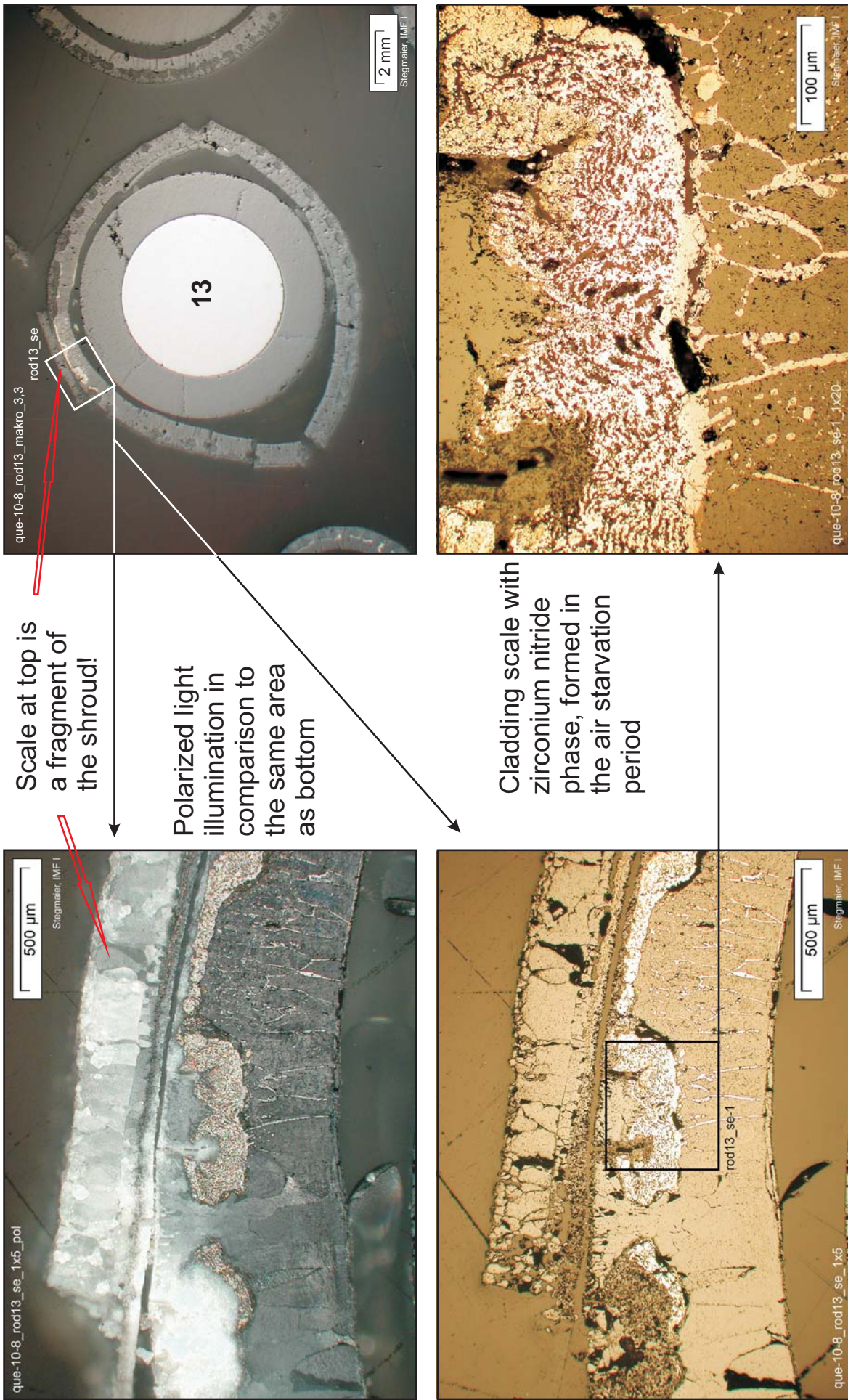


Fig. 92: QUENCH-10; Cross section at 800 mm bundle elevation (QUE-10-8). Attack of the cladding of rod 13 during the air exposure period, resulting in residual ZrN phase, embedded within the scale.

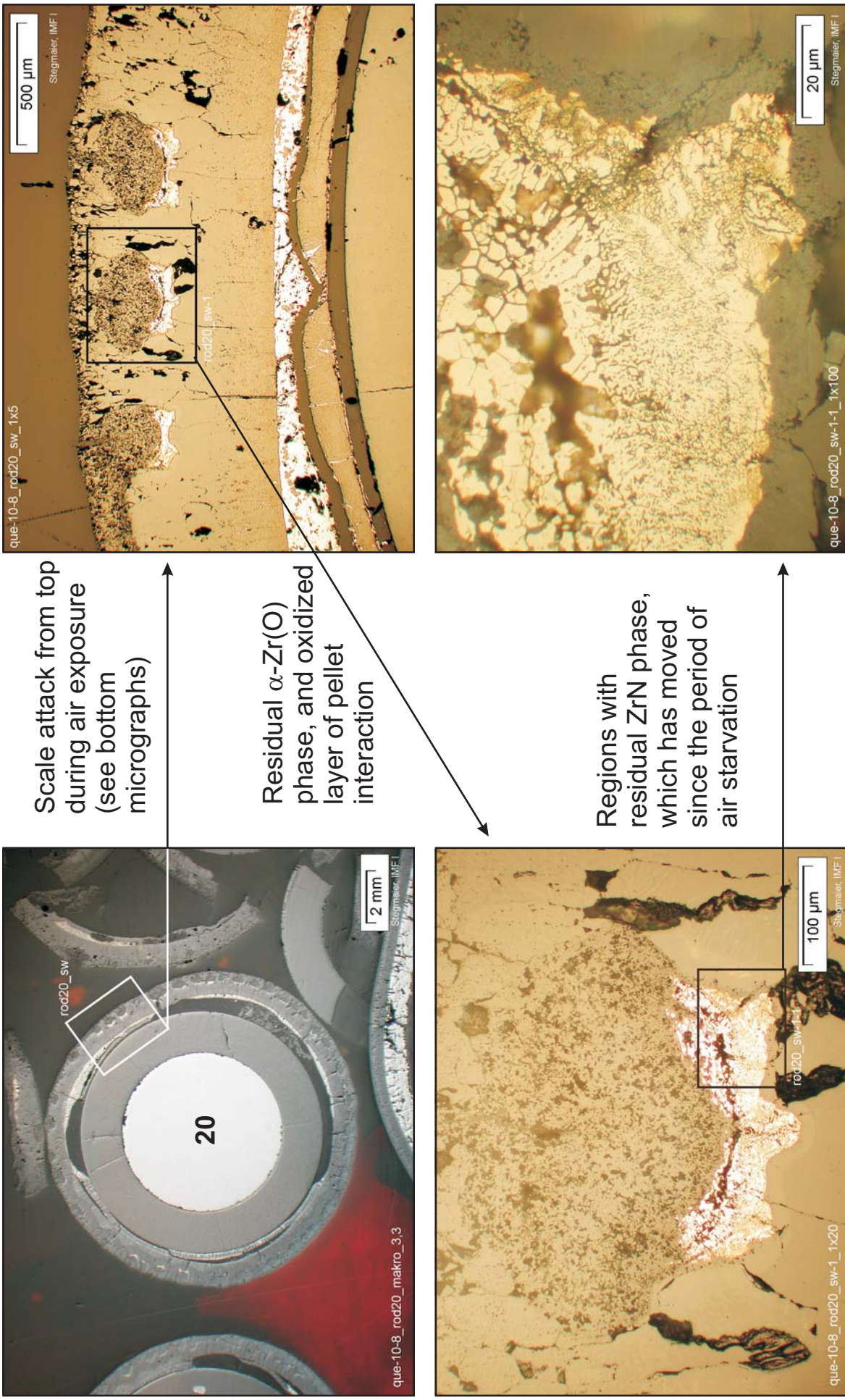


Fig. 93: QUENCH-10; Cross section at 800 mm bundle elevation (QUE-10-8). External attack of the cladding of rod 20 during the air exposure period, and residual, internally confined  $\alpha$ -Zr(O) cladding matrix.

Bottom of cross section slab, 835 mm elevation, inverted to top view

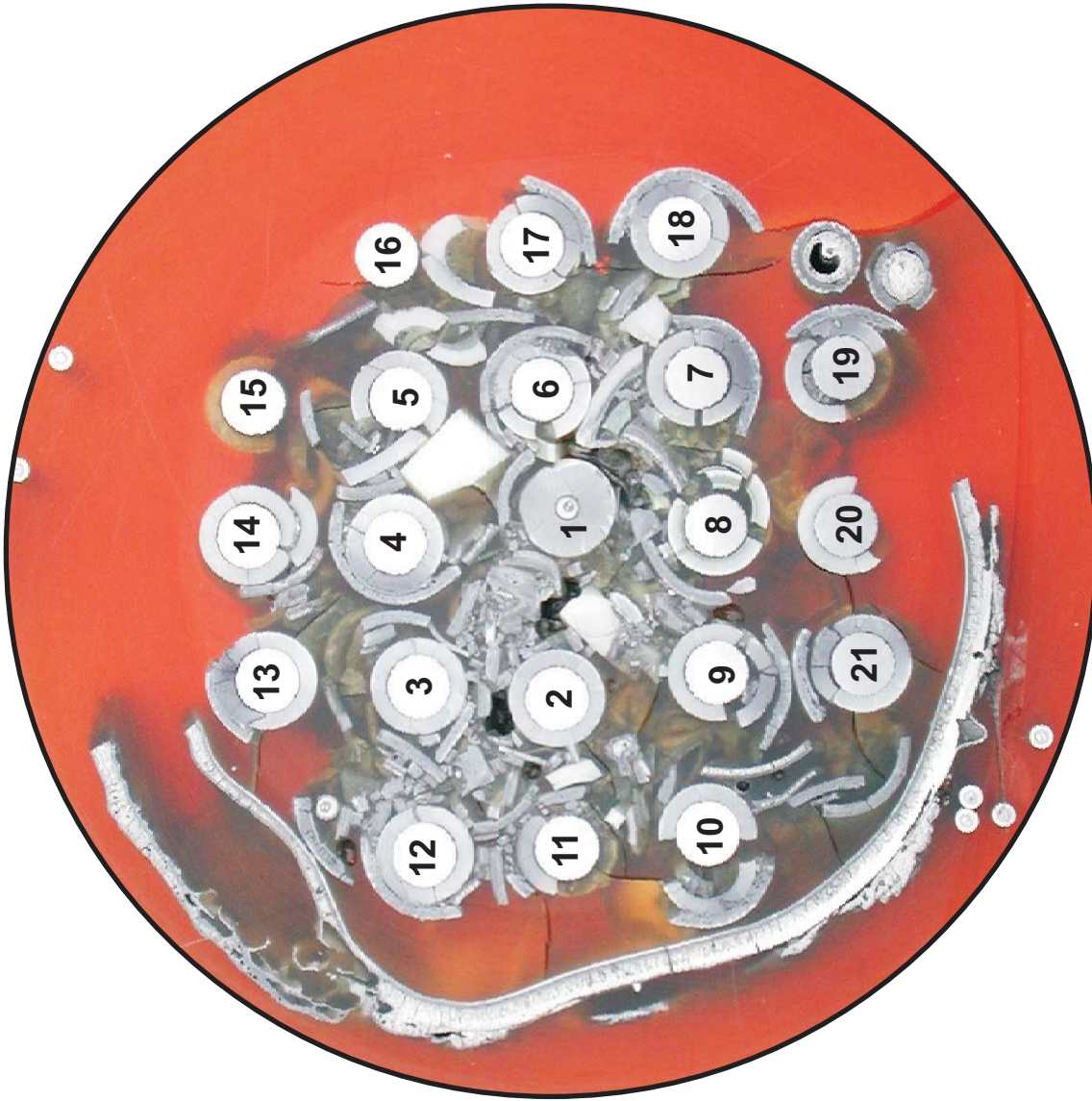
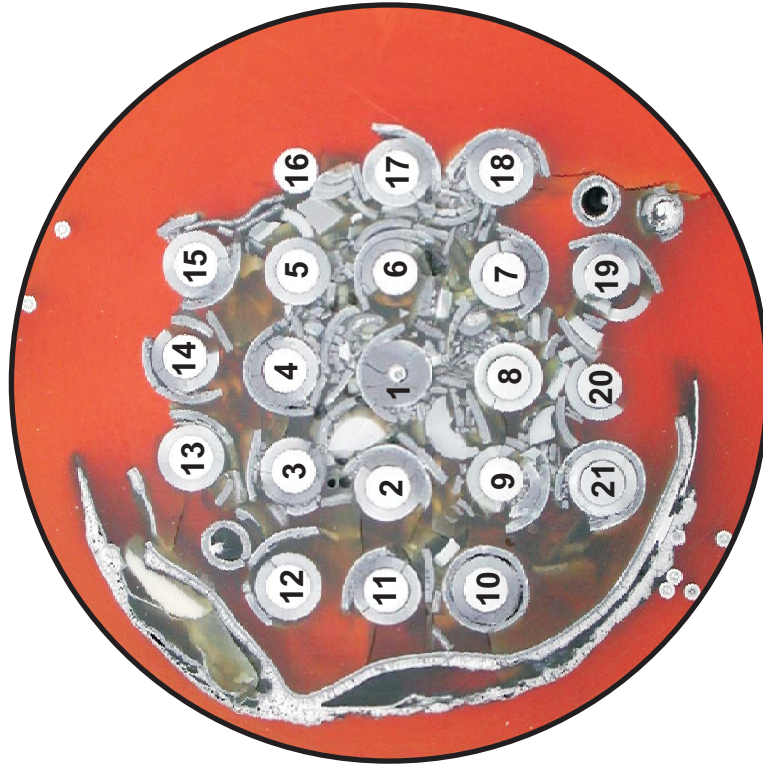
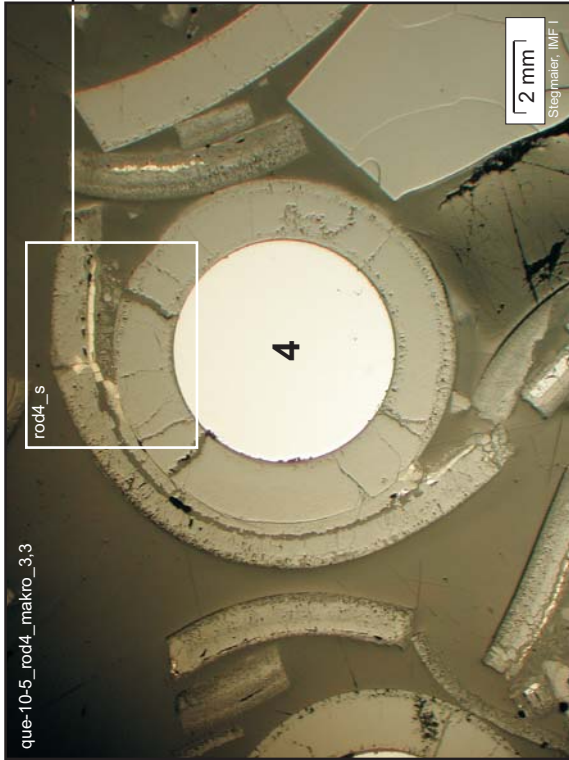
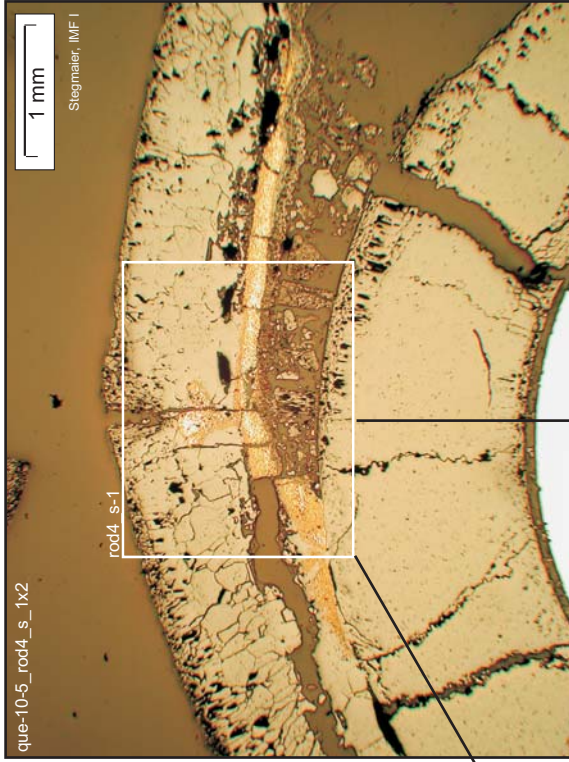


Fig. 94: QUENCH-10; Cross section at 850 mm bundle elevation (QUE-10-5); overview from top.



Air ingress into cladding scale and pellet gap



Regions with ZrN phase, formed during the air ingress period. The comparison of bright-field (left) and polarization (right) helps to distinguish the fine-grained ZrN microstructure

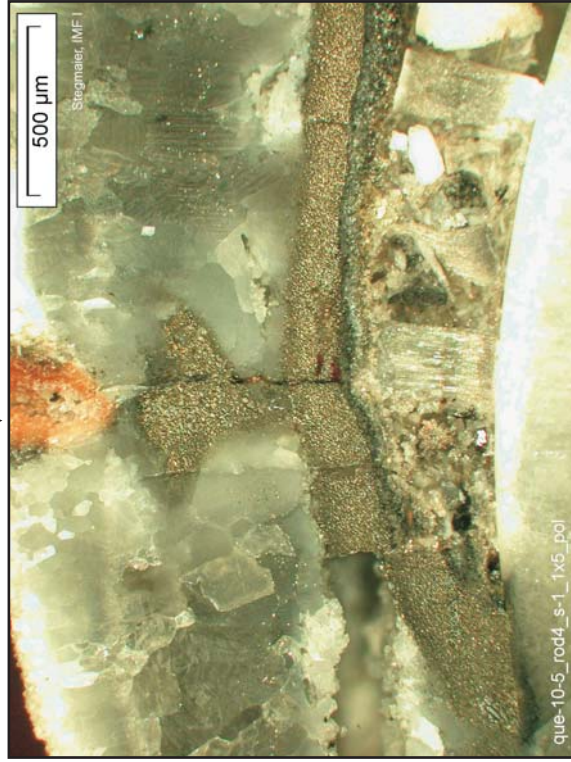
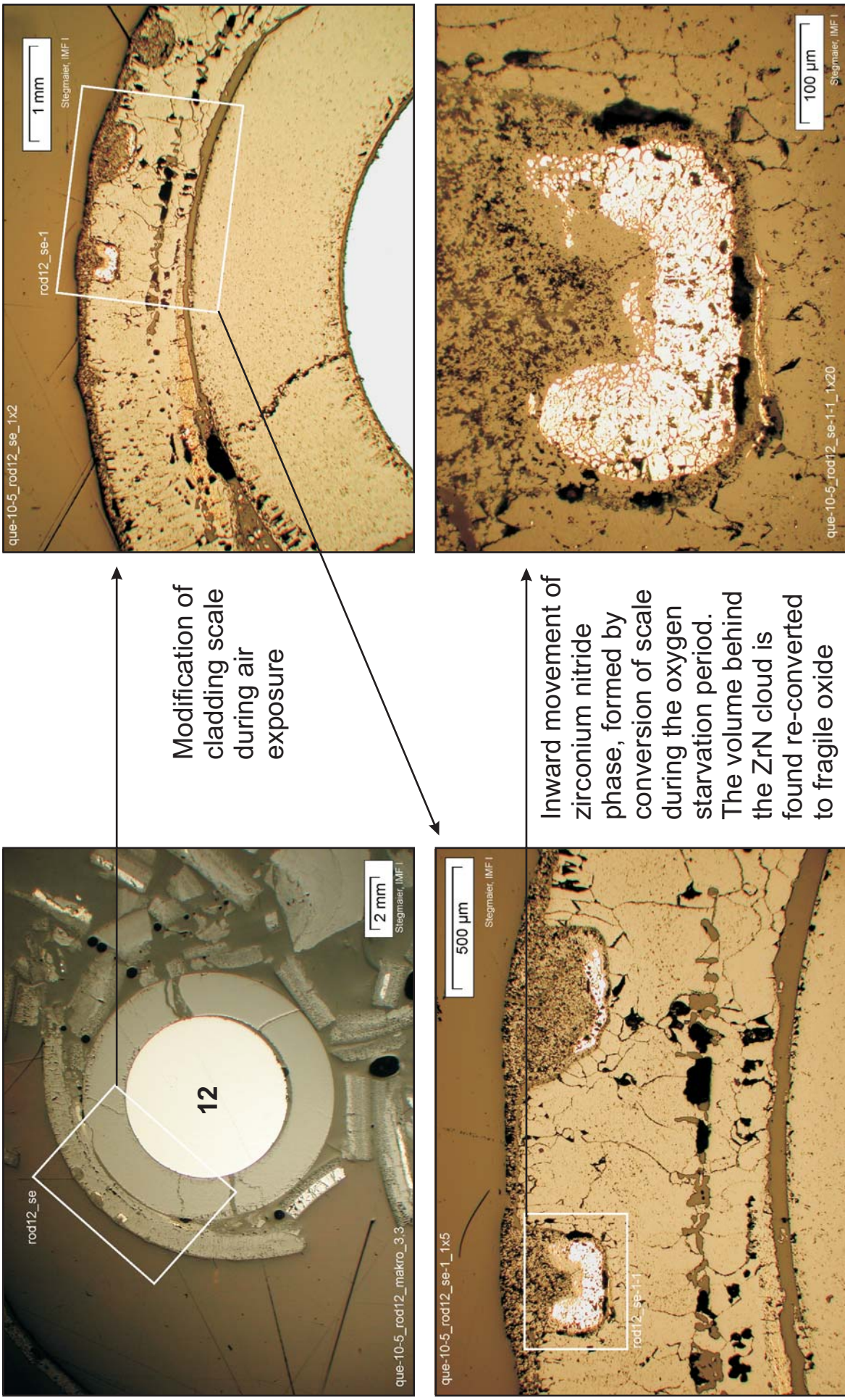


Fig. 95: QUENCH-10; Cross section at 850 mm bundle elevation (QUE-10-5). Region of rod 4, showing ZrN phase formation, related to air ingress into the cladding scale and the pellet gap.



Modification of cladding scale during air exposure

Inward movement of zirconium nitride phase, formed by conversion of scale during the oxygen starvation period. The volume behind the ZrN cloud is found re-converted to fragile oxide

Fig. 96: QUENCH-10; Cross section at 850 mm bundle elevation (QUE-10-5). Cladding scale of rod 12, showing locally concentrated ZrN phase penetration by conversion of scale.

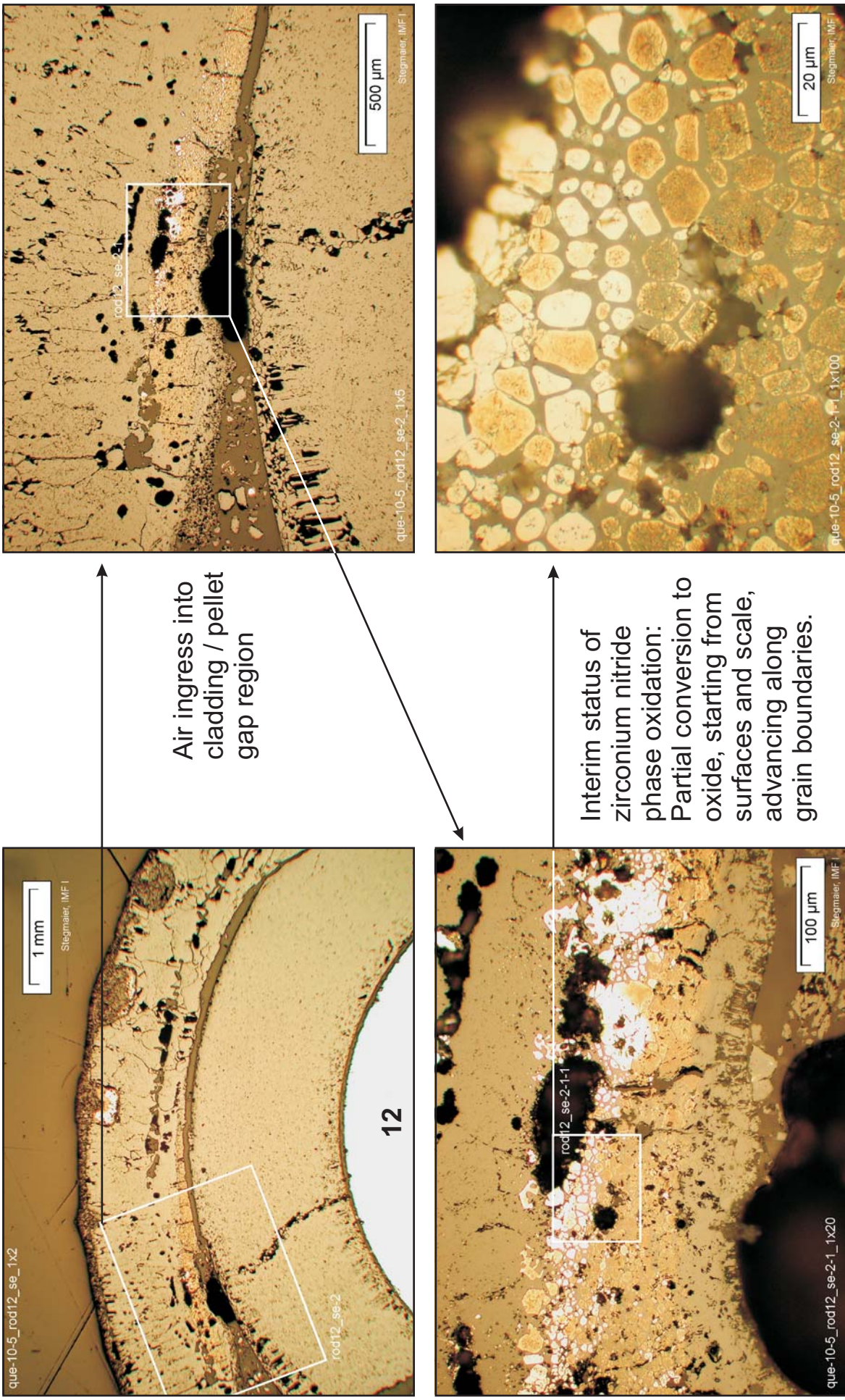
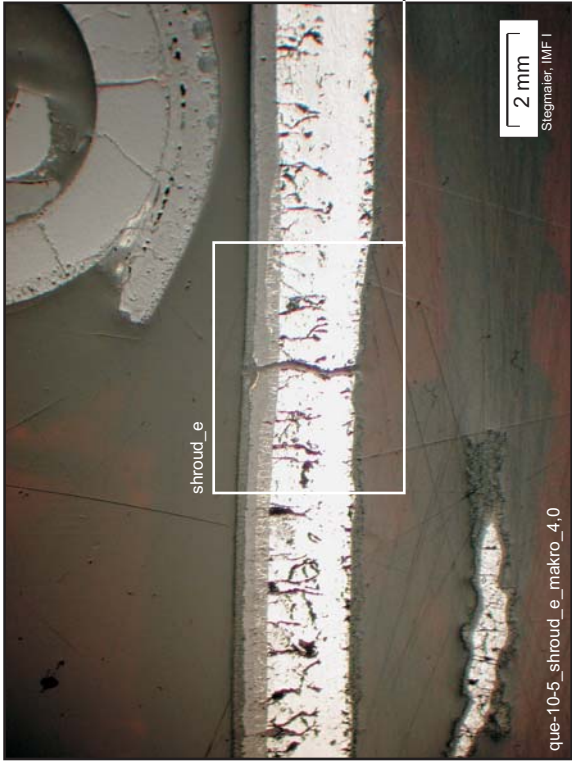
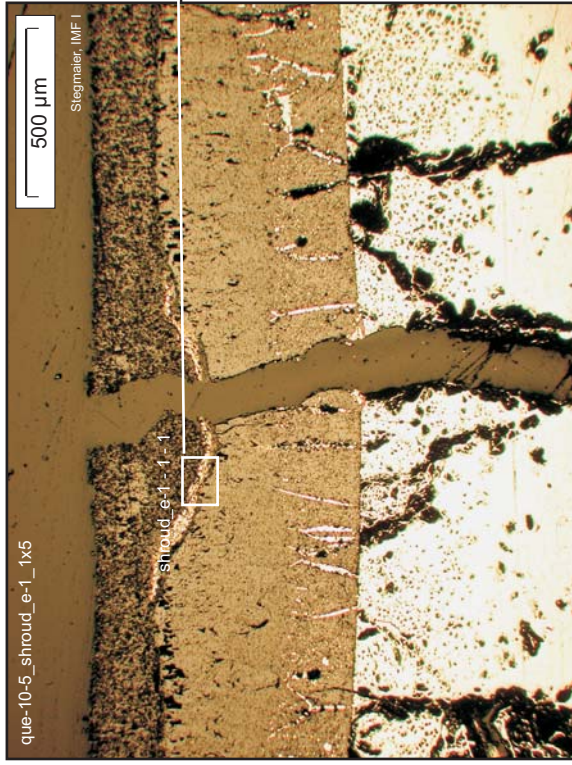
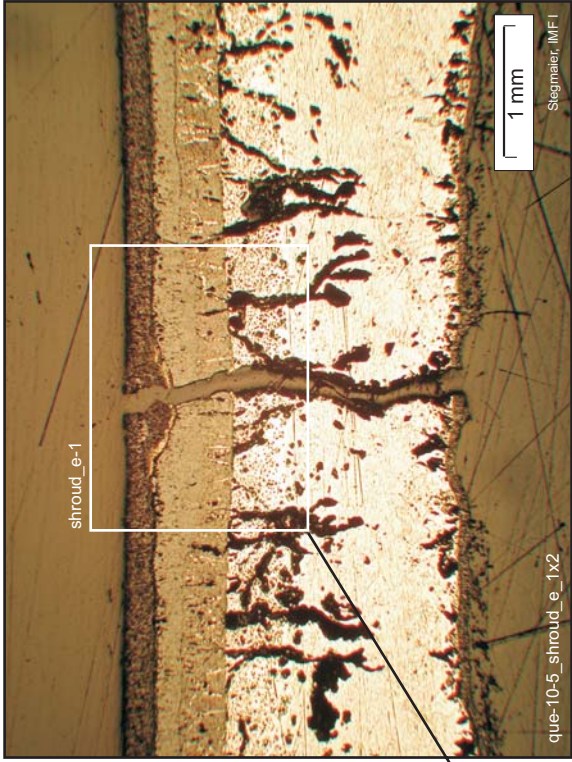


Fig. 97: QUENCH-10; Cross section at 850 mm bundle elevation (QUE-10-5). Cladding / pellet gap region of rod 12 after air-starved exposure and partial re-oxidation.



Scale modification from its surface during air exposure, re-oxidation and through-wall cracking during the cooldown phase



Interim status of the re-conversion of ZrN phase to oxide

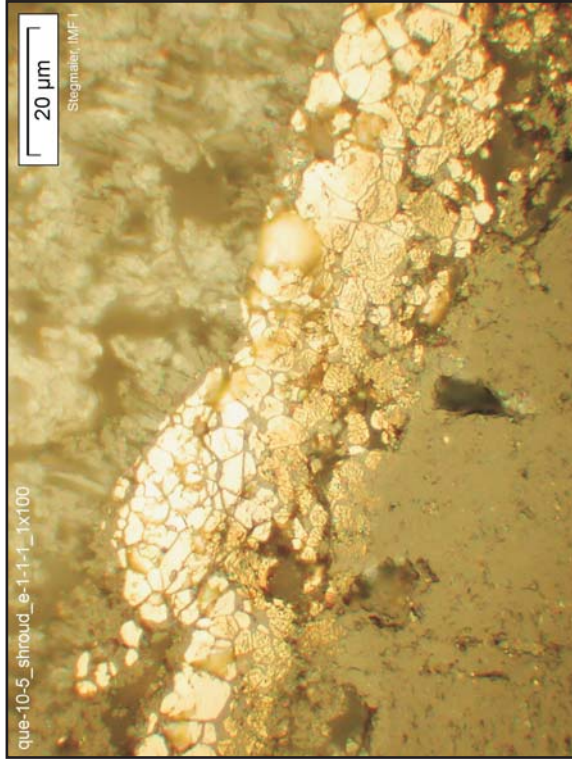
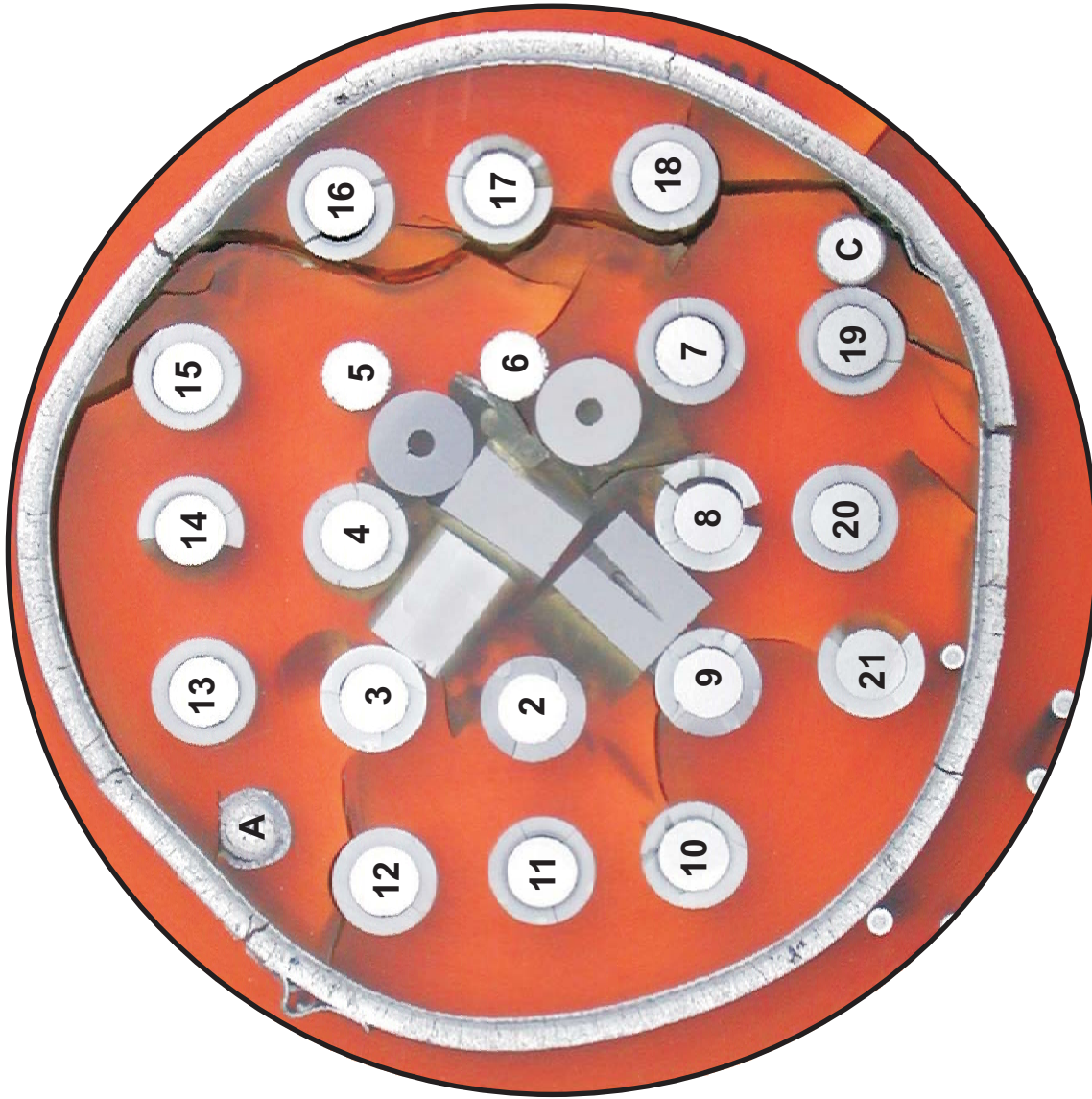


Fig. 98: QUENCH-10; Cross section at 850 mm bundle elevation (QUE-10-5). Inner side of shroud towards E, after air-starved (nitrogen-rich) exposure and movement of the re-oxidation front.



Bottom of cross section slab, 937 mm elevation, inverted to top view

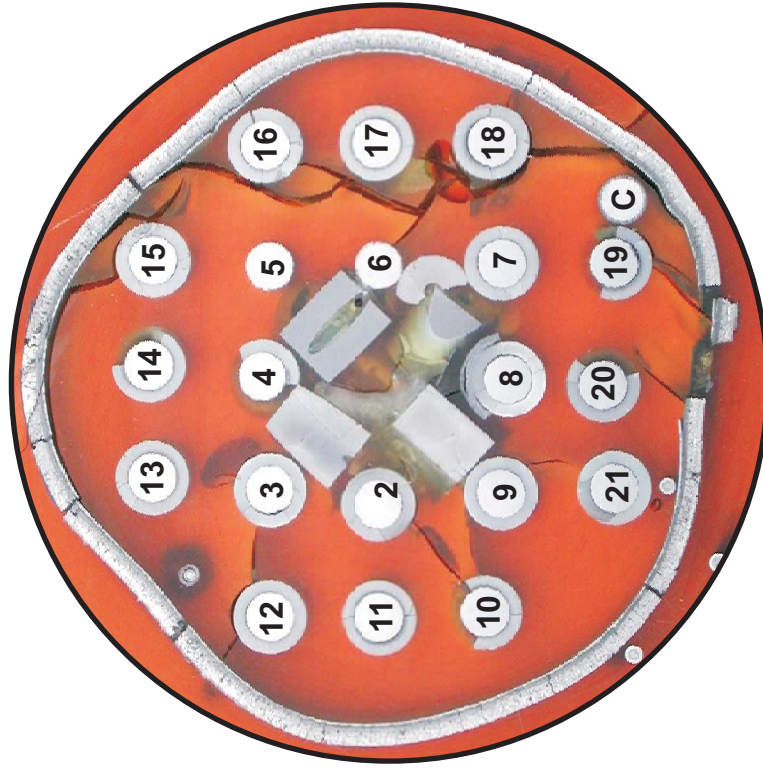
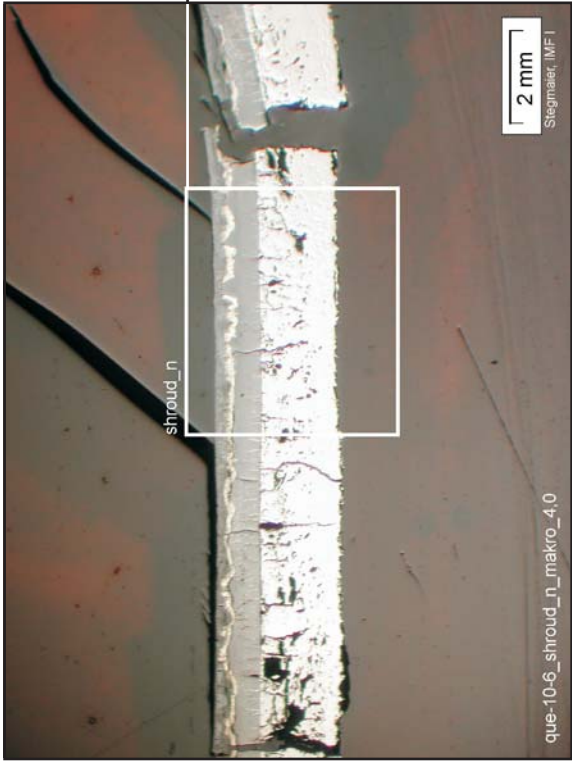
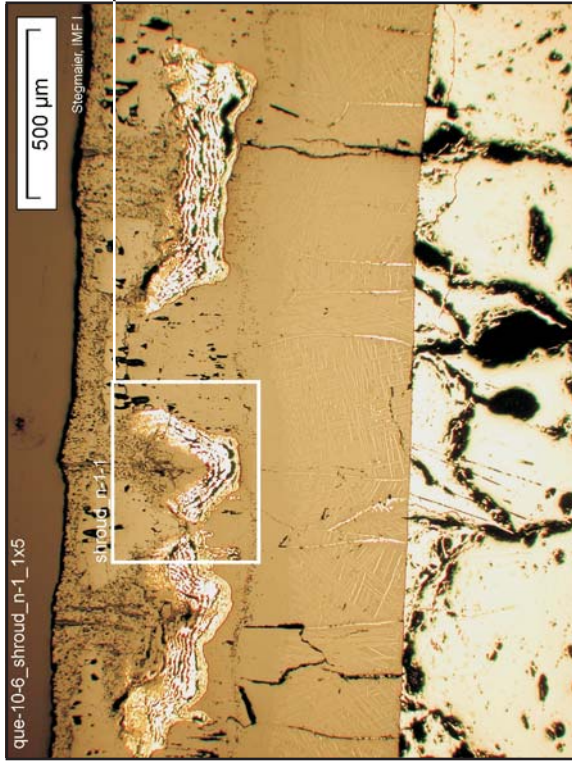


Fig. 99: QUENCH-10; Cross section at 950 mm bundle elevation (QUE-10-6); overview from top.



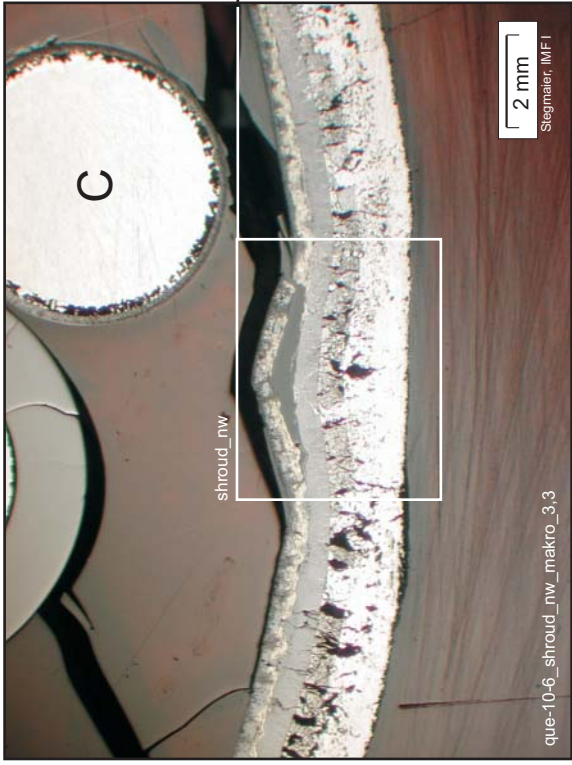
Scale modification during air exposure, re-oxidation and through-wall cracking during cooldown phase



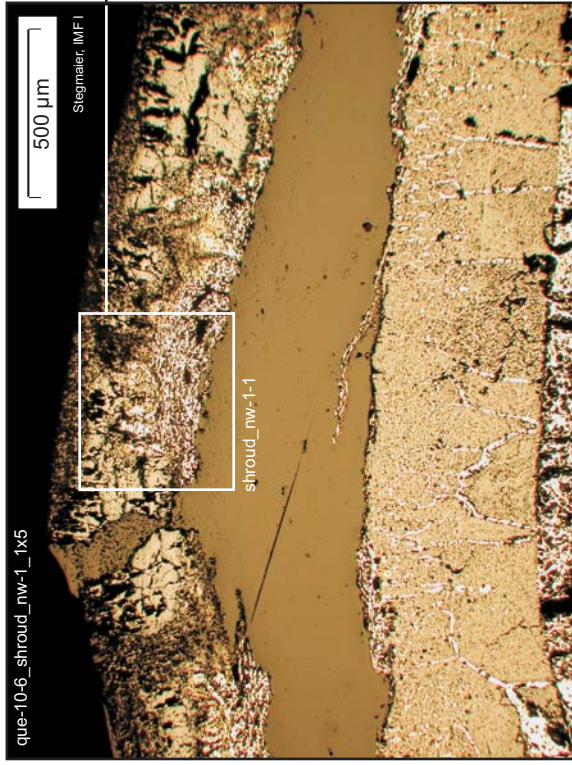
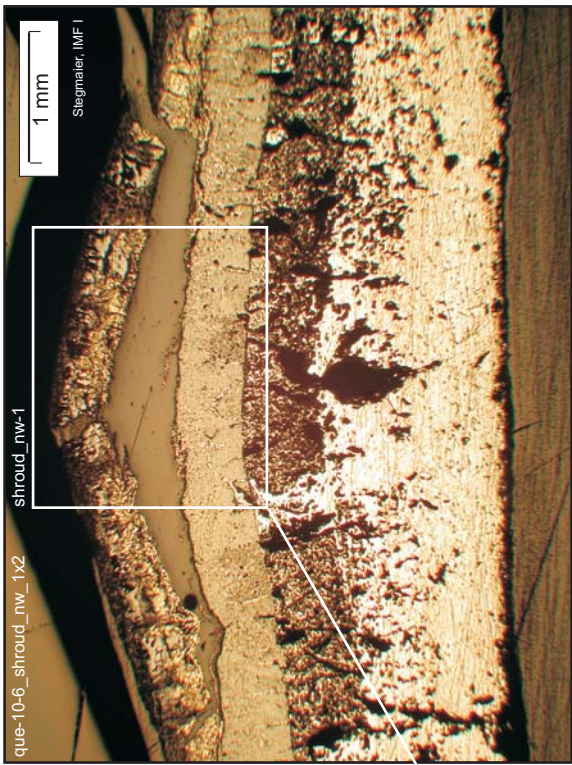
Interim status of zirconium nitride re-conversion to oxide



Fig. 100: QUENCH-10; Cross section at 950 mm bundle elevation (QUE-10-6). Shroud towards N, after the air-starved (nitrogen-rich) exposure of the inner scale, and the movement of a re-oxidation front.



Scale modification during air exposure, re-oxidation and partial layer spalling



The spalled scale top layer contains zones of zirconium nitride

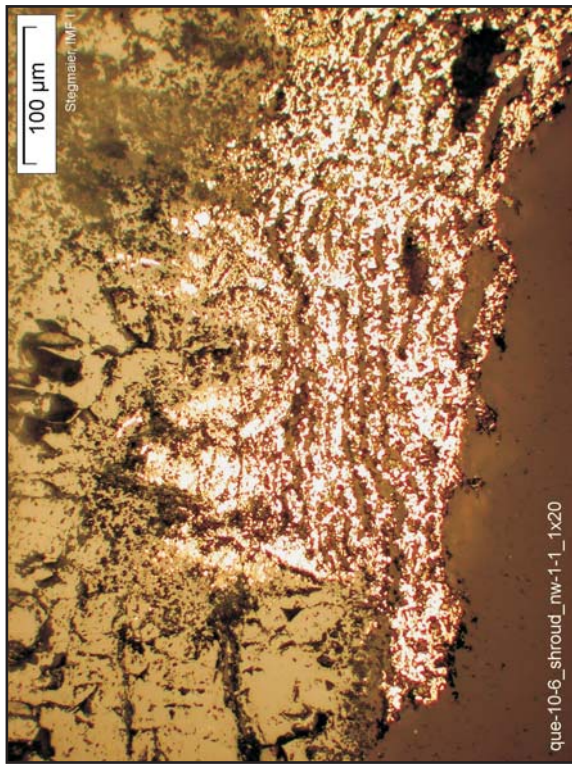
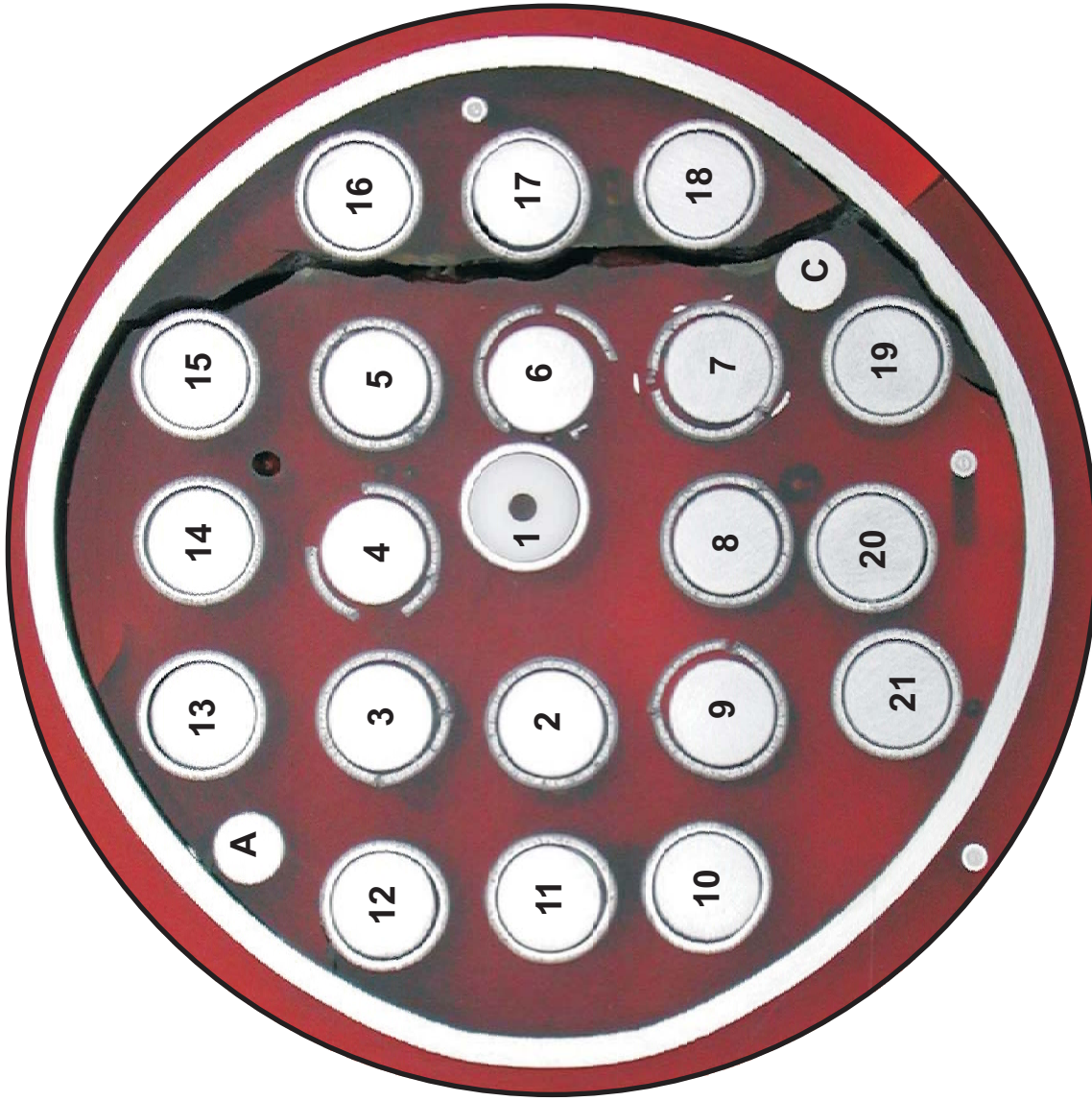


Fig. 101: QUENCH-10; Cross section at 950 mm bundle elevation (QUE-10-6). Shroud towards NW, after air-starved (nitrogen-rich) exposure, re-oxidation front movement, and top layer spalling.



Bottom of cross section slab, 1052 mm elevation, inverted to top view



Fig. 102: QUENCH-10; Cross section at 1080 mm bundle elevation (QUE-10-7); overview from top.

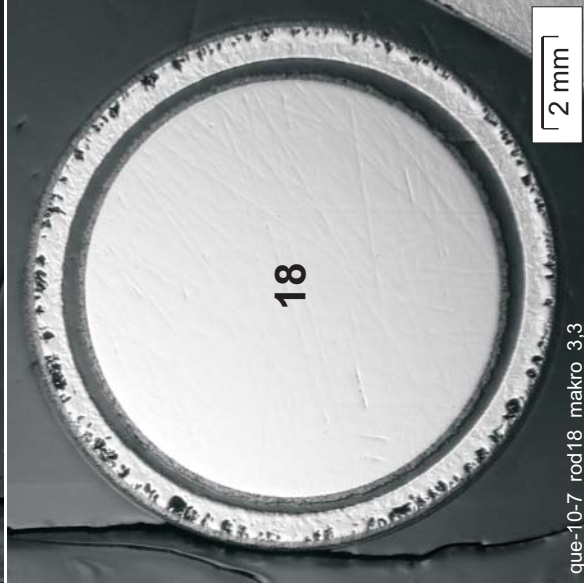
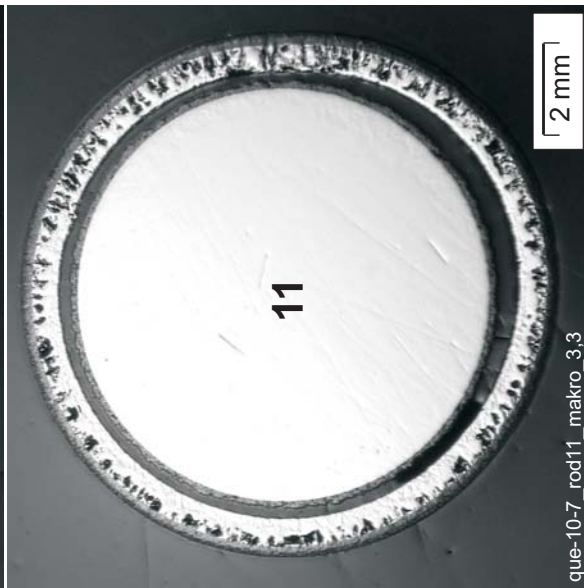
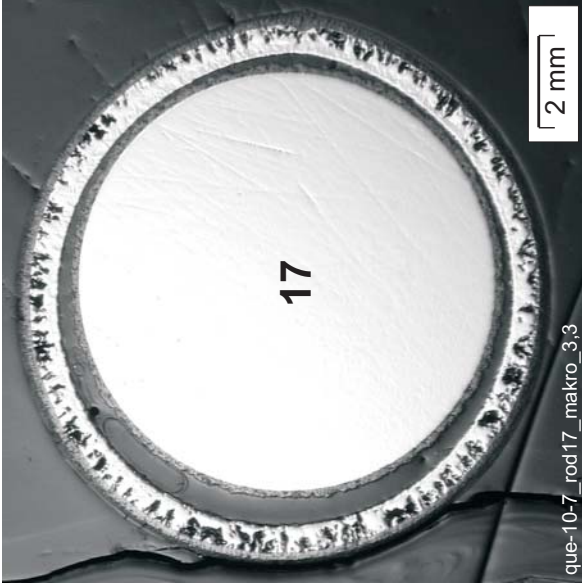
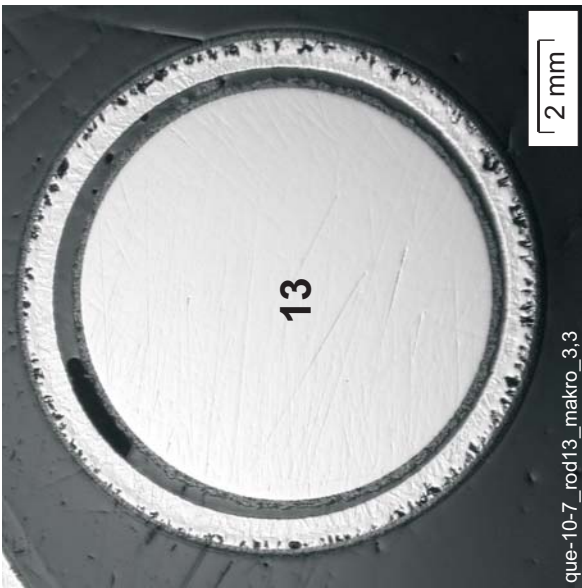


Fig. 103: QUENCH-10; Cross section at 1080 mm bundle elevation (QUE-10-7). Macrographs of selected rods, showing no localized effects of air exposure.

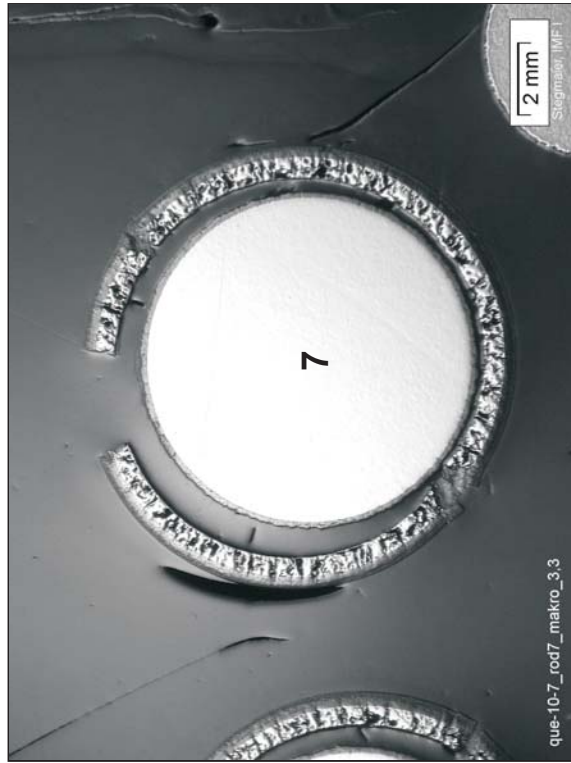
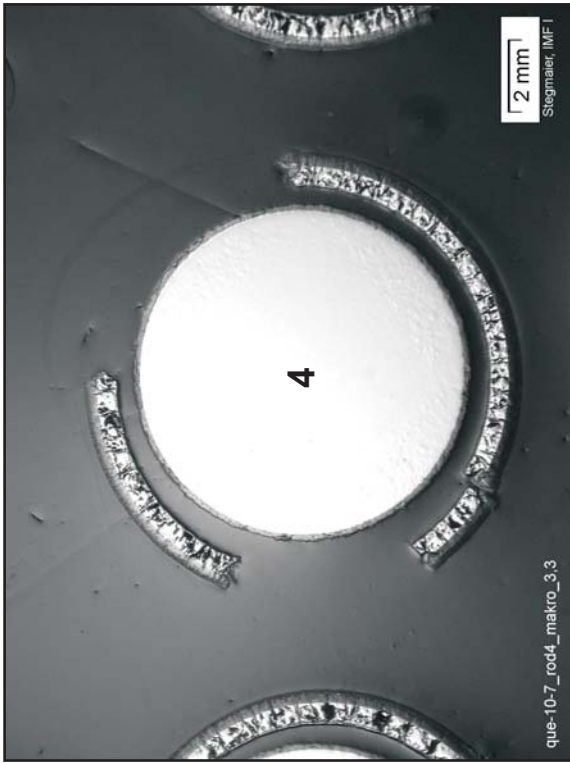
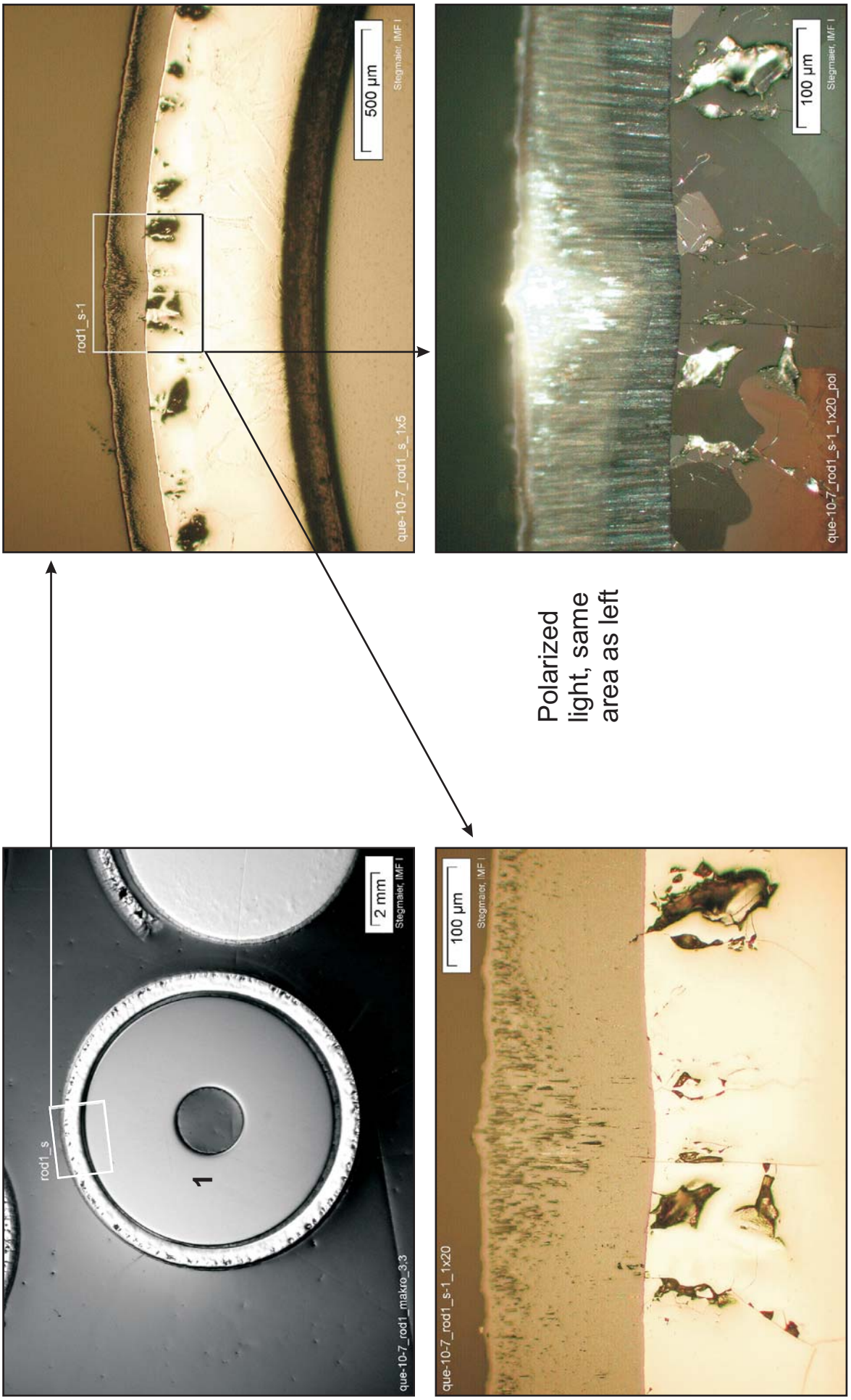
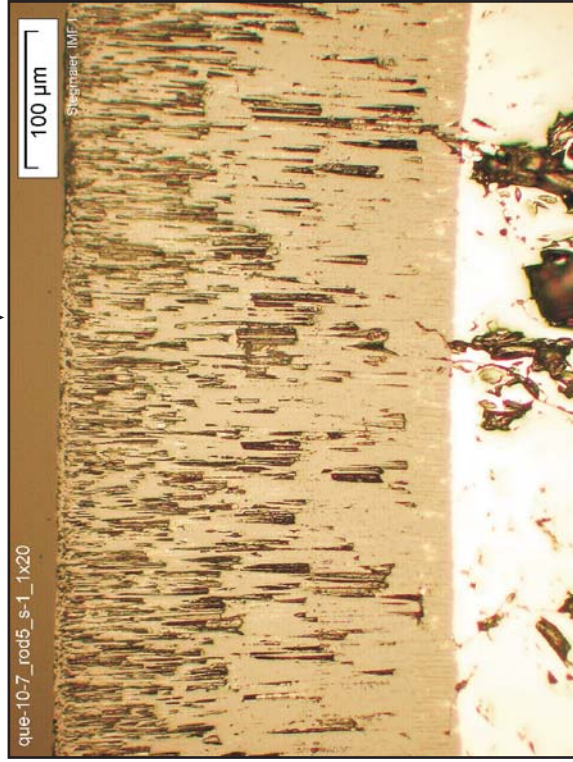
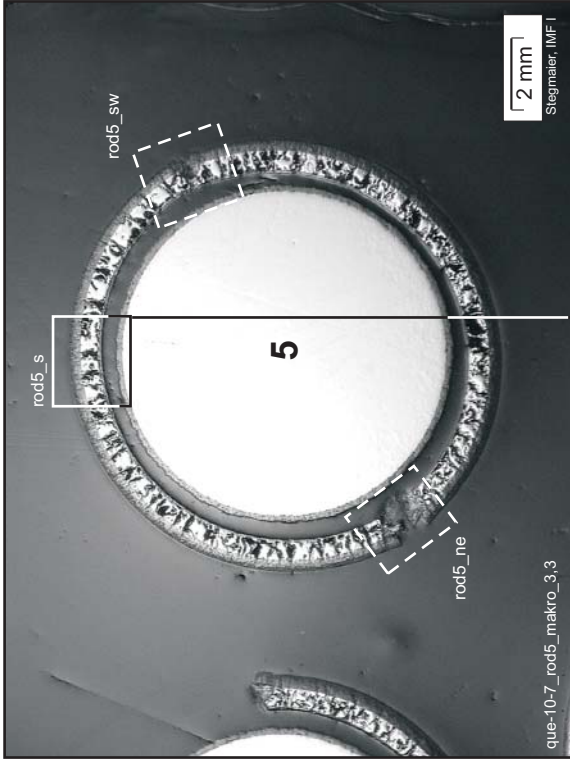
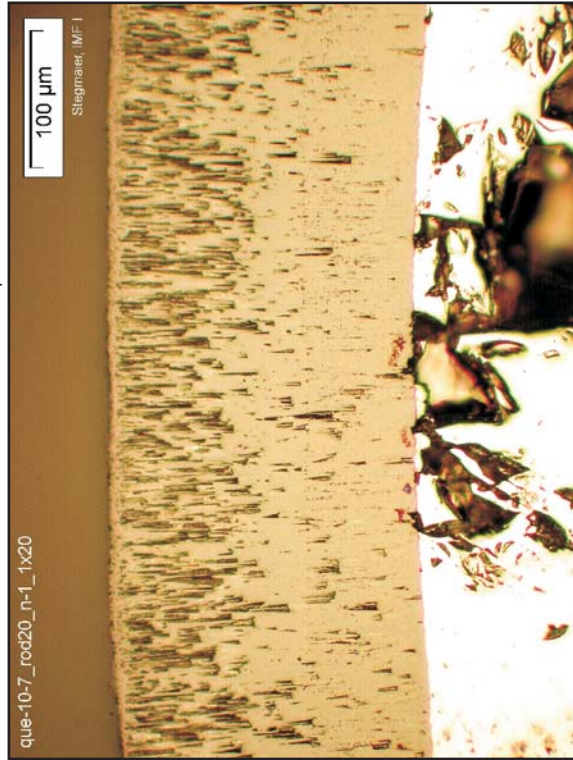


Fig. 104: QUENCH-10; Cross section at 1080 mm bundle elevation (QUE-10-7). Macrographs of selected rods, showing cladding fragmentation as effect of local attack of air.



Polarized light, same area as left

Fig. 105: QUENCH-10; Cross section at 1080 mm bundle elevation (QUE-10-7). Oxidation status of the central rod, showing minor scale irregularities.



Notice different  
scale thickness  
for the rods

Fig. 106: QUENCH-10; Cross section at 1080 mm bundle elevation (QUE-10-7). Oxidation status of rod 20 (left), compared to a regular position of rod 5 (right, see next figure).

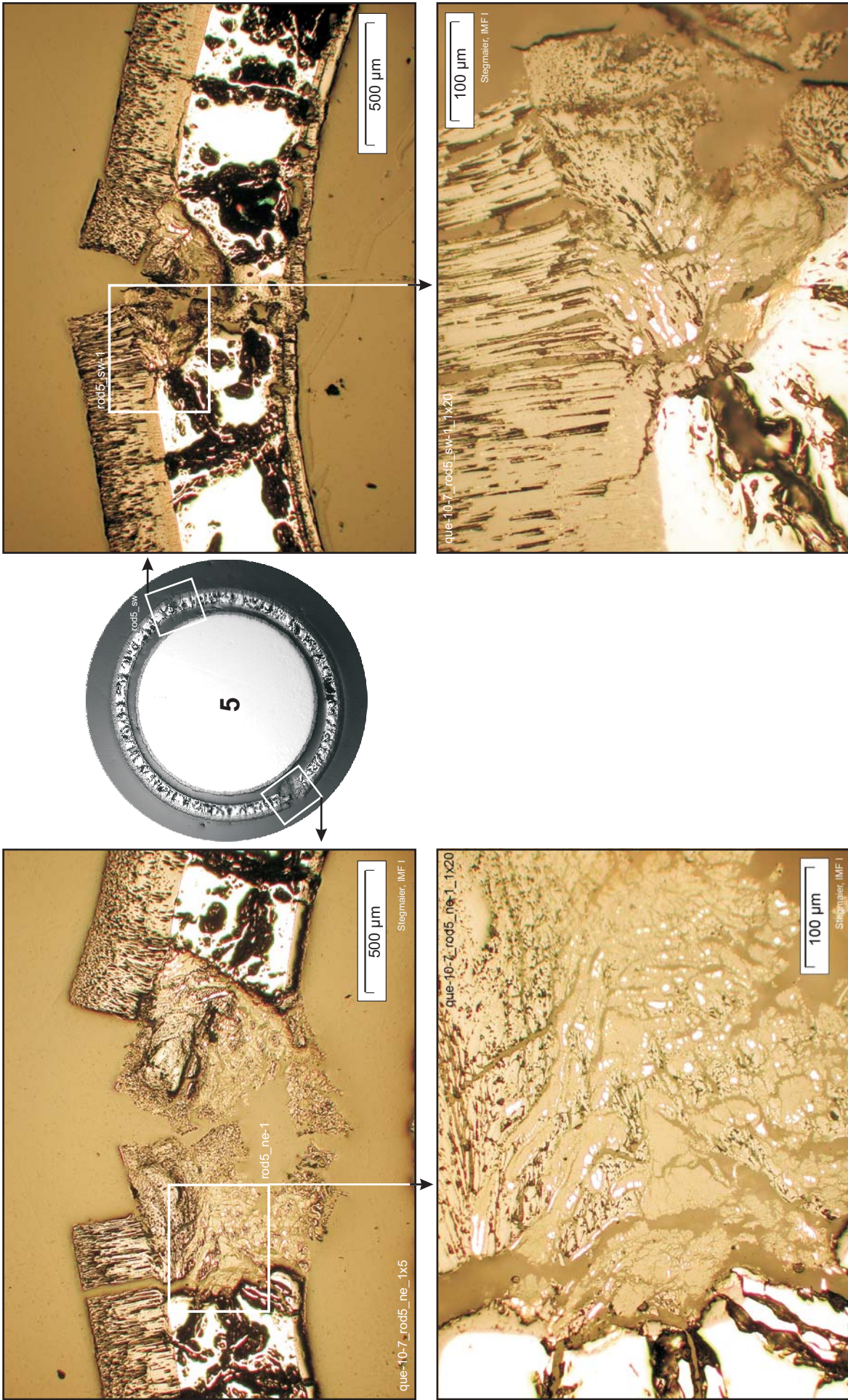
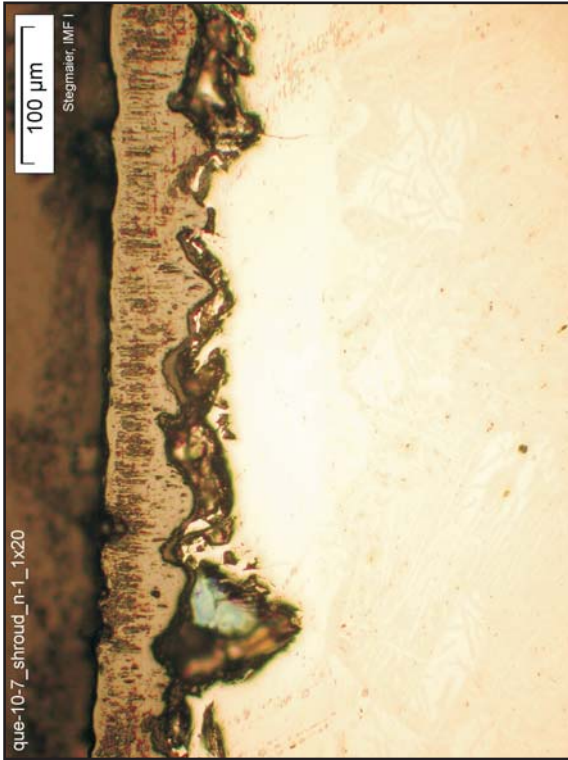


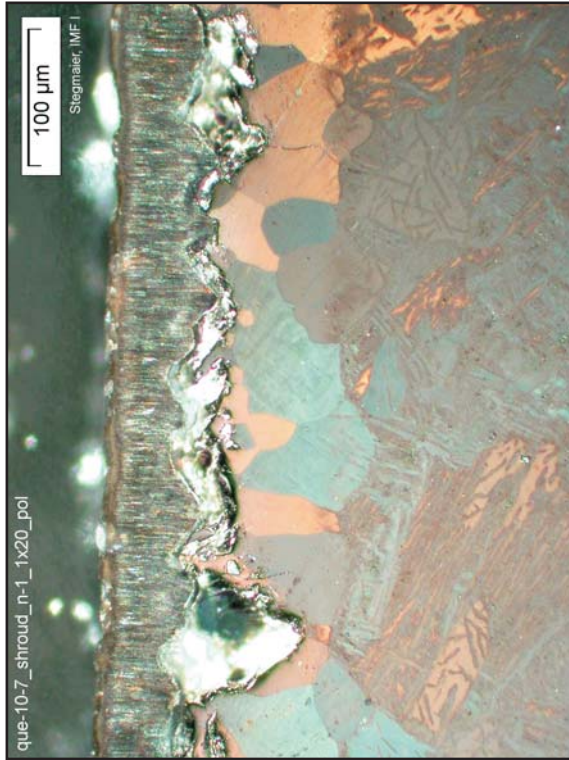
Fig. 107: QUENCH-10; Cross section at 1080 mm bundle elevation (QUE-10-7). Oxidation state of rod 5 at two positions, showing formation of scale fractures caused by air penetration.



Pre-transition scale with scalloped growth front



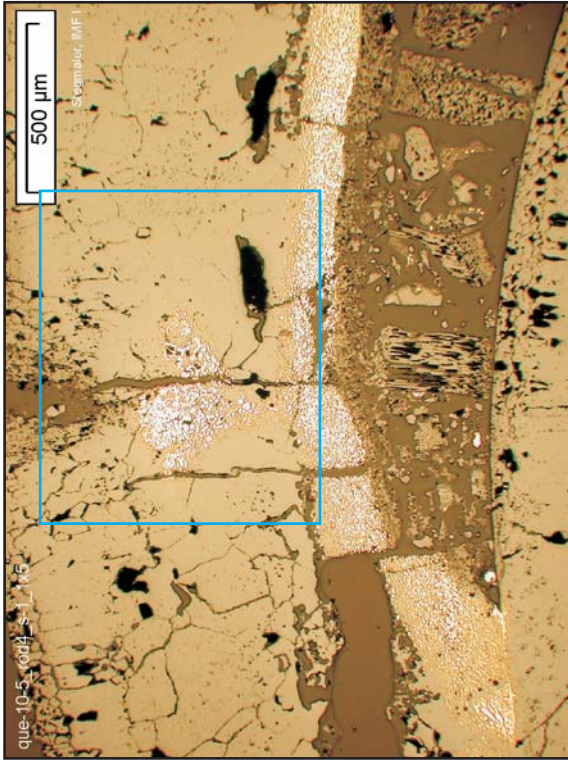
Post-transition scale with lateral cracks



Polarized light, same areas as above, respectively

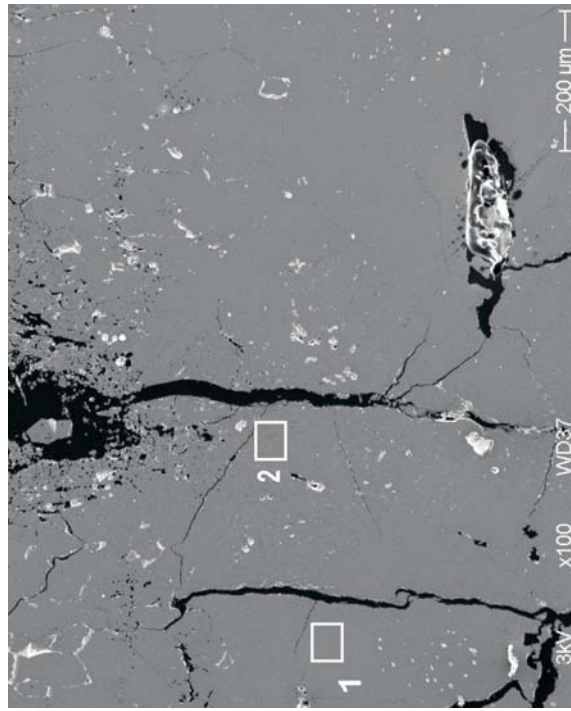


Fig. 108: Cross section at 1080 mm bundle elevation (QUE-10-7). Shroud oxidation, showing the typical pre-transition scale (left), compared to local presence of post-transition scale (right).



LM, overview;  
suspected ZrN  
phase bright

BSE image,  
similar area; no  
contrast between  
ZrN and ZrO<sub>2</sub>



SE image, areas  
of EDX analyses  
indicated

EDX spectrum  
for Pos. 2

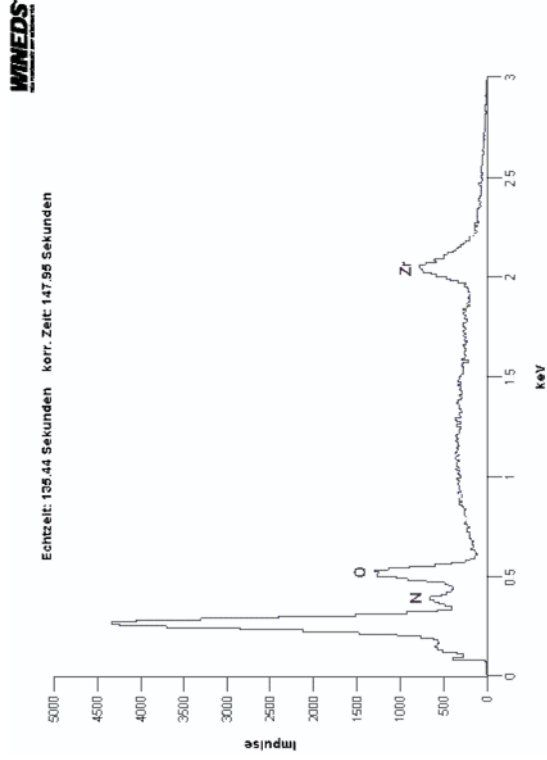
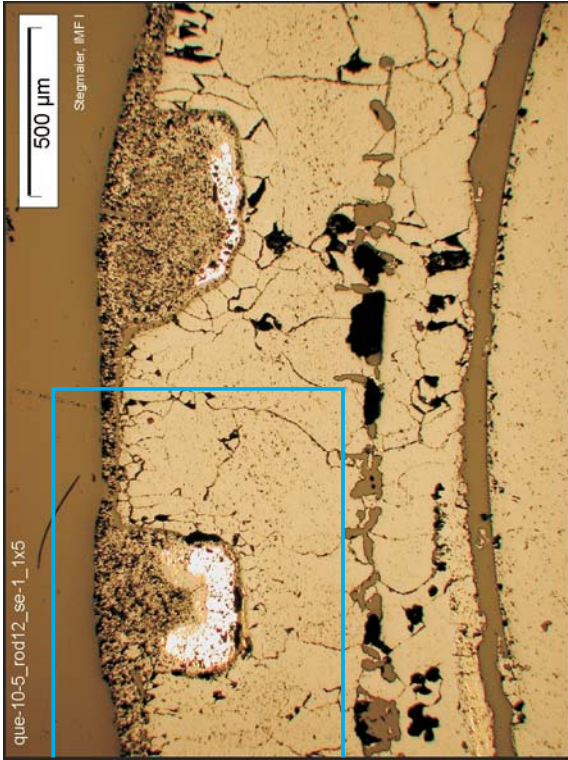
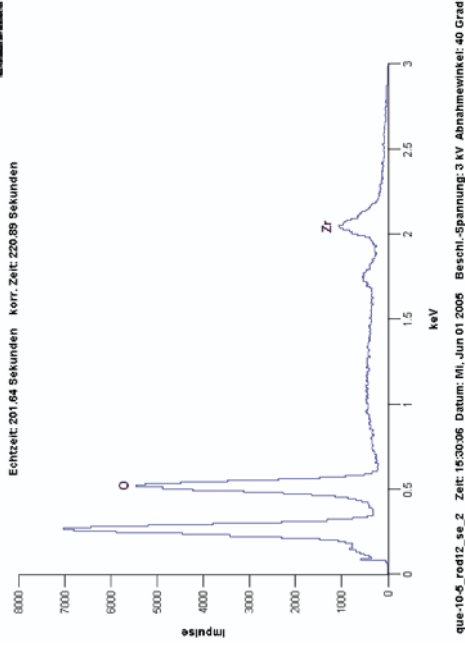


Fig. 109: QUENCH-10; SEM analysis of rod 4 at 850 mm elevation (QUE-10-5). Comparison of LM and BSE contrast indicates presence of ZrN phase, EDX spectrum confirms this. (See Fig. 95)

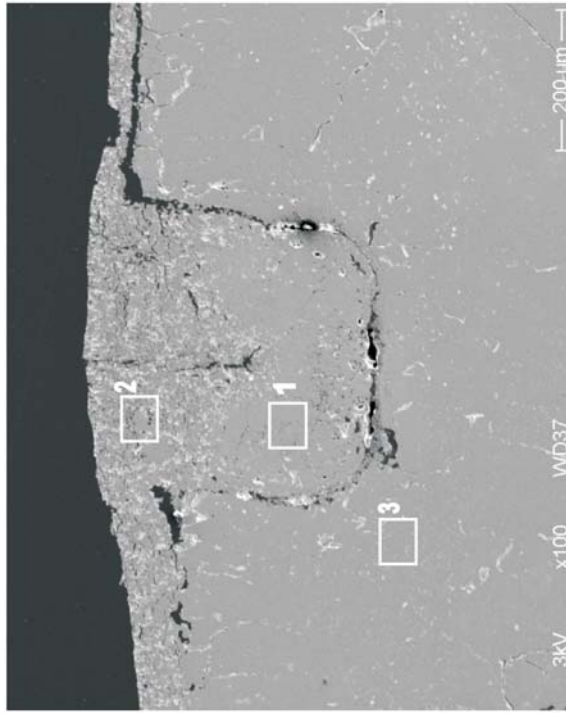


LM, overview;  
suspected ZrN  
phase bright

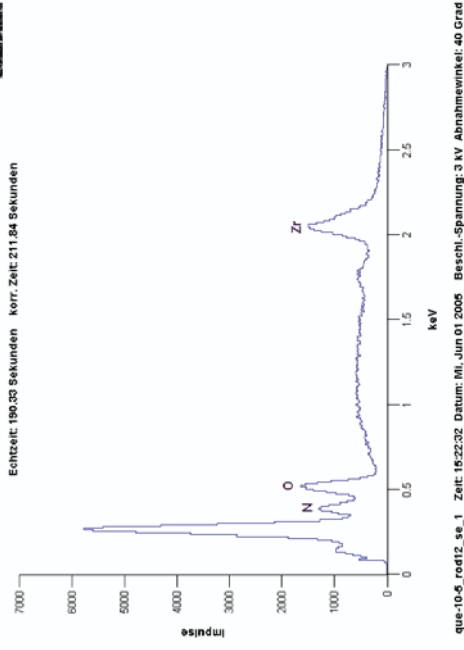
EDX spectrum  
for Pos. 2: ZrO<sub>2</sub>



SE image, areas  
of EDX analyses  
indicated

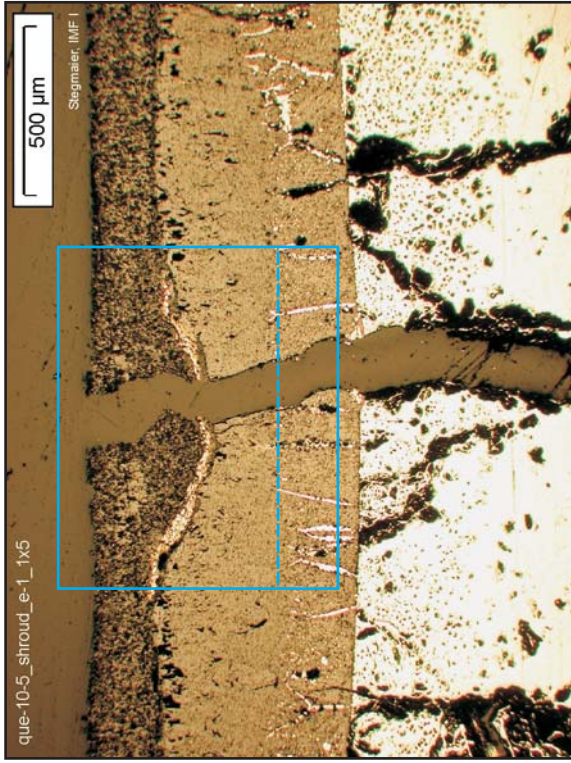


EDX spectrum  
for Pos. 1: ZrN



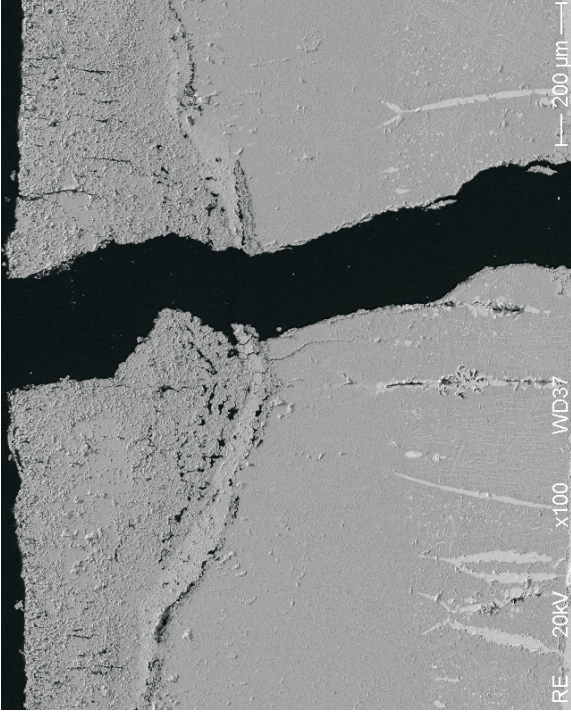
EDX spectrum for Pos. 3: ZrO<sub>2</sub>,  
not depicted, similar to Pos. 2

Fig. 110: QUENCH-10; SEM analysis of rod 12 at 850 mm elevation (QUE-10-5). Comparison of LM and SE contrast indicates presence of ZrN phase, EDX spectra confirm ZrN or ZrO<sub>2</sub>, respectively. (See Fig. 96)

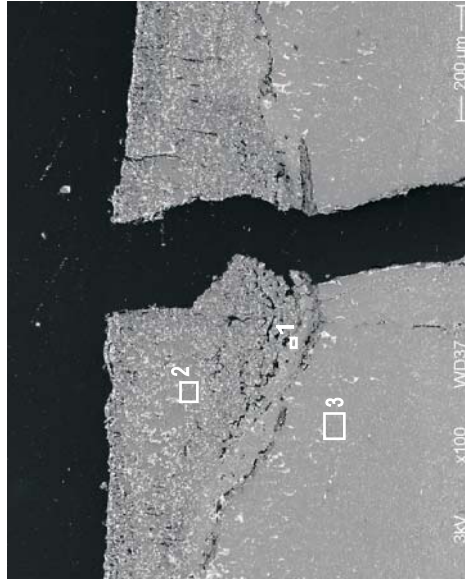


LM, overview;  
bright band within  
scale suspected to  
be ZrN phase

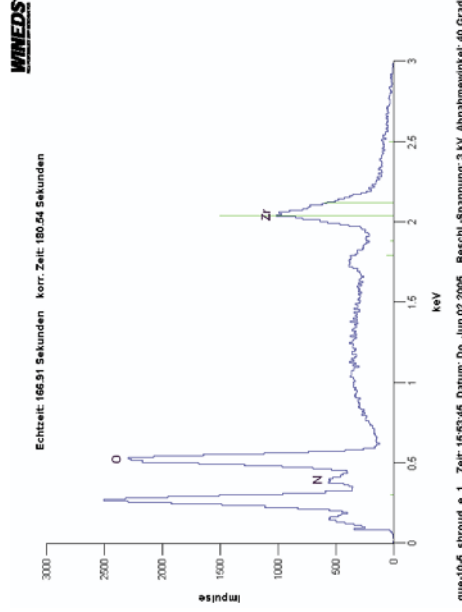
Magnified BSE image;  
ZrN and ZrO<sub>2</sub> not  
distinguished, contrast  
of α-Zr(O) phase



SE image, with areas of EDX analyses



EDX spectrum for Pos. 1



EDX spectrum for Pos. 3

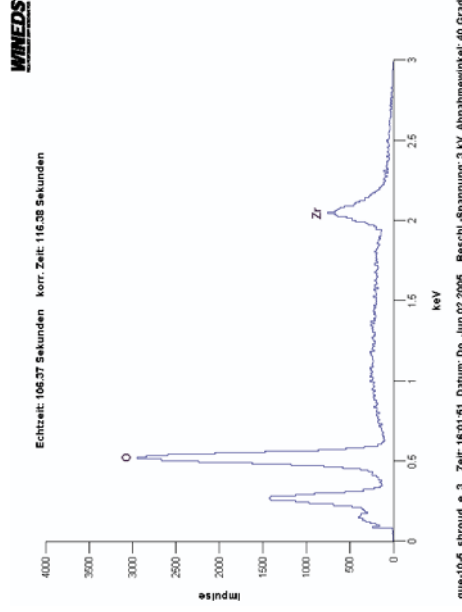
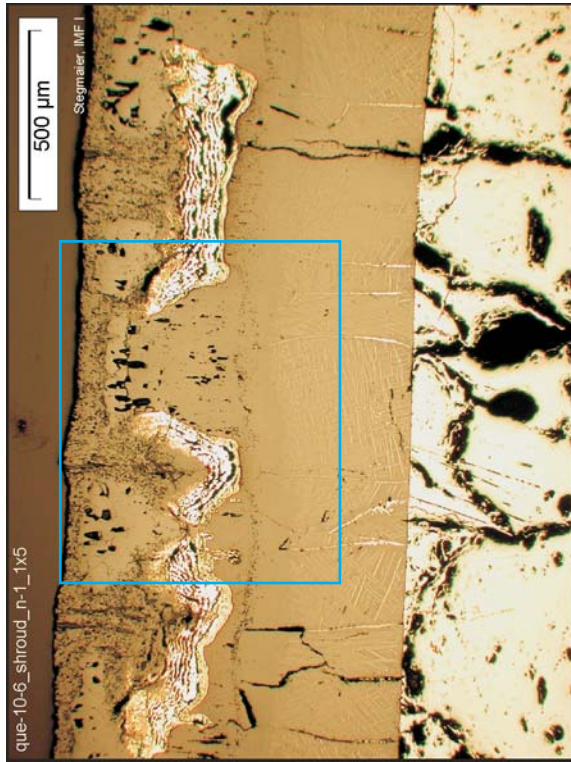


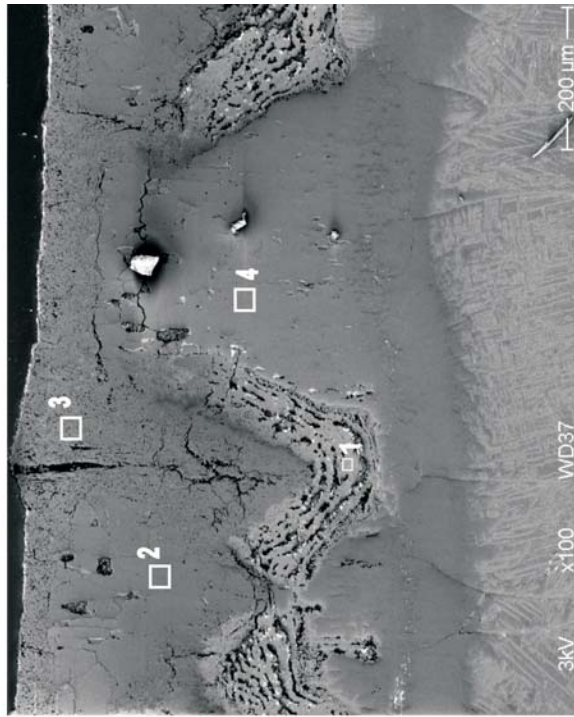
Fig. 111: QUENCH-10; SEM analysis of the shroud at 850 mm elevation (QUE-10-5). Comparison of LM, BSE and SE contrasts, and EDX spectra confirm presence of ZrN phase. (See Fig. 98)



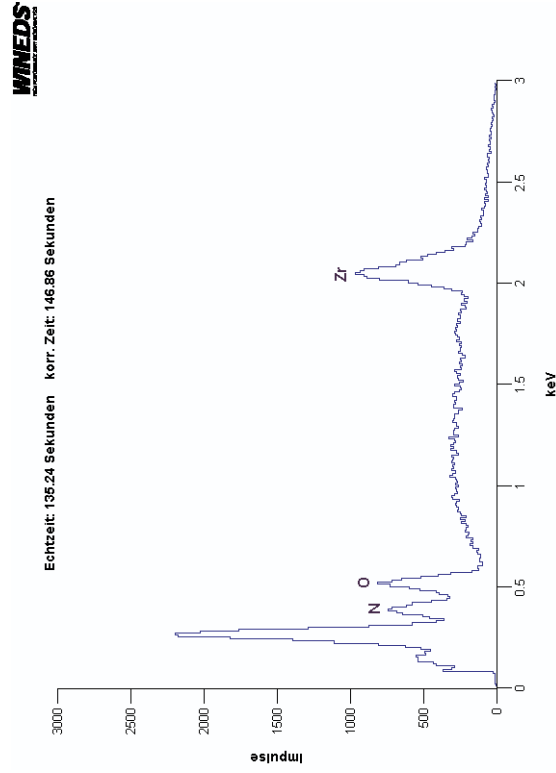
LM, overview;  
bright band within  
scale suspected to  
be ZrN phase



BSE image, overview;  
ZrN and ZrO<sub>2</sub> not  
distinguished, contrast  
of shroud matrix

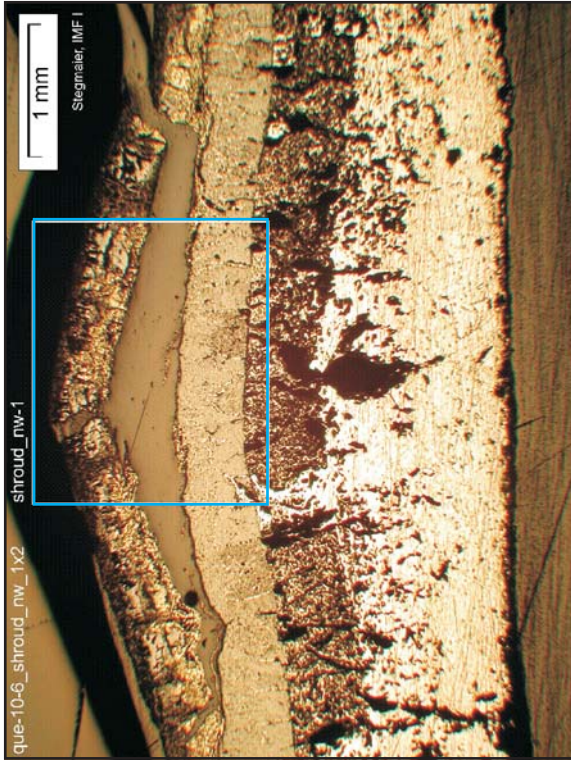


SE image, with areas  
of EDX analyses



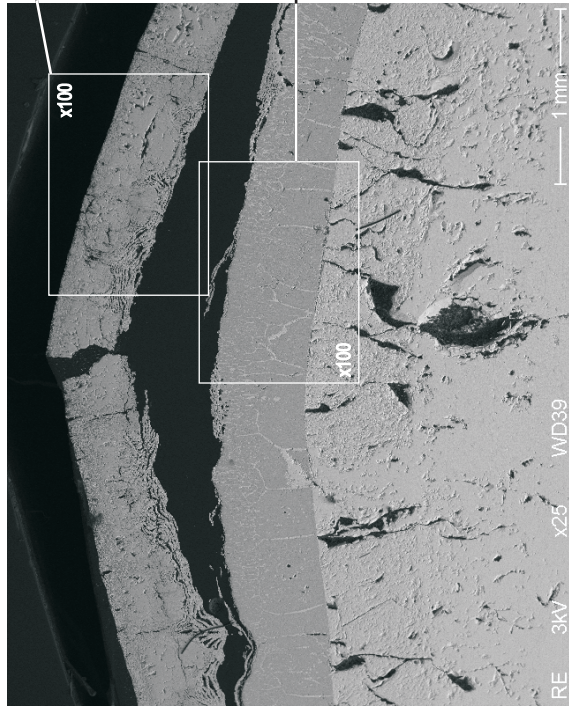
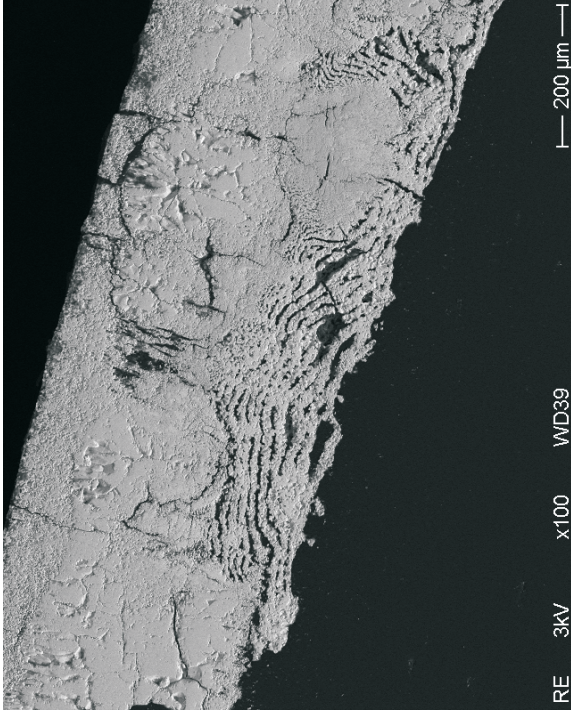
EDX spectrum  
for Pos. 1

Fig. 112: QUENCH-10; SEM analysis of the shroud at 950 mm elevation (QUE-10-6). Comparison of LM, BSE and SE contrasts, and EDX spectra confirm presence of ZrN phase. (See Fig. 100)



LM overview,  
showing spalled  
outer scale  
sublayer with  
suspected ZrN  
phase

BSE image of outer  
scale sublayer,  
showing crack  
system within ZrN  
regions



BSE image,  
overview

BSE image of inner  
scale sublayer with  
 $\alpha$ -Zr(O) precipitates

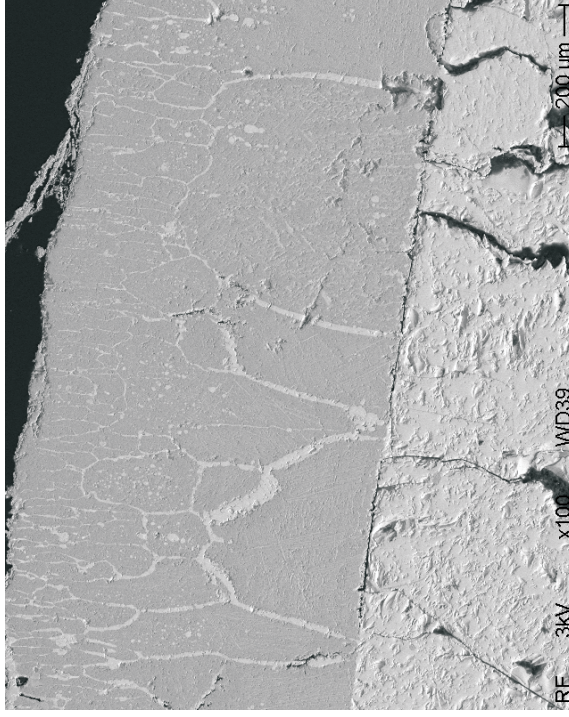


Fig. 113: QUENCH-10; SEM analysis of the shroud at 950 mm elevation (QUE-10-6). Comparison of LM and BSE contrast is sufficient to confirm presence of ZrN phase. (See Fig. 101)

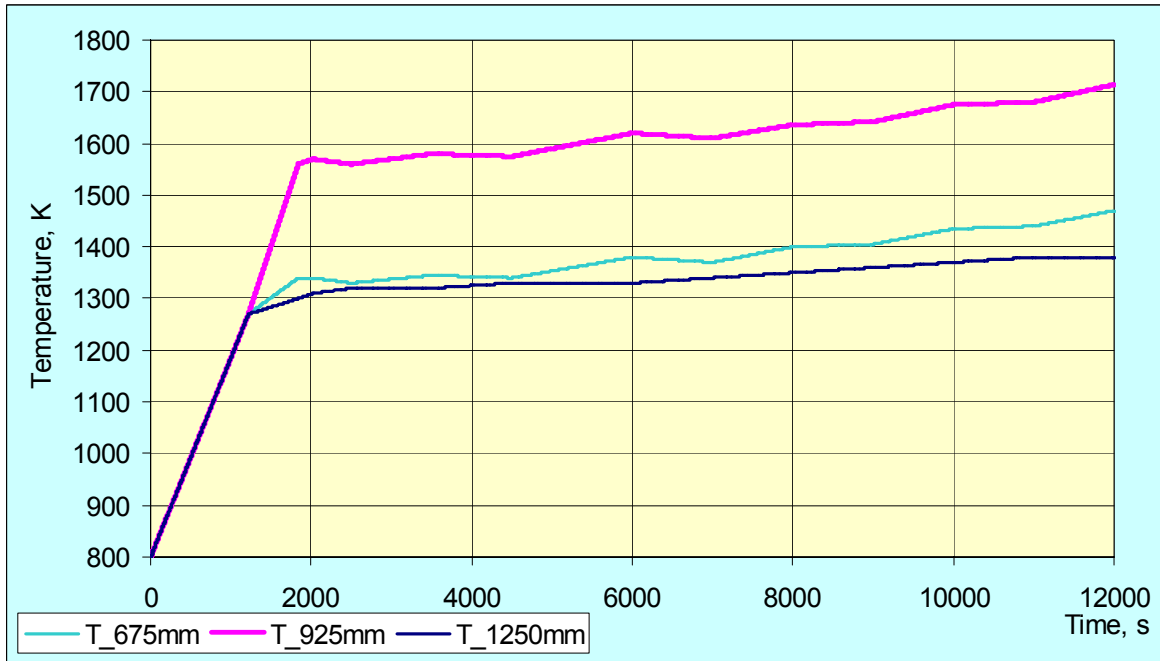


Fig. 114: Temperature profiles for three of eighteen meshes (elevations 675, 925, and 1250 mm) calculated with SCDAP/RELAP 5 and used as an input to the SVECHA computations of test QUENCH-10.

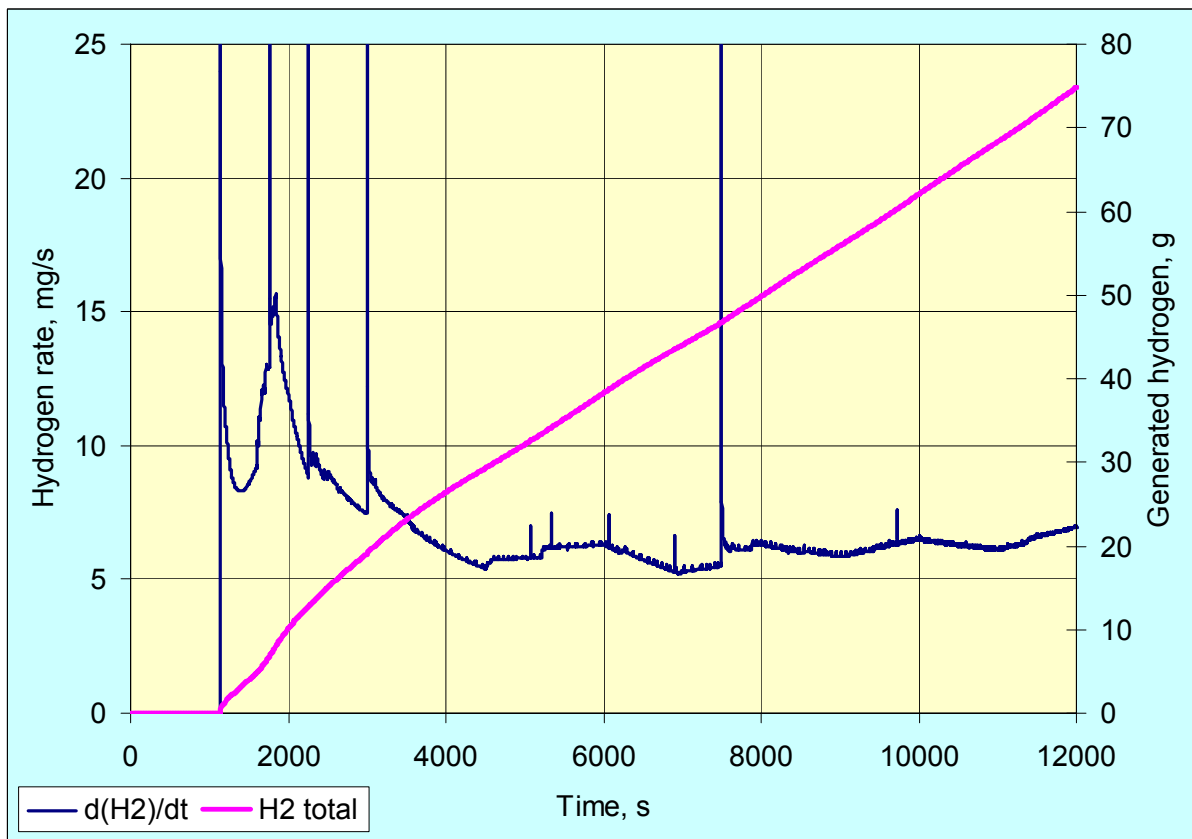


Fig. 115: SVECHA calculation of hydrogen production in QUENCH-10, extrapolated from the central rod to the whole bundle.

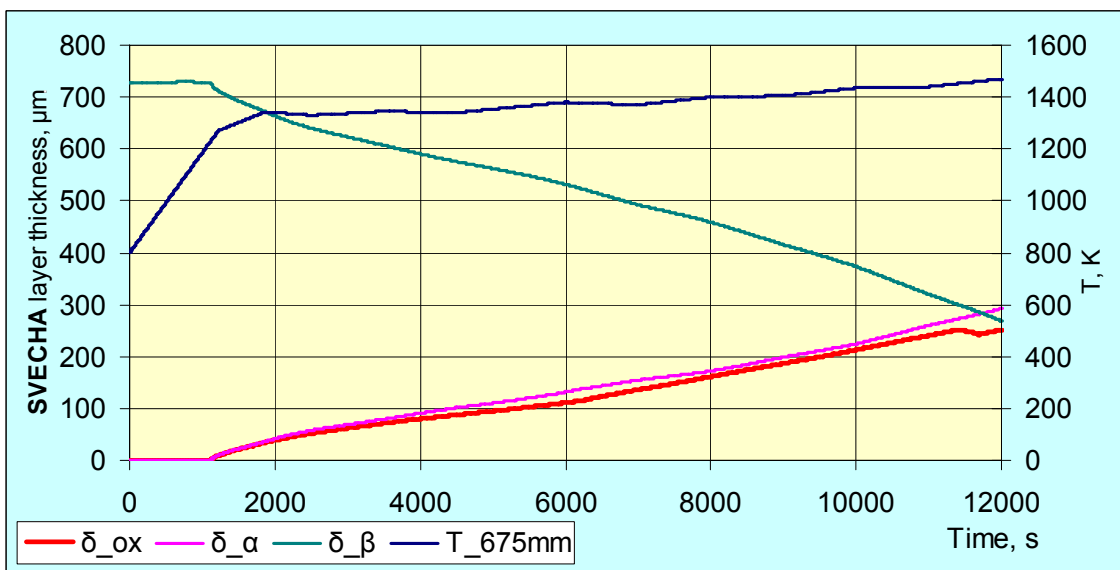
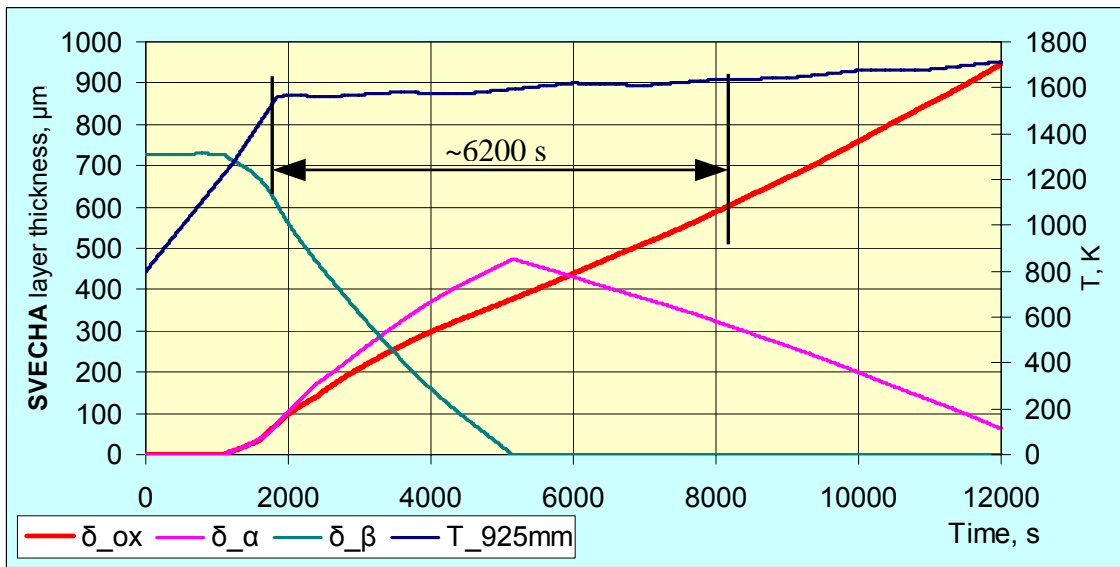
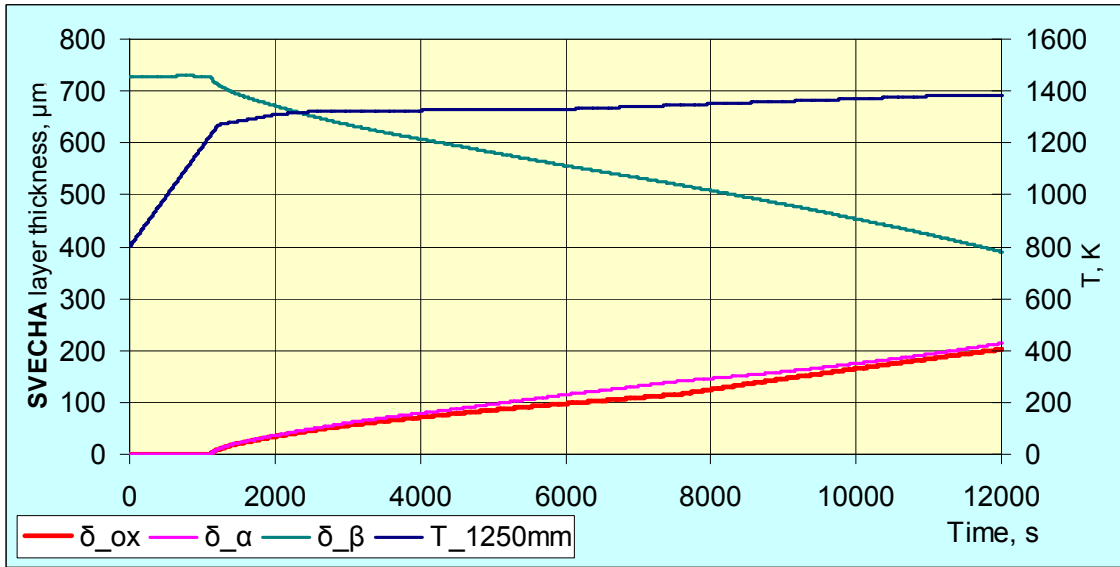


Fig. 116: Evolution of the cladding layer thickness at different bundle elevations computed by SVECHA for experiment QUENCH-10.

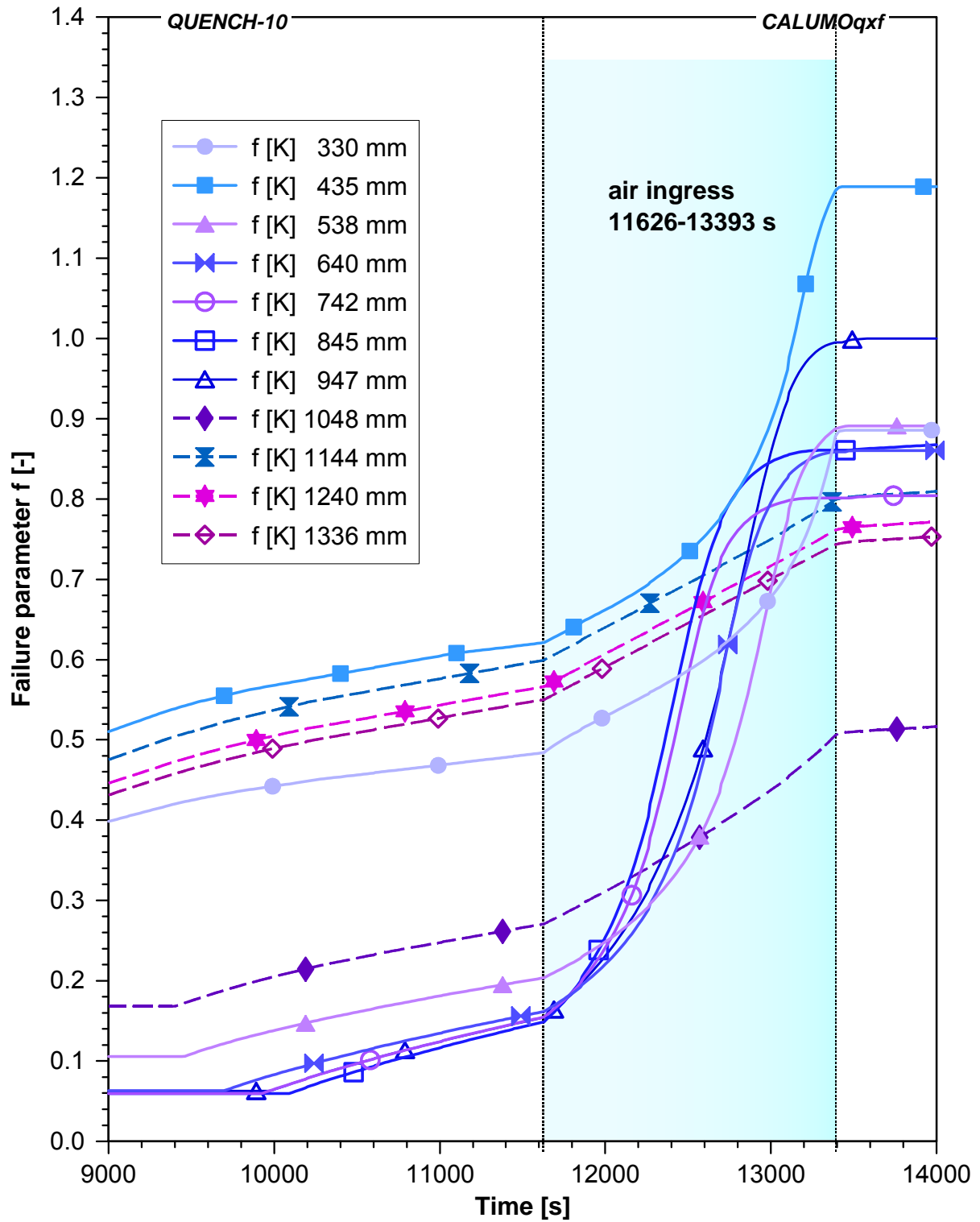


Fig. 117: Failure parameter  $f$  for for the inner row of heated fuel rod simulators versus time.

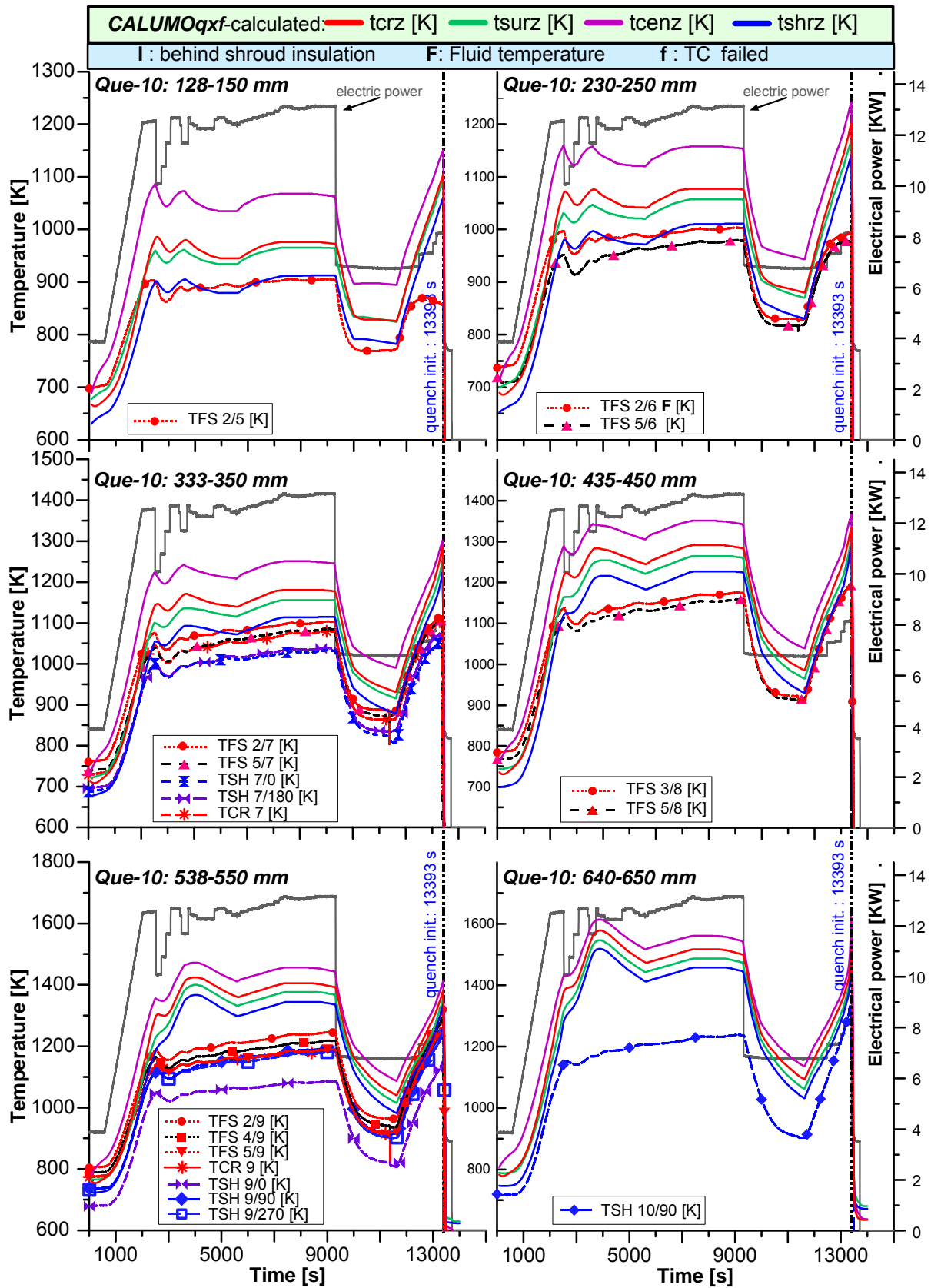


Fig. 118: Evolution of rod and shroud temperatures of QUEENCH-10 at elevations 128-650 mm; CALUMOqxf-calculated data in comparison with experimental values.

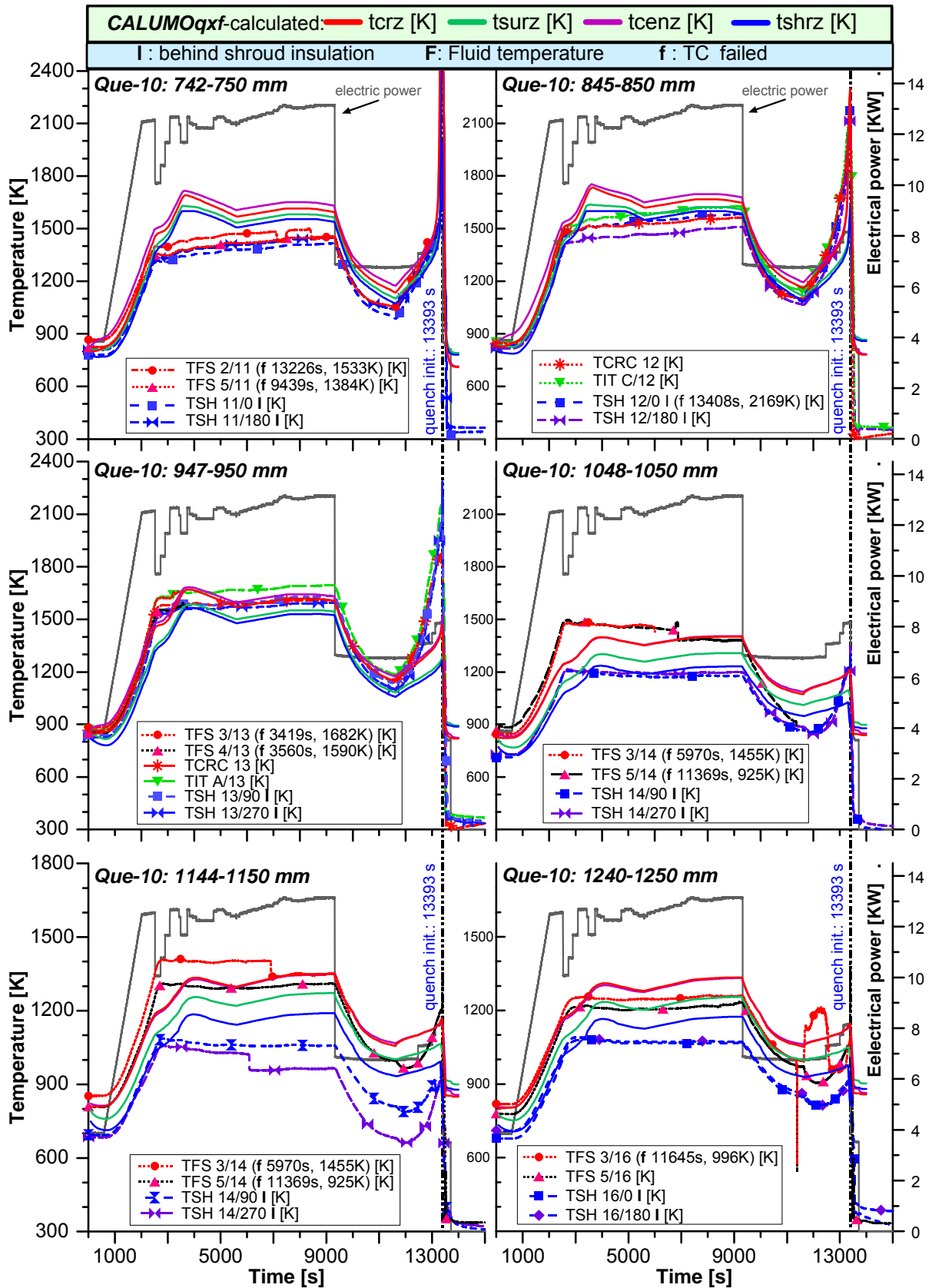


Fig. 119: Evolution of rod and shroud temperatures of QUENCH-10 at elevations 742-1250 mm; CALUMOqxf-calculated data in comparison with experimental values.

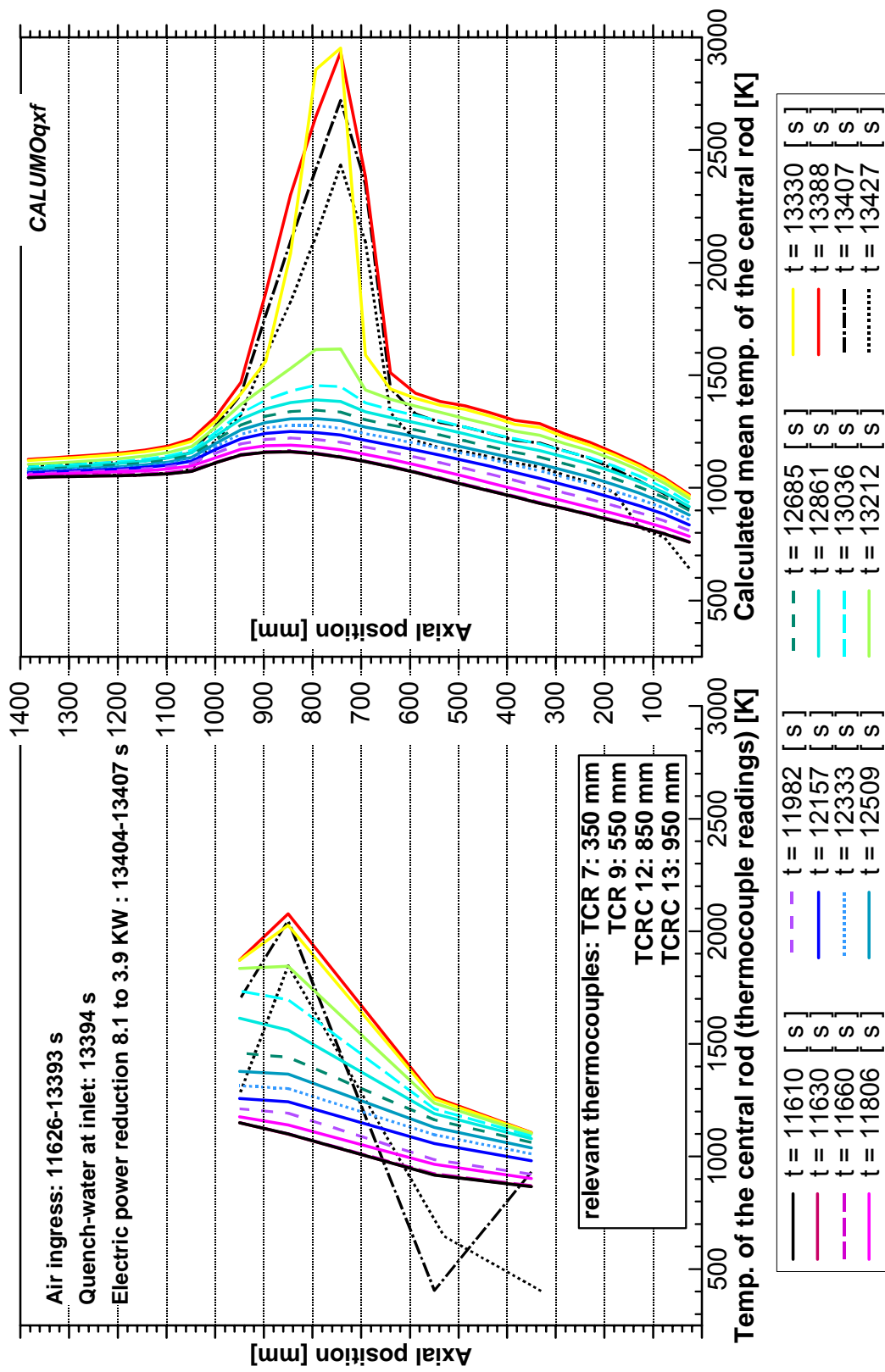


Fig. 120: Axial profile of the central rod temperature over the period of air ingress.

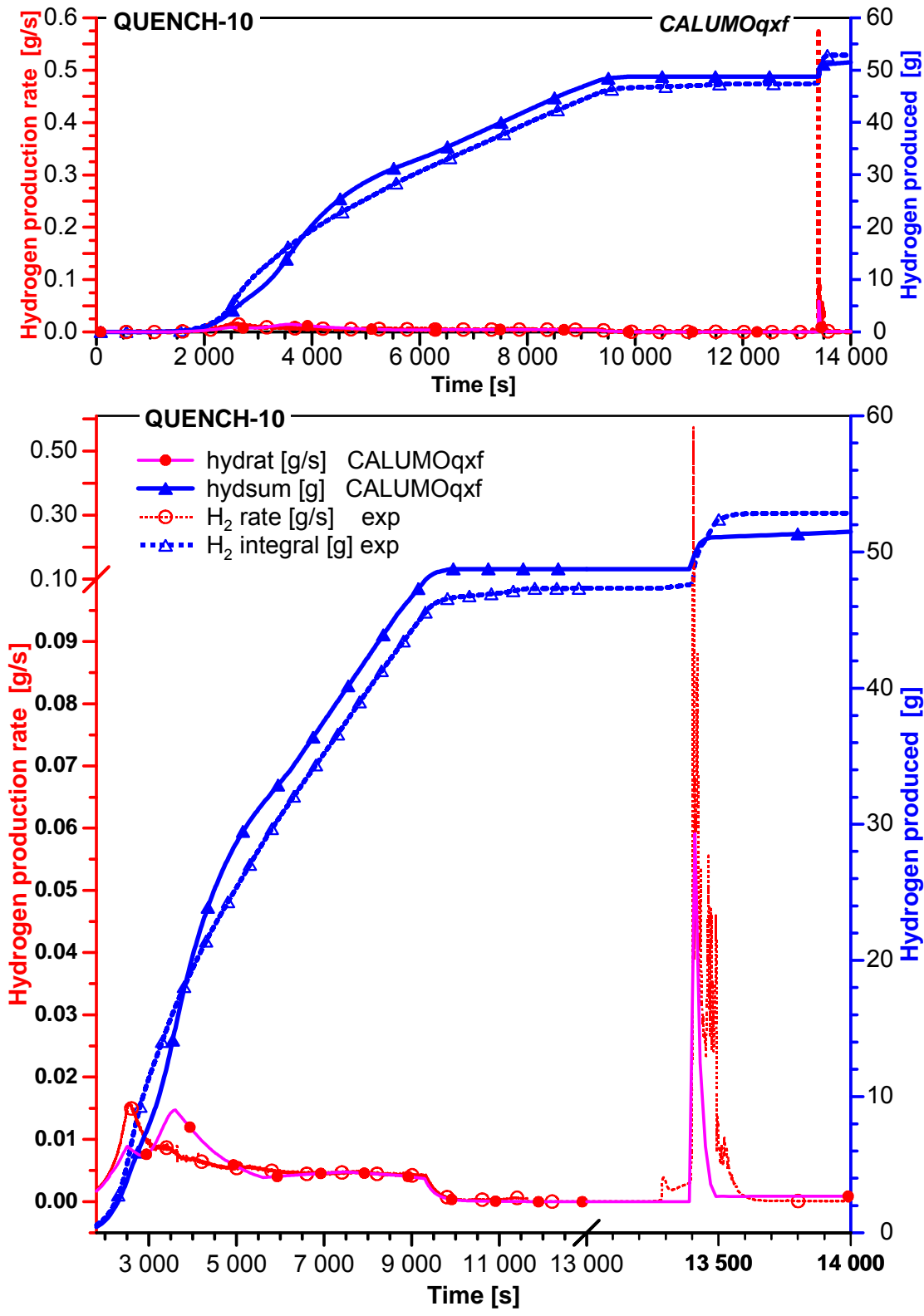


Fig. 121: Evolution of the hydrogen production rate and the overall produced hydrogen for QUENCH-10 calculated with CALUMOqxf (overview on top, detailed graph bottom).

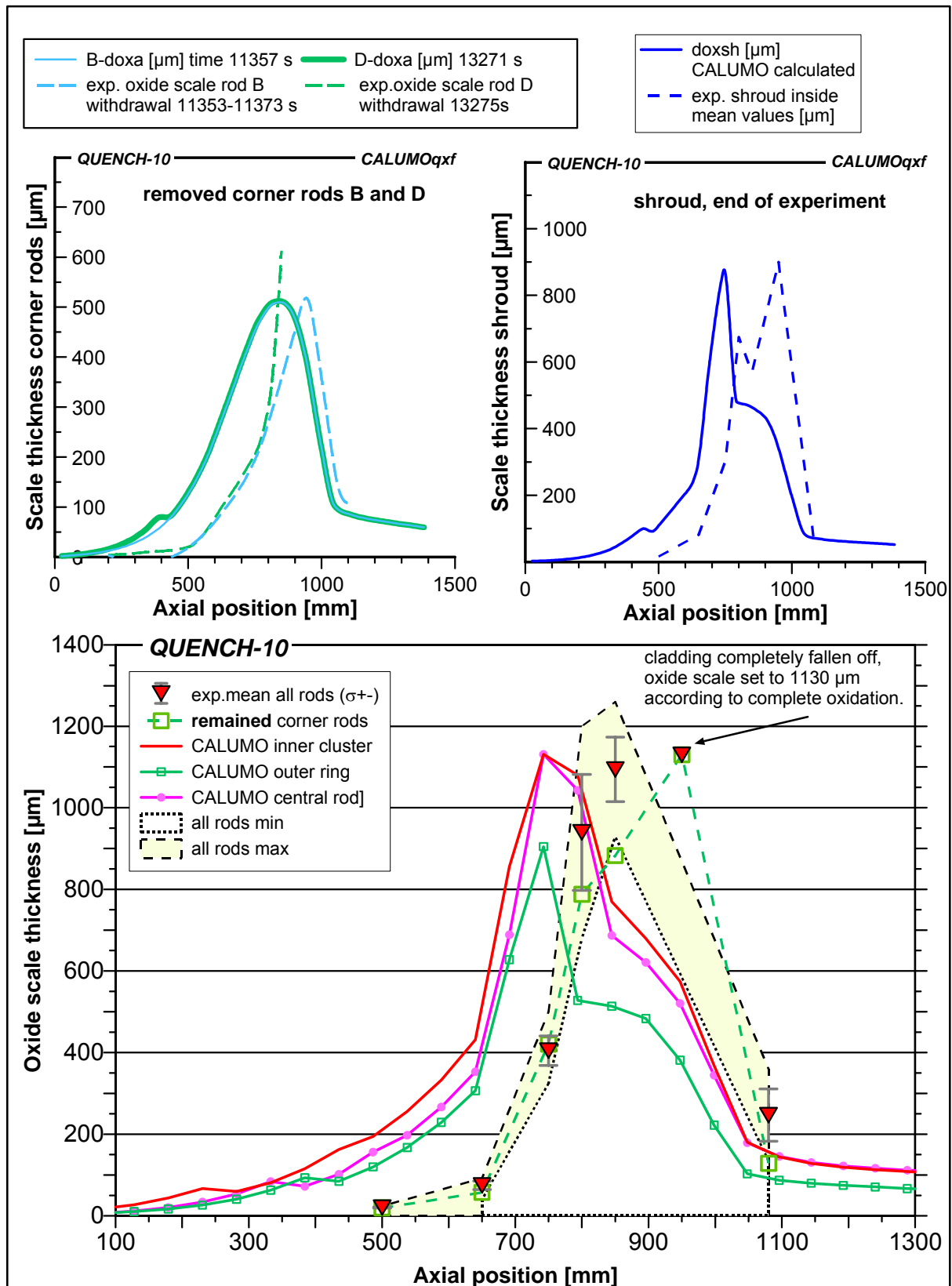


Fig. 122: Axial distribution of the oxide scale thickness for the removed corner rods B and D (top left); at the end of QUENCH-10 for the shroud (top right) and all rods (bottom).